Conformal and reconfigurable sparse metasurfaces : advanced analytical models and antenna applications

Uladzislau Papou

université
PARIS-SACLAY

Conformal and reconfigurable sparse metasurfaces: advanced analytical models and antenna applications

Thèse de doctorat de l'Université Paris-Saclay

École doctorale n° 575, Electrical, Optical, Bio : Physics and Engineering (EOBE)

Spécialité de doctorat: Génie électrique

Unité de recherche: Université Paris-Saclay, CentraleSupélec, ONERA, SONDRA, 91190, Gif-sur-Yvette, France

Référent: CentraleSupélec

Thèse présentée et soutenue à Palaiseau, le 16 juillet 2020 , par

Uladzislau PAPOU

Composition du jury:

Julien de ROSNY DR CNRS, Institut Langevin, ESPCI	Président
Stefan ENOCH DR CNRS, Institut Fresnel, Aix-Marseille Université	Rapporteur & Examinateur
Mauro ETTORRE CR CNRS/HDR, IETR, Université de Rennes 1	Rapporteur & Examinateur
Patrice GENEVET CR CNRS, CRHEA-CNRS	Examinateur
André de LUSTRAC Professeur Emérite, C2N, Université Paris-Saclay	Examinateur
Stefano MACI Professeur, Université de Sienne	Examinateur
Fabrice BOUST Dr Sc./Chercheur, ONERA	Directeur
Shah Nawaz BUROKUR MCF/HDR, LEME, Université Paris Nanterre	Codirecteur
Hervé JEULAND Dr/Ingénieur de Recherche, ONERA	Invité

Thèse de doctorat

NNT: 2020UPASC027

To those who will find it useful.

Acknowledgements

First of all, I would like to express my sincere gratitude to my supervisors, Dr. Fabrice BOUST and Prof. Shah Nawaz BUROKUR, for always believing in me, passing on your knowledge, experience and wisdom, helping me self-develop. Thank you for your enthusiasm and the autonomy that you granted me. Under your supervision, we managed to overcome many difficulties and obtain excellent results. Thank you for your patience and constant support on both work- and life-related matters. It was a pleasure and an honor for me to have you as my supervisors.

I am thankful to all members of the jury, who kindly accepted to evaluate this work in spite of major challenges the world faced in the year 2020. In particular, I express my gratitude to Dr. Stefan ENOCH and Dr. Mauro ETTORRE, who kindly agreed to review this work. I thank Dr. Julien de ROSNY, Prof. André de LUSTRAC. Dr. Patrice GENEVET and Prof. Stefano MACI for being exterminators of the work. Finally, I thank Dr. Hervé JEULAND for participating in the jury.

I am grateful to Dr. Badreddine RATNI for his warm-heartedness, altruism and constant support during all these three years.

I would like to warmly thank my first supervisor from Belarusian State University, Prof. Andrey NOVITSKY, without whom all this would not probably happen.

I am grateful to all members of SONDRA team, with whom I spent these three amazing years. I thank SONDRA's directors: Dr. Marc LESTURGIE, M. Sylvain AZARIAN and M. Stéphane SAILLANT, who warmly welcomed me in the laboratory. I am particularly grateful to the assistant administrator, Mme. Virginie BOUVIER, who helped me in so many situations it was difficult to keep track. I am thankful to SONDRA's permanent researchers: Dr. Israel HINOSTROZA, Dr. Chengfang REN, Dr. Giovanni MANFREDI, Dr. Jean-Philippe OVARLEZ, Dr. Thierry LETERTRE, Dr. Régis GUINVARC'H, Dr. Laetitia THIRION-LEFEVRE

and Dr. Chin Yuan CHONG, who were always there to give me a piece of advice. I am thankful to M. Anil CHERALY from ONERA for his help in conducting experiments and M. Maurice TORDJMAN from LEME for the realization of the mechanical parts. I thank my comrades PhD students: Dr. Pedro MENDES RUIZ, Dr. Samir OUEDRAOGO, Dr. Eugénie TERREAUX, Dr. Ammar MIAN, Dr. Ahmad BITAR, Bruno MERIAUX, Thibault TAILLADE, Dihia SIDI AHMED, Nathan PAILLOU, Jose Agustín BARRACHINA, Antoine COLLAS and Cyprien DOZ for their friendship, support and many pleasant moments we shared together. I wish to individually thank our kind friend, Orian COUDERC, who left us very young. You will always remain in our hearts.

In the first year of my PhD thesis I was very lucky to spend several weeks at Aalto University and work with the group of Prof. Sergei TRETYAKOV, where I learnt many things and met many friends. I am grateful to Prof. Sergei TRETYAKOV for warmly welcoming me in his laboratory. I am thankful to my friends and colleagues: Dr. Viktar ASADCHY, Dr. Svetlana TCVETKOVA, Dr. Ana DÍAZ-RUBIO, Grigorii PTITCYN, Dr. Xuchen WANG, Ms. Bhakti CHOWKWALE, Mr. Francisco CUESTA, Dr. Fu LIU for many happy memories and improved badminton skills.

There are no words enough to thank my family. I am thankful and indebted to my mother and father, my brother and sister, my uncle and my grandmother. I am grateful to my fiancée, who was side by side with me these years. Thank you for your love and your patience.

Contents

Résumé français

Introduction

Les travaux sur les métamatériaux ont pris leur essor au tournant des années 2000 suite notamment aux publications de D.R. Smith “Composite Medium with Simultaneously Negative Permeability and Permittivity” et de J. B. Pendry “Negative Refraction Makes a Perfect Lens”. Très rapidement, à la suite des métamatériaux volumiques 3D, sont apparues les métasurfaces, une version 2D des métamatériaux ne comportant qu'une seule cellule dans l'épaisseur. Ces métasurfaces présentent l'avantage de réduire les pertes et d'ouvrir la porte à de nouvelles fonctionnalités. En particulier, en introduisant des modulations spatiales à l'échelle de la longueur d'onde, il devient alors possible de manipuler l'onde incidente pour créer des phénomènes de réfraction ou de transmission anormaux. Ces métasurfaces prennent tout leur intérêt pour des applications antennaires de type reflectarray, transmitarray, antenne à cavité Fabry-Perot ou à onde de fuite. Dans la majorité des cas, la conception de ces métasurfaces repose sur une représentation des propriétés de la métasurface, à l'aide d'impédances de surface ou de coefficients de réflexion/transmission locaux, qui, d'une part requiert une forte densité d'éléments, et d'autre part, prend en compte les interactions entre éléments de manière approximative.

La démarche adoptée dans cette thèse est de chercher à dépasser ces approches conventionnelles pour, en particulier, améliorer les performances des métasurfaces électroniquement reconfigurables. Les applications visées en priorité sont les antennes capables de pointer leur faisceau dans différentes directions, opérant aux fréquences microondes. Le manuscrit comporte une introduction générale, un état de l'art sur les métasurfaces reconfigurables, quatre chapitres sur les travaux réalisés et une conclusion. Les travaux réalisés sont décomposés en deux thèmes: les métaréseaux et les métasurfaces éparses.

Métaréseaux

Les métaréseaux ont été introduits en 2017 par Y. Ra'di *et al.* (Ref. [45]). Ils sont constitués de réseaux de fils arrangés périodiquement. Ces fils sont structurés à une échelle petite devant la longueur d'onde de sorte qu'il soit possible d'introduire une impédance linéique (électrique ou magnétique) effective. En revanche, dans la direction perpendiculaire, les distances sont de l'ordre de la longueur d'onde. Les propriétés de ces fils se répètent périodiquement avec une période généralement plus grande que la longueur d'onde (définissant ainsi une "supercellule" élémentaire) ce qui est à l'origine d'ordres diffractés propagatifs.

Le chapitre 2 du manuscrit est consacré au développement de modèles analytiques qui permettent de calculer les amplitudes des ordres diffractés en fonction des impédances des fils. La configuration étudiée est celle d'un métaréseau placé devant un plan parfaitement réflecteur. Plus particulièrement, deux formules sont établies :

- la première relie les amplitudes diffractées aux intensités parcourant les fils Eq. (2.9);

- la seconde – qui n'est autre que l'équation d'Ohm – relie l'intensité parcourant le fil, l'impédance du fil chargé, son impédance d'entrée, les effets des autres fils via les coefficients de mutuelles impédances et le champ excitateur Eq. (2.11).

Par ailleurs, il est montré que l'énergie réfléchie peut être arbitrairement répartie parmi M ordres diffractés dès que le nombre de fils N par supercellule est égal à M. Dans le cas général, les impédances des fils doivent comporter une partie réactive ainsi qu'une partie active ou à pertes ce qui peut s'avérer très difficile à réaliser. Toutefois, il a pu être montré qu'un contrôle précis du champ proche à l'aide de fils supplémentaires permet de réaliser cette répartition entre ordres propagatifs en s'affranchissants de la présence d'éléments actifs ou à pertes, donc avec uniquement des éléments capacitifs ou inductifs. Ce résultat a été validé numériquement et expérimentalement en réalisant des réflexions anormales avec des supercellules comportant $N = 2M$ éléments purement réactifs. Les performances obtenues sont très élevées. Par exemple, dans le cas d'une réflexion à 80° pour une incidence normale, l'efficacité mesurée en chambre anéchoïde est supérieure à 95%. Les réalisations expérimentales ont porté sur des métaréseaux électriques (champ électrique parallèle au fils) mais la théorie a également été développée pour des métaréseaux magnétiques (champ magnétique parallèle au fils).

Approximation périodique locale et aide à la conception

L'approximation périodique locale (LPA) joue un rôle crucial dans la conception des méta-surfaces (Ref. [75] et [112]). Elle consiste à placer un motif élémentaire au sein d'un réseau périodique et à calculer numériquement les coefficients de réflexion et de transmission. Ensuite ces coefficients (ou les impédances qui en sont déduites) sont utilisés dans des arrangements non périodiques. Cette approche est inappropriée pour des métaréseaux où les interactions entre éléments sont prises en compte (rigoureusement) par ailleurs et où la distance entre éléments est susceptible de changer. En fait, il faut disposer d'un paramètre (impédance linéique par exemple) spécifique au fil indépendamment des autres fils et des caractéristiques du substrat. Une procédure a été développée pour cela dans le chapitre 3. Elle comporte toujours un calcul, à l'aide d'une simulation numérique, du coefficient de réflexion d'une cellule élémentaire assortie de conditions de périodicité. Ce coefficient de réflexion est utilisé pour remonter à l'intensité moyenne qui parcourt le fil; ce courant est ensuite introduit dans un modèle analytique qui soustrait les contributions du substrat et des autres fils. Cette nouvelle LPA a été développée pour les métaréseaux électriques et magnétiques.

La procédure de conception des métaréseaux est également détaillée dans ce chapitre. Les premiers paramètres à fixer sont la période et l'angle d'incidence de l'onde. Le nombre de modes propagatifs est alors donné par la formule classique des réseaux de diffraction. L'épaisseur du substrat est ensuite choisie de manière à éviter la présence de modes guidés dans le substrat. En parallèle, il faut concevoir un motif qui permette d'accéder à une gamme suffisante d'impédance quand on modifie un (ou plusieurs) de ses paramètres géométriques. On prépare alors, à l'aide de la LPA et de simulations numériques sur une cellule élémentaire, une bibliothèque d'impédances linéiques correspondant à l'ensemble des paramètres géométriques possibles. Pour résumer, les amplitudes des ordres diffractés sont fonction du nombre de fils et de l'intensité qui les parcourt Eq. (2.9); ces intensités sont reliées aux impédances via l'équation d'Ohm Eq. (2.11) et ces impédances sont reliées aux paramètres géométriques des motifs grâce à la LPA. Il reste donc à mettre en place une procédure d'optimisation qui permette de trouver les paramètres qui satisfont les objectifs en termes d'amplitude des ordres diffractés. L'algorithme retenu pour cette optimisation est celui de l'essaim de particules. Il est important de noter que les boucles d'optimisation ne font appel à aucune simulation "full-wave". Celles-ci sont faites une fois pour toutes lors du choix du motif élémentaire et ne portent que sur une cellule élémentaire assortie

de conditions périodiques.

Dans ce chapitre, pour illustrer la LPA et la méthode d'optimisation, deux exemples numériques et un exemple expérimental sont présentés. Dans les deux exemples numériques, le premier porte sur un métaréseau magnétique aux fréquences microondes et le deuxième sur un métaréseau électrique dans le domaine infrarouge. La démonstration expérimentale a été faite sur un métaréseau électrique aux fréquences microondes.

Métasurfaces conformes éparses

Les métaréseaux permettent de contrôler exactement l'énergie réfléchie dans les directions des ordres diffractés. Toutefois, ils souffrent de plusieurs limitations :

- leur caractère périodique ne leur permet de diriger l'énergie que selon un ensemble fini de directions, fixé par la dimension de la période et l'angle d'incidence (ce nombre peut être relativement élevé dans le cas de fils comportant des éléments accordables ce qui permet de faire varier le nombre d'éléments par période et donc sa taille);
- ils requièrent des surfaces planes;
- ils doivent être éclairés par une onde plane.

Dans le chapitre 4, la démarche appliquée aux métaréseaux est généralisée à des surfaces cylindriques quelconques éclairées par une onde cylindrique quelconque. De plus, le réseau de fils n'a plus aucun caractère de périodicité. Les distances entre fils peuvent être quelconques à condition d'être suffisantes pour que les interactions entre ces fils, qui sont structurés, puissent être représentées par des interactions entre des fils de diamètre nul. Il s'agit donc de métasurfaces à faible densité que nous appelons métasurfaces éparses. Concrètement, le champ rayonné par un réseau périodique infini de fil Eq. (2.4) qui s'exprimait par une somme de fonctions de Hankel, chacune étant pondérée par le courant du fil considéré, devient Eq. (4.1) une somme finie (autant que de fils) de fonctions de Green pondérées par un courant. L'équation d'Ohm qui relie l'intensité et le courant parcourant le fil est inchangée si ce n'est que les coefficients d'impédances mutuelles doivent également être calculés à l'aide de fonctions de Green Eqs. (4.2)–(4.4). Cette formulation montre bien que le problème résolu est global et que chaque contribution issue de chaque fil est bien prise en compte. Pour obtenir le diagramme de rayonnement désiré et pour une géométrie donnée, il faut encore déterminer le nombre de fils à placer et leur impédance.

Pour estimer le nombre de fils nécessaires, on décompose en série de Fourier, selon l'angle polaire, le diagramme que l'on désire obtenir. Si $2M + 1$ coefficients sont nécessaires pour obtenir une bonne approximation du diagramme désiré alors il faudra au moins $2M + 1$ fils. Comme pour les métaréseaux, les impédances requises dans ces conditions peuvent exiger des éléments actifs ou des pertes. En pratique, il faut donc un nombre d'éléments supérieur à $2M + 1$.

Par rapport aux métaréseaux, la mise en œuvre de cette approche demande une étape supplémentaire qui est le calcul des fonctions de Green. Dans la thèse, ce calcul est réalisé à l'aide du logiciel COMSOL. Chaque fil est positionné et excité successivement. Le champ ainsi calculé est relevé en champ lointain et aux emplacements des autres fils (pour le calcul des impédances mutuelles). Ensuite la démarche est identique à celle utilisée pour les métaréseaux. Il faut toutefois modifier l'objectif de la procédure d'optimisation qui ne porte plus sur les amplitudes des ordres diffractés mais sur, par exemple, les caractéristiques du diagramme en champ lointain ou en champ proche. Cette nouvelle approche est illustrée par plusieurs exemples validés à l'aide de simulations "full-wave" :

- réalisation d'un diagramme en forme de cardioïde;
- antenne semi-cylindrique d'épaisseur $\lambda/6$;
- antenne à cavité plane fermée par une métasurface éparse avec étude de l'influence du nombre de fils.

Une réalisation expérimentale a également été conduite sous la forme d'une antenne semi-cylindrique, excitée par deux dipôles et fermée une métasurface éparse souple. Trois différentes métasurfaces ont été testées (cf. Fig. 4.6). Il est important de souligner que dans ces exemples, la métasurface fonctionne en transmission bien qu'elle ne présente qu'une réponse électrique. Cette caractéristique est à mettre en regard avec les approches conventionnelles pour les métasurfaces fonctionnant en transmission qui généralement exigent de combiner une réponse électrique avec une réponse magnétique. En outre l'approche utilisée ici est globale et n'est pas confrontée aux limitations des approches conventionnelles qui imposent la conservation de la composante normale du vecteur de Poynting.

Métasurfaces reconfigurables fortement non locales

Le chapitre 5 présente une métasurface reconfigurable destinée à un fonctionnement de type reflect-array. Elle comporte 21 lignes de chacune 24 cellules élémentaires. Chaque cellule élémen-

taire comporte une diode varactor couplée à une ligne inductive de manière à réaliser les impédances linéiques nécessaires. L'ensemble de ces 21 lignes est connecté à une carte d'alimentation, elle-même pilotée par un Raspberry Pi. Avant la partie expérimentale, on revient sur le caractère non local de l'approche développée dans le chapitre 4 et ses avantages par rapport aux approches locales. Le cas considéré est celui de la réflexion anormale pour une incidence normale. Sont comparés, à l'aide de simulations 2D, les diagrammes d'une métasurface à gradient sans pertes, d'une métasurface à gradient avec pertes (pour limiter les lobes secondaires) et d'une métasurface éparse non locale. Il apparait que, pour les forts angles de réflexion anormale, l'approche non locale est la seule qui permet de conjuguer de faibles lobes secondaires et une forte efficacité. De plus, en relevant le champ réfléchi à proximité de la métasurface et en procédant à une analyse de Fourier, la présence d'ondes de surface apparait clairement. La cellule élémentaire comporte trois niveaux: un niveau supérieur composé d'une ligne chargée par une diode varactor, un niveau intermédiaire avec une ligne jouant le rôle d'inductance et le niveau inférieur avec le circuit de polarisation des diodes. Cette cellule a été optimisée pour fournir les impédances requises en minimisant les pertes en se basant sur les caractéristiques des diodes fournies par le constructeur. Ces données n'étant valides que pour des fréquences inférieures à 50 MHz, une étape de caractérisation est indispensable. Les résultats de cette étape ont conduit d'ailleurs au développement d'une deuxième version de cellules élémentaires.

Pour tester la cellule élémentaire, une tension identique est appliquée à toutes les diodes de la métasurface et l'on enregistre pour des fréquences comprises entre 8 et 16 GHz (ou 6.5 and 11.5 GHz pour la deuxième version), le coefficient de réflexion spéculaire sous une incidence de 5° ou de 45° pour la deuxième version (Fig. 5.9). La comparaison avec les simulations numériques permet d'établir l'évolution de la capacité de la diode en fonction de la tension appliquée ainsi que la valeur de la résistance parasite. Au final, on établit l'évolution de l'impédance de la cellule en fonction de la tension pour différentes fréquences (Fig. 5.10). Ces résultats sont finalement introduits dans l'algorithme d'optimisation qui détermine les tensions conduisant au diagramme de rayonnement requis. Expérimentalement, la métasurface est éclairée par un cornet situé à 35 cm de celle-ci. L'ensemble est monté sur une plateforme rotative tandis qu'un cornet récepteur fixe est placé à une distance de 4 m. Les diagrammes de rayonnement ont été mesurés pour un grand nombre de configurations montrant la possibilité de dépointer le faisceau réfléchi sur une très large plage de directions (Fig. 5.12) ou de créer plusieurs faisceaux (Fig. 5.13). Chacune de ces configurations résulte de l'optimisation de 21 tensions. L'efficacité de cette métasurface a

été évaluée en séparant les pertes par absorption dans les diodes et dans les lignes micro-rubans (par effet Joule) des pertes par diffusion dans les lobes secondaires. Typiquement, les pertes par absorption à 10 GHz sont de 50% à 60% tandis que les pertes par diffusion sont généralement de 10 à 15%. La directivité obtenue a été comparée à celle d'une ouverture uniforme et elle s'avère être à peine 2 dB en dessous.

Cette métasurface reconfigurable a également été utilisée à des fins de focalisation en champ proche. Dans ce cas, la métasurface est éclairée sous incidence normale par un cornet placé à 125 cm. Le champ au voisinage de la métasurface est relevé à l'aide d'une sonde qui permet d'accéder à l'amplitude et à la phase du champ électrique total. Différentes expériences ont été conduites en faisant varier la distance de focalisation et le nombre de points de focalisation. Dans tous les cas, un excellent accord entre expérience et simulation est observé. L'analyse des expériences montre que la taille du point focal ainsi obtenu est inférieure à la tâche d'Airy (on obtient par exemple une taille de 0.45λ à une distance de λ, soit une ouverture numérique de 0.98 alors que la tâche d'Airy est de $0.61\lambda/\mathrm{NA}$). Enfin, une transformée de Fourier discrète a été appliquée aux champs relevés juste à proximité de la métasurface (à $\lambda/10$). La présence d'ondes de surface apparait sans ambiguïtés, de la même façon qu'elle était apparue dans les simulations de réflexion anormale en début de ce chapitre. Le comportement fortement non local de cette métasurface est ainsi clairement établi.

Principaux résultats et perspectives

Cette thèse a permis d'établir plusieurs résultats importants :

- à l'aide de métaréseaux, l'énergie incidente peut être redistribuée arbitrairement dans les ordres diffractés à condition d'avoir autant de fils par période que d'ordres diffractés. Ce cas requiert des impédances comportant des éléments actifs ou à pertes. Il est cependant possible d'ajuster le champ proche en augmentant le nombre de fils par période et ainsi de réaliser une réflexion anormale parfaite avec des impédances purement réactives;

- une nouvelle approximation périodique locale a été développée. A l'instar de la LPA classique, elle repose sur le calcul numérique de la cellule élémentaire assortie de conditions de périodicité mais les résultats sont introduits dans une nouvelle expression qui permet de soustraire les effets des couplages et du substrat. Il devient alors possible de concevoir une métasurface à faible densité d'éléments, avec des cellules élémentaires quelconques

pouvant notamment incorporer des éléments accordables;

- la démarche utilisée pour les métaréseaux a été généralisée à des surfaces quelconques comportant des ensembles de fils non périodiques et éclairés par une onde cylindrique quelconque. Dans cette approche, le champ rayonné est exprimé à l'aide d'une somme de fonctions de Green pondérées par les intensités parcourant les fils. Ces fonctions de Green sont calculées à l'aide de simulations numériques 2D. Les paramètres des cellules élémentaires (géométrie ou tension appliquée à un élément accordable), conduisant aux impédances qui assurent les intensités nécessaires pour l'obtention du diagramme de rayonnement recherché, sont obtenus par optimisation par essaims particulaires;

- une métasurface éparse reconfigurable a été conçue et testée. Elle permet de rediriger efficacement l'onde incidente sur un très large domaine angulaire. Elle permet aussi de focaliser l'énergie incidente sous la limite de diffraction. En outre, il a été possible de montrer son comportement fortement non local.

Ce travail ouvre de multiples perspectives :

- la réalisation de métasurfaces conformes reconfigurables;

- le développement de métasurfaces éparses 2D. Les réseaux de fils devraient alors être remplacés par des réseaux de dipôles. Il n'est toutefois pas certain que ce modèle soit suffisamment précis pour décrire des motifs de la taille de ceux habituellement rencontrés;

- la formation simultanée de faisceaux pointant dans différentes directions pour des fréquences différentes;

- la réalisation de métaréseaux ou de métasurfaces éparses pour des applications en optique, car toutes les approches théoriques développées dans cette thèse sont directement transposables aux longueurs d'onde optique;

- le développement de métaréseaux ou de métasurfaces éparses en acoustique;

- le développement de métasurfaces conformes reconfigurables exploitant des déformations mécaniques.

General Introduction

From long ago, composite structures have been serving to go beyond characteristics of natural materials. A leap further from classical composites was made when the concept of metamaterials emerged as a way to knowingly engineer properties of artificial structures and adapt them to real-life applications. By an electromagnetic metamaterial, one generally understands a bulk structure represented by a periodic arrangement of subwavelength meta-atoms designed to obtain rare or non-natural *effective* material parameters (permittivity, permeability and magneto-electric coupling). Although the idea of adjusting material parameters of composites has been known at least from the beginning of the $20^{\mathbf{th}}$ century, an active research on metamaterials was initiated in 2000 by the experimental work "*Composite Medium with Simultaneously Negative Permeability and Permittivity*" of D. R. Smith *et al.* and the theoretical work "*Negative Refraction Makes a Perfect Lens*" of J. B. Pendry. Soon after metamaterials, metasurfaces, as one-meta-atom-thick metamaterials, were proposed to reduce the effect of material losses in bulk structures. By creating spatial modulation in the metasurface design at the wavelength scale, it becomes possible to perform wavefront transformations such as anomalous reflection and transmission, for example. Thus, metasurfaces found their application in antennas and have been studied, in particular, to improve performances of reflectarray and transmitarray antennas, Fabry-Perot cavity and leaky-wave antennas. Macroscopic models, based on electric and magnetic surface impedances or local reflection and transmission coefficients, were brought to facilitate the design of metasurfaces. However, the macroscopic character of these models substantially rubs out microscopic features of metasurfaces, such as the density of elements and mutual interactions between them, and results in appearance of fundamental performance limitations of metasurface-based antennas.

This PhD thesis focuses on advancement of current state-of-the-art electrically reconfigurable

metasurface-based antennas presented in the First Chapter. Within the framework of the thesis, the existing macroscopic models are put aside and metasurfaces are considered as arrays of discrete scatterers. To solve the inverse scattering problem and be able to create desirable radiation patterns while taking into account all interactions between elements of a metasurface, the manuscript develops novel analytical and numerical models. Specifically, the manuscript focuses on *sparse* arrays, periodic or not, of wires engineered at the subwavelength scale. The results of the work are presented in four chapters. In the Second Chapter, an analytical model for periodic arrays of wires, called metagratings, is developed. In contrast to conventional metasurfaces, metagratings are essentially discrete structures and cannot be described in terms of surface impedances. Theoretical conditions of arbitrary control of the diffraction patterns with metagratings, whose period is composed of multiple individually-engineered wires, are established and importance of the near-field regulation is highlighted. In particular, the question of the number of degrees of freedom necessary for manipulation of propagating diffraction orders at will is studied. A semi-analytical design procedure of microwave metagratings and an experimental validation of the developed concept is presented. In the Third Chapter, an analytical retrieval technique is developed and allows one to consider arbitrarily structured wires with the help of full-wave simulations. The developed design approach is validated by means of three-dimensional full-wave simulations for metagratings operating from microwave to optical domains and experimentally at microwave frequencies. In the Fourth Chapter, the analytical model of metagratings is generalized, from planar periodic, to arbitrarily-shaped non-periodic distributions of wires by means of numerical calculation of a Green's function. The concept of conformal sparse metasurfaces is presented. A design procedure of conformal sparse metasurfaces is demonstrated through the examples of semi-cylindrical and cavity-excited sparse metasurfaces. Designs of several semi-cylindrical sparse metasurfaces with different functionalities are validated experimentally at microwave frequencies, where beam-steering and excitation of multiple beams are demonstrated. Finally, in the Fifth Chapter, the analytical model of sparse metasurface is applied to design a reconfigurable planar sparse metasurface. A fabricated sample is exploited to experimentally demonstrate dynamic control of the far-field radiation pattern and the near-field intensity distribution. As such, beam-steering, manipulation of multiple beams (up to six), subdiffraction focusing and manipulation of multiple focal spots are demonstrated.

Chapter 1

State-of-the-art on reconfigurable metasurfaces for antenna applications

Contents

1.1. Introduction

From long ago, composite structures have been serving to go beyond characteristics of natural materials. A leap further from classical composites was made when the concept of metamaterials emerged as a way to knowingly engineer properties of structures and adapt them to real-life applications. Metasurfaces representing themselves as electrically very thin structures have been proposed as planar alternatives to metamaterials to exhibit light manipulation possibilities in various frequency domains, extending from microwave to visible frequencies. As such, metasurfaces have been used to perform functions including anomalous reflection and refraction [1, 2, 3, 4, 5, 6], deflection [7, 8, 9, 10, 11], lensing [7, 8, 12, 13, 14, 15], thin-film cloaking [16, 17, 18], coupling of propagating waves to surface waves [19, 20, 21], optical vortex beams generation [22, 23, 24, 25, 26, 27], and holographic imaging [28, 29, 30, 31, 32, 33], to name a few.

Nowadays, there is an increasing research interest in reconfigurable (or tunable) metasurfaces capable of dynamically changing their properties under external stimuli and integrate different functionalities in a single system [34, 35, 36, 37, 38, 39, 40, 41, 42, 43, 44, 45, 46, 47, 48, 49, 50, 51, 52, 53, 54, 55, 56, 57]. This activity is triggered by ongoing fundamental research on time-modulated and nonreciprocal systems [58, 59, 60, 61, 62, 63, 64, 65, 66, 67] on one hand and novel emerging applications on another hand. As such, concepts of analogue computing, computer vision, Internet of Things (IoT), smart homes and smart cities [52, 50, 53, 54, 55] create an ever increasing demand for compact, versatile and efficient microwave devices to manipulate electromagnetic wavefronts.

SONDRA laboratory and I are interested in the potential of using electrically reconfigurable metasurfaces for radar applications in the framework of this PhD Thesis. The foreseen work is exploratory in nature and does not imply implementation of a device answering concrete specifications. However, operating frequencies of experimental samples built to validate theoretical concepts were set to 5 GHz and 10 GHz. In what follows, I review state-of-the-art developments in the field of electrically reconfigurable metasurfaces, without intending to cover all works presented on the subject. Instead, I aim to present basic concepts and tools for describing and designing reconfigurable metasurfaces, understand their limitations and a source of these limitations, demonstrate principal configurations of metasurface-base reconfigurable antennas and

challenges of characterizing a reconfigurable metasurface.

1.2. Binary phase-state metasurfaces

A major type of reconfigurable metasurfaces for wavefront manipulation is represented by binary phase-state metasurfaces. Although such terms as "digital", "coding" and "programmable" metasurfaces were introduced in 2014 by T. J. Cui in Ref. [37], binary elements were used as building blocks of reflectarrays and transmitarrays before that [68, 69, 70, 71, 35, 72, 73]. Meanwhile, it should be noted that the problem of phase discretization was initially addressed in the general context of phased arrays which I do not intend to cover here [74]. In order to avoid using different terms for essentially the same physical structures, in what follows I use the term "binary phase-state metasurfaces". The operational principle of these metasurfaces is based on switching the local phase response $\phi_{m,n}$, i.e. the phase of the local reflection (or transmission) coefficient, of constituting meta-atoms between different discrete values. For example, a 1-bit element, see an example in Fig. 1.1, provides two phase states: 0 and π. In the case of a reflective metasurface, it effectively corresponds to either perfect magnetic conductor (PMC) or perfect electric conductor (PEC) local boundary conditions. The local reflection (or transmission) coefficient is calculated as a reflection coefficient of a plane wave form a periodic array of elements, all in the same state [75]. In the majority of works presented in the literature, the choice of the state relies on a simple theoretical model [72]

$$\phi(x_m, y_m) = \phi_{req}(x_m, y_m) - \phi_{inc}(x_m, y_m), \tag{1.1}$$

where $\phi_{req}(x_m, y_m)$ and $\phi_{inc}(x_m, y_m)$ are the required phase for desired wavefront transformation and the phase of the incident wave at the location x_m, y_m of the m^{th} unit cell. They depend on the antenna configuration (reflectarray, Fabry-Perot and etc.) and the type of the excitation source (plane-wave illumination, patch antenna and etc.). The phase $\phi(x_m, y_m)$ (0 or π in case of 1-bit unit cell) corresponds to the phase of the local reflection (or transmission) coefficient from the corresponding unit cell. The phase $\phi_{inc}(x_m, y_m)$ equals zero in case of a normally incident plane-wave illumination and $\phi_{inc}(x_m, y_m) = -k_0\sqrt{x_m^2 + y_m^2 + D^2}$ in case of an illumination created by a point source, where k_0 is the free-space wavenumber. The phase distribution required to perform beam-steering at elevation angle θ and azimuthal angle φ is $-k_0(\sin[\theta]\cos[\varphi]x_m + \sin[\theta]\sin[\varphi]y_m)$. It should be noted that Eq. (1.1) remains valid for con-

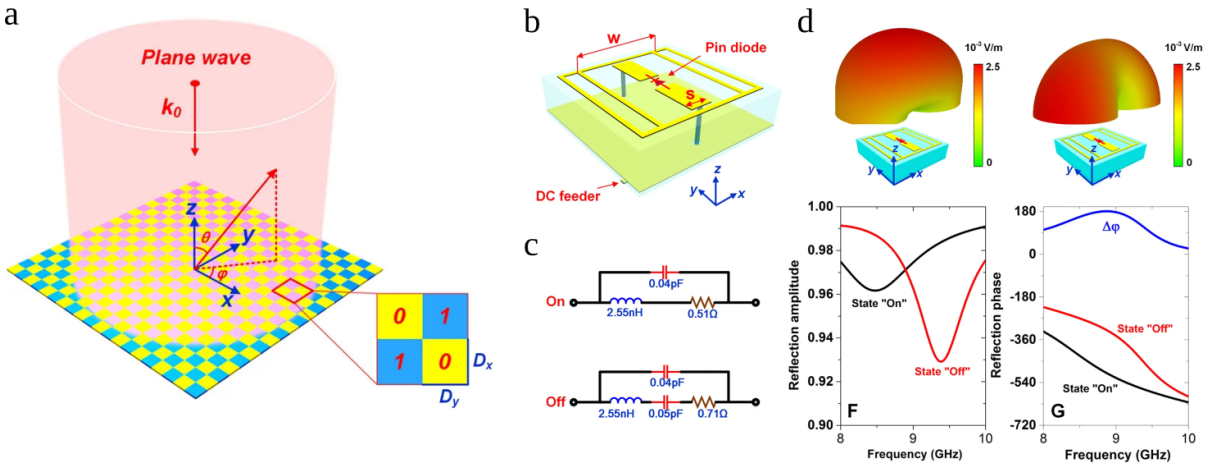

Figure 1.1: ***(a)*** *An illustration of a binary phase-state metasurface illuminated by a normally incident plane wave.* ***(b)*** *A schematics of a unit cell loaded with a PIN diode.* ***(c)*** *A circuit model of a PIN diode in ON and OFF states.* ***(d)*** *Radiation patterns and the local reflection coefficient from a binary phase-state unit cell [76].*

tinuous phase tuning metasurfaces (discussed further) as well.

By embedding tunable elements in every meta-atom, which change their properties under external stimuli, a metasurface as a whole can be controlled to adaptively synthesize a large range of antenna patterns. One usually harnesses resonances in meta-atoms to achieve a sufficiently large phase difference between the incident and scattered waves. However, it is not an easy task to design a resonant meta-atom exhibiting 2π-phase response. The choice of tunable elements is mainly determined by the amount of losses introduced in the target frequency range. Generally, one can distinguish digital and analog tunable elements, both of them can be used to implement a binary phase-state metasurface. In the microwave frequency range, one usually uses digital PIN diodes and RF-MEMS or analog varactor diodes and liquid crystals [72]. At THz, optical and visible frequencies, graphene, semiconductor and phase-change materials are in particular suggested to implement reconfigurable metasurfaces [77, 78].

A PIN diode contains an intrinsic semiconductor layer between the p- and n-type layers. When reverse biased, a small series junction capacitance leads to a relatively high diode impedance, while a forward bias current removes the junction capacitance and leaves the diode in a low-impedance state. A varactor diode produces a junction capacitance that varies smoothly with reverse bias voltage, thus providing an electrically adjustable reactive lumped element. PIN and varactor diodes are based on a mature technology and are easily available off-the-shelf and they do not require having an expertise either. It makes them the best choice in many designs of reconfigurable metasurfaces at microwave frequencies [35, 37, 39, 41, 42, 43, 44, 48, 50]. Relatively high ohmic losses are the well-known drawback of PIN and varactor diodes which imposes

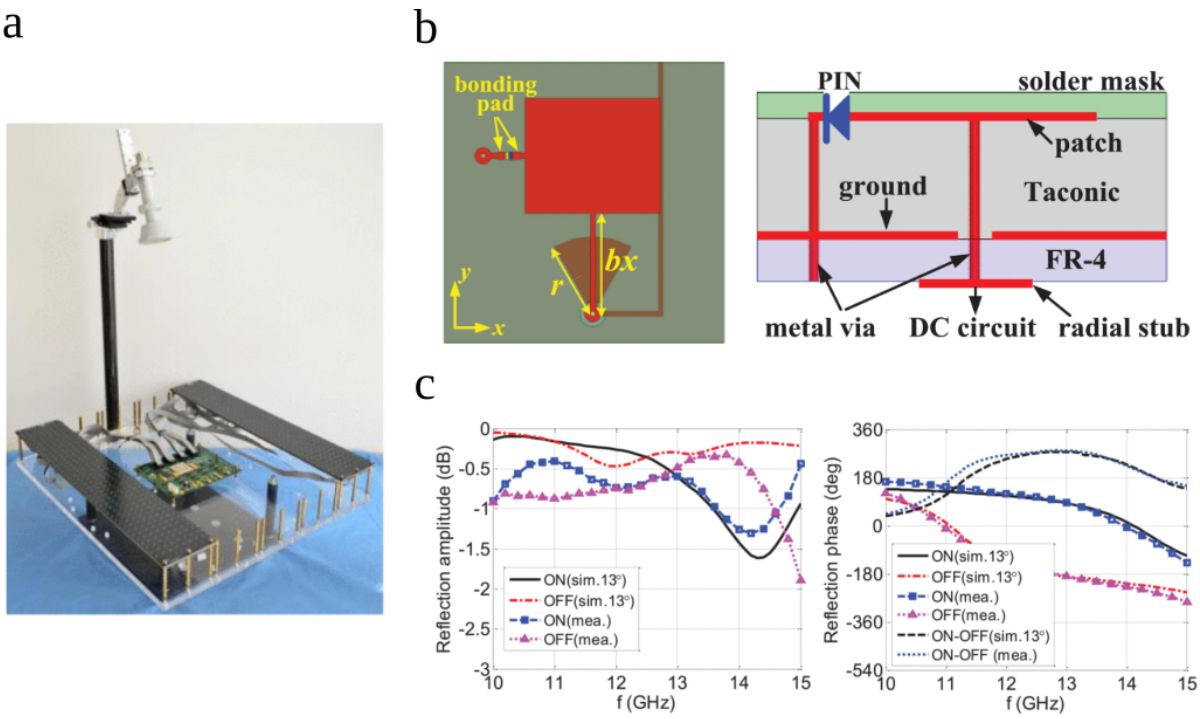

Figure 1.2: ***(a)*** *A photograph of the experimental sample, two of five segments of the reconfigurable metasurface are mounted.* ***(b)*** *A schematic of the designed reconfigurable unit cell.* ***(c)*** *The amplitude and the phase of the local reflection coefficient for the two states of the unit cell [79].*

limitations on their use. On the other hand, RF-MEMS technology is characterized by very low losses up to mm-wave frequencies, virtually zero power consumption, high linearity, and possibility of monolithic integration [72]. Unfortunately, the technology is not yet mature and reliable enough for uncomplicated incorporation in the design of a meta-atom. Liquid crystals can be a compromise between the amount of losses and simplicity of the technology, especially at frequencies around 100 GHz. A reconfigurability mechanism implemented on the base of a liquid crystal harnesses its property of changing dielectric permittivity under an external electric field created between two electrodes when applying a bias voltage. An appropriately chosen type of a metasurface-based antenna (reflectarray, transmitarray, Fabry-Perot, leaky-wave, etc.) together with an advanced theoretical design approach might also allow one to reduce the effect of lossy tunable elements.

Implementation examples

In this subsection, I describe state-of-the-art examples of binary phase-state reconfigurable metasurfaces used in different antenna configurations and demonstrating different examples of beamforming.

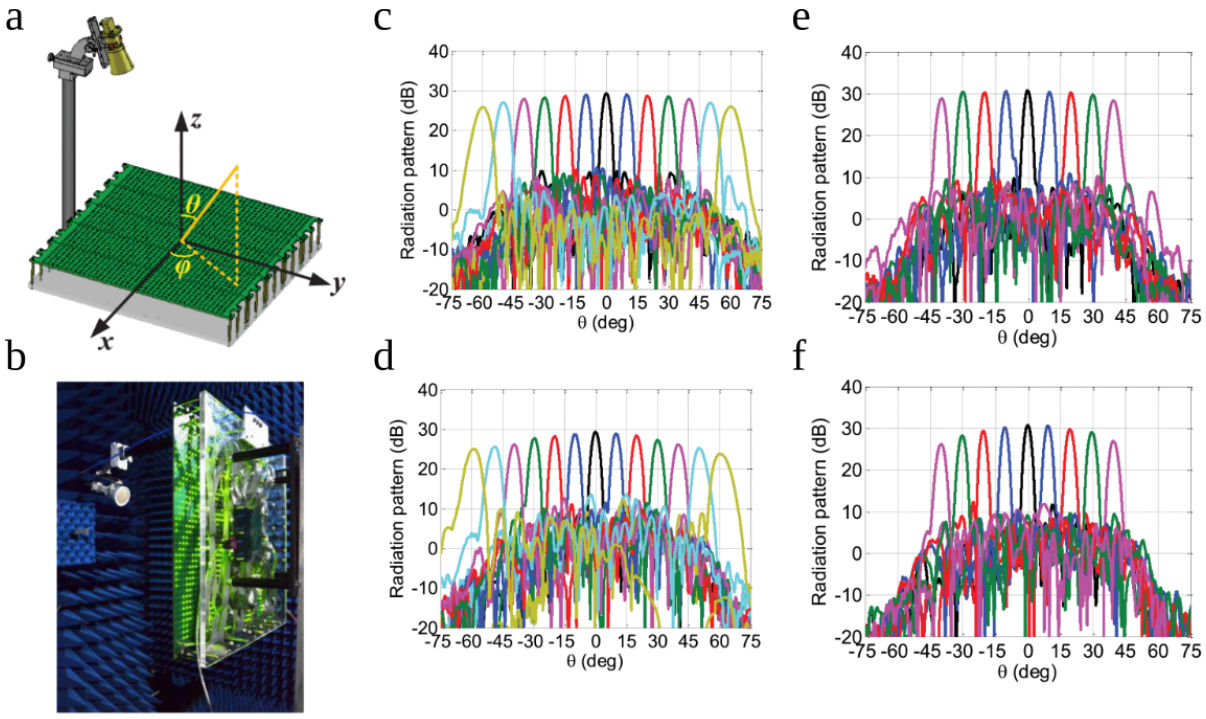

Figure 1.3: ***(a),(b)*** *A schematic of the assembled experimental sample* ***(a)*** *and its photograph in an anechoic chamber* ***(b)****.* ***(c)–(f)*** *Experimental results of beam-steering in different planes and at different frequencies. The panels* ***(c)*** *and* ***(d)*** *correspond to* $x0z$ *and* $y0z$ *planes, respectively, the operating frequency is* 11.1 *GHz. The panels* ***(e)*** *and* ***(f)*** *correspond to* $x0z$ *and* $y0z$ *planes, respectively, the operating frequency is* 14.3 *GHz [79].*

Reflectarray configuration. An exceptional beam-steering performance was demonstrated in Ref. [79] in X- and Ku-bands by the binary phase-state reconfigurable metasurface developed by H. Yang *et al.* in 2017. A photograph of the experimental sample is shown in Fig. 1.2(a). The layout of the metasurface repeats a general one of reflecting metasurfaces and is represented by an array of resonant scatterers on top of a metal-backed dielectric substrate. The array represents a quadratic lattice with the period of 12 mm, which approximately corresponds to $\lambda_0/2$ (λ_0 is the central vacuum wavelength). The scatterers are implemented as patch antennas loaded with PIN diodes (MACOM's MADP-000907-14020), as shown by the schematics of the unit cell in Fig. 1.2 . In order to achieve a desirable response at two operating frequencies (11.1 GHz and 14.3 GHz), a parametric study was performed by means of 3D full-wave simulations with respect to the width and the length of the patch and the height of the substrate. The PIN diode was modeled in simulations as an equivalent circuit according to the manufacturer's datasheet: RL circuit for ON state and LC circuit for OFF state. The comparison of characterization results obtained in simulations and experiment are shown in Fig. 1.2(c). The losses attributed to the reconfigurable elements do not exceed 1 dB and 1.5 dB at the two frequencies, respectively.

The developed design was realized by means of the printed circuit board technology (PCB)

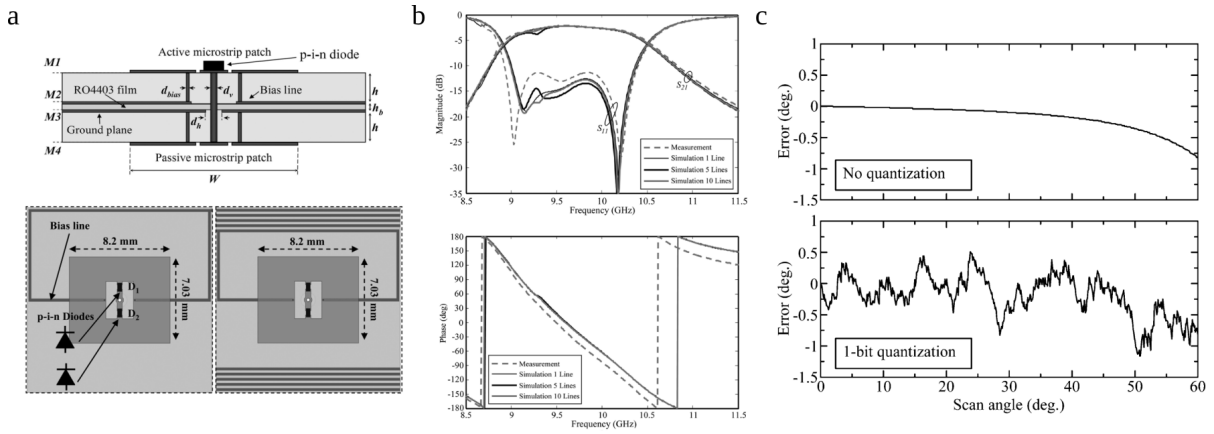

Figure 1.4: ***(a)*** *A schematic of the designed reconfigurable unit cell.* ***(b)*** *The amplitude and the phase of the local transmission coefficient.* ***(c)*** *Error (in degrees) of the position of the main beam in case of the continuous phase tuning and 1-bit phase quantization, when Eq.* (1.1) *is used to established required phase profile [35].*

in the fabricated sample containing 40 by 40 unit cells (total of 1600 unit cells). Each unit cell is controlled individually through a bias network appearing on the back side of the sample. The sample is illuminated by a corrugated conical horn antenna with the focal diameter ratio being 0.83 and the offset of 20° from z-axis as illustrated by Figs. 1.3(a) and (b). The beam-steering performances of the fabricated experimental sample are summarized in Figs. 1.3(c)–(f) for the two frequencies. The level of side lobes does not exceed −16 dB independently of the scanning angle. A slight asymmetry is present in the steering performance in $y0z$ plane because of the feed offset in this plane. At 14.3 GHz the beam-steering up to approximately ±40° is demonstrated because of grating lobes that appear outside the 48.4° angular range, the element periodicity is 12 mm (0.57λ at 14.3 GHz). The results at the two operating frequencies demonstrate an exceptionally good performance of the proposed binary phase-state metasurface by the authors.

Transmitarray configuration. A binary phase-state metasurface exhibiting exceptional beam-steering capabilities at X-band in the transmitarray configuration was presented in Ref. [35] by A. Clemente *et al.* in 2013. A reconfigurable unit cell comprising a transmitting metasurface is more complicated than its reflecting counterpart discussed above. Indeed, additionally to providing a large phase difference between incident and transmitted waves, a unit cell should have a negligible reflection in order not to deteriorate the efficiency. 2π-range phase control while maintaining full transmission is not possible to achieve for co-polarization with a single array of scatterers on top of a substrate (single-layer design) [73]. An array of scatterers with electric-only response creates symmetric scattered field in the forward and backward directions.

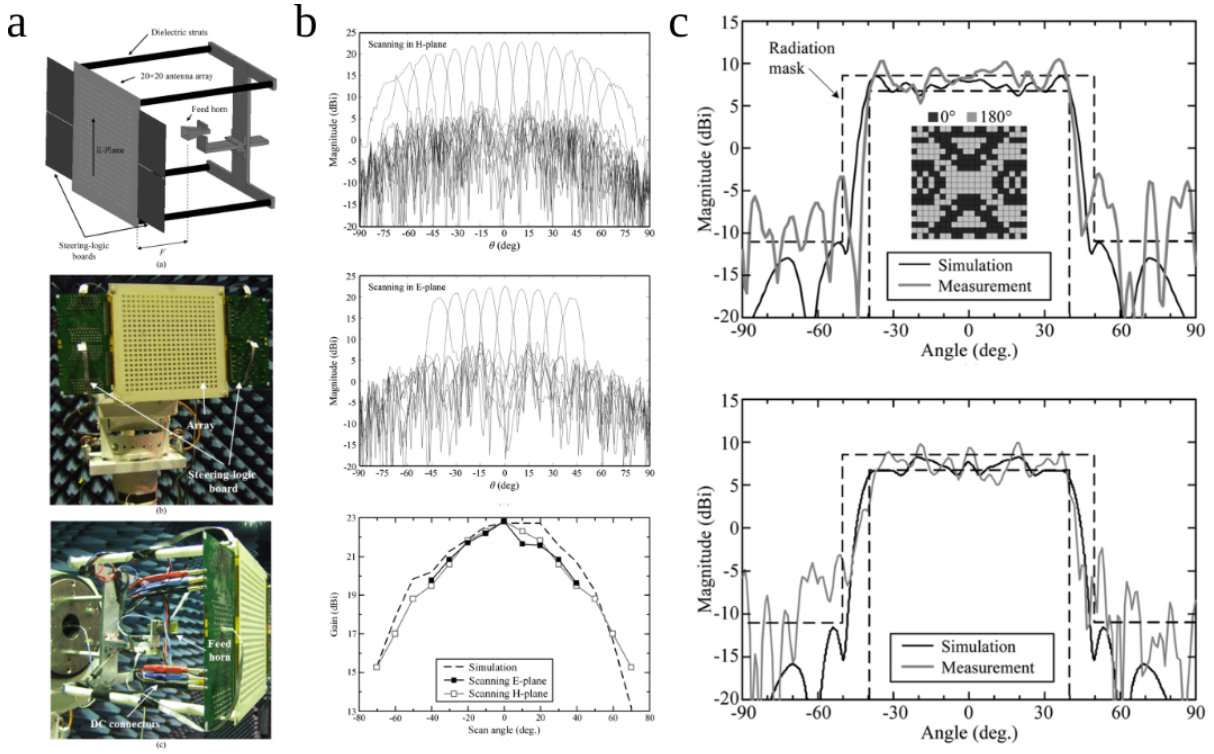

Figure 1.5: ***(a)*** *A schematic and photographs of the assembled experimental sample.* ***(b)*** *Experimental results of beam steering in H-plane (top) and E-plane (central). The bottom panel compares measured and simulated gain of the sample.* ***(c)*** *Experimental results of beam-shaping. The top and bottom panels correspond to H- and E-planes, respectively. The operating frequency is* 9.8 *GHz [35].*

In order to break this symmetry an effective magnetic response can be created by using multi-layer designs. The authors have developed a three-layer reconfigurable unit cell represented by receiving and transmitting patch antennas on outer faces connected by a metallic via through a ground plane on the inner face. Only the transmitting patch antenna is loaded with two PIN diodes, a schematic of the design is shown in Fig. 1.4(a). The total area of a unit cell is 15×15 mm^2 corresponding to $\lambda_0/2$ periodicity at 10 GHz. The grating lobes do not appear over the metasurface bandwidth, from 9 GHz to 10.6 GHz, and in the range of beam-steering angles from $-70°$ to $70°$ from the broadside. The receiving patch is connected to the ground plane by two metallic vias and the transmitting patch is connected to the bias line by two metallic vias. In this configuration both diodes are switched in opposite states by means of a single bias line. The unit cell demonstrates 1-bit tunable response as demonstrated in Fig. 1.4(b). The frequency response of the unit cell was, on the one hand, studied by means of 3D full-wave simulations with periodic boundary conditions and Floquet ports and on the other hand, tested experimentally by embedding a fabricated unit cell in a rectangular waveguide [71].

The proposed design of a unit cell was realized by means of PCB technology and a meta-

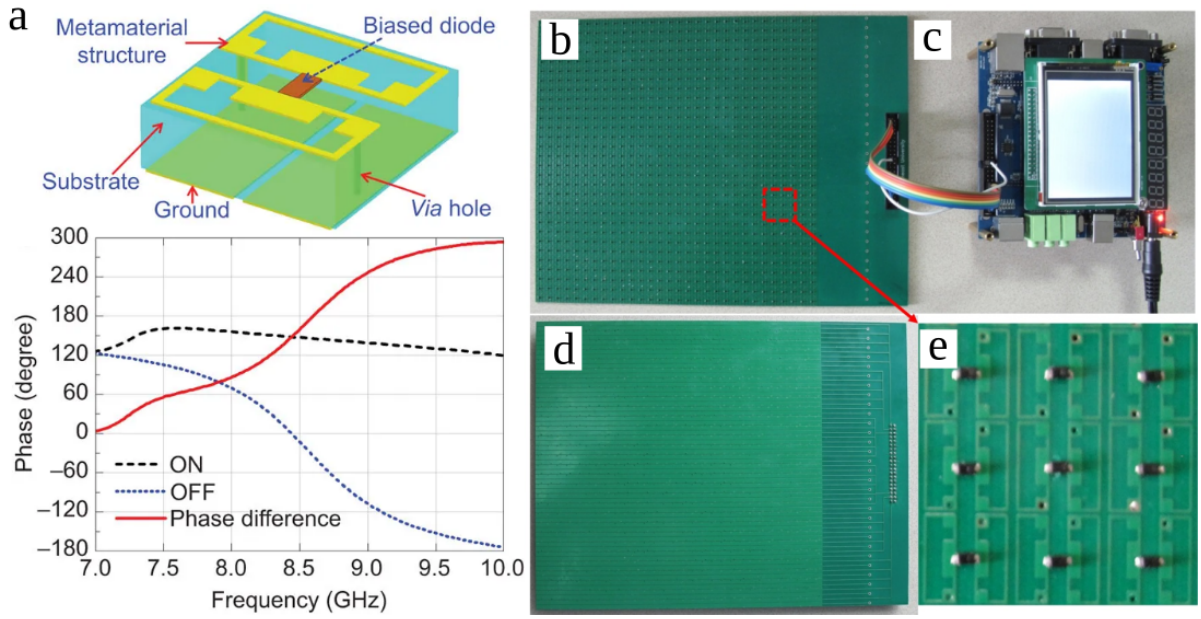

Figure 1.6: ***(a)*** *The top panel demonstrates a schematic of the designed reconfigurable unit cell. The bottom panel demonstrates the phase of the local reflection coefficient.* ***(b)****–****(e)*** *Photographs of the experimental sample* ***(b)****,****(d)****,****(e)*** *and field-programmable gate array* ***(c)*** *[37].*

surface consisting of 20 by 20 unit cells (total of 400 unit cells) was fabricated. Each unit cell is controlled individually through a bias network plugged along the edges of the sample. The sample is fed by a linearly-polarized pyramidal horn antenna having a gain of 11.1 dBi at 10 GHz. The horn is fixed at normal incidence as illustrated by Fig. 1.5(a). The focal diameter ratio can be adjusted in the range from 0.44 to 0.92. Photographs of the assembled sample are shown in Fig. 1.5(a).

Although only two phase states are available, the authors demonstrated theoretically, Fig. 1.4(c), that the error in the steering angle is negligible, when accounting for the beamwidth, and comparable to the case when a continuous phase tuning can be performed. The beam steering capabilities of the binary phase-state metasurface were demonstrated up to $\pm 70°$ in H-plane and $\pm 40°$ in E-plane, see Fig. 1.5(b). The beam-steering range in E-plane was mainly limited by experimental equipment the authors used. The level of side lobes does not exceed -10 dB up to $\pm 60°$ and increases to approximately -7 dB for $\pm 70°$. The measured directions of the main beam corresponds well to theoretical predictions. Although the radiation pattern degrades significantly when increasing the steering angle, the experimental results demonstrated by the authors are among the best examples that can be found in literature.

Manipulation of multiple beams and beam-shaping. While beam-shaping and manipu-

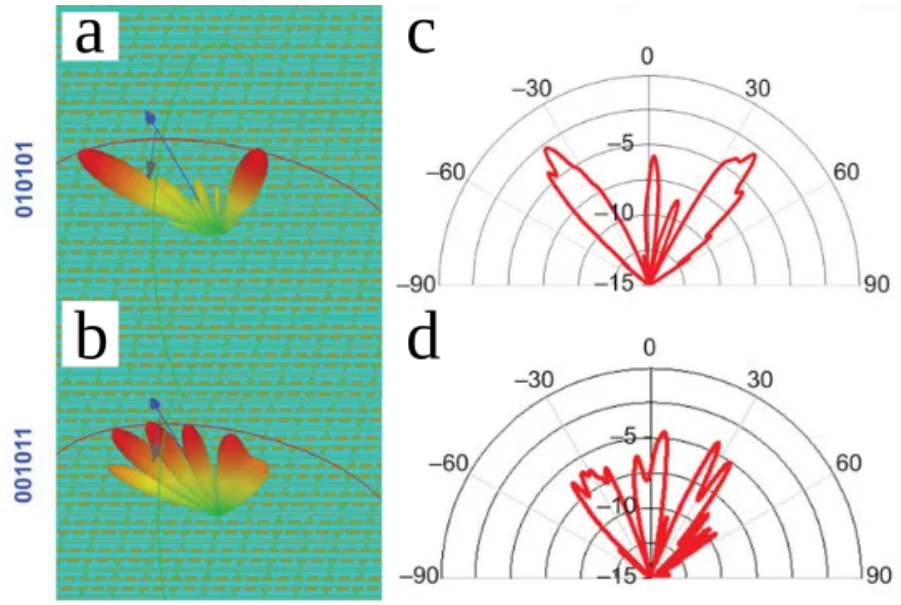

Figure 1.7: Simulation ***(a)***,***(b)*** *and experimental* ***(c)***,***(d)*** *results of excitation of multiple beams with the reconfigurable binary phase-state metasurface. The operating frequency is* 8.6 *GHz [37].*

lation of multiple beams is well studied for non-reconfigurable metasurfaces [80, 81, 6, 82], there are not many examples of reconfigurable metasurfaces demonstrating such capabilities.

When a binary phase-state metasurface is illuminated by a plane wave, multiple beams can be generated by applying establishing a periodic phase distribution along its aperture [37]. In 2014, T.J. Cui *et al.* presented a design of a reconfigurable subwavelength unit cell providing 1-bit control of the phase response in X-band as demonstrated in Fig. 1.6(a) [37]. The size of the unit cell is 0.17λ by 0.17λ at central operating frequency conversely to the examples demonstrated above. One PIN diode per unit cell is used as a tunable element. A binary phase-state metasurface was fabricated on the base of this design by means of the PCB technology and a field-programmable gate array (FPGA) was developed to control the phase distribution along the aperture. Figures 1.6(b)–(e) show photographs of the sample. Simulation and experimental results of excitation of multiple beam are presented in Fig. 1.7. Although establishing a periodic phase profile represents a very simple way to obtain multiple beams, it significantly lacks flexibility to accurately control directions of main beams and the level of side lobes. Indeed, the authors did not use any theoretical tool that would predict a binary phase profile required to established desirable radiation pattern. It results in overall poor beam-forming efficiency.

This problem can be approached by implementing an optimization procedure to achieve a desirable radiation pattern. For example, apart from the beam-steering in Ref. [35], A. Clemente *et al.* also demonstrated beam-shaping capabilities of their transmitting metasurface by synthesis-

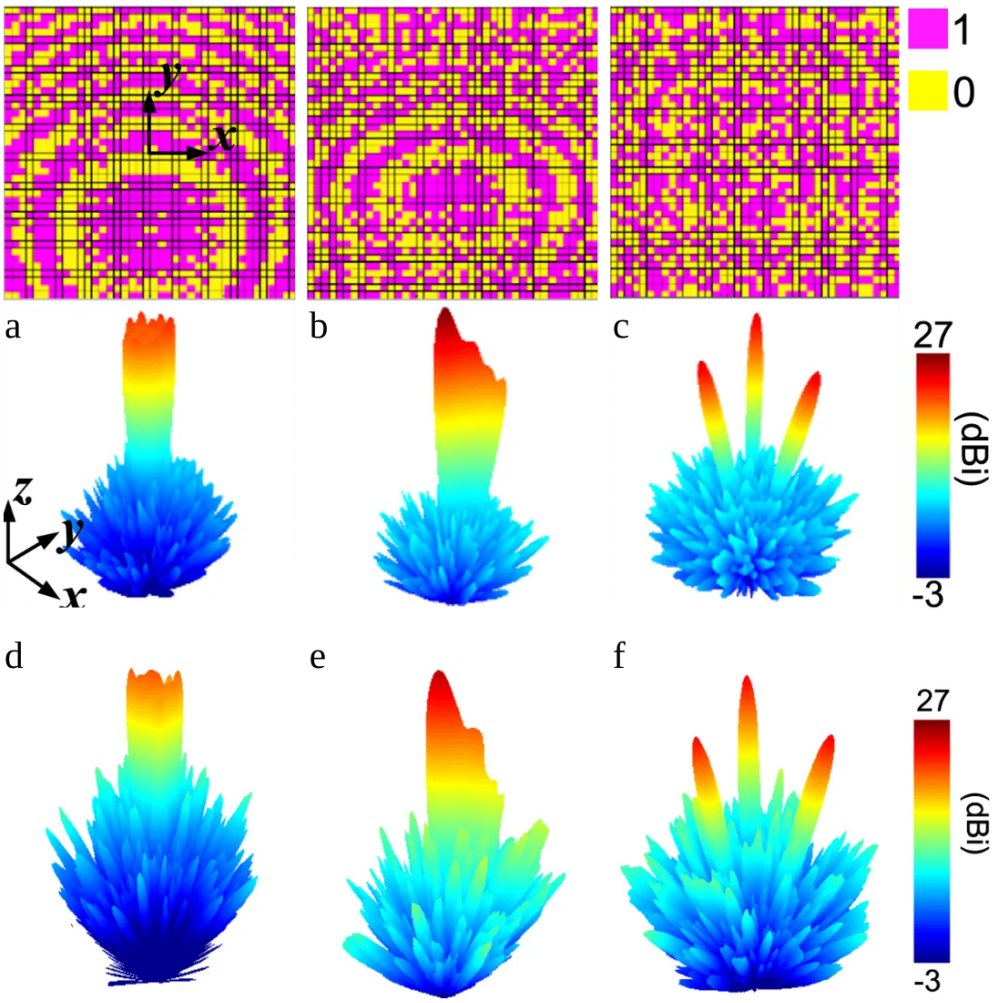

Figure 1.8: Simulation ***(a)–(c)*** *and experimental* ***(d)–(f)*** *results of beam-shaping and excitation of multiple beams. The top row demonstrates the phase distribution along the metasurface in each configuration. The operating frequency is* 11.1 *GHz [43].*

ing a flat-top beam pattern, as illustrated in Fig. 1.5(c). A genetic algorithm was realized to find the required phase profile along the metasurface at 9.8 GHz operating frequency. The beamwidth was set to $80° - 90°$ and the level of ripples was set less than 2 in the main beam and the level of side lobes was set below -20 dB. This mask is shown in Fig. 1.5(c) by the dashed lines. The resulted phase profile from the optimization procedure is shown in the inset of Fig. 1.5(c). The measured and simulated radiation patterns in E- and H-planes are demonstrated in the same figure. Although a good agreement between the experiment and the simulation is observed, the authors pointed out that the discrepancies might stem from, on the one hand, the measurement procedure performed in a 3m-long anechoic chamber where the far-field conditions are not met, and on the other hand, the spill-over radiation from the feeding horn and the diffraction from the edges of the sample could also contribute to the mismatch.

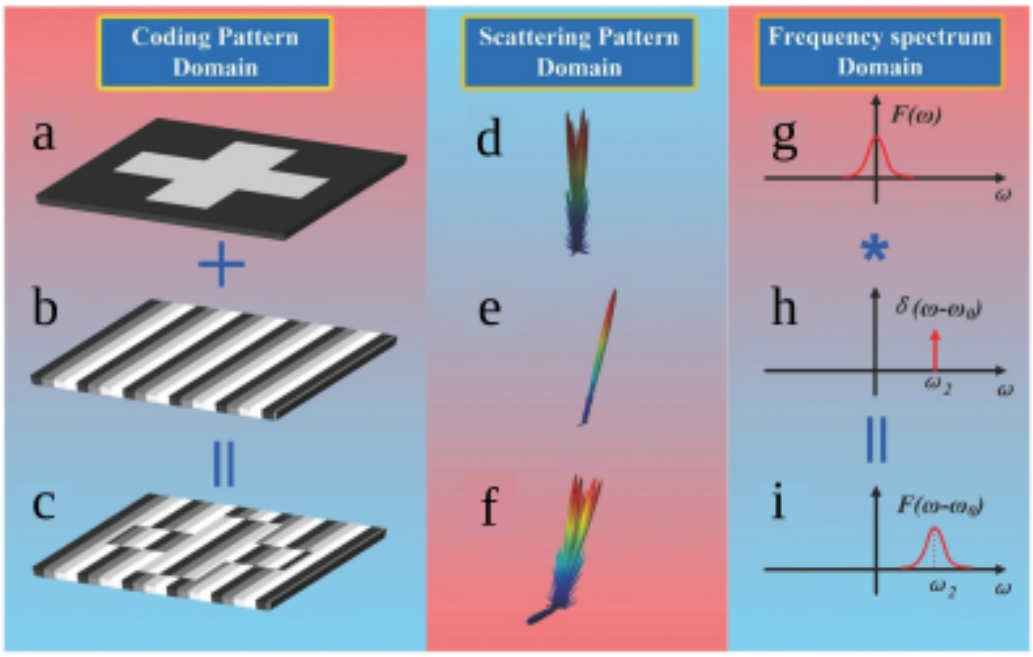

Figure 1.9: Schematic illustration to the principle of scattering-pattern shift in analogy to the Fourier Transform. ***(a)****–****(c)*** *Phase patterns of a cross, gradient distribution, and their modulus, respectively.* ***(d)****–****(f)*** *Scattering patterns calculated by FFT from the phase patterns in the panels* ***(a)****–****(c)****, respectively.* ***(g)****–****(h)*** *The analogical frequency spectra of the coding patterns in the panels* ***(a)****–****(c)****, respectively [83].*

In 2016, H. Yang *et al.* approximated the radiation from a reflecting binary phase-state metasurface by the array factor $\mathrm{AF}(\theta, \varphi)$

$$\mathrm{AF}(\theta,\varphi) = \sum_{m=1}^{N} \exp\left[j\left(\phi(x_m, y_m) + k_0 \sin[\theta]\cos[\varphi]x_m + k_0 \sin[\theta]\sin[\varphi]y_m\right)\right] \tag{1.2}$$

and used a genetic algorithm to optimize the phase distribution $\phi(x_m, y_m)$ along the aperture. The authors used the same metasurface as in Ref. [79] which is discussed above and shown in Fig. 1.2. Figure 1.8 demonstrates simulation and experimental results of beam-shaping (panels (a),(b) and (d),(e)), and excitation of three beams (panels (c) and (f)).

On the other hand, the synthesis of information theory and the concept of binary phase-state metasurfaces led to another way of wavefront manipulation. In 2016, S. Liu *et al.* demonstrated in Ref. [83] that by performing Fourier operations on binary phase-states along a metasurface and using the convolution theorem, a shift can be imposed on the radiation pattern created by a metasurface-based antenna. It allows steering the pattern to a desired direction as schematically shown in Fig. 1.9. The required phase distribution can be obtained by the modulus of two phase-mask matrices under the assumption that the amplitude of the local reflection coefficient is *independent* from the phase. The authors validated the concept by means of numerical simulations and demonstrated manipulation of multiple beams with a binary phase-state meta-

surface. However, the level of side lobes remains unoptimized and the spurious radiation can be significant, especially when a realistic binary unit cell, as shown for example in Fig. 1.2(c), is considered. This conclusion is confirmed by experimental works published in 2020 by the group of Prof. T. J. Cui [84, 85].

1.3. Continuous phase tuning metasurfaces

The implementation of continuous phase tuning metasurfaces can be traced back to the works of W. Lam *et al.* in 1988 [86], R. Waterhouse *et al.* in 1993 [87], L. B. Sjogren *et al.* in 1994 [88], Sievenpiper *et al.* in 2003 [89] and S. Hum *et al.* in 2004 and 2005 [90, 91]. In contrast to their binary phase-state counterparts, continuous phase tuning metasurfaces promise a more flexible solution of integrating multiple functionalities in a single metasurface and achieving real-time reconfigurablity due to their electromagnetic response that can be modified continuously with applied external stimuli. In order to implement a continuous phase tuning metasurface, analog tunable elements such as varactor diodes and liquid crystals are used.

1.3.1 Implementation examples

In this subsection, I describe state-of-the-art examples of continuous phase tuning metasurfaces used in different antenna configurations, operating at different frequencies and demonstrating different examples of beam-forming.

Reflectarray configuration. There are many examples of continuous phase tuning metasurfaces where the reconfigurability is implemented by means of semiconductor devices such as varactor diodes. In this case, the phase tuning mechanism is implemented by adjusting the resonant response of scatterers (e.g. patch antennas) constituting a metasurface. On the other hand, the technology of liquid crystals (LCs) provides another way to achieve reconfigurability by modifying the local material properties of the substrate [93, 94, 95, 96, 92]. The permittivity of LCs changes when applying a quasi-static electric field. Particularly, nematic LCs have demonstrated one of the best properties at microwave and mm-wave frequencies [96]. Resonant scatterers are non-reconfigurable in such a configuration and placed on top of the substrate.

In 2015, G. Perez-Palomino *et al.* reported an implementation of a continuous phase tuning metasurface based on the reconfigurable response of nematic LCs for antenna application in the

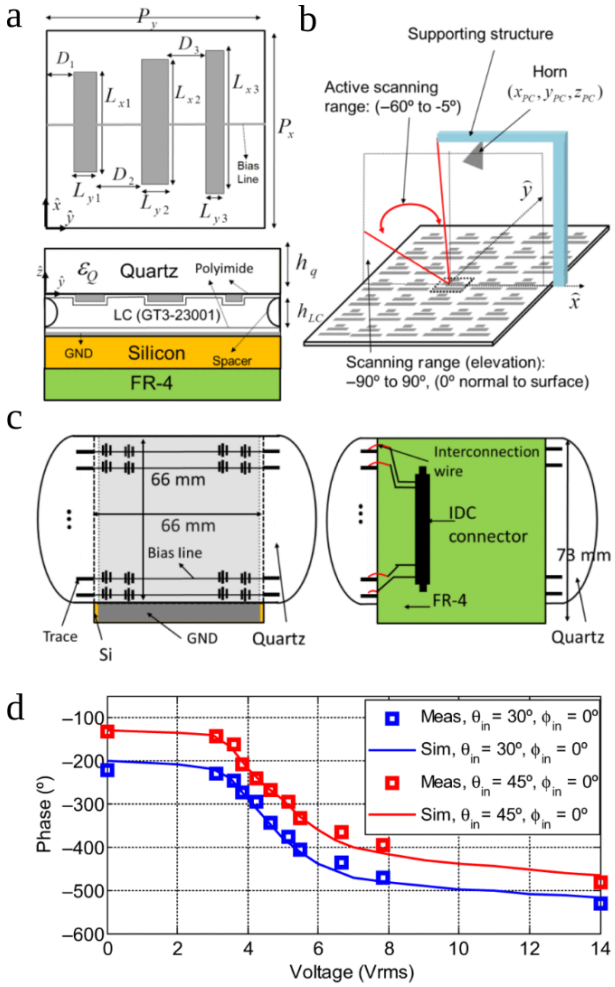

Figure 1.10: ***(a)–(c)*** *A schematic of a continuous phase tuning metasurface using a liquid crystal.* ***(a)*** *A layout of a unit cell with dimensions (mm): $P_y = 1.145$, $P_x = 1.093$, $L_{xl} = 0.707$, $L_{x2} = 0.748$, $L_{x3} = 0.792$, $L_{yl} = 0.20$, $L_{y2} = 0.211$, $L_{y3} = 0.20$, $D_l = 0.171$, $D_2 = 0.096$, $D_3 = 0.042$, $h_{LC} = 0.075$.* ***(b)*** *A reflectarray configuration.* ***(c)*** *Top (left) and bottom (right) views of the metasurface.* ***(d)*** *Simulation and experimental results of the unit cell phase response at 100 GHz vs. the applied (root mean square) bias voltage. The results for two incidence angles (30° and 45°) are shown. The AC bias voltage has the frequency of 0.33 Hz and the shape of a square wave [92].*

reflectarray configuration [92]. The developed reconfigurable unit cell, shown in Fig. 1.10(a), is composed of three parts: (i) a quartz wafer with three parallel dipoles of different lengths printed on its bottom face; (ii) a silicon wafer with the ground plane on its top face; (iii) a LC cavity inserted between the two wafers. The used LC is the mixture GT3-23001 manufactured by Merck. The unit cell size is 1.145×1.093 mm^2 that corresponds to $0.38\lambda_0 \times 0.36\lambda_0$ at the central operating frequency of 100 GHz. The geometrical parameters of the elements constituting the unit cell were selected to achieve a linear dependence of the phase on the frequency (in the range from 94 to 104 GHz) and a dynamic phase range approaching 2π. The fabricated metasurface is composed of 54×52 unit cells and a conical horn antenna (Millitech SGH-08) is used as a source. Figure 1.10(b) demonstrates a schematic of the assembled sample. In order to achieve beam-

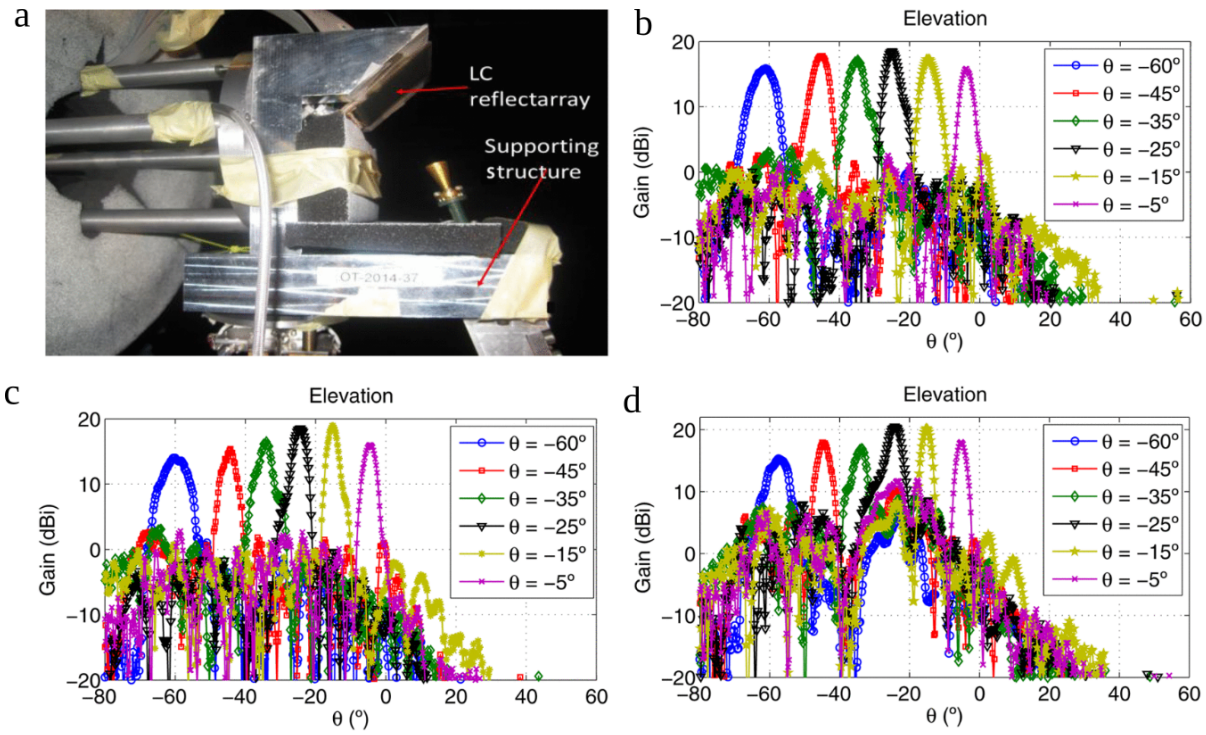

Figure 1.11: ***(a)*** *A photograph of the experimental setup.* ***(b)–(d)*** *Experimental results of beam-steering at* 96 *GHz* ***(b)***, 100 *GHz* ***(c)*** *and* 104 *GHz* ***(d)*** *[92].*

steering in elevation plane, see Fig. 1.10(b), a bias network allowing control of the unit cells by rows was implemented. Bias lines connect the printed dipoles as illustrated in Fig. 1.10(c). The bias network is powered by an AC voltage source. Simulated and experimentally measured phase response of the metasurface when equal voltages are applied to all unit cells are shown in Fig. 1.10(d) and the 330° dynamic range of the phase tuning is obtained. The modeling of the considered unit cell was performed by the authors in Ref. [97].

Measurements of the radiation patterns were performed in an anechoic chamber. A photograph of the experimental sample is shown 1.11(a). Experimental results of beam-steering in the range from −5° to −60° at three different frequencies are shown in Figs. 1.11(b)–(d). At 100 GHz, for example, the level of side lobes increases from −18 dB when steering away from the specular direction (−25°), but remains below −13 dB independently from the steering angle. However, as the authors pointed out, the beam-steering beyond −60° produces a significant increase of spurious radiation because of the phase errors resulted from using the local periodic approximation. The main reason of the pattern degradation within the steering range is that the amplitude of the local reflection coefficient is different for different values of the phase. Nonetheless, the experimental results demonstrated by the authors are among the best in the literature on LC-based continuous phase tuning metasurfaces.

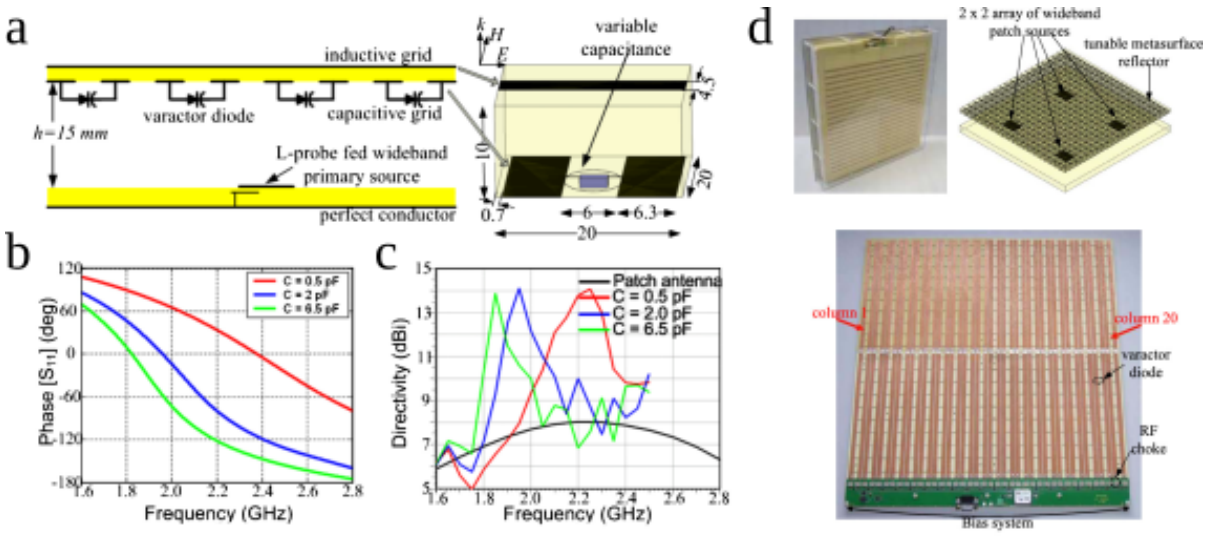

Figure 1.12: ***(a)*** *A schematic of a metasurface-based Fabry-Perot cavity antenna. The inset figure shows a layout of the design of the unit cell, all dimensions are in mm.* ***(b)*** *The phase of the reflection coefficient from designed reconfigurable metasurface.* ***(c)*** *Simulation results of the directivity vs. the frequency for different capacitances of varactor diodes. The directivity of the feeding patch antenna is plotted for comparison.* ***(d)*** *Photographs and a schematic of the assembled experimental sample [98].*

Fabry-Perot cavity configuration. Generally, a Fabry-Perot cavity antenna is represented by a source inserted between a ground plane and a partially reflecting surface (PRS). In 2010 [98], S. N. Burokur *et al.* reported a reconfigurable metasurface used as a PRS of a Fabry-Perot cavity antenna, as displayed in Fig. 1.12(a). The authors developed a bi-layer unit cell represented by inductive and capacitive grids, as shown in the inset of Fig. 1.12(a). The inductive and capacitive grids are mutually orthogonal, the electric field is parallel to the inductive grid. The dimensions of the unit cell were optimized via 3D full-wave simulations for the operating frequency of 2 GHz. An electronic reconfigurability is achieved by loading the capacitive grid with varactor diodes. It allows one to adjust reflection and transmission coefficients of the metasurface in a continuous manner. The metasurface is built as a periodic array of the designed unit cells. When changing the bias voltage applied to varactor diodes, their capacitance changes and so does the phase of the reflection coefficient. Figure 1.12(b) demonstrates how this phase changes for different values of the capacitance of the varactor diodes (BB857 from Infineon Technologies). When reducing the capacitance, the resonance shifts to higher frequencies.

Figure 1.12(c) demonstrates simulation results of reconfigurable frequency response, the directivity of the metasurface-based antenna is compared to the directivity of the feeding patch. It is important to note that the authors used a wideband patch antenna (operating frequency

band is $1.8 - 2.7$ GHz) to feed the cavity, it facilitates the implementation of the wideband frequency agility of the antenna system. A 400 mm by 400 mm metasurface (corresponding to 20 by 20 unit cells) was fabricated on the base of the developed design, four patch antennas were used to excite the cavity. RF chokes are used to avoid high frequency currents going to the bias system. A photograph and a schematic of the assembled experimental sample is shown in Fig. 1.12(d). Figure 1.13 shows experimental results and demonstrates that when changing the bias voltage (from 0 to 24 V), the cavity resonance frequency shifts. A well-defined beam is observed at each resonant frequency. Thus, the implemented reconfigurable metasurface allowed the authors to achieve continuous phase tuning and demonstrate smooth frequency agility of otherwise a narrow-band Fabry-Perot cavity antenna.

In order to implement beam-steering with a Fabry-Perot antenna, a phase gradient must be created along the partially reflecting surface. In Ref. [99], R. Guzmán-Quirós *et al.* proposed an electrically reconfigurable Fabry-Perot antenna capable of beam-steering in elevation and azimuth planes at a given frequency. In contrast to the previous example, a reconfigurable metasurface is placed at the bottom of the cavity. The metasurface realizes a high impedance surface (HIS) and is represented by an array of rectangular patches. The reconfigurability is achieved by loading the patches with varactor diodes. A partially reflecting surface covering the cavity is non-reconfigurable and creates a predefined reflection phase. Figure 1.14(a) shows the principal scheme of the assembled antenna.

The operation principle of the suggested reconfigurable Fabry-Perot antenna is based on changing the propagation constant of a leaky-wave excited in the cavity by adjusting the surface impedance of the reconfigurable metasurface. The authors performed the analysis of the dispersion of the leaky-wave with respect to the capacitance of varactor diodes by modeling a unit cell as a transverse equivalent network shown in Fig. 1.14(b). PEC (PMC) walls are used to model propagation of a TE (TM) leaky-wave along the y-direction (x-direction). Although the impedances of PRS and HIS depend on the polarization, the dispersion curves shown in Fig. 1.14(c) almost coincide for TE and TM leaky-waves. The authors observed that there are two different regimes of propagation of leaky-waves: (i) up to approximately 0.25 pF the leaky-wave is propagating and radiates in free space with the corresponding steering angle; (ii) for the capacitance greater than 0.25 pF, electromagnetic band gap appears and the leaky-wave becomes evanescent along the antenna aperture and the radiation is suppressed. Therefore, by individually adjusting the surface impedance of separate sectors of the metasurface, the leaky-wave can

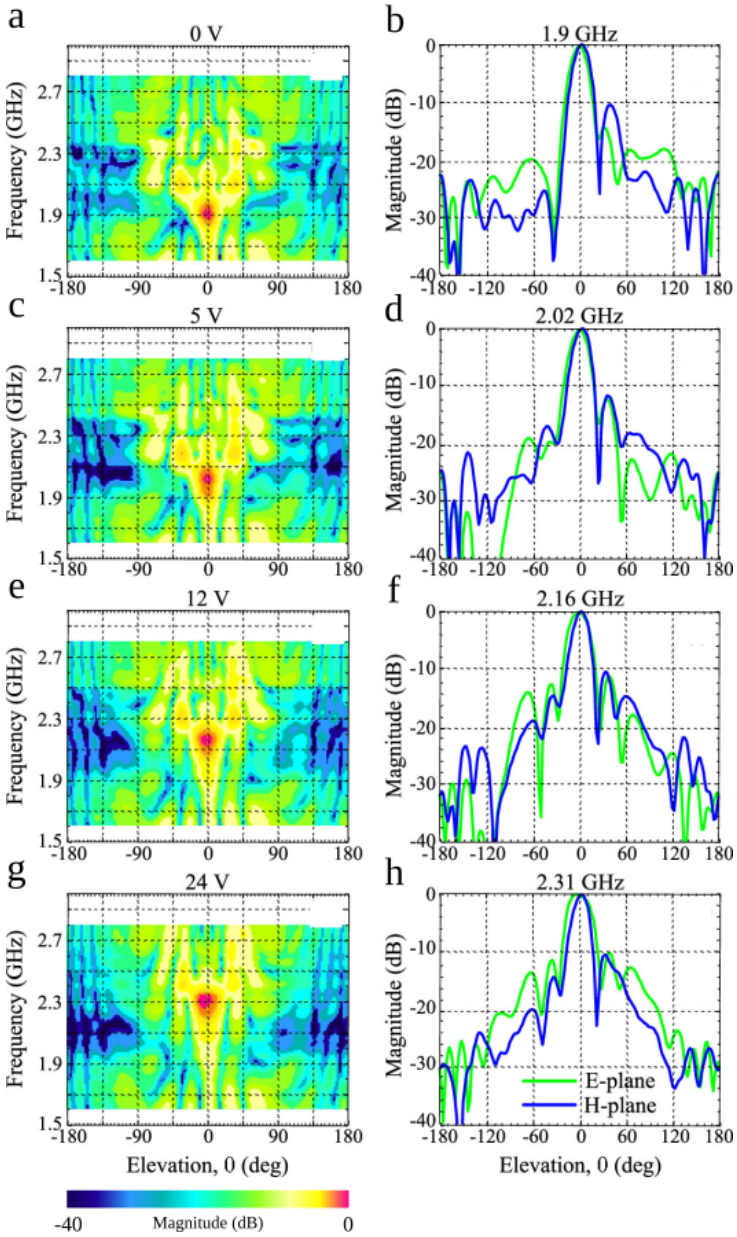

Figure 1.13: The panels ***(a)***,***(c)***,***(e)***,***(g)*** *demonstrate far-field intensity as function of the frequency and the elevation angle in E-plane. The panels* ***(b)***,***(d)***,***(f)***,***(h)*** *demonstrate measured radiation patterns in E- and H-planes at the frequencies of maximum gain. The bias voltages and corresponding operating frequencies are* 0 *V and* 1.9 *GHz in the panels* ***(a)*** *and* ***(b)***, 5 *V and* 2.02 *GHz in the panels* ***(c)*** *and* ***(d)***, 12 *V and* 2.16 *GHz in the panels* ***(e)*** *and* ***(f)***, 24 *V and* 2.31 *GHz in the panels* ***(g)*** *and* ***(h)*** *[98].*

be directed at a desired azimuth angle. In the considered work, the authors equally divided the metasurface into four such sectors that can be controlled individually (Fig. 1.14(d)). Meanwhile the elevation angle is adjusted by changing the bias voltage applied to the varactor diodes (and, thus, their capacitance) according to the dispersion curves highlighted in Fig. 1.14(c) by hollow circles.

The designed reconfigurable Fabry-Perot antenna was fabricated by means of the PCB tech-

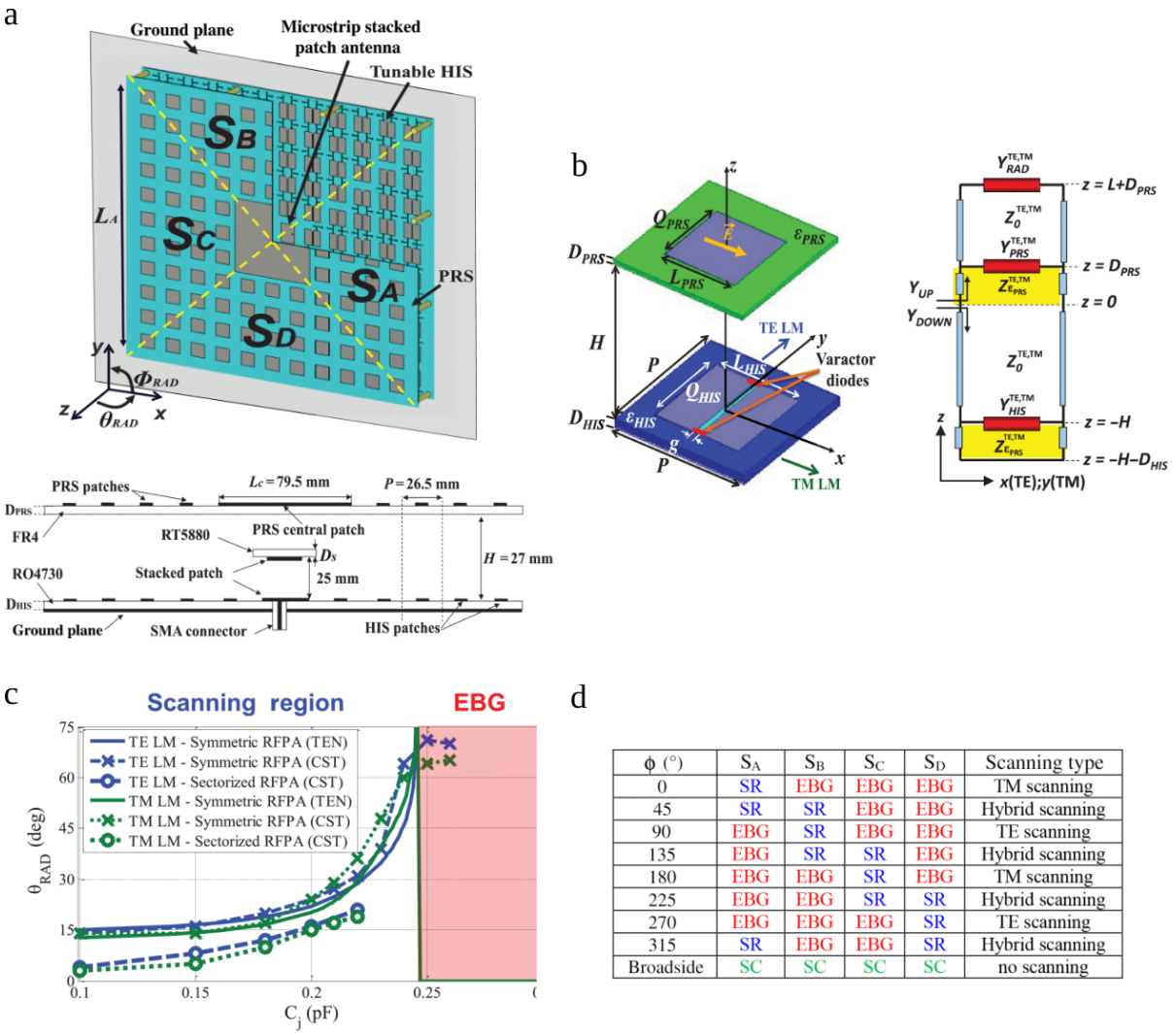

ϕ (°)	S_A	S_B	S_C	S_D	Scanning type
0	SR	EBG	EBG	EBG	TM scanning
45	SR	SR	EBG	EBG	Hybrid scanning
90	EBG	SR	EBG	EBG	TE scanning
135	EBG	SR	SR	EBG	Hybrid scanning
180	EBG	EBG	SR	EBG	TM scanning
225	EBG	EBG	SR	SR	Hybrid scanning
270	EBG	EBG	EBG	SR	TE scanning
315	SR	EBG	EBG	SR	Hybrid scanning
Broadside	SC	SC	SC	SC	no scanning

Figure 1.14: ***(a)*** *A schematic of a metasurface-based reconfigurable Fabry-Perot antenna.* ***(b)*** *A layout of a unit cell design (left) and the transverse equivalent network for TE- and TM-polarized leaky-waves.* ***(c)*** *Elevation scanning angle vs. the capacitance of varactor diodes at* 5.5 *GHz operating frequency.* ***(d)*** *The table shows azimuth scanning angle as function of activated sectors of the reconfigurable metasurface [99].*

nology. A figure of the assembled prototype is shown on the left of Fig. 1.15(a) and the photograph on the right shows the reconfigurable metasurface. Figure 1.15(b) demonstrates simulation and experimental results of beam-steering at different azimuth planes and elevation angles. Although the concept allows realizing beam-steering at arbitrary azimuth angles, the experimental results show very limited beam-steering capabilities in the elevation plane. Furthermore, when increasing the steering angle, the beam deforms and the level of side lobes increases. The approach lacks flexibility and the radiation performance cannot be improved by optimizing the local (not only sectorial) surface impedance. A possibility of a more complex beam-forming performance (beam-shaping and control of multiple beams) was not discussed.

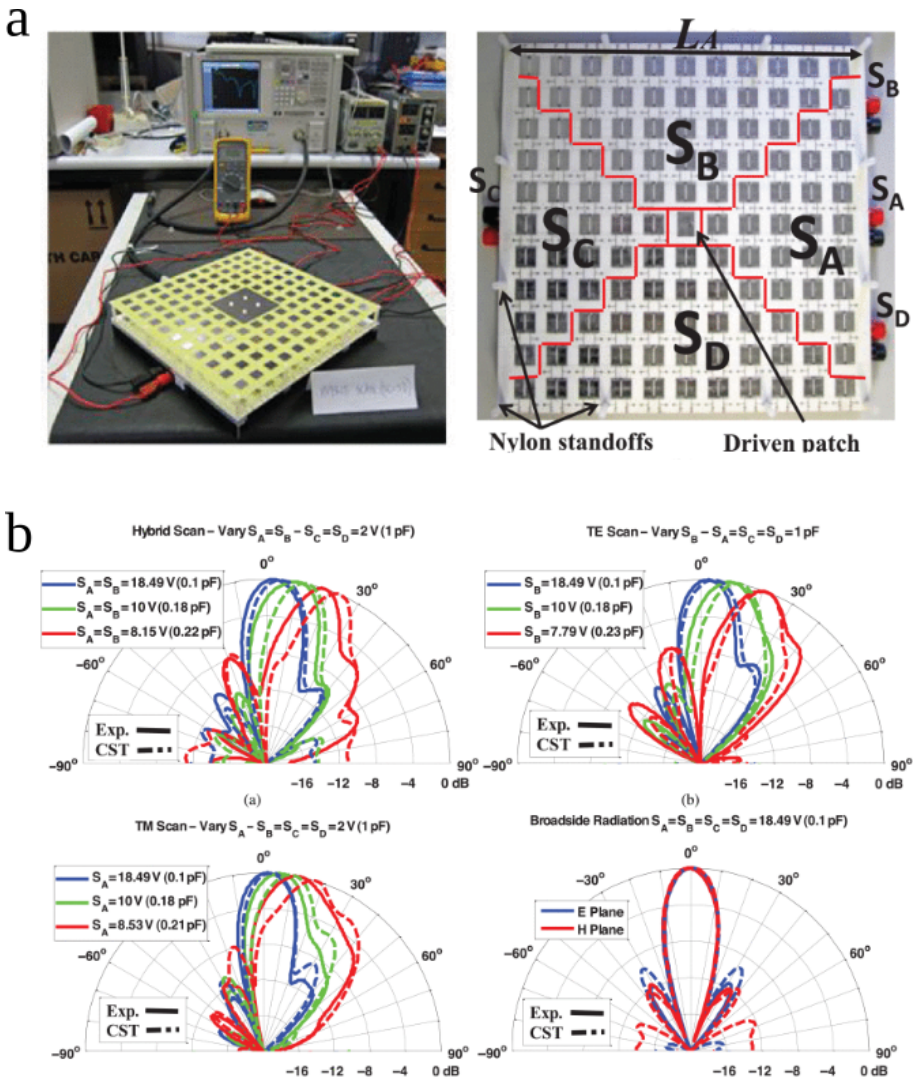

Figure 1.15: ***(a)*** *Photographs of the assembled antenna prototype (left) and the reconfigurable metasurface (right).* ***(b)*** *Simulation and experimental results of normalized radiation patterns at* 5. *GHz operating frequency for different azimuth and elevation steering angles [99].*

Conformal transmitarray configuration. The design of a conformal metasurface is generally based on Eq. (1.1) [100, 101, 102, 103, 104, 105, 106, 107], where a proper spatial distribution of *local* reflection (transmission) coefficient should be established along the reflecting (transmitting) metasurface. On the other hand, more rigorously, metasurfaces can be described by means of generalized sheet transition conditions [108]. Unfortunately, such a theoretical modelling of conformal metasurfaces appears to be exceptionally challenging, demanding accurate analysis of the metasurface geometry and dealing with curvilinear coordinates [109].

To the best of my knowledge, until recently there have been no reports on experimental implementation of conformal and reconfigurable metasurface-based antennas, neither in reflectarray nor in transmitarray configurations. In the end of 2019, H. Li *et al.* demonstrated in

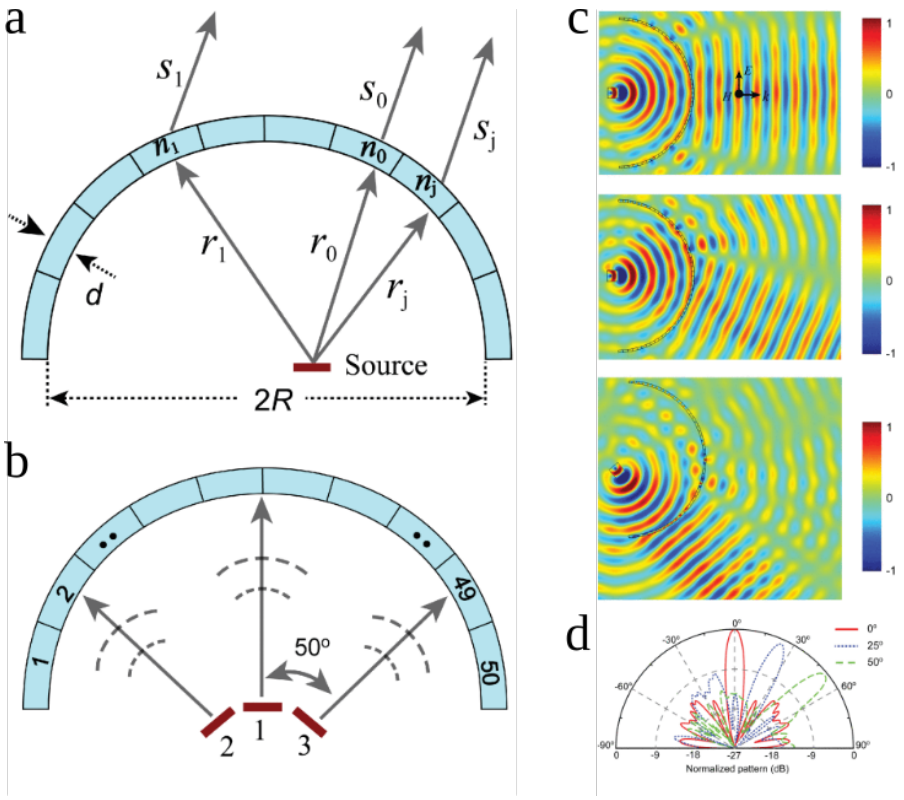

Figure 1.16: ***(a),(b)*** *The principle of beam-steering with a semi-cylindrical metasurface antenna when being illuminated by a single feeding antenna* ***(a)*** *or multiple feeding antennas* ***(b)****.* ***(c),(d)*** *Results of 2D simulations of a semi-cylindrical metasurface. The panel* ***(c)*** *demonstrates distributions of the electric field for beam-steering at* 0°*,* 25° *and* 50°*. The panel* ***(d)*** *shows corresponding far-field radiation patterns [100].*

Ref. [100] dynamic beam-steering with a semi-cylindrical reconfigurable metasurface whose operation principle is based on adjusting the local transmission coefficient according to Eq. (1.1). A schematic of the operational principle is shown in Fig. 1.16(a), where $\mathbf{r}_j$ is the location of the j^{th} unit cell and $\mathbf{S}_j$ shows a desired direction of the main beam. A distinct feature of the metasurface-based antenna presented by the authors is that a feeding system is represented by three independent antennas activated one at a time, see Fig. 1.16(b). Two-dimensional full-wave simulations were performed in order to validate the operational principle. Figures 1.16(c) and (d) demonstrate, respectively, the distribution of the electric field and the far-field radiation pattern for three examples of beam-steering when two different feeding sources are used. In the simulations, the semi-cylindrical metasurface has a radius of 400 mm and is divided into 50 unit cells. The operating frequency is 5.75 GHz. From the simulations, it is particularly observed that the level of side lobes can be reduced at off-broadside steering angles when rotating the excitation source (Fig. 1.16(d)).

The unit cell is represented by two single-layer PCBs separated by 5 mm air gap. A capacitive

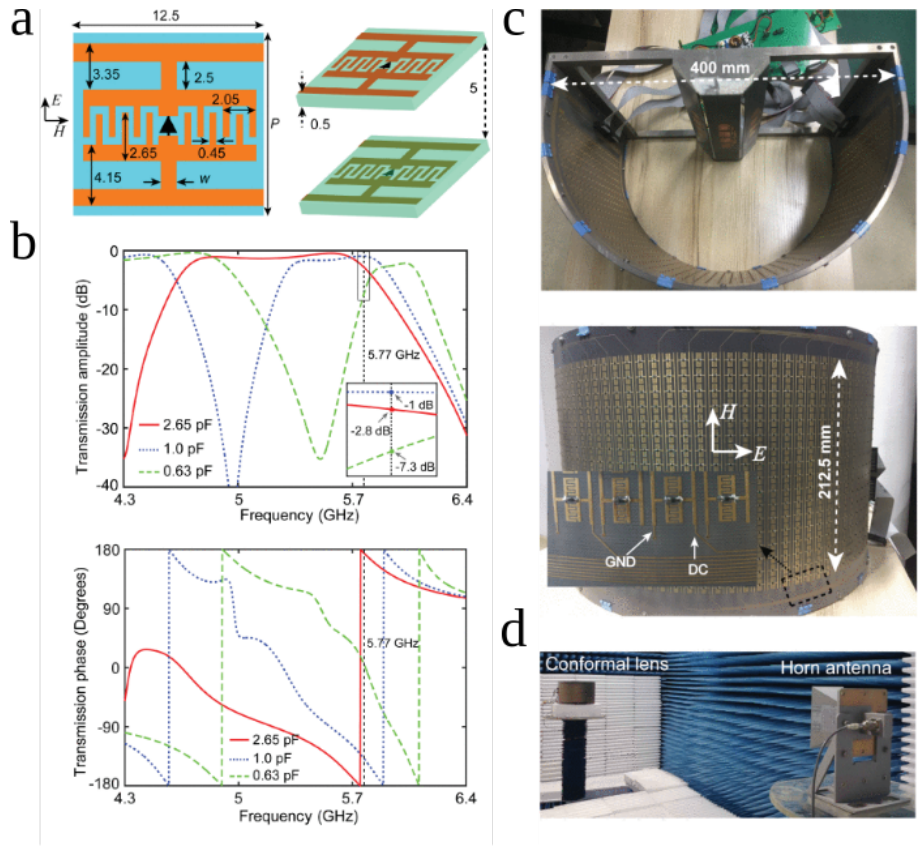

Figure 1.17: ***(a)*** *A schematic of the designed unit cell, all the dimensions are in mm.* ***(b)*** *Simulation results of the amplitude and the phase of the transmission coefficient.* ***(c)***,***(d)*** *Photographs of the assembled experimental sample* ***(c)*** *and the experimental setup* ***(d)*** *[100].*

element is printed on top face of each layer and is loaded with a varactor diode (Skyworks SMV1405). The layers have the thickness of 0.5 mm, which makes them flexible and allows one to conform the metasurface to a semi-cylindrical surface. The dynamic range of capacitances of the varactor is from 2.6 pF to 0.6 pF for the DC bias voltage from 0 V to 30 V. A schematic of the unit cell design and its dimensions are shown in Fig. 1.17(a). The unit cell has a size of approximately $\lambda_0/4$ at the central operating frequency of 5.75 GHz. To study the response of the designed unit cell, the authors performed 3D full-wave simulations and the SPICE model was used to describe the SMV1405 varactor diode. The amplitude and the phase of the transmission coefficient are plotted in Fig. 1.17(b) for different values of the capacitance of the varactor diodes.

On the basis of the developed design, a reconfigurable metasurface was fabricated and conformed to a semi-cylindrical metallic frame as shown in Fig. 1.17(c). The two layers composing the metasurface consist of 850 unit cells, 50 in a row and 17 in a column. A DC bias voltage (from 0 V to 30 V) can be independently applied to each column via the implemented bias network, the bias lines span along the horizontal edges of the sample, outside the metasurface area, as shown in Fig. 1.17(c). It allows one to perform beam-steering in horizontal plane, the

radiation pattern in the other plane mostly repeats that of the source. The feeding system is represented by three linear arrays of patch antennas, where each array has 4 patches. The arrays point in different directions (0° and ±50°) and used to illuminate the different regions of the metasurface.

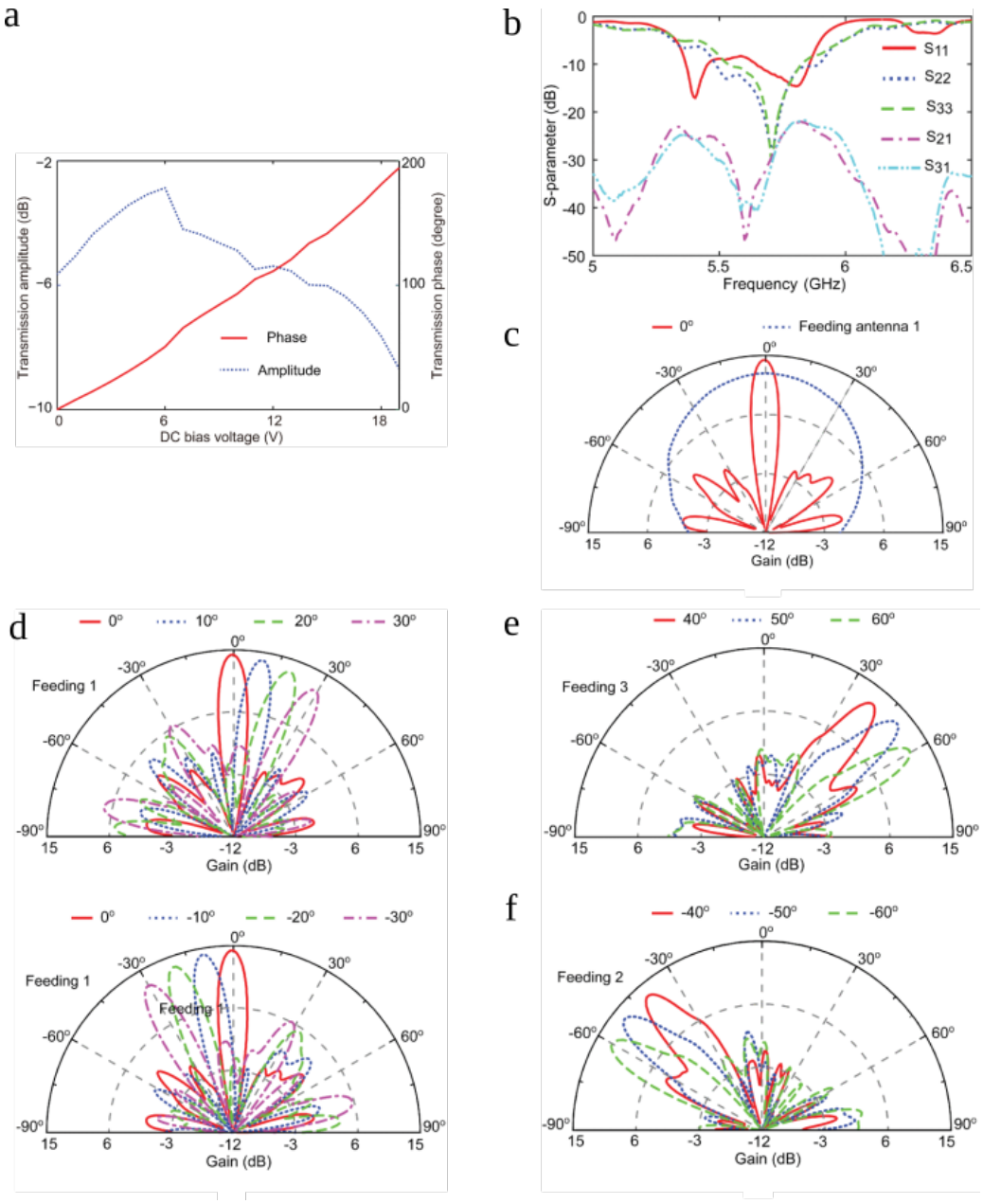

Figure 1.18: ***(a)*** *Measured amplitude and phase of the transmission coefficient at* 5.75 *GHz.* ***(b)****,****(c)*** *Experimental results of beam-steering at broadside (*0°*). The panel* ***(b)*** *demonstrates S-parameters of the three patch antenna arrays used to illuminate the metasurface. The panel* ***(c)*** *compares the radiation patterns at* 5.75 *GHz of the central source antenna alone and with the metasurface.* ***(d)****–****(f)*** *Beam-steering performances at* 5.75 *GHz when using the central* ***(a)****, the right* ***(e)*** *and the left* ***(f)*** *feeding antennas [100].*

An experimental characterization of the fabricated sample is of particular importance, the metasurface is used in a non-planar configuration and the conventional procedure may not

be accurate. The authors performed experimental measurements in an anechoic chamber as shown by Fig. 1.17(d). To calculate the transmission coefficient, the authors measured the S_{21} parameter between the 1st patch antenna array and the receiving horn antenna in the presence and the absence of the metasurface. The other two patch antenna arrays were connected to a matched load. In the first configuration, equal voltages were applied to all varactors; the second configurations is used for normalization. The transmission coefficient calculated in this way at 5.75 GHz is plotted in Fig. 1.18(a). 195° dynamic range of the phase is achieved when changing the voltage from 0 V to 19 V. The difference between the amplitude of the transmission coefficient obtained from simulations (Fig. 1.17(b)), and experiments may originate from the features of the sample itself (such as the metallic frame) and inaccuracies of the experimental characterization procedure.

Figures 1.18(b)–(f) present the results of beam-steering in the horizontal plane. Necessary bias voltages are found by means of Fig. 1.18(a) and Eq. (1.1) and the authors modeled the incident wave as a cylindrical wave. For the case of radiation at broadside, the authors present the frequency dependence of S_{11} parameter, as displayed in Fig. 1.18(b). It characterizes the matching of the feeding system, on the one hand, and the power reflected from the metasurface back to the source, on the other hand. Figure 1.18(c) allows one to see the impact of the metasurface on the radiation pattern in comparison to the radiation pattern of the source (patch antenna array radiating at 0°, see Fig. 1.18(c)). The beamwidth is reduced from approximately 72° to 8°. The instantaneous bandwidth is estimated as 100 MHz. The beam steering in the range ±30° at 5.75 GHz is demonstrated in Fig. 1.18(d) when the metasurface is illuminated by the central source radiating at 0°. The level of side lobes changes in the range from −12.3 dB to −5.0 dB for radiation from 0° to 30°. When further increasing the steering angle, the level of side lobes raises as well. The authors got around the problem by introducing two additional feeding antennas rotated at ±50° with respect to the central one. Each feeding antenna is responsible for its narrow steering range. Figures 1.18(e) and (f) demonstrate beam-steering at 5.75 GHz beyond ±30° when the metasurface is illuminated by the patch antenna array at +50° and −50°, respectively. The level of side lobes remains below −9.6 dB in these cases.

Overall, the authors demonstrated good beam-steering performance which, however, requires using multiple feeding antennas switched on selectively. A possibility of a more complex beam-forming performance (beam-shaping and control of multiple beams) was not discussed.

1.3.2 Huygens' metasurfaces

In 2013, C. Pfeiffer and A. Grbic presented in Ref. [110] the concept of Huygens' metasurfaces on the basis of the electromagnetic equivalence principle [111]. The electric and magnetic fields in a source-free region are determined by their tangential components along a closed surface. By the equivalence principle, the fields inside and outside the surface are obtained by placing over the surface suitable electric- and magnetic-current densities which satisfy the boundary conditions

$$\mathbf{n}_{12} \times (\mathbf{H}_2(\mathbf{r}) - \mathbf{H}_1(\mathbf{r})) = \mathbf{J}_s(\mathbf{r}), \quad \mathbf{n}_{12} \times (\mathbf{E}_2(\mathbf{r}) - \mathbf{E}_1(\mathbf{r})) = -\mathbf{M}_s(\mathbf{r}), \tag{1.3}$$

where $\mathbf{n}_{12}$ is a unit vector orthogonal to the surface and pointing outside it, the vector $\mathbf{r}$ corresponds to a point on the surface, $\mathbf{J}_s$ and $\mathbf{M}_s$ are equivalent electric- and magnetic-current densities, $\mathbf{H}_{1,2}$ and $\mathbf{E}_{1,2}$ are the magnetic and electric fields. The index 1 and 2 corresponds to the region inside and outside the closed surface, respectively. C. Pfeiffer and A. Grbic proposed to substitute the fictitious currents by polarization currents excited in electric- and magnetic-impedance sheets by an impinging wave

$$\mathbf{J}_s(\mathbf{r}) = \frac{1}{2} Y_{es}(\mathbf{r}) \left(\mathbf{E}_1(\mathbf{r}) + \mathbf{E}_2(\mathbf{r})\right), \quad \mathbf{M}_s(\mathbf{r}) = \frac{1}{2} Z_{ms}(\mathbf{r}) \left(\mathbf{H}_1(\mathbf{r}) + \mathbf{H}_2(\mathbf{r})\right), \tag{1.4}$$

where $Y_{es}(\mathbf{r})$ and $Z_{ms}(\mathbf{r})$ are electric surface admittance and magnetic surface impedance. Dense arrays of engineered scatterers are used to implement required surface impedances. Generally, both electric and magnetic responses are required in order to achieve asymmetric scattering. To achieve a magnetic response it is not necessary to use magnetic particles, an effective magnetic response can be obtained from an asymmetric ensemble of electric-only scatterers. The local periodic approximation allows one to relate the surface impedances with the local reflection coefficient $R(\mathbf{r})$ and the local transmission coefficient $T(\mathbf{r})$ [112]

$$Y_{es}(\mathbf{r}) = \frac{2\left(1 - T(\mathbf{r}) - R(\mathbf{r})\right)}{\eta\left(1 + T(\mathbf{r}) + R(\mathbf{r})\right)}, \quad Z_{ms}(\mathbf{r}) = \frac{2\eta\left((1 - T(\mathbf{r}) + R(\mathbf{r})\right)}{1 + T(\mathbf{r}) - R(\mathbf{r})}. \tag{1.5}$$

The theoretical framework developed by C. Pfeiffer and A. Grbic and represented by Eqs. (1.3)–(1.5) allows one to further advance the ideas behind reflectarray and transmitarray antennas and light propagation with phase discontinuities [1]. On the one hand, more complex than beam-steering and more efficient than within the framework of Ref. [1], wavefront transformations

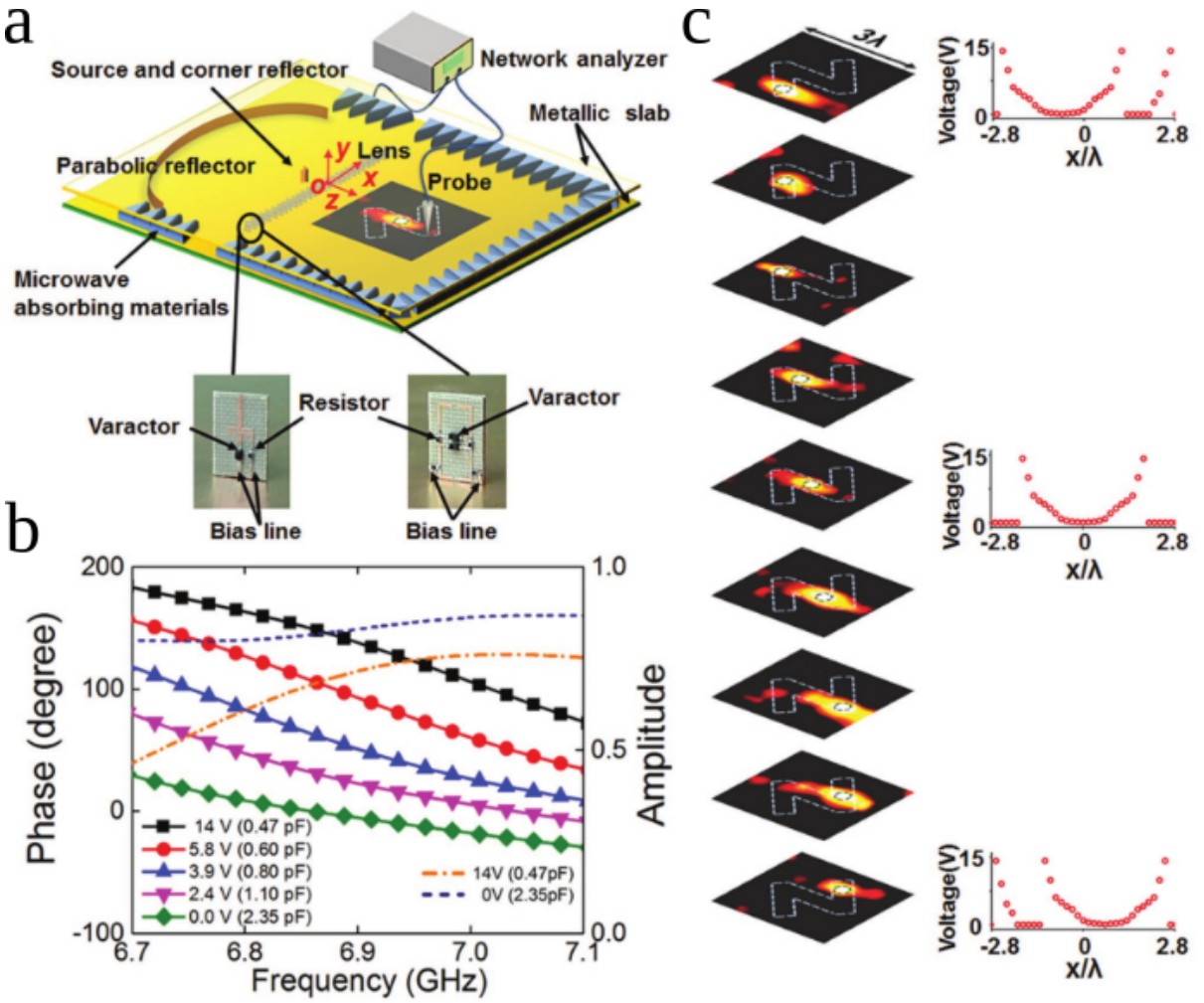

Figure 1.19: ***(a)*** *A schematic of the experimental setup. The inset figure shows photographs of the fabricated unit cell, frontside (right) and backside (left).* ***(b)*** *The phase and the amplitude of the local transmission coefficient under different applied bias voltages* ***(c)*** *Experimental results of the near-field scanning at* 6.9 *GHz, the focal spot is consequently moved along a trace of the letter "N" [47].*

were performed by means of Huygens' metasurfaces, as for example, Bessel [110, 113, 114] and Airy [115] beams excitation. On the other hand, the concept allowed one to find fundamental performance limitation of metasurfaces for wavefront manipulation in terms of efficiency [116, 117, 118, 119].

Generally, to implement a Huygens' metasurface characterized by electric- and magnetic-impedance densities, dense arrays (64 elements per λ_0^2 area) of meta-atoms are used. Both complicated designs of reconfigurable meta-atoms and ohmic losses inherent in tunable elements made it very challenging, especially in optical and visible domains [120, 121, 51, 78, 77], to implement reconfigurability in Huygens' metasurfaces. To the best of my knowledge, reconfigurable Huygens' metasurfaces were experimentally demonstrated only in a couple of studies presented in literature [36, 47, 122]. For instance, dynamic focusing with an electronically reconfigurable

Huygens' metasurface was presented in 2017 by K. Chen *et al.* in Ref. [47]. The authors implemented a single row of the metasurface and embedded it inside a parallel-plate waveguide, as illustrated in Fig. 1.19(a), to emulate an infinite array. The inset of the same figure shows a photograph of the designed unit cell incorporating varactor diodes as tunable elements. The size of the unit cell is $\lambda_0/4.35$ by $\lambda_0/6.21$ at the central operating frequency of 6.9 GHz. The experimental results of the metasurface characterization appear in Fig. 1.19(b) and show the phase and the amplitude of the local transmission coefficient. Figure 1.19(c) demonstrates experimental capabilities of the designed metasurface for dynamic focusing at 6.9 GHz. The authors estimated the total efficiency of the focusing, defined as the power measured in the focal spot over the input power, by approximately 36% . As it was also pointed out by the authors, the modest efficiency is due to lossy tunable elements and inaccuracies in the phase and amplitude of the local transmission coefficient.

1.4. Conclusion

In this Chapter, I reviewed the main theoretical and experimental developments in the field of reconfigurable metasurfaces for antenna applications. Experimental performances of reconfigurable metasurfaces operating within major theoretical approaches, binary phase-state and continuous phase tuning, and built around different tunable elements, PIN diodes, varactor diodes and liquid crystals, were analysed in detail. Utilization of metasurfaces in reflectarray, transmitarray, Fabry-Perot cavity and conformal transmitarray antenna configurations were considered. Beam-steering and beam-shaping capabilities and the potential of manipulating multiple beams by the considered metasurface-based antenna systems were discussed. To compare, the best and the worst results were demonstrated, respectively, by the binary phase-state metasurface in reflectarray configuration and the continuous phase tuning metasurface implementing a HIS in a Fabry-Perot cavity antenna. However, it should be noted that the performance efficiency is not the only restraint for the choice of an antenna configuration. Other characteristics such as geometric dimensions and shape, complexity of a feeding system and operating frequency bandwidth can be important factors as well.

1.4.1 Advantages and disadvantages of conventional approaches

The main advantage of binary phase-state and continuous phase tuning metasurfaces is the simple theoretical model expressed in the form of Eq. (1.1). This model allows one to achieve good efficiency of beam-steering up to 60° from the broadside. However, the presented state-of-the-art experimental results show that this theoretical approach is best suited for reflectarray and transmitarray antenna configurations. It shows moderate beam-steering performances for Fabry-Perot cavity and conformal transmitarray configurations. Furthermore, it was revealed that there are strong limitations in terms of efficiency and level of side lobes for beam-steering at larger angles [118, 119]. For performing beam-shaping and manipulating multiple beams, Eq. (1.1) should be complemented with optimization procedures. In Refs. [35, 79], a genetic algorithm was implemented to that end. This solution is however limited to reflectarray and transmitarray configurations and was not demonstrated for compact metasurface-based antenna systems such as a Fabry-Perot cavity antenna.

A crucial point of the development of a reconfigurable metasurface is the design of a unit cell. The design is performed within the local periodic approximation [75, 112], when the electromagnetic response of a unit cell in a nonuniform array is approximated by its response in a corresponding periodic arrangement. It allows one to avoid time-consuming numerical computations of large-area metasurfaces and significantly accelerate the design procedure. Ideally, a unit cell should be engineered to exhibit, under an external stimulus, the phase response in the full 2π-range. Meanwhile, the amplitude response should be kept independent from the stimulus. Unfortunately, there is not a single unit cell realized in practice that would possess such a behavior. Indeed, in order to achieve strong interaction of an electrically small unit cell with an incident wave, one harnesses resonant particles. The presence of electromagnetic resonances and losses (dielectric losses in a substrate, conduction losses in metals or losses in tunable elements) always implies a nonuniform amplitude response and results in a nonuniform absorption over the aperture of a metasurface. It further deteriorates the beam-forming efficiency performed in accordance with Eq. (1.1) under the assumption of a uniform distribution of the amplitude of the local reflection (transmission) coefficient. Furthermore, the local periodic approximation does not allow to account for mutual interactions between unit cells in a metasurface exhibiting actually a nonuniform response along its aperture. The assumption of the local periodicity can be overcome by more detailed analyses that account for mutual coupling effects by simulating

each radiating cell with its actual neighbouring cells [123, 124]. However, these more elaborate techniques are not widely used.

Neither Eq. (1.1) nor the design procedure within the local periodic approximation sets constraints on the total size of a unit cell. According to the theory of antenna arrays [125], the size of a unit cell should be $\lambda_0/2$ by $\lambda_0/2$ to avoid the appearance of grating lobes at the operating frequency. However, as it was seen throughout the state-of-the-art examples, the shortest dimension of a unit cell composing a reconfigurable Huygens' metasurface can be as small as $\lambda_0/6.21$ [47]. Although Huygens' metasurfaces promise to improve efficiency of wavefront manipulation [118, 119, 126, 117, 127, 128, 129, 130, 131] in comparison to conventional approach, a higher density of unit cells might lead to increased absorption (because of losses in tunable elements) and reduced total efficiency.

Summarizing the aforesaid, the motivation for the research executed in this Thesis can be formulated as follows

- Fundamental performance limitations of binary phase-state and continuous phase tuning metasurfaces;
- Inaccuracies of the design procedure based on the conventional local periodic approximation;
- Open question of the density of unit cells composing a metasurface and its impact on the absorption;
- Limited capabilities and moderate efficiency of antenna configurations such as Fabry-Perot cavity and conformal transmitarray antennas.

Chapter 2

Multi-element reflective metagratings

Contents

2.1. Introduction

A diffraction grating, defined as a periodic optical structure with infinite extent in one direction diffracts waves incident on its surface [132]. Being imposed by the periodicity of a grating, which can be of the order of a free-space wavelength or greater, an incident wave is scattered as propagating diffraction orders only in certain directions. Back at the beginning of the 20$^{\text{th}}$ century, the problem of intensity distribution among diffraction orders produced by a grating was referred to as one of the most important topic in optics [133]. The intensity distribution is defined by the geometric profile of a grating and its period, both can be arbitrary in a general case. It makes a rigorous analysis particularly difficult. A particular class of gratings maximizing the intensity in a given diffraction order referred to as blazed gratings was studied in detail [133, 134, 135, 136] and perfect blazing was demonstrated in nonspecular direction when there are only two propagating orders [137, 138]. Classical blazed gratings are three-dimensional (3D) structures that generally take the form of right-angle sawtooths [139, 138], sinusoidal shape [138] and rectangular grooves [137, 138].

In the last decade, metasurfaces have been applied to mimic blazed gratings functionality [140]. While in the First Chapter, I refer to any structured surface as a metasurface, in this case metasurfaces presented in the literature are essentially dense structured surfaces. In course of extensive research, effective-medium theoretical models were established to arbitrary control reflection and refraction of an incident plane wave [1, 110]. Then a metasurface is characterized by a surface impedance and represents a planar grating. Perfect (without spurious scattering in the far-field) refraction in the first diffraction order and beam splitting in transmission with equal excitation of -1$^{\text{st}}$ and 1$^{\text{st}}$ diffraction orders by means of passive and lossless bianisotropic metasurfaces were presented in Refs. [117, 141, 142] and [126], respectively. To achieve perfect nonspecular reflection with passive and lossless metasurfaces, auxiliary surface waves have to be additionally excited [126, 129, 143, 144]. Otherwise, it is required to engineer active and lossy response of a metasurface [118, 119, 143]. Although it seems possible to design such metasurfaces, the design procedure is not well-defined [143, 144]. Multichannel reflection with metasurfaces was also demonstrated in Ref. [6].

In 2017, Y. Ra'di *et al.* in Ref. [145] and A. Epstein *et al.* in Ref. [146] demonstrated theoretically and via 3D full-wave simulations the possibility of perfect nonspecular reflection [145]

and beam-splitting [146] with a periodic array of meta-atoms over a perfect electric conductor (PEC) and consisting of a single meta-atom per period. Such type of structures, periodic arrays of meta-atoms with the inter-element distance being of the order of the operating wavelength, were called *metagratings*. In strong contrast to a metasurface, the sparse arrangement of scatterers does not allow one to describe a metagrating in terms of surface impedances or local reflection and transmission coefficients. On the other hand, a rigorous microscopic model of a metagrating together with judicious engineering of the electromagnetic response of meta-atoms allow one to overcome the fundamental limitations of metasurfaces in terms of efficiency.

In this Chapter, I build a microscopic analytical model of one-dimensional (1D) reflective metagratings with multiple meta-atoms composing a period. Traditionally, in 1D gratings there is a profile modulation in one direction and a translational symmetry in the other. In 1D metagratings, identical meta-atoms are arranged in a line to form a wire along the translation invariant direction such that it becomes possible to define an averaged macroscopic quantity like an impedance density [146]. A reflective configuration implies that wires are placed on top of a metal-backed dielectric substrate, as illustrated in Fig. 2.1. Then, a theoretical study on the number of different wires necessary for total control of propagating diffraction orders is performed. To experimentally validate theoretical findings, I design several metagratings based on concrete physical structures. Finally, a comparison in terms of efficiency with conventional gradient metasurfaces is made.

2.2. Total control of diffraction pattern

2.2.1 Inverse scattering problem

A metagrating is modeled as a 1D periodic array of polarization line currents excited in thin loaded wires by a TE-polarized plane wave incident at an angle θ and having the electric field along the wires. I consider a reflective-type metagrating when the wires are placed on top of a perfect electric conductor (PEC)-backed dielectric substrate. Schematics of the system under consideration is depicted in Fig. 2.1(a). The incident plane wave is reflected from the grounded substrate resulting in the excitation field of the following form

$$E_x^{(exc)}(y, z \leq -h) = \left(e^{-j\beta_0 z} + R_0^{\mathrm{TE}} e^{j\beta_0(z+2h)}\right) e^{-jk\sin[\theta]y}. \tag{2.1}$$

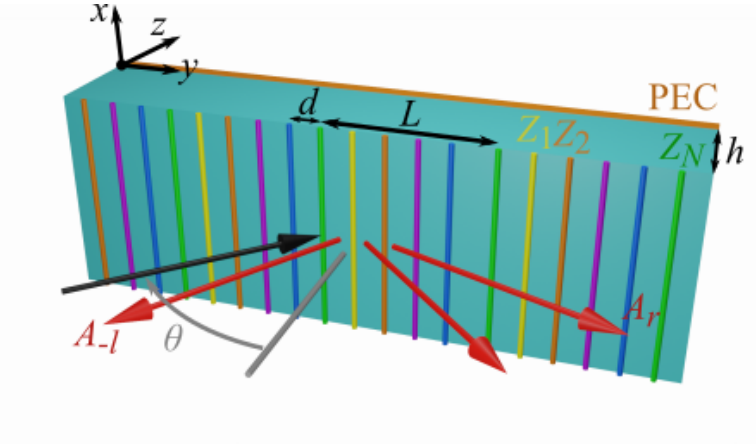

Figure 2.1: System under consideration: a periodic array of thin loaded wires (represented by color cylinders) placed on a PEC-backed dielectric substrate having relative permittivity ε_s, permeability μ_s and thickness h. The array is excited by a plane wave incident at the angle θ (black arrow). Propagating diffraction orders are illustrated by red arrows.

Thus, the grounded substrate should be carefully chosen in order to provide efficient excitation of line currents, i.e. $h \sim \lambda/(4\sqrt{\varepsilon_s\mu_s - \sin(\theta)^2})$.

Since the illuminated structure is periodic, with the period L, the scattered field $E_x^{(sct)}(y, z < -h)$ can be represented as a superposition of plane waves

$$E_x^{(sct)}(y, z < -h) = \sum_{m=-\infty}^{+\infty} A_m^{\mathrm{TE}} e^{-j\xi_m y + j\beta_m z}. \tag{2.2}$$

The plane waves have the tangential and normal components of wave vector equal to $\xi_m = k\sin(\theta) + 2\pi m/L$ and $\beta_m = \sqrt{k^2 - \xi_m^2}$, respectively, with k being the wavenumber of free space. A simple model of metagratings allows one to find the amplitudes A_m^{TE} analytically. Indeed, a single electric line current $\mathbf{J}(\mathbf{r}) = I\delta(y, z)\mathbf{x}_0$ radiates a cylindrical wave with the electric field in the form of Hankel function of the second kind zeroth order $H_0^{(2)}[k\sqrt{y^2 + z^2}]$ (see Ref. [147])

$$E_x(y, z) = -\frac{k\eta}{4} I H_0^{(2)}[k\sqrt{y^2 + z^2}], \quad E_y = E_z = 0, \tag{2.3}$$

where η is the characteristic impedance of free space. The electric field created by an infinite array of N equidistant line currents per period L is given by the following series

$$E_x(y, z) = -\frac{k\eta}{4} \sum_{q=1}^{N} \sum_{n=-\infty}^{\infty} I_q e^{-jk\sin[\theta]nL} H_0^{(2)}[k\sqrt{(y - nL - (q-1)d)^2 + z^2}], \tag{2.4}$$

where the phase $\exp[-jk\sin[\theta]nL]$ appears because of the plane wave illumination at angle θ.

The Poisson's formula applied to the series of the Hankel functions

$$\sum_{n=-\infty}^{+\infty} f(nL) = \sum_{m=-\infty}^{+\infty} \int_{-\infty}^{+\infty} \frac{dw}{L} f(w) e^{-j\frac{2\pi m}{L}w},$$
$$f(nL) = e^{-jk\sin[\theta]nL} H_0^{(2)}[k\sqrt{(y-nL-(q-1)d)^2+z^2}] \tag{2.5}$$

is used to express the series (2.4) as a faster converging series of plane waves

$$E_x(y,z) = -\frac{k\eta}{2L} \sum_{q=1}^{N} \sum_{m=-\infty}^{\infty} \frac{I_q e^{j\xi_m(q-1)d}}{\beta_m} e^{-j\xi_m y - j\beta_m|z|}. \tag{2.6}$$

The Fourier transformation of the Hankel function is given by the following formula

$$\int_{-\infty}^{+\infty} dw H_0^{(2)}[k\sqrt{(y-w)^2+z^2}] e^{-j\xi_m w} = 2\frac{e^{-j\xi_m y - j\beta_m|z|}}{\beta_m}. \tag{2.7}$$

The magnetic fields corresponding to Eqs. (2.3) and (2.6) can be found by means of the Maxwell's equations

$$H_y(y,z) = \frac{j}{k\eta}\frac{\partial E_x(y,z)}{\partial z}, \quad H_z(y,z) = -\frac{j}{k\eta}\frac{\partial E_x(y,z)}{\partial y}. \tag{2.8}$$

The effect of the grounded substrate on the field radiated by the array can be derived in the same manner as in Ref. [148]. After some algebra, one would arrive at the following expressions for the amplitudes of the reflected plane waves (2.2)

$$A_m^{\mathrm{TE}} = -\frac{k\eta}{2L}\frac{(1+R_m^{\mathrm{TE}})e^{j\beta_m h}}{\beta_m} \sum_{q=1}^{N} I_q e^{j\xi_m(q-1)d} + \delta_{m0} R_0^{\mathrm{TE}} e^{2j\beta_0 h}, \tag{2.9}$$

where δ_{m0} is the Kronecker's delta representing the specular reflection of the incident wave from the grounded substrate and R_m^{TE} is the Fresnel's reflection coefficient

$$R_m^{\mathrm{TE}} = \frac{j\gamma_m^{\mathrm{TE}}\tan[\beta_m^s h]-1}{j\gamma_m^{\mathrm{TE}}\tan[\beta_m^s h]+1},$$
$$\gamma_m^{\mathrm{TE}} = \frac{k_s\eta_s\beta_m}{k\eta\beta_m^s}, \quad \beta_m^s = \sqrt{\varepsilon_s\mu_s k^2 - \xi_m^2}, \quad \eta_s = \eta\sqrt{\frac{\mu_s}{\varepsilon_s}}, \quad k_s = k\sqrt{\varepsilon_s\mu_s}. \tag{2.10}$$

Equation (2.9) reveals that each of N line currents in a supercell contributes to each of the reflected plane waves through the discrete Fourier transformation of the sequence I_q. Although there is an infinity of reflected plane waves, only a finite number $M = r + l + 1$ of them is scattered in the far-field corresponding to propagating diffraction orders and determining the diffraction pattern. r and l are the largest integers such that $\mathrm{Im}(\beta_r) = 0$ and $\mathrm{Im}(\beta_{-l}) = 0$. Thus,

currents I_q can be considered as degrees of freedom to control the amplitudes of propagating diffraction orders. Assigning arbitrary values to the amplitudes A_m^{TE}, $-l \leq m \leq r$, one can find corresponding necessary currents I_q in a unique manner when the number of wires N *equals* to the number of propagating diffraction orders M.

2.2.2 Load-impedance density

Each polarization line current is excited in a thin wire characterized by its input-impedance Z_{in} and load-impedance Z_q densities. The currents I_q found when solving the inverse scattering problem (2.9) can be obtained by loading wires with proper load-impedance densities Z_q calculated by means of Ohm's law

$$Z_q I_q = E_q^{(exc)} - Z_{in} I_q - \sum_{p=1}^{N} Z_{qp}^{(m)} I_p. \tag{2.11}$$

The right-hand side of Eq. (2.11) represents the total electric field at the location of the q^{th} wire, $E_q^{(exc)}$ represents the excitation field (2.1), $Z_{qp}^{(m)}$ are the mutual-impedance densities which account for the interaction between the wires and between the wires and the grounded substrate. Mutual impedance densities $Z_{qp}^{(m)}$ take into consideration the interaction of the q^{th} wire (located in the zero$^{\mathrm{th}}$ period) with the substrate and adjacent wires and being expressed via the following formulas

$$\begin{aligned} Z_{qq}^{(m)} &= \frac{k\eta}{2} \sum_{n=1}^{+\infty} \cos[k \sin[\theta] nL] H_0^{(2)}[knL] + \frac{k\eta}{2L} \sum_{m=-\infty}^{+\infty} \frac{R_m^{\mathrm{TE}}}{\beta_m} \\ Z_{qp}^{(m)} &= \frac{k\eta}{4} \sum_{n=-\infty}^{+\infty} H_0^{(2)}[k|(q-p)d - nL|] e^{-jk \sin[\theta] nL} \\ &+ \frac{k\eta}{2L} \sum_{m=-\infty}^{+\infty} e^{j\xi_m (p-q)d} \frac{R_m^{\mathrm{TE}}}{\beta_m}, \quad q \neq p. \end{aligned} \tag{2.12}$$

The series containing R_m^{TE} correspond to the interaction with the substrate. The electric field at the location of the q^{th} wire in the zero$^{\mathrm{th}}$ period created by the rest of q^{th} wires and all other wires ($q \neq p$) is associated with the first terms constituting $Z_{qq}^{(m)}$ and $Z_{qp}^{(m)}$, respectively.

2.2.3 Reactive metagratings

A reactive metagrating redistributes the energy of the incident wave between M propagating diffraction orders. Then, the desired amplitudes A_m^{TE}, $-l \leq m \leq r$, (when assuming a unitary

amplitude of the incident wave) must satisfy the following condition

$$\sum_{m=-l}^{r} \left|A_m^{\mathrm{TE}}\right|^2 \frac{\beta_m}{\beta_0} = 1, \tag{2.13}$$

where $\left|A_m^{\mathrm{TE}}\right|^2 \beta_m/\beta_0$ is the part of the incident energy going in the m^{th} diffraction order. Although total control of the diffraction pattern is possible with $N = M$ wires per supercell, the currents found from (2.9) in a general case correspond to active and/or lossy load-impedance densities Z_q calculated afterwards from (2.11). Since in practice it can be challenging to engineer judiciously the real part of a complex load-impedance density, one is particularly interested in purely reactive solutions of Eq. (2.11). Equations (2.9) and (2.11) represent two systems of coupled equations. While, on the one hand, currents I_q should ensure desirable amplitudes of propagating diffraction orders, they should also satisfy the conditions of passivity and absence of loss $\mathrm{Re}(Z_q) = 0$ expressed as follows

$$\mathrm{Re}\left[\left(E_q^{(exc)} - \sum_{p=1}^{N} Z_{qp}^{(m)} I_p\right) I_q^*\right] = \mathrm{Re}[Z_{in}]|I_q|^2, \tag{2.14}$$

where the asterisk symbol stands for the complex conjugate. Equation (2.14) represents a set of N quadratic algebraic equations with real and imaginary parts of currents being the variables and simply means that the q^{th} current radiates all the power spent on its excitation. Additional M (complex-valued) currents are required to satisfy Eq. (2.14). Thus, $N = 2M$ reactively-loaded wires per supercell are necessary for establishing arbitrary diffraction patterns exactly. Although there can be many wires per period, the distance between them is of the order of $\lambda/4$ (λ is the operating wavelength), which does not allow one to perform homogenization and introduce surface impedance generally used to describe metasurfaces.

From the physical point of view, the additional M wires are used to set the amplitudes A_m^{TE} of the surface waves (or nonpropagating diffraction orders, $m > r$ and $m < -l$) which would ensure Eq. (2.14). For a better understanding, let me consider an example of a perfect reflection in the 1^{st} diffraction order of a plane wave at normal incidence ($r = l = 1$). The period L is fixed such that there are $M = 3$ propagating diffraction orders in total: -1^{st}, 0^{th} and 1^{st}. In this case, one has to cancel the two remaining propagating orders and the necessary number of wires per period N equals 6. First of all, one sets the amplitudes of the plane waves in the far-field as $A_{-1}^{\mathrm{TE}} = 0$, $A_0^{\mathrm{TE}} = 0$ and $A_1^{\mathrm{TE}} = e^{j\phi_1}\sqrt{\beta_0/\beta_m}$, where ϕ_1 is the phase of the anomalously reflected wave.

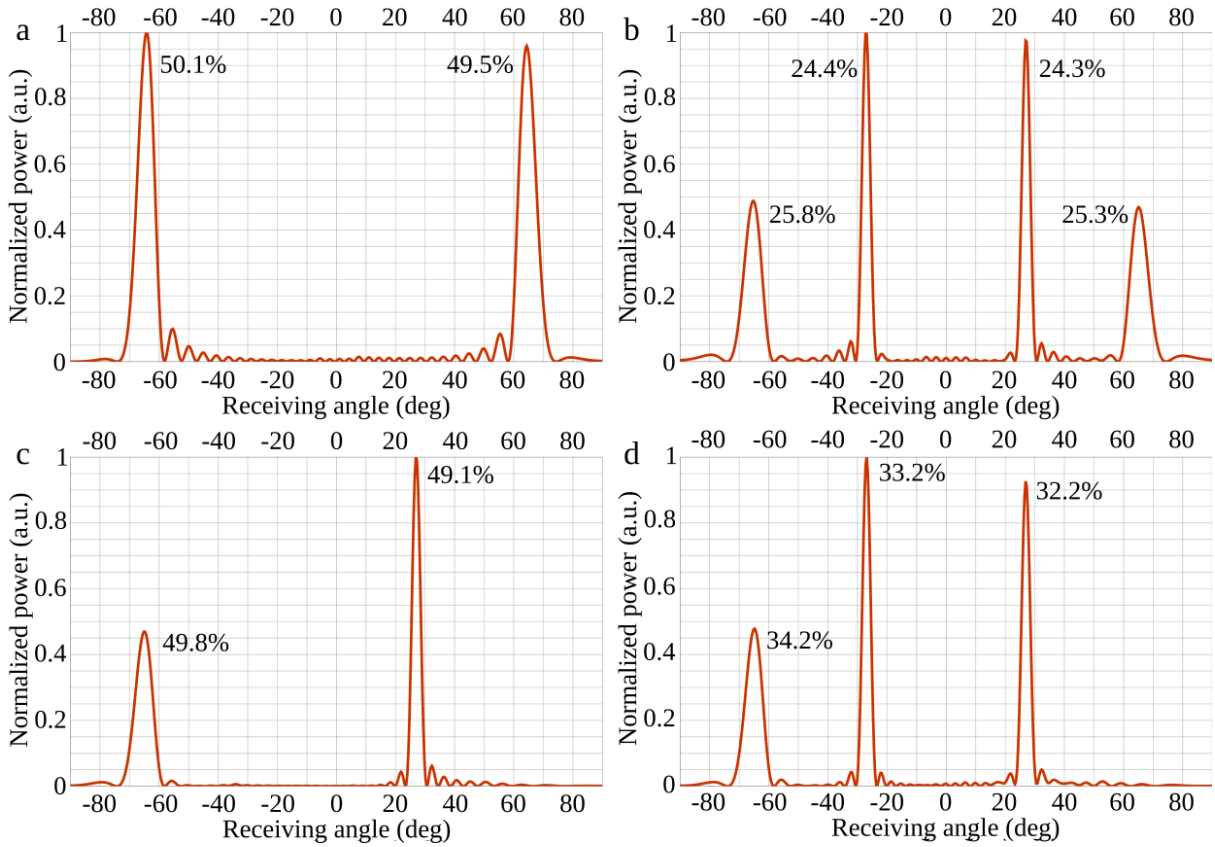

Figure 2.2: Far-field scattering patterns from finite size metagratings under normally incident plane wave obtained by means of 2D full-wave COMSOL simulations. Each finite size metagrating has 8 supercells. Numbers next to each lobe represent the part of power in a given lobe. All represented examples aim to demonstrate equal distribution of incident power between all excited propagating diffraction patterns. ***(a)–(d)*** *Period $L = 2 \times 30/(\sin(65^\circ))$, there are five propagating diffraction orders.* ***(a)*** -2^{nd} *and* 2^{nd} *orders are excited.* ***(b)*** -2^{nd}, -1^{st}, 1^{st} *and* 2^{nd} *orders are excited.* ***(c)*** -2^{nd} *and* 1^{st} *orders are excited.* ***(d)*** -2^{nd}, -1^{st} *and* 1^{st} *orders are excited.*

Then the currents I_q $(q = 1, 2, ..., 6)$ found from Eq. (2.9) $(m = -3, -2, ..., 2)$ are substituted into Eq. (2.14). The unknown (complex) amplitudes A_{-3}^{TE}, A_{-2}^{TE} and A_{2}^{TE} of the surface waves are found by solving Eq. (2.14), which automatically ensures reactive load-impedance densities Z_q calculated afterwards from Eq. (2.11).

2.2.4 Proof-of-concept via 2D simulations

The developed approach allows one to realize arbitrary diffraction patterns with passive structures illuminated by a plane wave. Figures 2.2 and 2.3 demonstrate different configurations of the far-field scattering pattern from metagratings of two different periods. The scattering pattern was obtained with 2D full-wave simulations performed by means of COMSOL Multiphysics as described below. Metagratings in Figs. 2.2 and 2.3 were designed to equally split the power of normally incident plane wave between excited propagating diffraction orders. Numbers next to each lobe represent the part of total power carried by a given beam. The imperfection are only

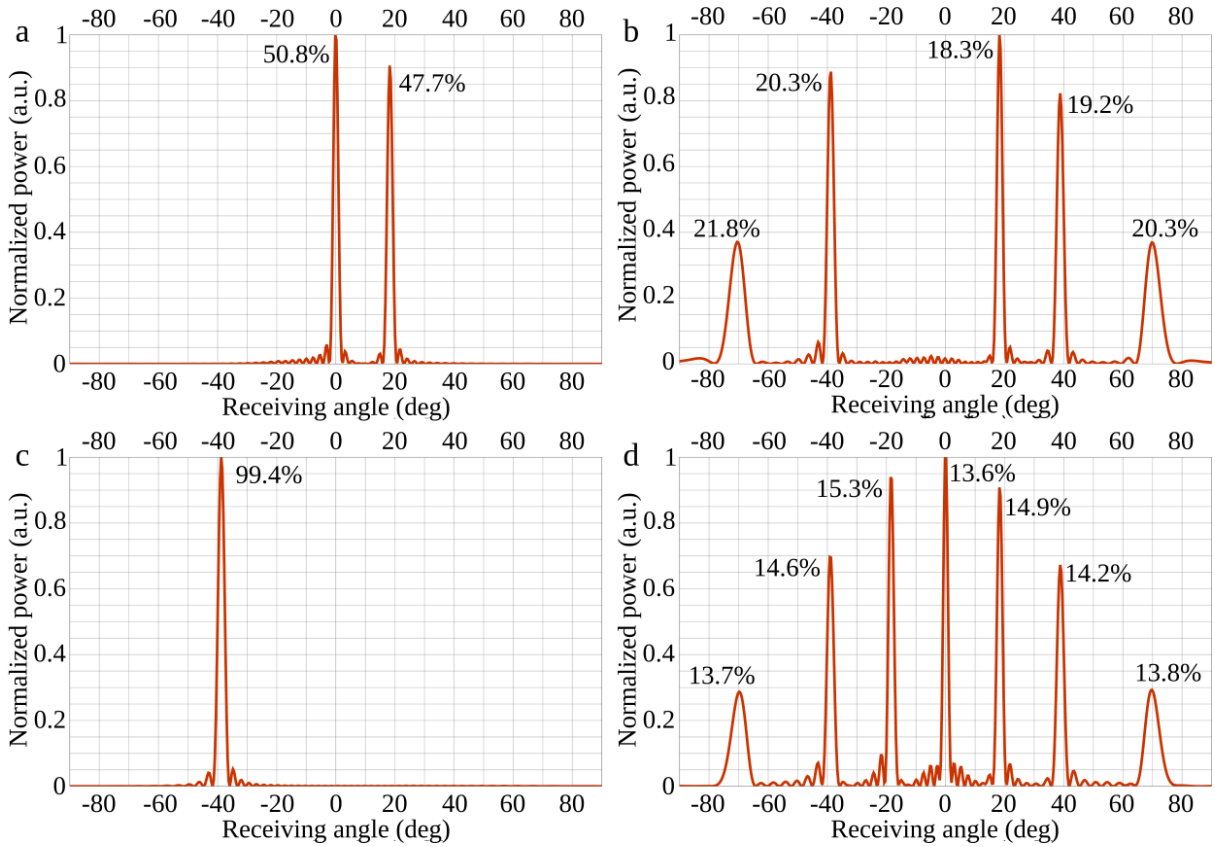

Figure 2.3: ***(a)–(d)*** *Period $L = 3 \times 30/(\sin(70^\circ))$, there are seven propagating diffraction orders.* ***(a)*** *0^{th} and 1^{st} orders are excited.* ***(b)*** *All orders are excited apart from 0^{th} and -1^{st}.* ***(c)*** *only -2^{nd} order is excited.* ***(d)*** *All propagating orders are excited.*

due to the finite size of metagratings in the y-direction, i.e. finite number of periods. Indeed, the scattering problem for finite size objects is more complex than in case of infinite, truly periodic structures. Strictly speaking, the developed theory is valid for finite size metagratings only when an incident wave effectively illuminates a metagrating's area much greater than its period and much less than its whole size. For instance, it is the case for a Gaussian beam with the waist w_{GB} such that $1 \ll w_{GB}/L \ll N_s$ (N_s is the total number of supercells).

A COMSOL model for 2D full-wave simulations of metagratings can be built in the following way. The principal element of a metagrating is a polarization line current which is modeled in COMSOL as surface current density assigned to the boundary of a circle, as shown in Fig. 2.4. The radius of the circle r_{eff} should be equal to the effective radius of a thin wire in order to get the correct value of the input-impedance density. It is important to exclude from the model the interior of the circles, otherwise one would get an incorrect value of the input-impedance density. The surface current density $\mathbf{J}_{es}$ is set as follows: $E_x/Z_q/(2\pi r_{eff})\mathbf{x}_0$ (Z_q is the load-impedance density of the q^{th} thin wire). The array of circles is placed on a PEC-backed substrate (the circles' centers are on the top of the substrate) as shown in Fig. 2.4. In order to excite the model

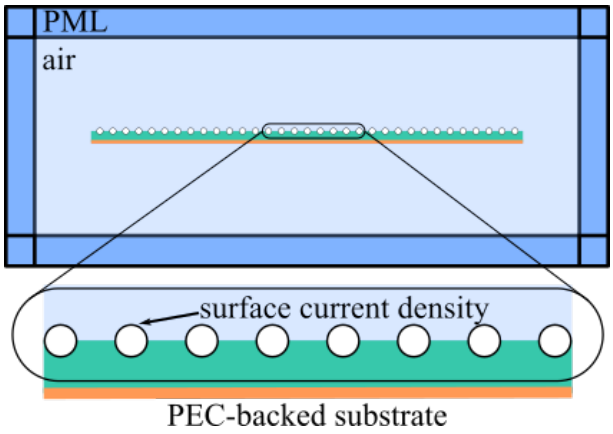

Figure 2.4: Schematics of the 2D COMSOL model used for simulating metagratings. The white regions inside the circles are excluded from the model. Polarization line currents of effective radius r_{eff} (radius of the circles, it represents the input-impedance density) are simulated as surface current density: $\boldsymbol{J}_{es} = E_x/Z_q/(2\pi r_{eff})\boldsymbol{x}_0$ ($\boldsymbol{x}_0$ is the unit vector in the x direction). The total number of line currents (circles) is number of line currents per period times the number of periods.

I use scattered field formulation and set a background field. The rest of the model is standard and can be understood from Fig. 2.4.

2.3. Design, 3D simulations and experiments

Once the necessary load-impedance densities are known, one has to come up with a practical implementation of the loads. In a general case, capacitive and inductive loads are required for such design implementation. As a proof of concept, I demonstrate the design procedure for metagratings operating at microwave frequencies near 10 GHz. Thin metallic wires are realized as PEC strips having the input-impedance density $Z_{in} = k\eta H_0^{(2)}[kw/4]/4$ with $H_0^{(2)}$ being the Hankel function of the second kind and w being the width of strips. Capacitive and inductive responses can be achieved with the printed microstrip capacitors and inductors schematically shown in Fig. 2.5. Load-impedance density Z_c of the printed capacitors can be approximately calculated by means of analytical formulas for the grid impedance of a PEC strips based capacitive grid [149, 150, 151]

$$Z_c = -j\kappa_c \frac{\eta_{eff}}{2A\alpha}, \quad \alpha = \frac{k_{eff}B}{\pi} \ln\left[\frac{1}{\sin[\frac{\pi w}{2B}]}\right], \tag{2.15}$$

where A is the arms' length, κ_c is a scaling parameter, $\eta_{eff} = \eta/\sqrt{\varepsilon_{eff}}$, $k_{eff} = k\sqrt{\varepsilon_{eff}}$, $\varepsilon_{eff} = (1+\varepsilon_s)/2$, α is the grid parameter and B is the period along the x-direction. The formula (2.15) was already used in the context of metagratings in Ref. [148]. Since PEC strips act intrinsically

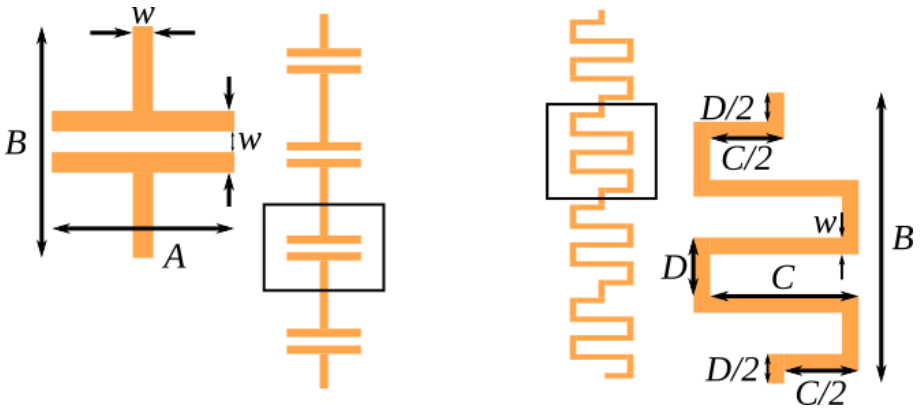

Figure 2.5: Schematics of implementation at microwave frequencies of capacitively (left) and inductively (right) loaded PEC strips.

as inductors themselves ($\Im[Z_{in}] > 0$), the inductive load can be implemented by modulating the effective length of the strip through a meandering design process [151]. Then, the inductive load-impedance Z_i density can be estimated as

$$Z_i = j\frac{1}{\kappa_i}\frac{l_{eff}\Im[Z_{in}]}{B}, \quad l_{eff} = C\left(\frac{B}{D} - 1\right), \quad \Im[Z_{in}] \approx -\frac{k\eta}{2\pi}\left(\ln\left[\frac{kw}{8}\right] + \gamma\right), \tag{2.16}$$

where l_{eff} is the effective length of the meander, κ_i is a scaling parameter, C and D are the parameters of the meander, see Fig. 2.5, and $\gamma \approx 0.5772$ is the Euler constant. Formula (2.16) is a rough approximation of the inductive load-impedance since it does not take into account the interaction between the meander strips and capacitive response on the incident wave. Geometrical parameters w, B and D are the same for all unit cells and fixed. Parameters A and C are found from Eqs. (2.15) and (2.16) for each unit cell accordingly to load-impedance densities calculated beforehand. The last step of the design procedure is to additionally adjust parameters A and C by performing a parametric sweep with respect to the scaling parameters κ_c and κ_i which are the same for different unit cells. In contrast to the design procedure of metasurfaces, here I perform simulations of a whole supercell having κ_c and κ_i as the only two free parameters. This allows one to account for interaction between unit cells and immediately arrive at the ultimate design. A more detailed description of the design procedure based on concrete examples is given below.

The importance of the near-field control can be demonstrated by considering a simple example of a nonspecular reflection at extreme angles [126, 143, 144]. Namely, I consider the reflection of a normally incident plane wave at the angle of 80°. In this studied case, there are only three propagating diffraction orders (-1$^{\text{st}}$, 0$^{\text{th}}$ and 1$^{\text{st}}$), as shown by the schematics in

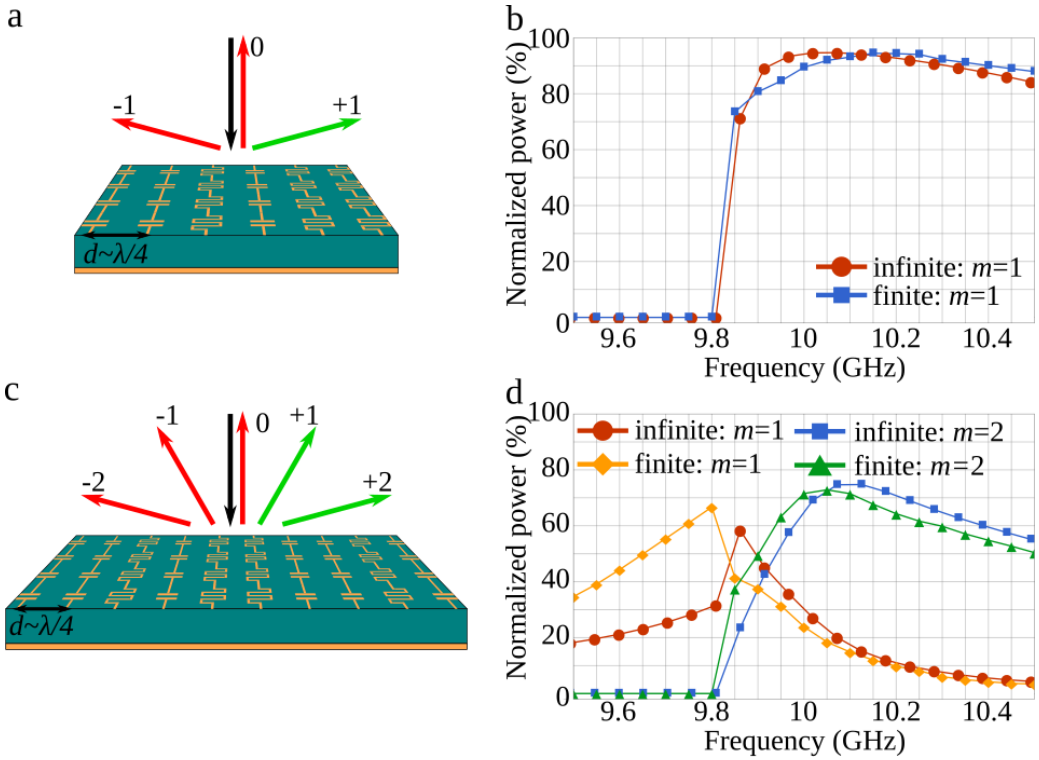

Figure 2.6: Power management between propagating diffraction orders by the considered metagratings with six and ten unit cells per period: schematics (top row) and simulation data (bottom row). Result for infinite and finite size metagratings are presented. Figures in the top row depict excited (green lobes) and canceled (red lobes) propagating diffraction orders corresponding to the plots in the bottom row showing the 3D full-wave simulated frequency responses of the metagratings (i.e. part of total power scattered in a given diffraction order versus frequency). ***(a)***, ***(b)*** *Example of nonspecular reflection at an angle of* $80°$ *by means of a metagrating with* $N = 6$ *unit cells per period. The finite size metagrating has* 16 *supercells.* ***(c)***, ***(d)*** *Example when out of five plane waves reflected in the far-field, only the first* (1/3 *of total power) and second* (2/3 *of total power) propagating diffraction orders are excited with a metagrating having* $N = 10$ *unit cells in a period. The finite size metagrating has* 8 *supercells. In both examples, normal incidence is assumed.*

Fig. 2.6(a). Thus, for realizing the anomalous reflection one has to cancel scattering in the -1$^{\text{st}}$ and 0$^{\text{th}}$ diffraction orders, which requires six loaded wires per supercell implemented by passive and lossless elements. The second example I consider is the splitting of the normally incident plane wave into two reflected plane waves propagating at 30° (first diffraction order) and 80° (second diffraction order). In contrast to commonly demonstrated examples of beam splitting, here the incident wave power is not equally distributed between the excited diffraction orders. Particularly, I design the sample to steer 1/3 of the total power in the first diffraction order and 2/3 in the second one. This scenario is schematically depicted in Fig. 2.6(c) where there are five propagating diffraction orders controlled by ten loaded wires in a supercell.

These two metagratings were designed to operate at 10 GHz ($\lambda \approx 30$ mm). In order to get the load-impedance densities, I start by setting the amplitudes of propagating diffraction orders. In the first case of nonspecular reflection of normally incident plane wave at 80°, period of the

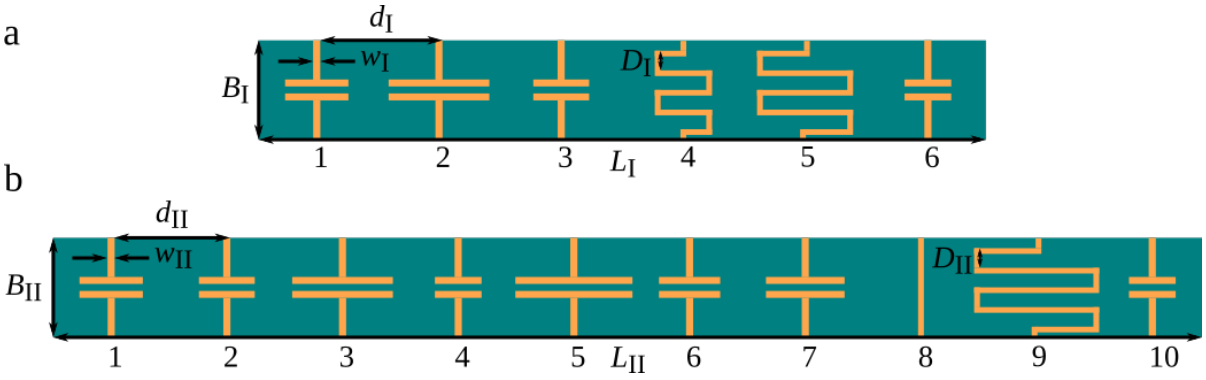

Figure 2.7: Outline of the metagratings supercells geometry performing ***(a)*** *nonspecular reflection at* $80°$ *(*$w_I = 0.25$ *mm,* $B_I = 3$ *mm and* $D_I = 0.6$ *mm) and* ***(b)*** *beam splitting in the first (*$1/3$ *of power) and second (*$2/3\%$ *of power) diffraction orders (*$w_{II} = 0.25$ *mm,* $B_{II} = 3.75$ *mm and* $D_{II} = 0.75$ *mm). The used substrate is the F4BM220 with* $\varepsilon_s = 2.2(1 - j10^{-3})$*,* $\mu_s = 1$*, thickness of the substrate is* $h = 5$ *mm. Each unit cell of the metagratings is numbered in correspondence with Tab. 2.1.*

structure is $L_I = 30/\sin(80°)$ mm and there are three propagating diffraction orders $A_{-1} = 0$, $A_0 = 0$ and $A_1 = 1/\sqrt{\cos(80°)}$. It requires six polarization line currents per period separated by the distance $d_I = L_I/6$. The complex amplitudes of three nonpropagating diffraction orders A_{-3}, A_{-2} and A_2 are found by numerically solving the system of equations (2.14). After all six amplitudes are known, I calculate the six polarization currents I_q form Eq. (2.9). Then, the load-impedance densities are found from Eq. (2.11). The same procedure is repeated for the other metagrating performing the splitting of normally incident plane wave between the first (1/3 of power) and second (2/3 of power) propagating diffraction orders. Period of the metagrating is $L_{II} = 2 \times 30/\sin(80°)$ mm and there are ten polarization line currents separated by the distance $d_{II} = L_{II}/10$. The complex amplitudes of the five propagating diffraction orders are set as $A_{-2} = 0$, $A_{-1} = 0$, $A_0 = 0$, $A_1 = \sqrt{\frac{1}{3}/\sqrt{1 - (\lambda/L_{II})^2}}$ and $A_2 = \sqrt{\frac{2}{3}/\cos(80°)}$. Again, the complex amplitudes of nonpropagating diffraction orders A_{-5}, A_{-4}, A_{-3}, A_3 and A_4 are solutions of Eq. (2.14). Computed load-impedance densities can be found in Table 2.1.

To design experimental samples parameters w, B and D are fixed and kept the same for all unit cells in a metagrating, as shown in Fig. 2.7. In order to find parameters A and C of each unit cell I use equations (2.15) and (2.16) presented in the main text and 3D full-wave simulations of a metagrating single supercell (as the ones in Fig. 2.7) with imposed periodic boundary conditions. We perform a parametric sweep with respect to the scaling parameters κ_c and κ_i until the model acts as desired. For the first and second samples the optimal parameters are $\kappa_c = 0.9$, $\kappa_i = 1.35$ and $\kappa_c = 0.92$, $\kappa_i = 2.66$, respectively. It is important to note that the scaling parameters are independent of the unit cell. In contrast to the design procedure of metasurfaces, here I perform simulations of a whole supercell having κ_c and κ_i as the only

Load-impedance density (η/λ)	Z_1	Z_2	Z_3	Z_4	Z_5	Z_6	Z_7	Z_8	Z_9	Z_{10}
Nonspecular reflection	$-j10.6$	$-j6.27$	$-j12.2$	$j12.5$	$j22.4$	$-j15.7$	–	–	–	–
Beam splitting	$-j9.32$	$-j6.88$	$-j2.77$	$-j8.57$	$-j2.60$	$-j6.03$	$-j4.10$	$j0.38$	$j13.0$	$-j8.98$
Geometrical parameters (mm)	A_1	A_2	A_3	C_4	C_5	A_6	–	–	–	–
Nonspecular reflection	2.0	3.3	1.7	2.9	5.2	1.3	–	–	–	–
Geometrical parameters (mm)	A_1	A_2	A_3	A_4	A_5	A_6	A_7	C_8	C_9	A_{10}
Beam splitting	1.7	2.3	5.6	1.8	6.0	2.6	3.8	0	7.0	1.7

Table 2.1: Parameters of metagratings presented in the main text. The indexes correspond to the numbered unit cells in Fig. 2.7.

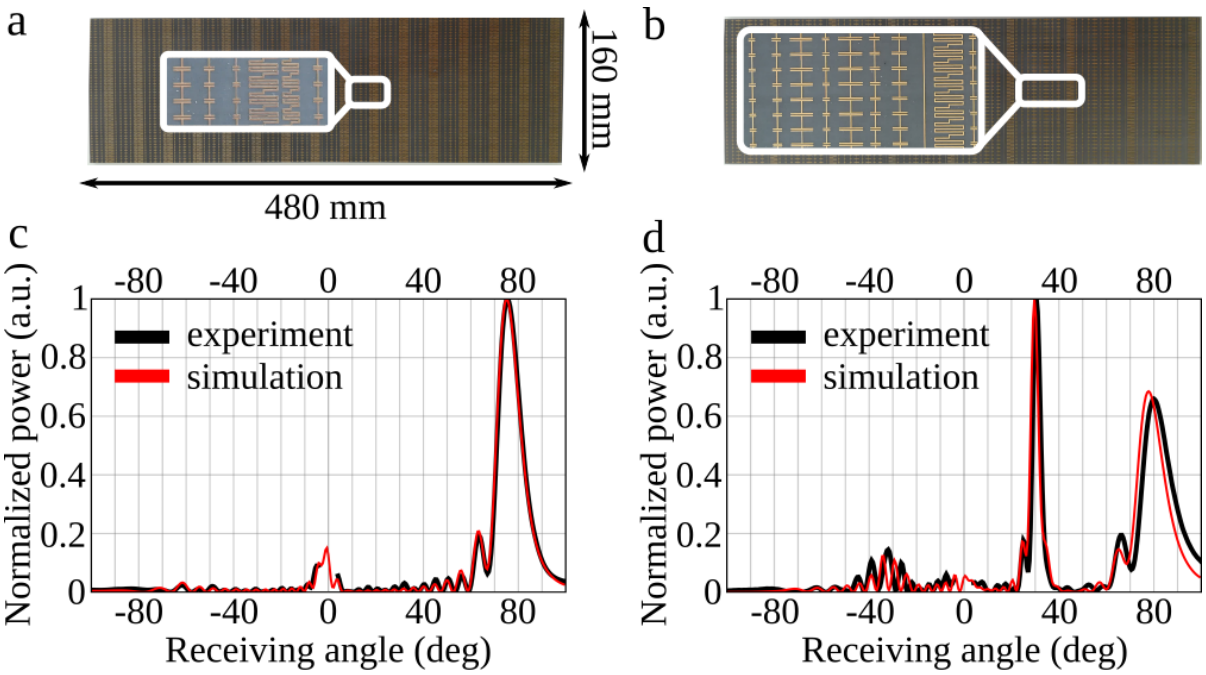

Figure 2.8: Fabricated samples and comparison of the simulation and experimental data. ***(a)***, ***(b)*** *Photograph of the samples performing* ***(a)*** *nonspecular reflection at* $80°$ *(*$N = 6$*) and* ***(b)*** *splitting into two plane waves propagating at* $30°$ *and* $80°$ *(*$N = 10$*).* ***(c)***, ***(d)*** *Experimentally measured and numerically simulated scattering patterns:* ***(c)*** *nonspecular reflection at* 10.1 *GHz (main beam has* 93% *of total power),* ***(d)*** *unequal splitting into two plane waves at* 9.95 *GHz (there are* 31.5% *of power in the* 1^{st} *order and* 63.5% *in the second one).*

two free parameters. In this way I account for interaction between different unit cells and immediately arrive at the ultimate design. Geometrical parameters of the fabricated samples are specified in Table 2.1.

The two metagratings were fabricated and tested in the following three steps. First, by means of 3D full-wave simulations, I test the metagratings designs in an infinite array configuration by imposing periodic boundary conditions to a single supercell and by assuming plane wave illumination. Figures 2.6(b) and (d) demonstrate the frequency response of the infinite metagratings. It is seen that the efficiency is above 95% in both considered examples at the frequency of operation. The remaining 5% power is dissipated as heat in the substrate due to dielectric losses and as spurious scattering due to imperfections of the design. In a second step,

3D full-wave simulations are used to test finite size physical metagratings with a number of supercells corresponding to that used for fabrication of the experimental samples. In order to be able to further compare the results of these simulations to the experimental data, features of the experimental setup have to be taken into account. The fabricated samples have been tested in an anechoic chamber dedicated to radar cross section (RCS) bistatic measurements. Transmitting and receiving horn antennas are mounted on a common circular track of 5 m radius. Physical sizes of the experimental samples are approximately 480 mm (y-direction) by 160 mm (x-direction), as illustrated in Figs. 2.8(a) and (b). Thus, the wavefront of the incident wave in the y-direction cannot be approximated by a plane wave. To take this configuration into account, simulations are performed assuming a cylindrical incident wave with periodic boundary conditions applied in the x-direction. The scattered fields are calculated on a circle enclosing the metagratings and are then extrapolated to a 5 m radius with the help of the Chu-Stratton formula [152, 153]. Details on the simulation data processing technique are given in Subsections 2.3.1 and 2.3.2. Figures 2.6(b) and (d) allow one to compare the efficiency of the finite size metagratings with the ideal case of the infinite metagratings. The discrepancy in Fig. 2.6(d) at low frequencies stems from disappearance of the second orders, which clearly has an impact on the performance of a finite size metagrating. However, this issue is yet to be studied. Finally, I compare the simulation results of the finite size metasurfaces with experimental data. In the current experiment, the transmitter is fixed and the receiver moves with 0.5° step. The minimum angle value between the transmitter and the receiver for the scanning is 4°. Under this experimental setup configuration, it is not possible to measure specular reflection. Therefore, the performance of the fabricated samples can be estimated from the simulation data depicted in Figs. 2.6(b) and (d). Figures 2.8(c) and (d) compare the measured and simulated scattered patterns, where a very good agreement can be observed.

2.3.1 Near far-field and Chu-Stratton formula

In the measurement setup shown in Fig. 2.9(a), the distance between the antennas and the sample is 5 m. This distance is not large enough to assume that the measurements are performed under the far-field condition. Indeed, the physical dimensions of the experimental samples are approximately 480 mm in the y-direction by 160 mm in the x-direction, as shown in Figs. 2.8(a) and (b). Thus, the wavefront of the incident wave in the y-direction cannot be approximated by a plane wave. To take it into account, simulations of the finite number of supercells (shown

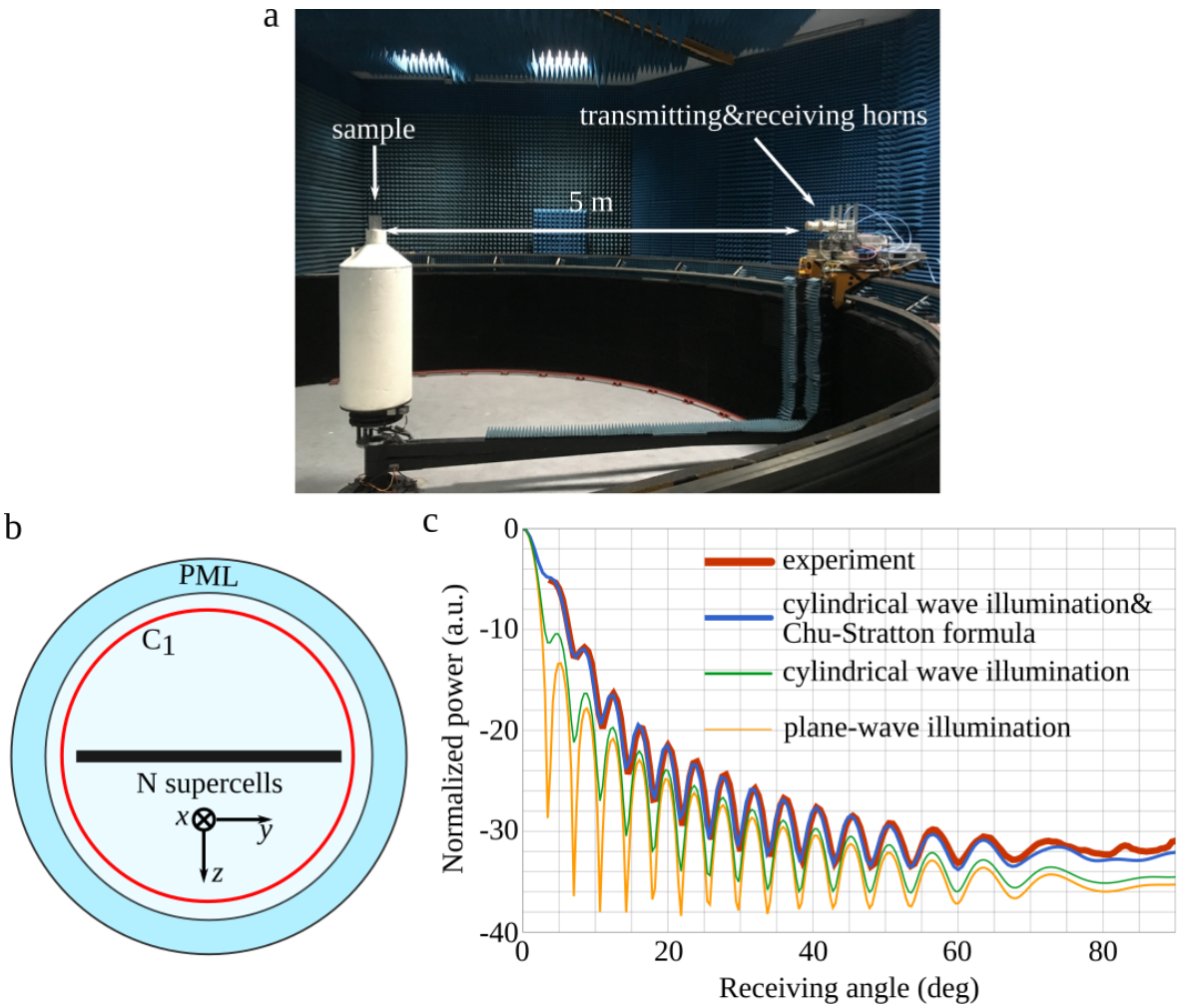

Figure 2.9: ***(a)*** *Photograph of the experimental setup used to measure the scattering patterns.* ***(b)*** *2D cross section of the 3D full-wave simulation model of a finite size metagrating. The red curve depicts the circle where the scattered fields were extracted.* ***(c)*** *Power scattering pattern from a metallic plate of length* 485 *mm simulated numerically under different conditions and compared to the experimental curve, frequency is* 10 *GHz.*

in Fig. 2.7) were performed assuming a cylindrical incident wave (phase center is 5 m away) with periodic boundary conditions applied in the x-direction. In order to correctly compare the simulation and measurement results, I harness the Chu-Stratton integration formula [153, 152] to extrapolate the field calculated on the circle C_1 of radius 258.7 mm (red curve in Fig. 2.9(b)) enclosing the sample to the circle C_2 with 5 m radius

$$\mathbf{E}(y_2, z_2) = \frac{1}{4\pi} \oint_{C_1} (j\omega\mu[\mathbf{m} \times \mathbf{H}(y_1, z_1)] + [\mathbf{m} \times \mathbf{E}(y_1, z_1)] \times\nabla + [\mathbf{m}\mathbf{E}(y_1, z_1)]\nabla)\, G(y_2 - y_1, z_2 - z_1) dl. \tag{2.17}$$

Here y_2 and z_2 are the coordinates of a point belonging to C_2, the integrand contains the fields computed on C_1, G is the free space green function and $\mathbf{m}$ is the unit normal vector directed

outward C_1. The radius of C_1 was chosen as half length of simulated metagratings (16 and 8 supercells were simulated in the two cases) plus half of the central operating wavelength (15 mm). As the simulations are performed with periodic boundary conditions in the x-direction, a 2D symmetry is assumed and thus, I used $G(y,z) = jH_0^{(2)}[k\sqrt{y^2+z^2}]/4$ as a Green function.

Fig. 2.9(c) demonstrates the importance of the Chu-Stratton formula. It compares the scattering patterns from a metallic plate measured experimentally and obtained via numerical simulations under different conditions: (i) the metallic plate is under the normally incident plane wave, far-field is calculated; (ii) the metallic plate is under the cylindrical wave illumination, phase center is at the distance 5 m, far-field is calculated; (ii) the metallic plate is under the cylindrical wave illumination, scattered field is processed by means of Chu-Stratton formula and pattern at the distance 5 m is built.

2.3.2 Calculation of the power scattered in given diffraction order

The diffraction pattern appeared when a plane wave reflects from an infinite metagrating is represented by a finite number of plane waves propagating at certain angles. The power scattered in the m^{th} propagating diffraction order is then calculated as $|A_m^{\text{TE}}|^2\beta_m/\beta_0$ (assuming unit amplitude of the incident wave). However, when it comes to a finite size periodic structure under a plane-wave-like illumination the pattern of the scattered field is much more complex. The following formula is used to estimate the part of total power scattered $\alpha_m(\nu)$ in a given diffraction order

$$\alpha_m(\nu) = \left(\int_{\theta_1^m}^{\theta_2^m} P(\nu,\theta)d\theta\right) \Big/ \left(\sum_{m=-l}^{r}\int_{\theta_1^m}^{\theta_2^m} P(\nu,\theta)d\theta\right). \tag{2.18}$$

Here, $P(\nu,\theta)$ represents the power scattered in the receiving angle θ, with ν being the frequency. The integration is performed only over the receiving angle range of half the maximum power of the beam corresponding to the m^{th} diffraction order. The summation in the denominator includes all propagating diffraction orders at the frequency ν. Angles θ_1^m and θ_2^m are found as follows. First, I accurately localize the maximum of the m^{th} diffraction order around the receiving angle $\sin^{-1}(\xi_m/k)$. Then, θ_1^m and θ_2^m correspond to the -3 dB of the power attenuation from the found maximum value.

2.4. Comparison to gradient metasurfaces

In this Section, I would like to compare theoretical efficiencies of multi-element metagratings and conventional gradient metasurfaces well-studied in the literature, see for e.g. Refs. [1, 118, 119]. The anomalous reflection of a normally incident plane wave at an angle φ is chosen as a benchmark functionality, and TE polarization is considered. *Passive* gradient metasurfaces are compared to *reactive* metagratings.

A gradient metasurface can be described by means of the local reflection coefficient $R(y)$, the passivity condition implies that $|R(y)| \leq 1$. The generalized law of reflection [1] suggests that a constant phase gradient $-k\sin(\varphi)$ should be created along a metasurface in order to reflect a normally incident plane wave at a desired angle φ. It makes the local reflection coefficient to be $R(y) = \exp[-jk\sin(\varphi)y]$ and corresponds to a reactive metasurface.

More rigorously, the local reflection coefficient can be found from the ansatz of the incident (i) and the reflected (r) waves and by means of the electromagnetic equivalence principle [119]

$$R(y) = -1 + \frac{2\left(E_x^{(i)}(y,0) + E_x^{(r)}(y,0)\right)}{E_x^{(i)}(y,0) + E_x^{(r)}(y,0) + \eta\left(H_y^{(i)}(y,0) + H_y^{(r)}(y,0\right)}. \tag{2.19}$$

The incident wave is a normally incident plane wave, the reflected wave is a plane wave propagating at the angle φ from the broadside

$$\begin{aligned} &E_x^{(i)}(y,z) = e^{-jkz}, \quad H_y^{(i)}(y,z) = \frac{1}{\eta}e^{-jkz}, \\ &E_x^{(r)}(y,z) = e^{-jk(\sin[\varphi]y - \cos[\varphi]z)}, \quad H_y^{(r)}(y,z) = -\frac{\cos[\varphi]}{\eta}e^{-jk(\sin[\varphi]y - \cos[\varphi]z)}. \end{aligned} \tag{2.20}$$

The resulted amplitude of the local reflection coefficient in this case can take values less than 1. It implies that a gradient metasurface should implement control of both the phase and the amplitude of the local reflection coefficient through engineering of the local absorption.

To calculate the theoretical efficiency of the anomalous reflection by a gradient metasurface, I perform 2D full-wave simulations by means of COMSOL Multiphysics. In simulations, a gradient metasurface is modeled as a boundary condition and characterized by an input-impedance $Z_{in}(y)$. A schematic of the simulation model is shown in Fig. 2.10(a). The input-impedance is

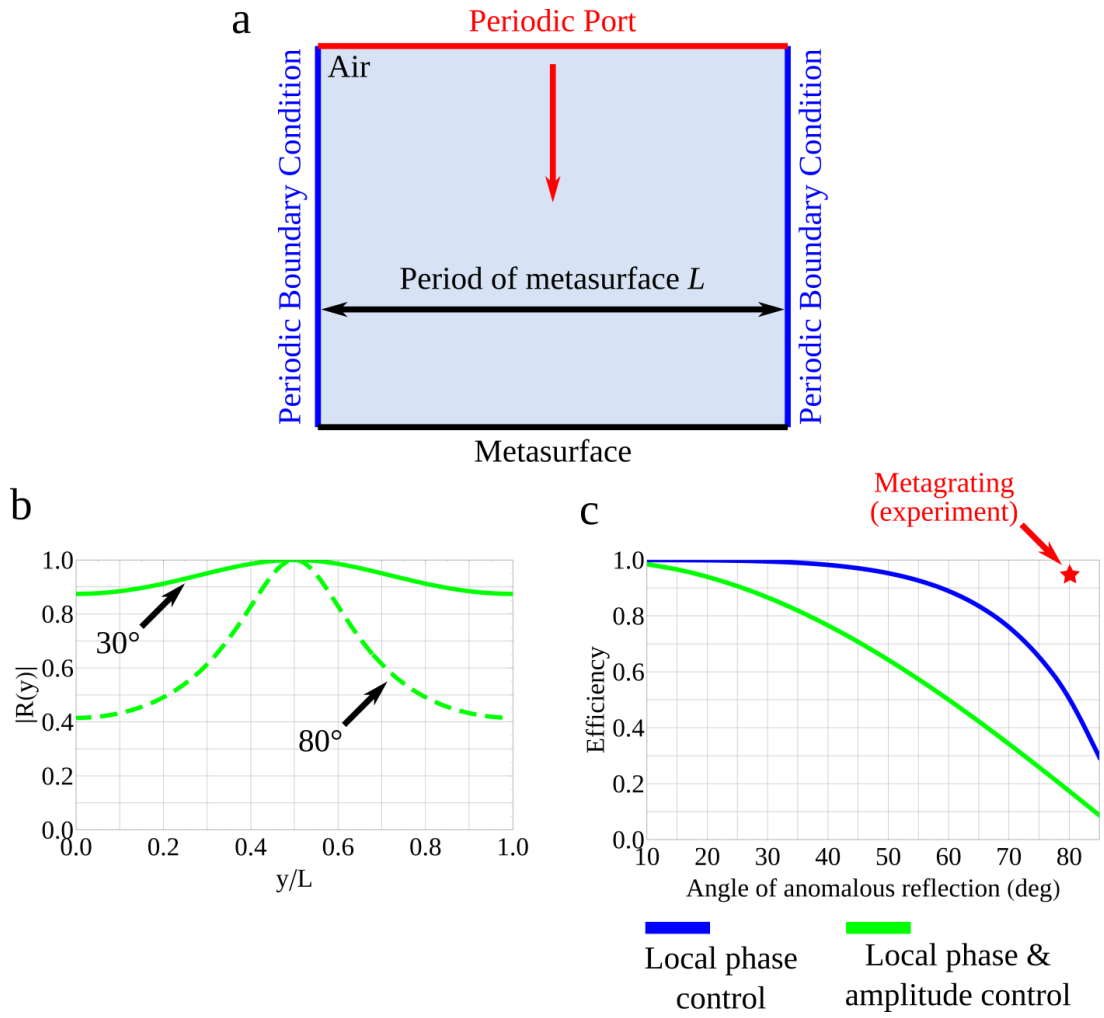

Figure 2.10: ***(a)*** *A schematic of 2D COMSOL model used to simulate gradient metasurfaces.* ***(b)*** *Spatial profile of the amplitude $|R(y)|$ of the local reflection coefficients Eq.* (2.19) *corresponding to the anomalous reflection at* 30° *(solid curve) and* 80° *(dashed curve).* ***(c)*** *Efficiency vs. the angle of anomalous reflection. The blue and green curves correspond to a constant phase-gradient metasurface [1] and a gradient metasurface implementing local phase and amplitude control [119]. Normally incident plane-wave illumination is assumed. The red star corresponds to the experimental efficiency of the metagrating performing the anomalous reflection at* 80° *as demonstrated in Section 2.3.*

found from the local reflection coefficient $R(y)$ by means of the following expression

$$Z_{in}(y) = \eta \frac{1 + R(y)}{1 - R(y)}. \tag{2.21}$$

Figure 2.10(c) demonstrate theoretical efficiencies of gradient metasurfaces implementing local phase control according to the generalized law of reflection (blue curve) and local phase and amplitude as required by the ansatz of the fields in Eq. (2.20). The efficiency of both metasurfaces drops to 0 when approaching 90°. It should be noted that while in the first case the efficiency decreases due to spurious scatterings in parasitic propagating diffraction orders, in the second case the spurious scattering is completely suppressed but the power dissipates in a metasurface

as heat. It is also seen that a constant phase-gradient metasurface outperforms (in terms of total efficiency) a more sophisticated gradient metasurface requiring engineering local absorption. As it was shown theoretically in Section 2.2, a multi-element reactive metagrating can be engineered to perfectly redirect the incident wave in a desired diffraction order, the corresponding efficiency is, obviously, 1 independently of the angle of anomalous reflection. Experimental validation presented in Section 2.3 endorses exceptionally high efficiency of the designed metagrating, red star in Fig. 2.10(c), in comparison to theoretical efficiencies of conventional gradient metasurfaces.

2.5. Magnetic metagratings

In the previous sections, I have discussed in details the physics of metagratings built-up from loaded wires excited by the electric field. However, the theoretical approach can be generalized on magnetic metagratings represented by a one-dimensional array of magnetically polarizable wires placed on top of a PEC-backed dielectric substrate. Microscopically, a magnetic wire can be envisaged as a dense, deeply subwavelength, array of identical magnetic particles arranged in a line. The next two subsections explain in detail the physics of magnetic metagratings for diffraction pattern manipulation.

2.5.1 Radiation of an array of magnetic currents

When excited by an external magnetic field, the radiation of a magnetic wire is modeled by the radiation of a magnetic line current. A single magnetic line current $\mathbf{M}(\mathbf{r}) = V\delta(y,z)\mathbf{x}_0$ radiates a TM-polarized wave with the magnetic field being along the x-direction [147]

$$H_x(y,z) = -\frac{k}{4\eta}VH_0^{(2)}\left[k\sqrt{y^2+z^2}\right], \quad H_y = 0, \quad H_z = 0, \tag{2.22}$$

where $H_0^{(2)}\left[k\sqrt{y^2+z^2}\right]$ is the Hankel function of the second kind and zero$^{\text{th}}$ order. Consequently, the magnetic field radiated by a periodic phased array of magnetic line currents

$$\mathbf{M}(\mathbf{r}) = \mathbf{x}_0\sum_{q=1}^{N}\sum_{n=-\infty}^{+\infty}V_q e^{-jk\sin(\theta)nL}\delta(y-nL-(q-1)d,z) \tag{2.23}$$

is given by the series of Hankel functions

$$H_x(y,z) = -\frac{k}{4\eta}\sum_{q=1}^{N}\sum_{n=-\infty}^{+\infty}V_q e^{-ik\sin[\theta]nL}H_0^{(2)}[k\sqrt{(y-nL-(q-1)d)^2+z^2}]. \tag{2.24}$$

By means of the Poisson's formula (2.7), the radiation of the periodic array (2.24) can be expressed as the series of plane waves

$$H_x(y,z) = -\frac{k}{2\eta L}\sum_{q=1}^{N}\sum_{m=-\infty}^{+\infty}\frac{1}{\beta_m}V_q e^{j\xi_m(q-1)d}e^{-j\xi_m y}e^{-j\beta_m|z|}. \tag{2.25}$$

The introduction of a PEC-backed dielectric substrate is accounted via the Fresnel's reflection coefficient and, thus, the magnetic field outside the substrate ($z<-h$) can be found to be

$$H_x(y,z<-h) = -\frac{k}{2\eta L}\sum_{q=1}^{N}\sum_{m=-\infty}^{+\infty}\frac{(1+R_m^{\mathrm{TM}})e^{j\beta_m h}}{\beta_m}V_q e^{j\xi_m(q-1)d}e^{-j\xi_m y+j\beta_m z}, \tag{2.26}$$

where

$$R_m^{\mathrm{TM}} = -\frac{j\gamma_m^{\mathrm{TM}}\tan[\beta_m^s h]-1}{j\gamma_m^{\mathrm{TM}}\tan[\beta_m^s h]+1}, \quad \gamma_m^{\mathrm{TM}} = \frac{k\eta_s\beta_m^s}{k_s\eta\beta_m}. \tag{2.27}$$

2.5.2 Inverse scattering problem

When the magnetic line currents are excited in magnetically polarizable wires by an incident TM-polarized plane wave at the angle θ, the scattered magnetic field can be represented as a superposition of plane waves

$$H_x^{(sct)}(y,z<-h) = \sum_{m=-\infty}^{+\infty}A_m^{\mathrm{TM}}e^{-j\xi_m y+j\beta_m z}. \tag{2.28}$$

Amplitudes of the plane waves are found from Eq. (2.26) and can be expressed as follows

$$A_m^{\mathrm{TM}} = -\frac{k}{2\eta L}\frac{(1+R_m^{\mathrm{TM}})e^{j\beta_m h}}{\beta_m}\sum_{q=1}^{N}V_q e^{j\xi_m(q-1)d}+\delta_{m0}R_0^{\mathrm{TM}}e^{2i\beta_0 h} \tag{2.29}$$

where δ_{m0} is the Kronecker delta representing the reflection of the incident wave from the PEC-backed substrate.

It can be noticed that the result of Eq. (2.29) could be obtained from Eq. (2.9) by applying duality relations [147]: $\mathbf{E}\to\mathbf{H}$, $\mathbf{H}\to-\mathbf{E}$, $I\to V$ and $\eta\to 1/\eta$. Since the PEC-backed dielectric substrate is not replaced by the corresponding dual equivalent (PMC-backed substrate) in case of a magnetic metagrating, one has to additionally make the following substitution $R_m^{TE}\to R_m^{TM}$.

As in the case of TE polarization treated above, Eq. (2.29) demonstrates that the magnetic line currents contribute to the scattered plane waves via the discrete Fourier transform $\sum_{q=1}^{N}V_q e^{j\xi_m(q-1)d}$. Magnetic line currents V_q can thus be used to control propagating diffraction orders. Necessary currents V_q can be obtained by loading wires with appropriate load-admittance

densities Y_q found from Ohm's law

$$Y_q V_q = H_x^{(exc)}((q-1)d, -h) - Y_{in} V_q - \sum_{p=1}^{N} Y_{qp}^{(m)} V_p. \tag{2.30}$$

The right-hand side of Eq. (2.30) represents the total magnetic field at the location of the q^{th} wire. The incident TM-polarized plane wave together with its specular reflection from the grounded substrate create the external excitation field

$$H_x^{(exc)}(y, z \leq -h) = \left(e^{-j\beta_0 z} + R_0^{\text{TM}} e^{j\beta_0(z+2h)}\right) e^{-jk\sin(\theta)y}. \tag{2.31}$$

The input-admittance density Y_{in} characterizes the self-interaction of the q^{th} wire. On the other hand, the mutual-admittance densities $Y_{qp}^{(m)}$ take into account the interaction with the substrate and adjacent wires. The magnetic field created by q^{th} line current from all periods (except the zero$^{\text{th}}$ one) is given by the following series

$$-\frac{k}{2\eta} V_q \sum_{n=1}^{+\infty} \cos[k\sin[\theta]nL] H_0^{(2)}[knL]. \tag{2.32}$$

The magnetic field created by all other line currents can be accounted for as follows

$$-\frac{k}{4\eta} \sum_{p=1, p\neq q}^{N} V_p \sum_{n=-\infty}^{+\infty} e^{-jk\sin[\theta]nL} H_0^{(2)}[k|(q-p)d - nL|]. \tag{2.33}$$

The waves reflected from the PEC-backed substrate create the following magnetic field at the location of the q^{th} wire (zeroth period)

$$-\frac{k}{2\eta L} \sum_{p=1}^{N} V_p \sum_{m=-\infty}^{+\infty} e^{j\xi_m(p-q)d} \frac{R_m^{\text{TM}}}{\beta_m}. \tag{2.34}$$

However, in contrast to the case of TE polarization discussed in Section 2.2, the series in Eq. (2.34) does not converge when $q = p$. Indeed, R_m^{TM} goes to $(\varepsilon_s - 1)/(\varepsilon_s + 1)$ when m tends to infinity, $\beta_m \sim -jm$ for large m. The divergence can be avoided by using the Poisson's formula backwards. To that end, I perform the following transformation of the series

$$\sum_{m=-\infty}^{+\infty} \frac{R_m^{\text{TM}}}{\beta_m} = \sum_{m=-\infty}^{+\infty} \frac{1}{\beta_m} \left(R_m^{\text{TM}} - \frac{\varepsilon_s - 1}{\varepsilon_s + 1}\right) + \frac{\varepsilon_s - 1}{\varepsilon_s + 1} \sum_{m=-\infty}^{+\infty} \frac{1}{\beta_m}. \tag{2.35}$$

The first series on the right hand side of Eq. (2.35) now converges while the second one contains the singularity and should be transformed by means of the Poisson's formula in the following

way

$$\frac{\varepsilon_s-1}{\varepsilon_s+1}\sum_{m=-\infty}^{+\infty}\frac{1}{\beta_m}=L\frac{\varepsilon_s-1}{\varepsilon_s+1}\sum_{n=1}^{+\infty}e^{-jk\sin[\theta]nL}H_0^{(2)}[knL]+\frac{L}{2}\frac{\varepsilon_s-1}{\varepsilon_s+1}H_0^{(2)}[kr_0]. \tag{2.36}$$

Summarizing Eqs. (2.32), (2.33), (2.34) and (2.36), one arrives at the explicit expression for the mutual-admittance density

$$\begin{aligned}
Y_{qp}^{(m)}&=\frac{k}{4\eta}\sum_{n=-\infty}^{+\infty}e^{-ik\sin[\theta]nL}H_0^{(2)}[k|(q-p)d-nL|]+\frac{k}{2\eta L}\sum_{m=-\infty}^{+\infty}e^{j\xi_m(p-q)d}\frac{R_m^{\mathrm{TM}}}{\beta_m},\quad q\neq p,\\
Y_{qq}^{(m)}&=\frac{\varepsilon_s-1}{\varepsilon_s+1}\frac{k}{4\eta}H_0^{(2)}[kr_0]+\left(1+\frac{\varepsilon_s-1}{\varepsilon_s+1}\right)\frac{k}{2\eta}\sum_{n=1}^{+\infty}\cos[k\sin[\theta]nL]H_0^{(2)}[knL]\\
&+\frac{k}{2\eta L}\sum_{m=-\infty}^{+\infty}\frac{1}{\beta_m}\left(R_m^{\mathrm{TM}}-\frac{\varepsilon_s-1}{\varepsilon_s+1}\right).
\end{aligned} \tag{2.37}$$

Equations (2.29),(2.30) and (2.37) allow one to calculate load-admittance densities to establish a desired diffraction pattern. In order to deal only with reactive load-admittance densities, one has to additionally satisfy the equation of power conservation

$$\mathrm{Re}\left[\left(H_x^{(exc)}((q-1)d,-h)-\sum_{p=1}^{N}Y_{qp}^{(m)}V_p\right)V_q^*\right]=\mathrm{Re}[Y_{in}]|V_q|^2. \tag{2.38}$$

When satisfying this equation, arbitrary diffraction patterns for TM polarization can be constructed with reactive magnetic metagratings. Practical implementation of polarizable particles composing a magnetic wire is considered in the following chapter.

2.6. Conclusion

In this Chapter, I have presented analytical models of multi-element electric and magnetic metagratings operating in the reflective configuration. It has been shown that the power of an incident wave can be arbitrarily redistributed between different M propagating diffraction orders by means of $N=M$ loaded wires in a supercell. In a general case, it requires loading wires with engineered active and lossy elements, which appears to be exceptionally challenging in practice. However, I also demonstrated that accurate adjustment of the near-field (via nonpropagating diffraction orders) facilitating to establish power balance with purely reactive metagratings becomes possible by introducing additional wires in a supercell. Meanwhile, it is important to note that no strict proof has been provided regarding the exact number of reactive

wires (in a supercell) necessary to arbitrarily control the diffraction pattern in a general case. Equation (2.14) represents a set of quadratic equations with complex-valued coefficients and *real-valued* roots ($\mathrm{Re}[I_q]$ and $\mathrm{Im}[I_q]$). Since Eq. (2.14) involves such operators as Re, complex conjugate and modulus, it is not an ordinary algebraic equation and a rigorous mathematical analysis becomes particularly difficult. Therefore, in each particular situation the number of reactive wires should be found individually.

To validate the theoretical findings, several examples to establish desired diffraction patterns with $N = 2M$ reactive wires per period have been demonstrated via 2D full-wave simulations. For an experimental validation, I have demonstrated the design procedure of electric metagratings at microwave frequencies by using printed capacitor and inductor as building blocks for loaded-wires. The experimental validation results represent extreme examples in the control of diffraction patterns which are challenging or impossible to realize by other means. For instance, in order to perform large angle nonspecular reflection using a scalar reflective metasurface, one has to significantly rely on numerical optimization techniques [143, 144]. Otherwise, one has to design a three layer scalar metasurface emulating omega-bianisotropic response or a tensorial reflective metasurface [126, 129]. It is also interesting to note that when looking at the photographs of the fabricated metagratings shown in Figs. 2.8(a) and (b), one could reasonably argue that they remind a lot of conventional dense metasurfaces and, therefore, can be homogenized and described in terms of surface impedances. However, such an attempt would lead to the conclusion that the metagratings locally radiate and absorb (real part of surface impedance would take positive and negative values), when in fact they are reactive structures. It highlights yet another time the importance of adopted theoretical models, which may lead to opposite conclusions even though being applied to describe the same physical structures.

Although the proof-of-concept demonstration is done at microwave frequencies under the assumption of TE polarization, the main theoretical result is general. Significantly decreasing the number of unit cells per wavelength (compared to metasurfaces) greatly relaxes the fabrication constraints which makes it easier to develop metagratings operating in the optical domain and capable of controlling all propagating diffraction orders. Moreover, recent advances in the area of manipulating acoustic wavefronts [154, 155, 156, 157] suggest that the developed theory can be also generalized for the needs of the acoustics community. The possibility to develop metagratings operating at different frequency ranges as well as for other domains of physics such as acoustics opens an avenue for a plethora of applications.

Chapter 3

Local Periodic Approximation and Optimization-Aided Design

Contents

3.1. Introduction

A metasurface is represented by a distribution of engineered subwavelength scatterers over a surface and can be described by means of surface impedances. It can perform wavefront transformations when the surface impedances are spatially modulated [1, 110]. The local periodic approximation (LPA) plays a crucial role in designing such metasurfaces [75, 112] and has been already used for long time as it is discussed in the First Chapter. The LPA serves to estimate scattering properties of a unit cell embedded in a *nonuniform* array. To that end, the unit cell is placed in a corresponding *uniform* array whose reflection and transmission coefficients are then attributed to it in the nonuniform array. Scattering parameters of a uniform array are usually calculated from full-wave numerical simulations. However, there are particularly simple cases (e.g. metallic patches) that can be treated analytically [150, 151]. Importantly, scattering parameters of a unit cell obtained with the LPA represent its integral characteristics and sum up contributions from the substrate, a meta-atom and the interaction between meta-atoms forming the uniform array. It makes scattering parameters change, when one thickens the substrate or changes the inter-element distance without altering a meta-atom. The analytical model of metagratings is based on their discrete representation and allows to calculate the interaction between neighboring wires. It therefore requires characterizing a loaded-wire with proper parameters, which depends on neither the substrate nor the inter-wire distance. Input- and load-impedance densities are the parameters that characterize a loaded-wire. It makes the conventional LPA unsuitable to that end.

Practically, a wire is constituted from subwavelength meta-atoms arranged in a line. The electromagnetic response of a wire, input- and load-impedance densities, is determined by geometrical parameters of constituting meta-atoms. Initially, metagratings were designed either by performing 3D full-wave numerical optimization of a whole metagrating's period, as in Ref. [145], or semi-analytically, as discussed in the Second Chapter and demonstrated in Refs. [158, 146, 148]. While the first approach can be very time consuming when it comes to designing metagratings having many wires per period, the second one allows one to consider only very simple meta-atom designs such as printed capacitors and inductors [146, 148, 159] or dielectric cylinders [158]. Although semi-analytical approaches represent a simple tool for designing metagratings, it has to be completed with a phenomenological scaling parameter which is found

by means of 3D full-wave simulations of an entire supercell and, thus, is not unique for different supercells [146, 159]. In this Chapter, I develop an analog of the LPA to design metagratings with the help of 3D full-wave numerical simulations. To conform with the above mentioned requirements, the LPA is accompanied with an analytical procedure allowing to subtract the contributions from the substrate and the interaction with neighboring wires in a uniform array. In comparison to a straightforward numerical optimization, it significantly reduces the time spent on the design of metagratings since within the LPA one deals with a single unit cell at a time. Conversely to analytical models, simulation-based approaches are advantageous for being able to consider complex designs of meta-atoms and account for such practical aspects as finite thickness of the metal cladding, conduction and dielectric losses. Next in the Chapter, I combine the analytical model developed in the Second Chapter and the LPA with an optimization procedure to solve the inverse scattering problem and find an optimal number of wires in a supercell. The optimization procedure allows to tackle the problem of the number of wires in a supercell outlined in the end of the Second Chapter. The developed design procedure is validated by means of 3D full-wave simulations and experimentally.

3.2. Retrieval procedure

I consider reflecting metagratings operating either under TE or TM incident wave polarization. Therefore, each wire composing a metagrating can be characterized by a *scalar* electric impedance density Z_q (or scalar magnetic admittance density Y_q in the case of a wire possessing a magnetic response). Previously, I have distinguished between load- and input-impedance densities which I do not separate in the present Chapter dealing only with impedance density as the principal characteristic of a wire. To be more accurate, I assume that the impedance density represents the sum of the load-impedance density and reactive part of the input-impedance density. The reason for such an adjustment is that it is difficult to define input-impedance density for a complex design of a wire.

According to the LPA, in order to find the impedance density, a wire from a nonuniform array (Fig. 3.1(a)), is placed in the corresponding uniform array of period d illuminated by a plane wave incident at angle θ, as illustrated in Fig. 3.1(b). I start by describing a way to retrieve electric-impedance Z_q and magnetic-admittance Y_q densities from scattering parameters. Since Z_q (Y_q) represents itself as a complex number and an electric (magnetic) line current radiates TE

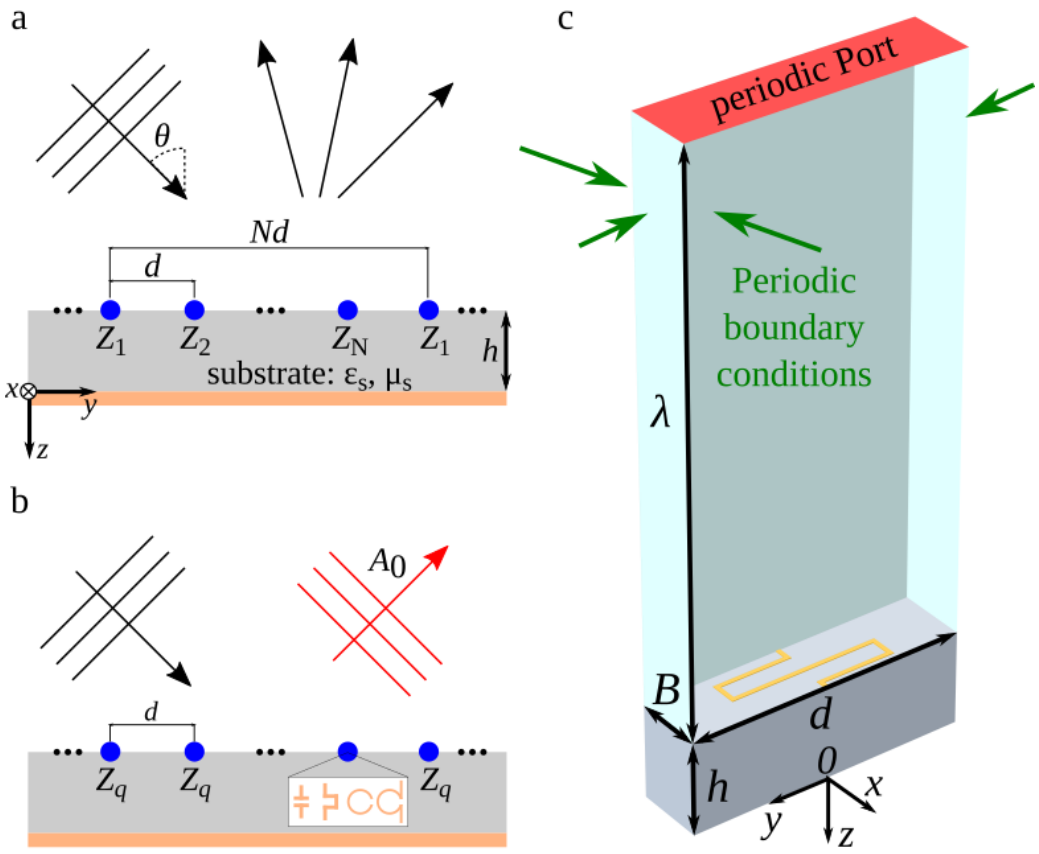

Figure 3.1: ***(a)*** *Schematic diagram of a metagrating: a periodic array of thin wires placed on a dielectric substrate backed by a metal plate and having relative permittivity ε_s, permeability μ_s and thickness h. The array is excited by a plane wave incident at an angle θ.* ***(b)*** *Schematic diagram of a uniform array of wires characterized by the same impedance density Z_q. The inset represents the different meta-atoms composing a wire.* ***(c)*** *Principal model used in numerical simulations to calculate the reflection coefficient from a uniform array of wires implemented with meta-atoms.*

(TM) wave, it is sufficient to deal only with the complex amplitude of the specularly reflected TE (TM) plane wave.

3.2.1 Electric response, TE polarization

An electric polarization line current I, excited by TE plane wave in a wire composing the uniform array, is linked to the complex amplitude A_0^{TE} of the electric field of the specularly reflected wave via the following formula

$$I = -\frac{2d}{k\eta}\frac{(A_0^{\mathrm{TE}} - R_0^{\mathrm{TE}} e^{2i\beta_0 h})\beta_0}{(1 + R_0^{\mathrm{TE}})e^{j\beta_0 h}}. \tag{3.1}$$

Indeed, the scattered electric field can be represented via a plane-wave expansion and only a single wire per period is considered within the LPA. Then, the amplitudes of these plane waves

can be obtained from Eq. (2.9) by setting $N = 1$

$$A_m^{\mathrm{TE}} = -\frac{k\eta}{2L}\frac{(1+R_m^{\mathrm{TE}})e^{j\beta_m h}}{\beta_m} I + \delta_{m0} R_0^{\mathrm{TE}} e^{2j\beta_0 h}. \tag{3.2}$$

The amplitude of the specularly reflected wave corresponds to $m = 0$ and used to express the current I in Eq. (3.1). The Fresnel's reflection coefficient R_m^{TE} from the substrate backed by perfect electric conductor (PEC) is given by Eq. (2.10). When the metal backing the dielectric substrate cannot be modeled as PEC, one has to correspondingly modify the reflection coefficient.

Since it is assumed that wires have a deeply subwavelength cross section, polarization currents are modeled mathematically by Dirac delta function $\delta(y, z)$. Consequently, the interaction with the substrate and between adjacent wires can be taken into consideration analytically by means of the mutual-impedance density Z_m found from Eq. (2.12) as $Z_{qq}^{(m)}$

$$Z_m = \frac{k\eta}{2}\sum_{n=1}^{+\infty}\cos[k\sin[\theta]nL]H_0^{(2)}[knd] + \frac{k\eta}{2d}\sum_{m=-\infty}^{+\infty}\frac{R_m^{TE}}{\beta_m}. \tag{3.3}$$

It allows one to obtain the characteristic of a wire itself, independent of the substrate's thickness h and the inter-wire distance d. Electric-impedance density Z_q of a wire is found from Ohm's law as follows

$$Z_q = \frac{E_0}{I} - \frac{k\eta}{4} - Z_m, \tag{3.4}$$

where $E_0 = (1 + R_0^{TE})\exp[j\beta_0 h]$ represents the value of the external electric field (incident wave plus its reflection from the metal-backed substrate) at the location of the wire $y = 0$ and $z = -h$. The radiation resistance of a wire is equal to $k\eta/4$ being independent of its particular implementation as it follows from power conservation conditions [149]. It is important to note that mutual-impedance density depends only on the period of the uniform array and parameters of the metal-backed substrate, but does not depend on the current I. It means that the impedance density given by Eq. (3.4) accurately represents the characteristic of the corresponding wire in a *nonuniform* array.

3.2.2 Magnetic response, TM polarization

The case of TM polarization and wires possessing magnetic response can be treated with the help of duality relations [147]: $\mathbf{E} \to \mathbf{H}$, $\mathbf{H} \to -\mathbf{E}$, $I \to V$ and $\eta \to 1/\eta$. Since the metal-backed dielectric substrate is not replaced by the corresponding dual equivalent, I have to additionally make the following substitution $R_0^{TE} \to R_0^{TM}$. Thus, from Eq. (3.1), one can arrive at the

formula for retrieving the magnetic current V from the complex amplitude of the magnetic field of the specularly reflected plane wave

$$V = -\frac{2d\eta}{k}\frac{(A_0^{TM} - R_0^{TM}e^{2i\beta_0 h})\beta_0}{(1+R_0^{TM})e^{j\beta_0 h}}, \tag{3.5}$$

where R_0^{TM} is the Fresnel's reflection coefficient from the metal-backed substrate of a TM-polarized plane wave at incidence angle θ. As previously, the interaction with the substrate and between adjacent wires can be taken into account by means of the mutual-admittance density Y_m calculated analytically in Eq. (2.37) and reduced to

$$\begin{aligned} Y_m = &\left(1+\frac{\varepsilon_s-1}{\varepsilon_s+1}\right)\frac{k}{2\eta}\sum_{n=1}^{+\infty}\cos[k\sin[\theta]nL]H_0^{(2)}[knd] \\ &+\frac{k}{2d\eta}\sum_{m=-\infty}^{+\infty}\frac{1}{\beta_m}\left(R_m^{TM}-\frac{\varepsilon_s-1}{\varepsilon_s+1}\right)+\frac{\varepsilon_s-1}{\varepsilon_s+1}\frac{k}{4\eta}. \end{aligned} \tag{3.6}$$

Then, the magnetic admittance density Y_q can be found as

$$Y_q = \frac{H_0}{V} - \frac{k}{4\eta} - Y_m. \tag{3.7}$$

Here $H_0 = (1+R_0^{TM})\exp[j\beta_0 h]$ is the value of the external magnetic field at the wire located at $y = 0$ and $z = -h$, $k/(4\eta)$ represents the radiation conductance.

3.2.3 Look-up table

In practice, a wire is implemented by arranging identical subwavelength meta-atoms in a line. The ultimate goal of the developing approach is to construct a look-up table linking geometrical parameters of meta-atoms with corresponding impedance (admittance) densities. To that end, one can use 3D full-wave numerical simulations software. Here I demonstrate simulation results obtained with the help of COMSOL Multiphysics. It allows one to take into account such practical features of meta-atoms as dielectric and conduction losses, finite thickness of metallic traces and etc. A geometry of a simulation model is schematically shown in Fig. 3.1(c). It consists of two principal parts: a considered unit cell, illustrated as a printed inductance on a metal-backed dielectric substrate, and an air region. Periodic boundary conditions are imposed on the side faces. The model is excited by a periodic port assigned to the face of the air region opposite to the unit cell, highlighted by the red color in Fig. 3.1(c). The periodic port creates a plane wave incident at angle θ. It is important to take into account the angle θ as meta-atoms

are usually spatially dispersive [112]. The thickness of the air region equals operating vacuum wavelength λ which is normally enough to register only the amplitude of the specular reflection eliminating higher order evanescent modes. The periodic port is also used as a listening port to calculate the scattering parameter S_{11}. It is related to the complex amplitude A_0 in Eq. (3.1) as

$$S_{11} = A_0^{TE} e^{-2i\beta_0(h+\lambda)}. \tag{3.8}$$

In the case of TM polarization

$$S_{11} = -A_0^{TM} e^{-2i\beta_0(h+\lambda)}. \tag{3.9}$$

3.3. Optimization-aided design procedure

This section provides a step-by-step guide to design metagratings by means of the local periodic approximation. The case of TE polarization and electric metagrating is considered without loss of generality. The design procedure can be decomposed into four main steps, as outlined in the flowchart depicted in Fig. 3.2. The design procedure begins by setting the period L of a metagrating and the incidence angle θ_i of a plane-wave illumination. It defines the set of Floquet-Bloch modes representing the scattered field. Diffraction angles of the propagating diffraction orders θ_m can be found via the grating formula: $L(\sin[\theta_m] - \sin[\theta_i]) = m\lambda$, where m represents the number of an order. The amplitudes A_m^{TE} of the Floquet-Bloch modes are given by Eq. (2.9) which I repeat here for sake of the reader's convenience

$$A_m^{\mathrm{TE}} = -\frac{k\eta}{2L}\frac{(1+R_m^{\mathrm{TE}})e^{j\beta_m h}}{\beta_m}\sum_{q=1}^{N} I_q e^{j\xi_m(q-1)d} + \delta_{m0} R_0^{\mathrm{TE}} e^{2j\beta_0 h}. \tag{3.10}$$

Next, an appropriate dielectric substrate for a given frequency range is chosen: its thickness h and relative permittivity ε_s should not support propagation of waveguide modes in the frequency range of interest. Waveguide modes are analog of surface plasmon-polaritons responsible for well-known grating anomalies (or Wood's anomalies) in optics. The presence of waveguide modes also implies divergence of certain Fresnel's reflection coefficients R_m^{TE} that manifests itself in significant numerical errors. Thus, in order to select a good substrate for a given period L of a metagrating, one can plot the absolute value of the first few Fresnel's reflection coefficients corresponding to *nonpropagating* diffraction orders as a function of the substrate's parameters (thickness and permittivity) and avoid poles. As a rule of thumb, a substrate with

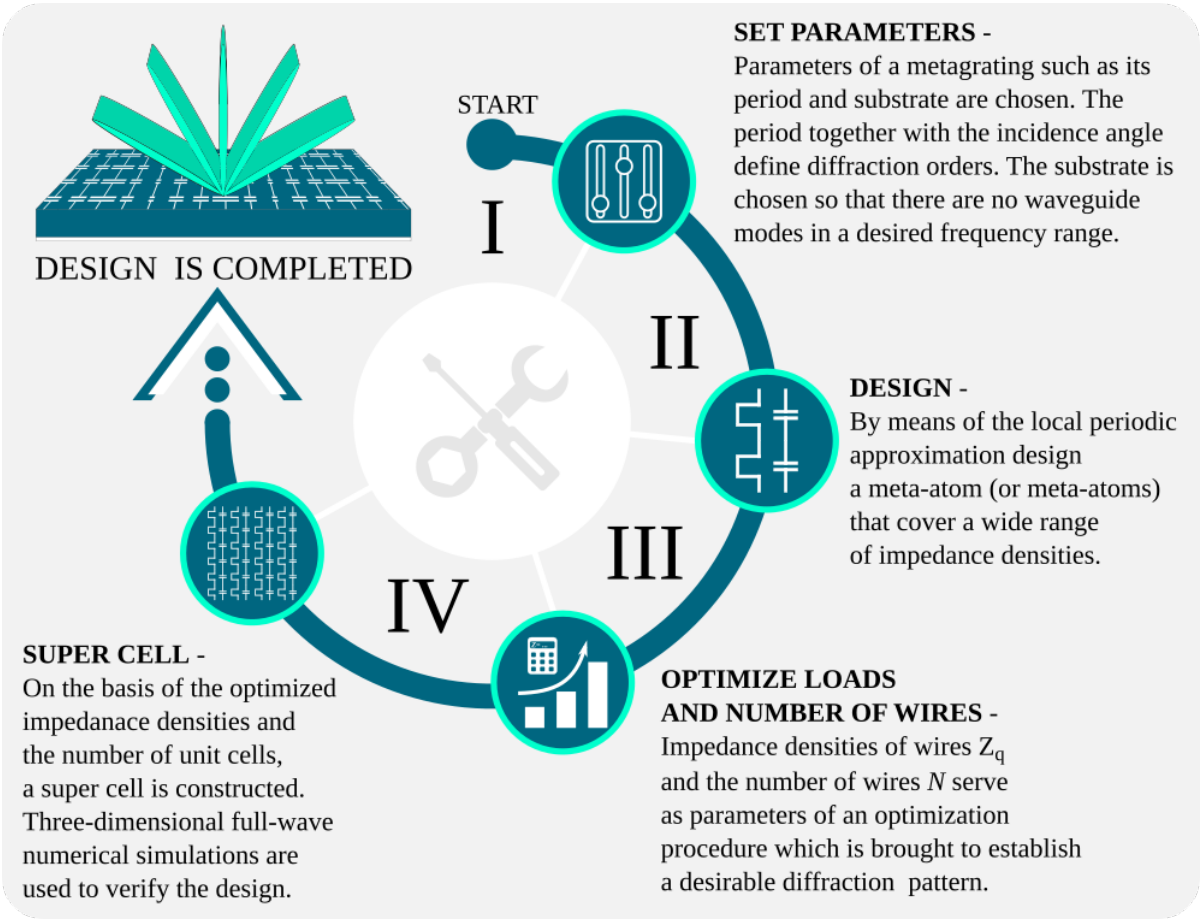

Figure 3.2: A flowchart of the design procedure of a metagrating.

low permittivity and thickness of the order of $\lambda/(4\sqrt{\varepsilon_s})$ is a good candidate for the design of metagratings. Although it is known that thin substrates are better for avoiding waveguide modes, they might not allow efficient excitation of polarization current in wires as the excitation field vanishes at the ground plate.

The second step is independent of the first one and requires to design a meta-atom (or meta-atoms) that will form the wires of a metagrating. To that end, the local periodic approximation is used. A meta-atom's design should provide a wide range of achievable impedance densities of a corresponding wire when changing its geometrical parameters (or an external bias if there are embedded tunable elements).

Each desired configuration of the diffraction pattern requires different set of impedance densities which obey Ohm's law:

$$Z_q I_q = E_q^{(exc)} - \frac{k\eta}{4} I_q - \sum_{p=1}^{N} Z_{qp}^{(m)} I_p. \tag{3.11}$$

The incident plane wave plus its specular reflection from the PEC backed substrate act as an

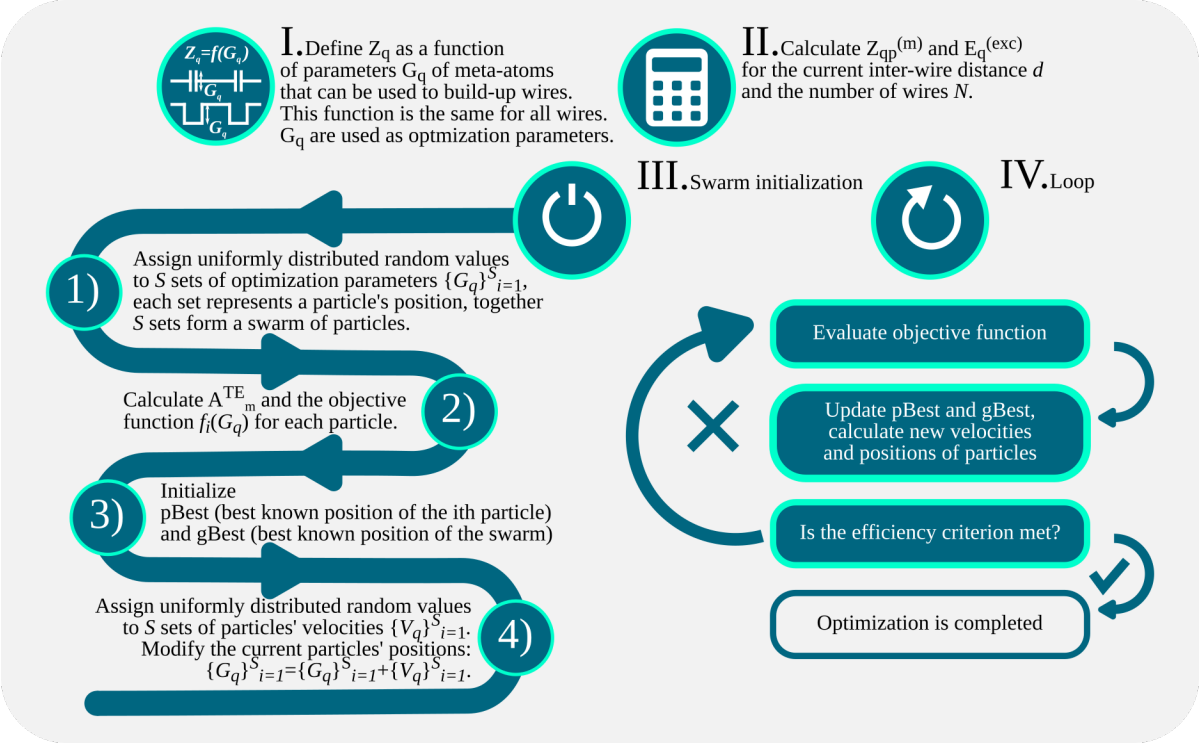

Figure 3.3: A block diagram of a particle swarm optimization algorithm.

external excitation $E_q^{(exc)} = (1 + R_0^{\mathrm{TE}}) \exp[j\beta_0 h - j\xi_0(q-1)d]$ of polarization currents I_q. The scattered field is established depending on excited currents and in accordance with Eq. (3.10). In the third step of the procedure, one finds impedance densities of wires composing a metagrating and required to establish a desired diffraction pattern. In general case, arbitrarily chosen amplitudes A_m^{TE} of propagating diffraction orders, as it is stressed in Section 2.2, require impedance densities that have $\mathrm{Re}[Z_q] \neq 0$ and imply engineering of active and/or lossy elements. Including additional wires in the period and satisfying the power conservation conditions

$$\mathrm{Re}\left[\left(E_q^{(exc)} - \sum_{p=1}^{N} Z_{qp}^{(m)} I_p\right) I_q^*\right] = \frac{k\eta}{4}|I_q|^2, \tag{3.12}$$

makes it sufficient to use purely reactive loads. On the other hand, any realistic passive meta-atom possesses inevitable resistive response whether because of conduction and/or dielectric losses or embedded lossy tunable elements (such as varactor diodes, for instance). Although the LPA allows one to account for these practical aspects of a meta-atom's design, the capacity to judiciously engineer $\mathrm{Re}[Z_q]$ independently from $\mathrm{Im}[Z_q]$ can be very limited. Furthermore, the

Impedance density (η/λ)	Z_1	Z_2	Z_3	Z_4	Z_5	Z_6	Z_7
Microwaves: TE	$-i4.87$	$-i1.16$	$i6.88$	$i17.16$	$-i0.33$	$i3.97$	$-i0.81$
Infrared: TE	$-i0.30$	$-i3.06$	$-i3.20$	$i3.61$	$-i1.63$	$-i1.04$	$-i11.59$
Admittance density ($\eta\lambda$)	Y_1	Y_2	Y_3	Y_4	Y_5	Y_6	Y_7
Microwaves: TM	$-i3.61$	$i4.42$	$i0.89$	$i3.05$	$i0.31$	$i0.71$	$i4.51$
Geometrical parameters (mm)	A_1	A_2	A_3	A_4	A_5	A_6	A_7
Microwaves: TE	1.48 (cap. uc)	2.74 (cap. uc)	3.08 (ind. uc)	7.88 (ind. uc)	3.26 (cap. uc)	10.33 (cap. uc)	2.94 (cap. uc)
Geometrical parameters (mm)	$R_{out,1}$	$R_{out,2}$	$R_{out,3}$	$R_{out,4}$	$R_{out,5}$	$R_{out,6}$	$R_{out,7}$
Microwaves: TM	1.348	1.4065	1.382	1.397	1.378	1.381	1.4071
Geometrical parameters (nm)	$w_1,\ B_1,\ g_1$	$w_2,\ B_2,\ g_2$	$w_3,\ B_3,\ g_3$	$w_4, t_{m,4} = w_4$	$w_5,\ B_5,\ g_5$	$w_6,\ B_6,\ g_6$	$w_7,\ B_7,\ g_7$
Infrared: TE	175, 1600, 350	59, 800, 100	53, 800, 100	73 (ind. uc)	157, 800, 100	260, 800, 100	137, 800, 350

Table 3.1: Parameters of the metagratings demonstrated as examples in Section 3.4. The indexes correspond to the numbered wires in Figs. 3.6(a) and 3.8(a). The other parameters are fixed and given in the captions to Figs. 3.4, 3.5 and 3.7. Where it is necessary the type of a used unit cell (uc) is specified in the brackets. In the example demonstrated by Fig. 3.6(b), inductive unit cells are represented only by meanders with the parameters $B/C = 3$ illustrated in Fig. 3.4(c).

set of equations (3.12) should be modified to the following set of inequalities

$$\mathrm{Re}\left[\left(E_q^{(exc)} - \sum_{p=1}^{N} Z_{qp}^{(m)} I_p\right) I_q^*\right] > \frac{k\eta}{4}|I_q|^2 \tag{3.13}$$

which accounts for the resistance of wires and indicates that the power received by a wire is greater than the power it radiates. In many situations it is preferable to minimize the impact of $\mathrm{Re}[Z_q]$ resulting in increased ohmic losses. Instead of elaborating on the analytical procedure developed in the Second Chapter and justifying the number of wires per period, the inverse scattering problem can be efficiently solved by means of a numerical optimization procedure. As optimization parameters, it uses geometrical parameters of meta-atoms (or external biases) and the number of wires per period. The geometrical parameters of meta-atoms are related to the impedance density of a wire in the look-up table constructed by means of the LPA. In their turn, impedance densities determine polarization currents and, consequently, amplitudes of diffraction orders found from Eqs. (3.11) and (3.10). The objective function may vary depending on the needs. The one that I used to *equally* split the incident wave between an *arbitrary* number of propagating diffraction orders when minimizing the parasitic scattering in the far-field is given as

$$f(Z_q) = t^t \left(\prod_{n\in\mathbb{D}} |A_n^{\mathrm{TE}}|^2 \beta_n/\beta_0\right) \Big/ \left(\sum_{m=-l}^{r} |A_m^{\mathrm{TE}}|^2 \beta_m/\beta_0\right)^t. \tag{3.14}$$

Here, $\mathbb{D}$ represents a discrete set of desired orders and t is the size of this set, $M = r + l + 1$ is the total number of propagating diffraction orders. As a concrete optimization algorithm, I implemented a particle swarm optimization, as illustrated by the block diagram in Fig. 3.3, which showed better performances than a real-valued genetic algorithm. Once the optimal impedance densities are found, the second step of the design procedure is completed.

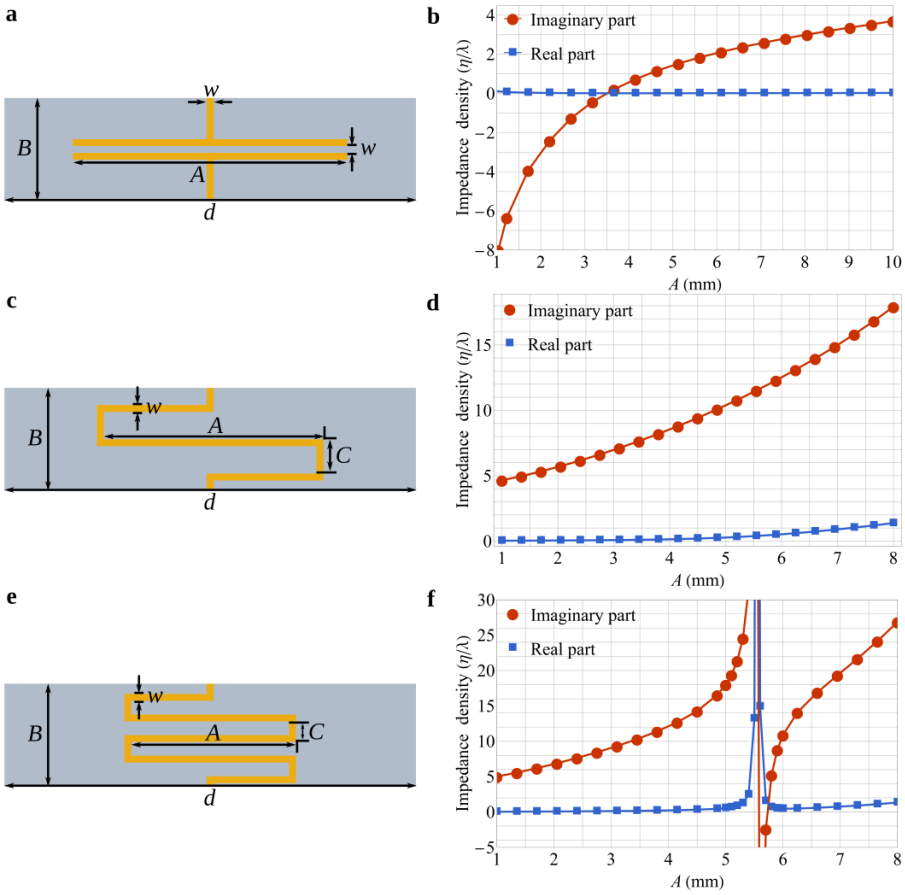

Figure 3.4: Examples and characteristics of unit cells that can be used to compose wires in a metagrating. The top row represents the schematics of printed capacitor ***(a)*** *and inductances* ***(c)*** *and* ***(e)****. The bottom row demonstrates impedance densities found by means of the LPA as functions of geometrical parameters of unit cells and corresponding (from* ***(b)*** *to* ***(f)****), respectively, to wires built up from printed capacitor shown in figure (a) and printed inductances in figures* ***(c)*** *and* ***(e)****. Other parameters are fixed: dielectric substrate is F4BM220 of permittivity* $\varepsilon_s = 2.2(1-10^{-3}j)$ *and thickness* $h = 5$ *mm,* $B = 3.75$ *mm,* $d = 15$ *mm,* $w = 0.25$ *mm, (*$B/C = 3$ *in figure* ***(d)*** *and* $B/C = 5$ *in figure* ***(f)****). Working frequency is set to* 10 *GHz, corresponding to the vacuum wavelength of* 30 *mm. Normally incident plane wave is assumed where electric field is oriented along the B dimension.*

The fourth and the final step of the design procedure is to compose a supercell out of the designed meta-atoms with optimized geometrical parameters and validate the final design using 3D full-wave numerical simulations. It is important to note that the developed optimization procedure itself does not include full-wave simulations and utilizes only numerical arrays calculated beforehand. It makes the optimization and the development of a final design *much* faster than in the case when only direct optimization of a supercell is performed.

3.4. Numerical examples via 3D simulations

In order to validate the developed design procedure, I first employ the LPA to construct look-up tables and then implement metagratings to control propagating diffraction orders. In what

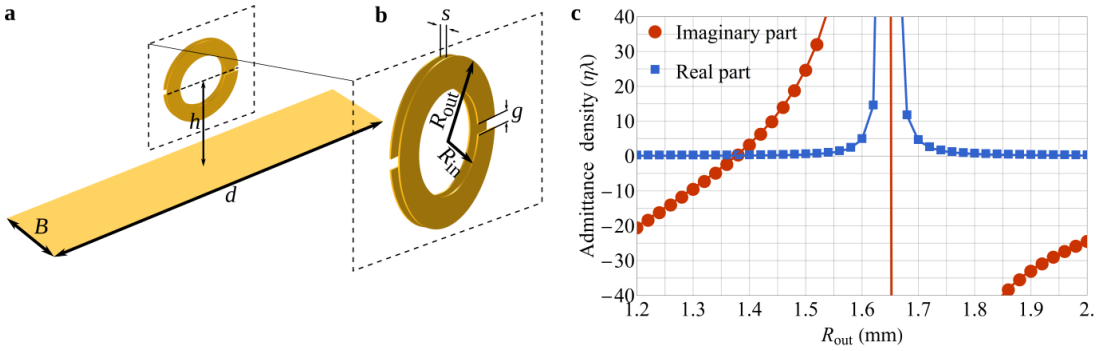

Figure 3.5: ***(a)*** *Schematic of a unit cell based on two split ring resonators and having an inversion center.* ***(b)*** *Zoom view of the magnetic meta-atom with defined parameters.* ***(c)*** *Calculated by means of the LPA, admittance density of the wire built up from the magnetic meta-atoms versus the outer radius* R_{out} *of the split ring resonator. Other parameters are fixed: no substrate (air is considered as spacer),* $h = 3.75$ *mm,* $B = 3.75$ *mm,* $d = 15$ *mm,* $s = 0.15$ *mm,* $g = 0.20$ *mm. Working frequency is set to* 10 *GHz (vacuum wavelength of* 30 *mm). Normally incident plane wave is assumed where magnetic field is oriented along the* B *dimension.*

follows, I focus on two frequency domains: microwave (operating vacuum wavelength 30 mm) and infrared (operating vacuum wavelength 4 μm). Table 3.1 provides the impedance (admittance) densities as well as the geometrical parameters of the wires composing the metagratings demonstrated in this section.

3.4.1 Microwave frequency range

I start by considering simple meta-atoms represented by printed capacitors and inductors, schematically shown in Fig. 3.4, that I have already considered in the Second Chapter. Such practical aspects of the design as finite thickness of the copper traces ($t_m = 35$ μm) and dielectric losses introduced by the substrate (F4BM220, $\varepsilon_s = 2.2$ with loss tangent 10^{-3}) are taken into account in simulations. Figure 3.4 shows the impedance densities calculated by means of the developed LPA at 10 GHz, the corresponding vacuum wavelength λ is 30 mm. It is seen that with printed capacitor and inductor at hand, one is able to cover a broad range of impedance densities (imaginary part) that is normally enough to realize any diffraction pattern for TE polarization. It is important to note that wires can exhibit significant resistive response at resonance (Fig. 3.4(f)), which should be kept in mind when designing metagratings. If one compares the results of the LPA with the analytical models described by Eqs. (2.15) and (2.16), one would see a very good agreement for the imaginary part of the impedance density for small values of the parameter A. Meanwhile, the resonance in Fig. 3.4(f) appearing when decreasing the parameter C cannot be captured by such a simple analytical formula as Eq. (2.16).

In order to build a magnetic metagrating operating under a TM-polarized illumination, I use

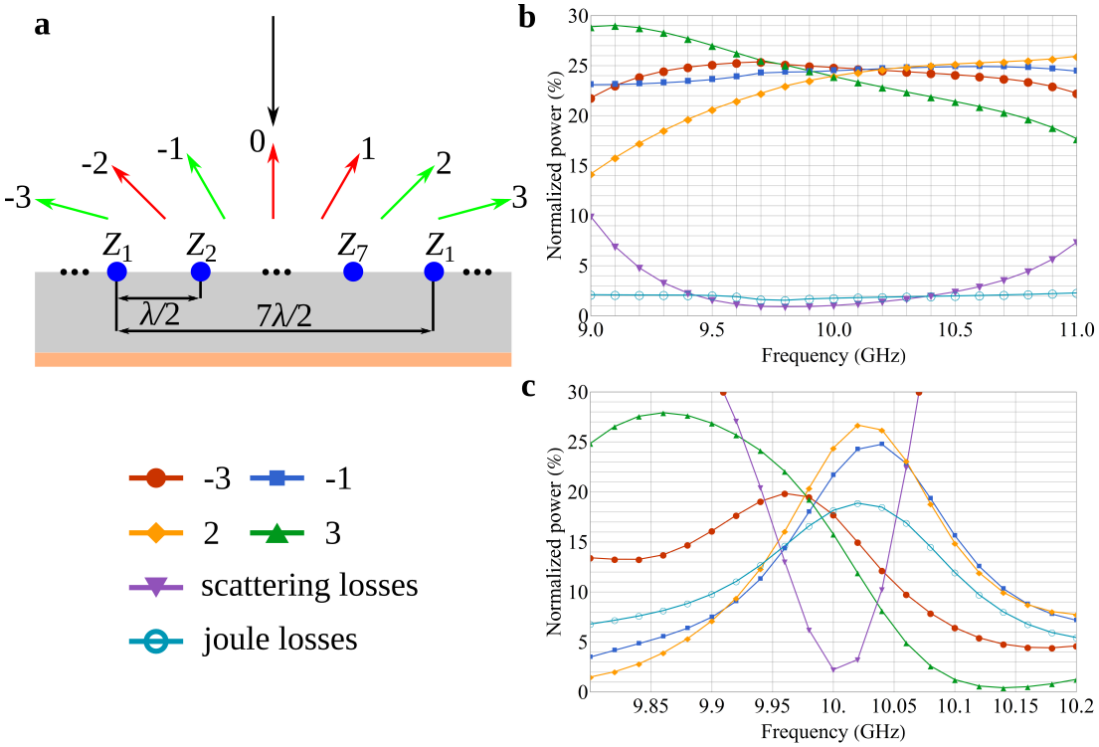

Figure 3.6: ***(a)*** *Schematic of a metagrating having period* $7\lambda/2$ *(*λ *is the operating vacuum wavelength) and exciting seven propagating diffraction orders under normally incident plane wave. The red and green beams represent suppressed and equally excited orders, respectively.* ***(b)***, ***(c)*** *Simulated frequency response (normalized power scattered in propagating diffraction orders versus frequency) of the metagrating operating under* ***(b)*** *TE and* ***(c)*** *TM polarizations and establishing the diffraction pattern illustrated by the panel* ***(a)****. Both metagratings are designed to operate at* 10 *GHz. Impedance and admittance densities as well as geometrical parameters of the wires composing the metagratings are given in Tab. 3.1.*

split ring resonators (SRRs) excited by the magnetic field and possessing an effective magnetic response. Figure 3.5(a) illustrates the schematics of the unit cell which at close look consists of two SRRs separated by a short distance as seen from the close-up in Fig. 3.5(b). The unit cell has an inversion center allowing to eliminate the bianisotropic response attributed to single and double SRRs [160, 161]. In order to adjust the response of a wire represented by a 1D array of SRRs, I use the outer radius R_{out} as a tuning parameter. The result of applying the LPA to find an equivalent admittance density is shown in Fig. 3.5(c). Due to the small separation distance between the two SRRs it is possible to obtain strong magnetic response with the outer radius being of the order of $\lambda/20$. As in the case of TE polarization discussed above, it is seen that when approaching the resonance there is a drastic increase of the real part of the admittance density resulting in enhanced absorption.

In order to validate calculated impedance and admittance densities, an electric and a magnetic metagratings establishing a prescribed diffraction pattern are designed based only on the data from Figs. 3.4 and 3.5. The particle swarm optimization is used to solve the inverse scatter-

ing problem and construct a desired diffraction pattern. Particularly, the splitting of a normally incident plane wave equally between four propagating diffraction orders (-3$^{\text{rd}}$, -1$^{\text{st}}$, +2$^{\text{nd}}$ and +3$^{\text{rd}}$) out of seven existing is demonstrated. Schematically, it is illustrated in Fig. 3.6(a). To that end, the result of the optimization procedure have shown that it is sufficient to have seven reactive wires per period, with the inter-wire distance being $\lambda/2$. Figures 3.6(b) and (c) demonstrate simulated frequency responses of the electric and magnetic metagratings designed for 10 GHz operation. Overall, one can see that despite all practical limitations, the designed metagratings almost perfectly perform the desired splitting of the incident wave. It should be noted that the response of the electric metagrating, shown in Fig. 3.6(b), is more broadband than the one of the magnetic metagrating (Fig. 3.6(c)). It is naturally explained by the resonant behavior of the considered SRR-based unit cell, as shown in Fig. 3.5(b). Indeed, printed capacitor and inductor used for the electric metagrating do not exhibit resonances as shown by Figs. 3.4(b) and (d). The other feature of the magnetic metagrating is the enhanced level of absorption when comparing to the electric metagrating. However, it does not deteriorate the overall performance of the magnetic metagrating.

3.4.2 Infrared frequency range

In this subsection, I give an example of possible designs of meta-atoms that can be used as building blocks for metagratings operating at infrared frequencies. The chosen operation frequency is 75 THz corresponding to the vacuum wavelength of 4 μm. In order to implement capacitive and inductive meta-atoms for infrared domain, I consider metallic (gold) rectangular wires with and without an introduced air gap. Gold elements are placed on top of a dielectric substrate (silicon dioxide) backed with gold as illustrated by Figs. 3.7(a) and (b). The capacitive response is attributed to the gap between two parts of the wire. By changing the width of the gap and the cross section area of the wire one is able to adjust the capacitive response. The inductance of a metallic wire is determined only by its cross section area. While the design of these meta-atoms is relatively simple, it allows one to obtain impedance densities in a quite wide range of values as shown in Figs. 3.7(c) and (d). Interestingly, the real part of the impedance density remains very small due to nonresonant response of the unit cells even though the simulation model takes into account ohmic losses in gold and silicon dioxide. It is worthwhile to note that a single straight metallic wire may not be sufficient when a strong inductive response (large positive imaginary part of the impedance density) is required. Cross section area is usually restricted by fabrication

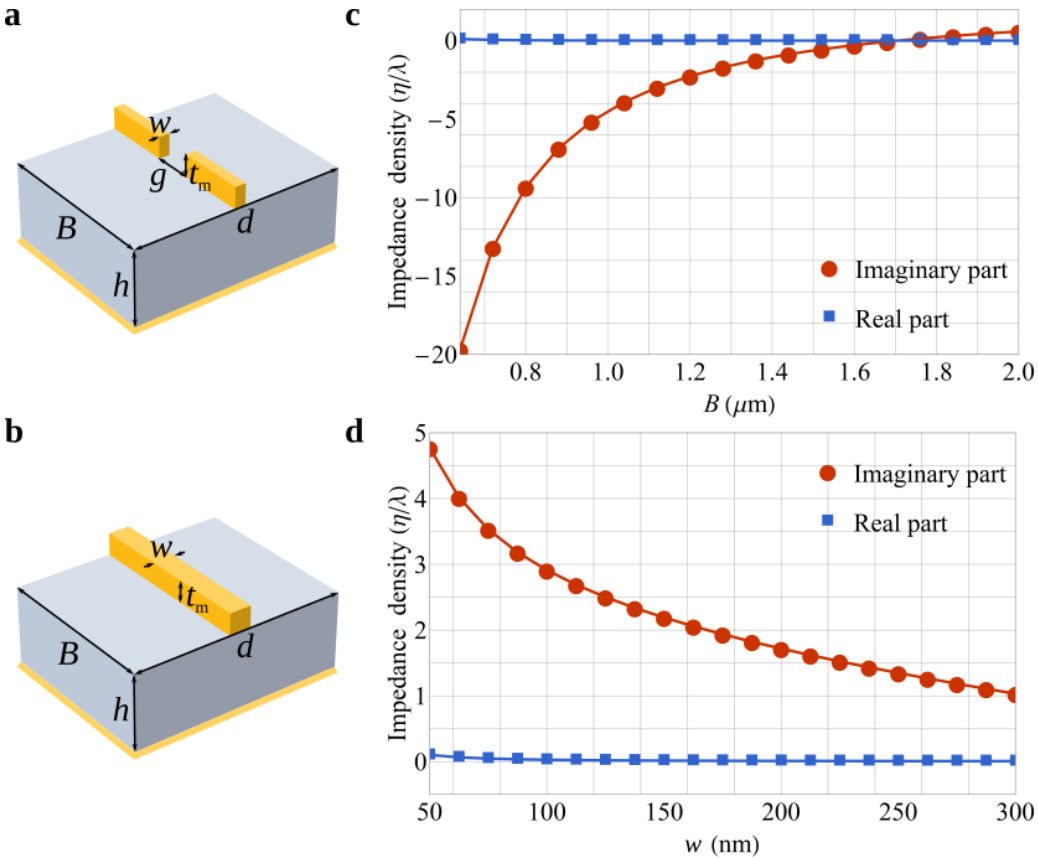

Figure 3.7: ***(a)***, ***(b)*** *Schematic diagrams of* ***(a)*** *two gold patches and* ***(b)*** *a gold wire exhibiting capacitive and inductive responses, respectively. The gold elements are placed on a silicon dioxide layer backed by a gold plating.* ***(c)***, ***(d)*** *Impedance densities calculated by means of the LPA as functions of geometrical parameters of the unit cells and corresponding, respectively, to wires built up from gold patches shown in the panel* ***(a)*** *and gold wires in the panel* ***(b)****. Other parameters are fixed: the silicon dioxide layer has permittivity* $\varepsilon_s \approx 1.93$ *and thickness* $h = 700$ *nm,* $d = 2$ μm*,* $w = 200$ *nm,* $t_m = 200$ *nm (*$t_m = w$ *in case of the panel* ***(d)****),* $g = 350$ *nm. Working frequency is set to 75 THz (the corresponding vacuum wavelength is 4* μm*). Normally incident plane wave is assumed where the electric field is oriented along the* B *dimension.*

tolerances that does not allow one to infinitely reduce it. Meandering can be a solution, as in Figs. 3.4(c) and (e), though it might complicate the fabrication.

In order to validate calculated impedance densities, I demonstrate a design of an infrared metagrating equally splitting a normally incident plane wave between three propagating diffraction orders (-2$^{\text{nd}}$, 0$^{\text{th}}$ and +3$^{\text{rd}}$), while the rest four are suppressed. A schematics is shown in Fig. 3.8(a). As in the examples of the microwave metagratings demonstrated in the previous subsection, the infrared metagrating is built-up of seven wires per period. The design is performed relying on the data from Fig. 3.7 and the analytical model described in the Second Chapter. Simulated frequency response of the infrared metagrating is shown in Fig. 3.8(b). The incident wave is equally, within a range of several percentages, distributed by the metagrating between desired diffraction orders. Furthermore, it is seen that the scattering in the parasitic,

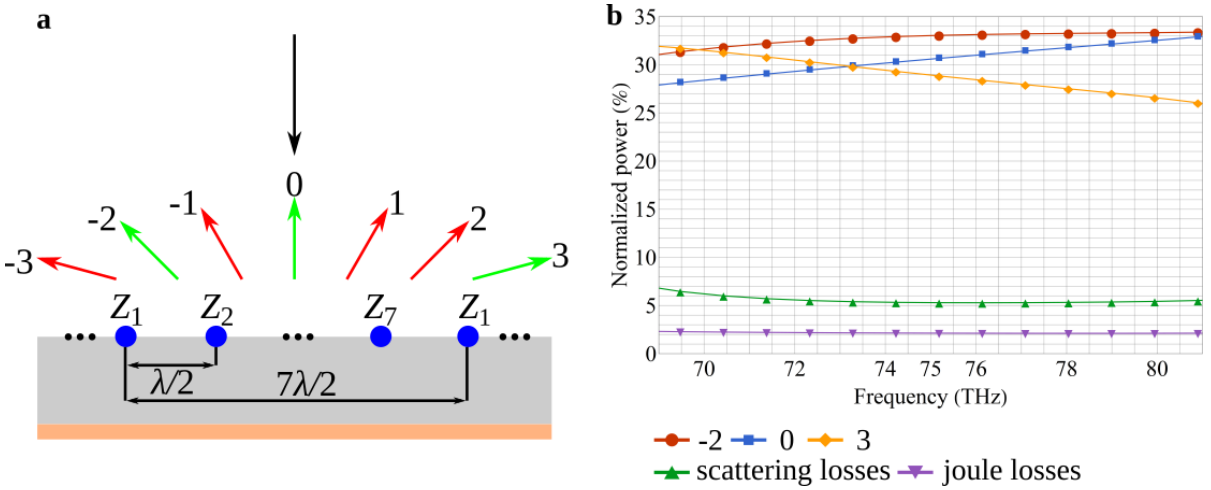

Figure 3.8: ***(a)*** *A schematics of a metagrating with the period of* $7\lambda/2$ *(λ is the operating vacuum wavelength) and exciting seven propagating diffraction orders under normally incident plane wave. The red and green beams represent suppressed and equally excited orders, respectively.* ***(b)*** *Simulated frequency response (normalized power scattered in different propagating diffraction orders versus frequency) of the metagratings operating under TE polarization and establishing the diffraction pattern illustrated by figure* ***(a)****. The metagrating is designed for 75 THz operating frequency. Impedance densities as well as geometrical parameters of the wires composing the metagrating are given in Tab. 3.1.*

-3$^{\text{rd}}$, -1$^{\text{st}}$, +1$^{\text{st}}$ and +2$^{\text{nd}}$, propagating orders remains suppressed in a wide frequency range due to the nonresonant nature of the meta-atoms. The absorption constitutes only 2% of the total incident power. The 5% level of scattering losses can be further reduced by introducing in the period additional wires as discussed in the Second Chapter.

To conclude this subsection, let me make a few practical comments. Extracted impedance densities shown in Fig. 3.7, slightly depend on the exact permittivity of gold since the skin depth at 75 THz constitutes approximately 25 nm, being less than the geometrical dimensions of the elements. In the simulations, dielectric permittivities of gold and silicon dioxide were taken from Refs. [162] and [163], respectively. Silicon dioxide was chosen as a substrate due to its low loss and low refractive index at 4 μm wavelength. It allows one to use a thick substrate while avoiding excitation of waveguide modes. If the dielectric substrate is thin, it may not be possible to model real wires as having infinitely small cross section area and accurately account for the interaction with the substrate. Another practical feature is that between gold parts and a silicon dioxide substrate there is usually a thin chromium (or titanium) adhesion layer of a few nm thickness. Although all practical aspects should be taken into account while designing an experimental sample, I do not expect that the influence of such a thin intermediate layer can lead to a qualitative change and therefore, I did not include it in the simulation model.

3.5. Experimental validation

In order to perform an experimental proof-of-concept demonstration, I design three experimental samples of metagratings operating at 10 GHz and excited by a normally incident plane wave. The prescribed functionalities of these three samples are schematically illustrated in Figs. 3.9(a)–(c). The first sample manages three diffraction orders, maximizing the power scattered in the $+1^{\text{st}}$ order and suppressing scattering in the the -1^{st} and 0^{th} orders. The period is $L = \lambda/\sin(60°)$, which corresponds to 60° anomalous reflection. It is composed of three wires per period, which is the minimum number of wires required to achieve an asymmetric diffraction pattern for plane-wave illumination at normal incidence. The second and third samples, is each composed of five wires per period of length $L = 2\lambda/\sin(50°)$. It allows one to control five diffraction orders: -2^{nd}, -1^{st}, 0^{th}, $+1^{\text{st}}$ and $+2^{\text{nd}}$. The second sample maximizes the power scattered in the $+1^{\text{st}}$ propagating diffraction order and thus performs small angle anomalous reflection, corresponding to approximately 23° at 10 GHz. The third sample equally excites the -2^{nd} and $+1^{\text{st}}$ orders while suppressing the three others. As a substrate, F4BM220 with the permittivity $\varepsilon_s = 2.2(1 - j10^{-3})$ and of $h = 5$ mm thickness is selected. To achieve such performances, it is enough to consider only capacitively-loaded wires. A schematic of a capacitive unit cell is shown in Fig. 3.10(a). Parameters w and B are fixed to 0.25 mm and 3 mm, respectively. The arm's length A of the printed capacitance is used as a tuning parameter for the load-impedance density. The load-impedance densities are first extracted from the S_{11} parameter of the unit cell as required by the LPA and then plotted as function of A in Fig. 3.10(b). Although being built for two different parameters d, $\lambda/[3\sin(60°)]$ and $2\lambda/[5\sin(50°)]$, the two curves in Fig. 3.10(b) almost coincide. It shows that the analytical model complementing the LPA to take into account the interaction between adjacent wires and the substrate, allows one to obtain the impedance density of a wire itself and not of a corresponding array. However, it is well known that the electric response of a microstrip printed capacitance depends on the relative permittivity of the substrate as well [150, 164]. It is due to the fact that a strong and highly localized electric field penetrating the substrate is established in the gap between the two arms of the printed capacitor. Being *microscopic*, this effect cannot be taken into account by the *macroscopic* model employed in the LPA to account for the interaction with the substrate. Thus, when substituting a substrate, changing its permittivity, one has to repeat the whole

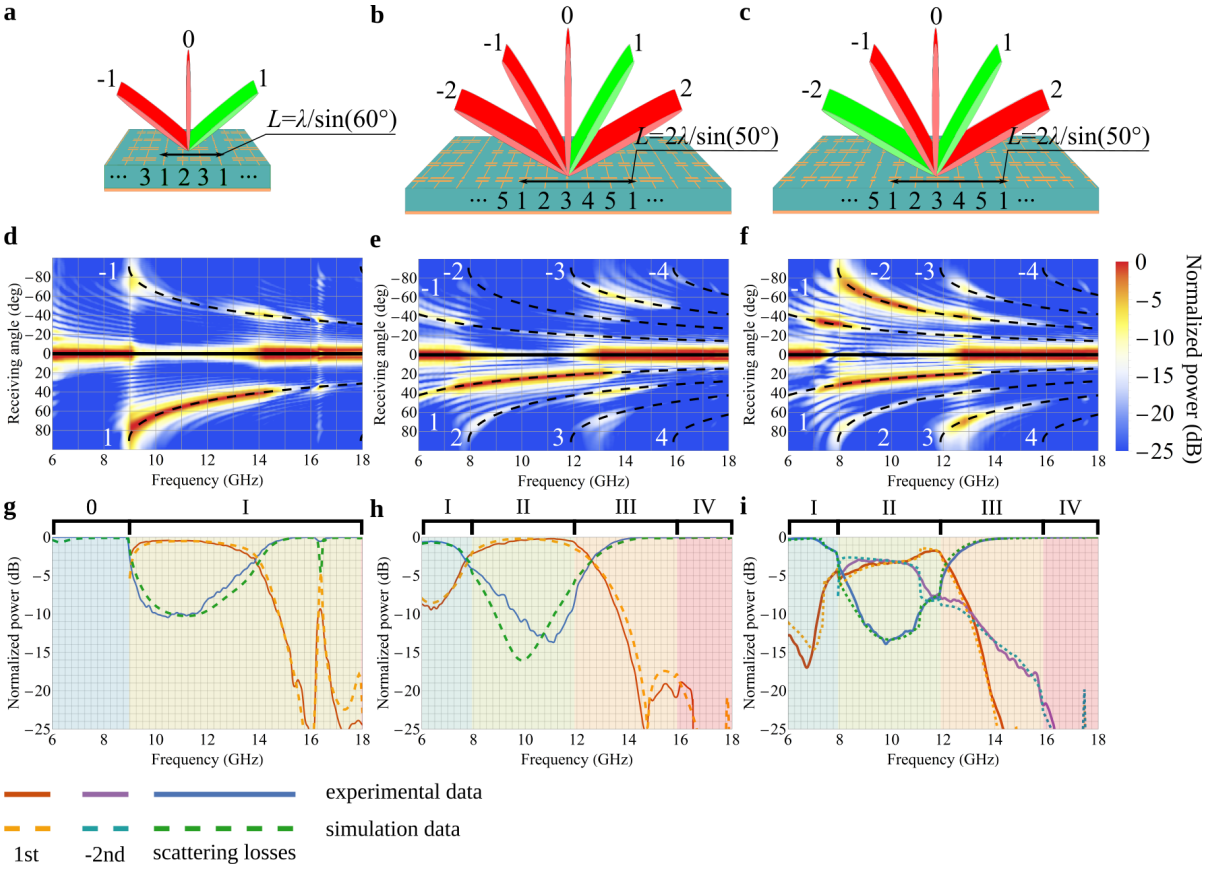

Figure 3.9: ***(a)–(c)*** *Schematics of prescribed diffraction patterns established by the three different designed metagratings with:* ***(a)*** *nonspecular reflection at an angle of* $60°$ *with* $N = 3$ *unit cells per period,* ***(b)*** *nonspecular reflection at an angle of* $23°$ *with* $N = 5$ *unit cells per period, and* ***(c)*** *equal excitation of the* -2^{nd} *and* $+1^{\text{st}}$ *orders out of five diffraction orders, respectively. The green and red beams correspond to excited and suppressed diffraction orders, respectively.* ***(d)–(f)*** *Measurement results of the scattered power in the [6 GHz – 18 GHz] frequency range.* ***(g)–(i)*** *Power management in the excited diffracting orders and scattering losses, the roman digits correspond to the highest propagating diffraction order in a given frequency range.*

design procedure from the beginning. The developed optimization procedure is brought to find arm's lengths of printed capacitors according to the prescribed diffraction patterns and the results of the design procedure are listed in Table 3.2. Photographs of the fabricated metagratings are displayed in Figs. 3.11(a)–(c) and their physical size is approximately 480 mm (y-direction) by 160 mm (x-direction).

The samples are tested by means of the same experimental setup as the one described in the Section 2.3. A schematic representation of the experimental setup is shown in Figs. 3.11(d) and (e). In the current experiments, the transmitter is fixed and the receiver moves with 1° step and the minimum angle between the transmitter and receiver for the scanning is 4°. In order to be able to measure the specular reflection, the transmitter is fixed at $\mp 2°$. Thus, the experiments are conducted in two steps: when the transmitter is fixed at $\mp 2°$, the receiver moves form $\pm 2°$ to $\pm 90°$.

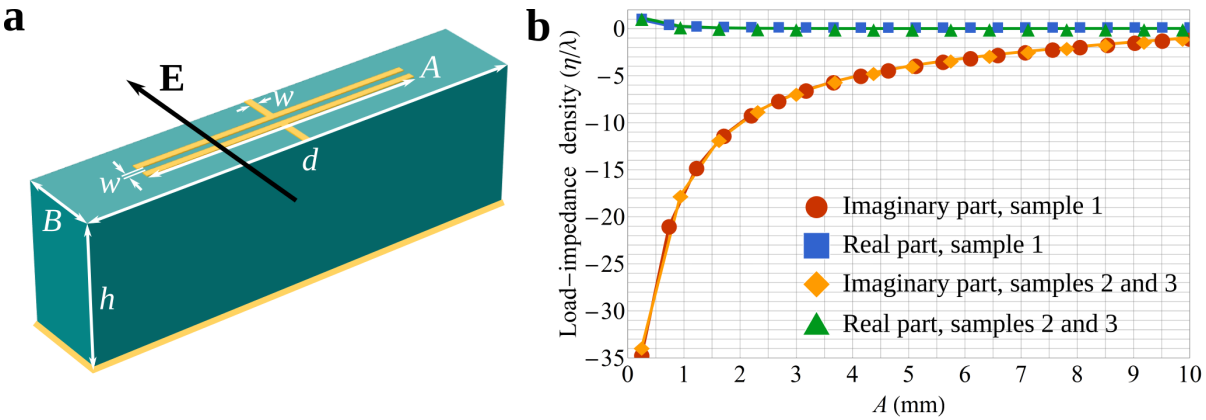

Figure 3.10: ***(a)*** *A schematic illustration of a capacitive unit cell: printed capacitor on top of a grounded dielectric substrate.* ***(b)*** *Load-impedance density of the printed capacitance extracted from specular reflection.* $d \approx 11.6$ *mm for the first sample and* $d \approx 15.7$ *mm in case of the second and third samples. Geometrical parameters are:* $w = 0.25$ *mm,* $B = 3$ *mm and* $h = 5$ *mm and operating frequency is set to* 10 *GHz. The corresponding input-impedance density is calculated as* $k\eta H_0^{(2)}[kw/4]/4$. *Thickness of the metallic cladding is* 35 μm.

Table 3.2: Found optimal load-impedance densities (left) and corresponding arm's lengths of printed capacitors (right) implemented in the fabricated metagratings. The indexes correspond to the numbered unit cells in Figs. 3.9(a)–(c).

Loads (η/λ)	Z_1	Z_2	Z_3	Z_4	Z_5	Arm's length (mm)	A_1	A_2	A_3	A_4	A_5
Sample 1	$-j30.3$	$-j6.35$	$-j1.57$	-	-	Sample 1	0.37	3.25	8.70	-	-
Sample 2	$-j3.77$	$-j0.43$	$-j31.2$	$-j7.06$	$-j5.27$	Sample 2	5.23	11.2	0.33	2.91	3.90
Sample 3	$-j3.75$	$-j4.84$	$j0.05$	$-j2.94$	$-j8.86$	Sample 3	5.25	4.22	12.3	6.28	2.27

Figures 3.9(d)–(f) present angle measurements of the scattered power in the frequency range spanning from 6 to 18 GHz. It is clearly observed that the positions of the main lobes (corresponding to diffraction orders) are in perfect agreement with the results given by the grating formula $\theta_m = \sin^{-1}(mc/(\nu L) + \sin[\theta_i])$ (represented by black dashed curves). Here, c is the speed of light in vacuum and ν is the frequency. In order to estimate the efficiency of the samples and be able to compare to 3D full-wave simulations of a supercell, I employ here the same method as in the Second Chapter, see Subsection 2.3.2. Figures 3.9(g)–(i) show the performance of the experimental samples (solid curves obtained by means of Eq. (2.18)) as function of the frequency, scattering losses represent the power scattered in undesired diffraction orders. The dashed curves demonstrate the results obtained from 3D full-wave simulations (a supercell with imposed periodic boundary conditions and excited by a periodic port). By comparing the solid and dashed curves, one can observe a good agreement between the experimental and simulation results.

Although the samples were designed to operate at a single frequency (10 GHz), it is seen that the scattering losses remain low in a wide range of frequencies. One of the most important factors affecting an operating frequency range is the frequency response of unit cells. Resonant

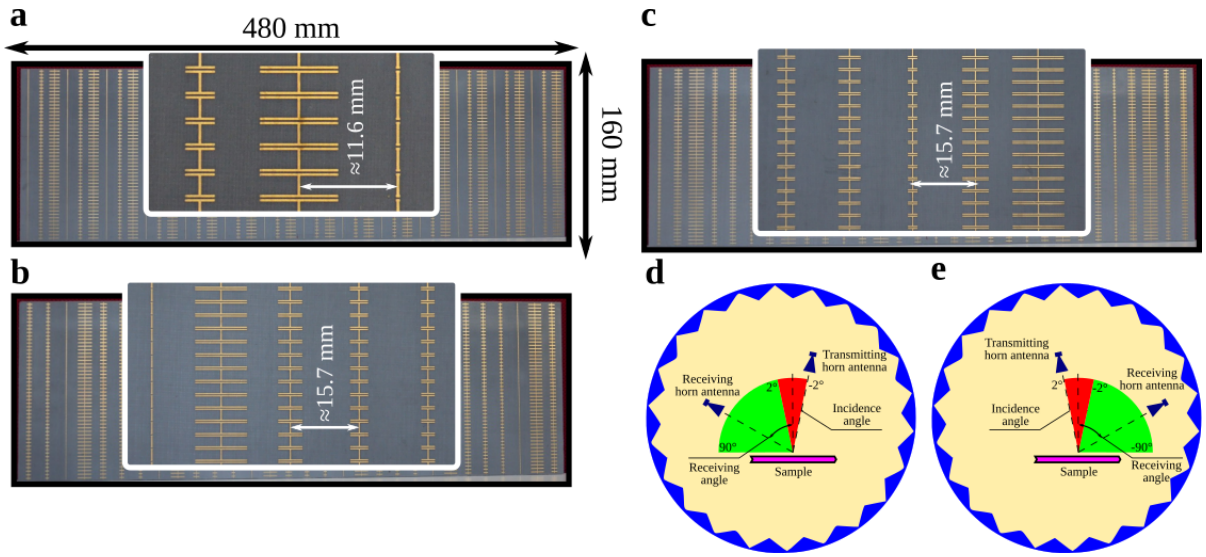

Figure 3.11: ***(a)***–***(c)*** *Photograph of the first, second and third samples (from top to bottom, respectively).* ***(d)***, ***(e)*** *Schematics of the experimental setup: to measure the scattering range of angles from* $-90°$ *to* $90°$ *the experiment is performed in the two steps illustrated by figures* ***(d)*** *and* ***(e)****.*

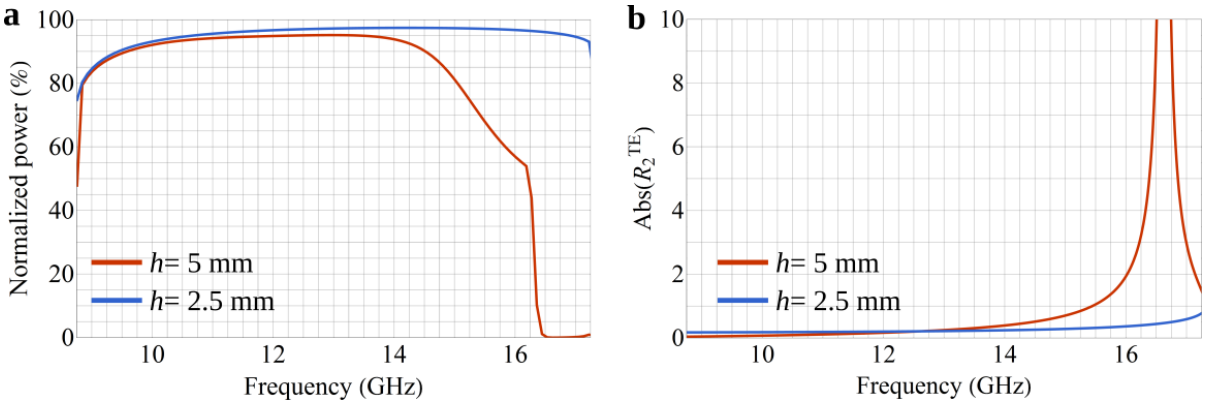

Figure 3.12: ***(a)*** *Computational results of the normalized power scattered by a reflective metagrating (having three reactive wires per period* $L = \lambda/\sin(60°)$*) in the* $+1^{\text{st}}$ *diffraction order vs. the frequency. Normally incident plane wave is assumed. Optimal reactive load-impedance densities are found at each frequency.* ***(b)*** *Absolute value of the Fresnel's reflection coefficient corresponding to the second (nonpropagating in the considered frequency range) diffraction order.*

elements, in a general manner, significantly decrease an operating frequency range as shown in the Sections 2.3 and 3.4. As demonstrated by Fig. 3.10(b), capacitively-loaded wires used to construct experimental samples do not exhibit resonances at 10 GHz. Since each metagrating was designed to handle a certain number of propagating diffraction orders, it is expected that the scattering losses increase when approaching frequencies where the number of propagating diffraction orders changes (corresponding to different areas in Figs. 3.9(g)–(i) labeled with roman digits). While it is the case for the second and third samples, the performance of the first one decreases far before the appearance of the second propagating diffraction orders, as shown in Fig. 3.9(g). It unveils yet another crucial factor influencing an operating frequency range: exci-

tation of waveguide modes discussed in the very beginning of Section 3.3. Although I managed to avoid waveguide modes around the design frequency of 10 GHz, they may appear at lower or higher frequencies and this is exactly what happens in the case of the first sample. Waveguide modes are eigenmodes of the grounded substrate and their eigenfrequencies correspond to poles of the Fresnel's reflection coefficients R_m^{TE}. At the eigenfrequency of a waveguide mode, the incident plane wave is not only specularly reflected from the grounded substrate, but it is also partially coupled to the waveguide mode. The excitation field $E_q^{(exc)}$ in Eq. (3.11) is no longer represented by the sum of the incident wave and its specular reflection from the grounded substrate. It should be modified to include the waveguide mode, which cannot be done within the framework of an infinite periodic structure. Indeed, an excited waveguide mode exponentially grows along the propagation direction (one can track the analogy with a receiving leaky-wave antenna) meaning that the phase factor $\exp(-jk\sin[\theta_i]L)$ providing the field evolution over a period of the structure along the y-direction will be modified as well. Specifically, the absolute value of the factor will be different from unit, which leads to the divergence of the field when $y \to +\infty$ or $y \to -\infty$. In the case of the first sample, a waveguide mode is excited at the frequency when the Fresnel's reflection coefficient R_2^{TE} diverges. It should be noted that in the considered frequency range, Fresnel's reflection coefficients corresponding to other nonpropagating diffraction orders are regular. In the experimental and simulation data, the waveguide mode manifests itself in the resonance observed around 16.4 GHz, as shown in Figs. 3.9(d) and (g). As demonstrated in Fig. 3.12, the excitation of the waveguide mode can be suppressed by choosing a thinner substrate (for e.g. 2.5 mm instead of 5 mm) which enables restoring the performance over the entire range of frequencies where there are three propagating diffraction orders (see blue curves in Fig. 3.12). Figure 3.12(a) presents the computational results of maximizing at each frequency the power of a normally incident plane wave coupled to the $+1^{\mathrm{st}}$ propagating diffraction order, where reactive impedance densities of three wires composing a period of a metagrating are assumed. Alternatively, eigenfrequencies and the number of waveguide modes in a given frequency range can be changed by adjusting the relative permittivity of the substrate or the period of the structure.

3.6. Conclusion

In this Chapter, I have presented a simulation-based design approach to construct metagratings in the "wire by wire" manner. It represents an analog of the local periodic approximation that has been used to design space modulated metasurfaces and in comparison to a brute force numerical optimization (that deals straight with a whole supercell of a metagrating), it can considerably reduce the time spent on the design. Indeed, let me assume that each wire constituting a N-wires period of a metagrating has only one parameter to be adjusted and this parameter takes in total P different values during a parametric sweep. Then, one would have to perform P^N 3D full-wave simulations in order to cover all possible combinations of parameters of wires and find optimal configuration of a metagrating's supercell [assuming no "smart" algorithms (like genetic) are employed]. Clearly, this number strongly depends on the number of wires constituting a supercell N. Meanwhile, the LPA deals with one unit cell at a time, which makes the number of required 3D full-wave simulations to be as small as P and it does not depend on the number N. As an example, I have validated the developed approach via 3D full-wave simulations by demonstrating designs of metagratings controlling diffraction patterns at microwave and infrared frequencies for both TE and TM polarizations. Both electric metagratings (TE polarization) required two different types of meta-atoms (capacitive and inductive) and overall I have performed $2P$ simulations, while the magnetic metagrating required a single type of a meta-atom and, thus, only P simulations. Finally, simple and accurate analytical model describing metagratings allows one to subtract the impact of the metal-backed dielectric substrate and the interaction between neighboring wires. It makes the developed local periodic approximation not only fast but also a rigorous approach to design metagratings represented by nonuniform arrays of wires, in bright contrast to metasurfaces. Importantly, the permittivity of the substrate may have a microscopic effect which cannot be accounted for in the analytical retrieval procedure. The analytical model of 1D metagratings is effective in the translation invariant direction and disregards related microscopic effects. For example, changing the permittivity may have an impact on strong field localization in metallic gaps, as in the case of printed capacitors, and lead to a change in the impedance density. However, there is no need to repeat 3D simulations, if one decides to modify the thickness of the substrate (not its permittivity) or the inter-wire distance.

To solve the inverse scattering problem and find an optimal number of wires per period in

each particular configuration, I have developed an optimization procedure on the basis of particle swarm optimization algorithm. As optimization parameters, the procedure uses geometrical parameters of meta-atoms related to retrieved impedance densities. Together with the analytical model of metagratings it allows one to solve the inverse scattering problem numerically but without involving 3D full-wave simulations of supercells, which makes the procedure fast. At the same time, one does not have to deal with mathematically complex Eq. (2.14) to determine the number of reactive wires per period necessary to set up a desired diffraction pattern. Instead, the number of wires is included in the list of optimization parameters, which, however, does not slow the optimization procedure significantly.

The design procedure in the form of the LPA and optimization procedure has been validated by means of both 3D full-wave simulations and experimentally. In both cases, the optimization procedure resulted in metagratings having, in a period, as few as one reactively-loaded wire per propagating diffraction order. The simulation results were obtained for both electric and magnetic metagratings operating at microwave and optical frequencies. Next, I have designed and tested three experimental samples able to establish prescribed diffraction patterns in a wide frequency range. The experimental results have demonstrated a good agreement with 3D full-wave simulations. Furthermore, I have identified the main factors affecting the operating frequency range of metagratings: frequency response of constituting wires, appearance of new propagating diffraction orders and excitation of waveguide modes.

Chapter 4

Conformal sparse metasurfaces

Contents

4.1. Introduction

A commonly accepted definition of a conformal array antenna is specified by the IEEE Standard Definition of Terms for Antennas (IEEE Std 145-2013 [165]) as follows:

conformal antenna [conformal array]: An antenna [an array] that conforms to a surface the shape of which is determined by considerations other than electromagnetic: for example, aerodynamic or hydrodynamic.

Indeed, a present-day airplane carries many antennas for navigation and communication systems. Integrating these antennas into its aerodynamic shape is highly desirable to avoid protruding parts. The same is true for high-speed trains and other vehicles. On the other hand, the emerging concepts of the IoT, smart homes and smart cities demand antenna integration in various household items and urban places to make the antenna less disturbing and more hidden for the human perception. Contrary to the IEEE definition, conformal antennas may have their shape determined for certain beam-forming specifications such as the shape of a beam and beam-steering angular range. As such, antennas composed of elements on the surface of a cylinder, sphere, or cone are also called conformal [166]. Finally, conformal array antennas do not only allow one to meet the aerodynamic specifications of aircrafts and satellites but also break the fundamental constraint of their planar counterparts. For instance, the aperture of a flat metasurface antenna vanishes when the beam steering angle increases [167].

The history of conformal arrays can be traced back to the investigation of circular arrays of dipoles [166] by H. Chireix in 1936 [168], H. L. Knudsen in 1936 [169] and the French RIAS radar system in th 1990s [170, 171]. A particular interest in circular arrays can be explained by their rotational symmetry which allows to perform 360° beam-steering relatively easy. Recently, metasurface have been proposed to transfer such benefits of reflectarray- and transmitarray-antenna configurations as a straightforward design procedure, simple feeding system and low-cost fabrication [101, 102, 107, 100]. Additionally, conformal metasurface can be used to improve performances of antenna radomes or even make them reconfigurable to facilitate beam-steering at large angles. As it is also discussed in the First Chapter, the design of a conformal metasurface is generally relies on a proper spatial distribution of the local reflection or transmission coefficient

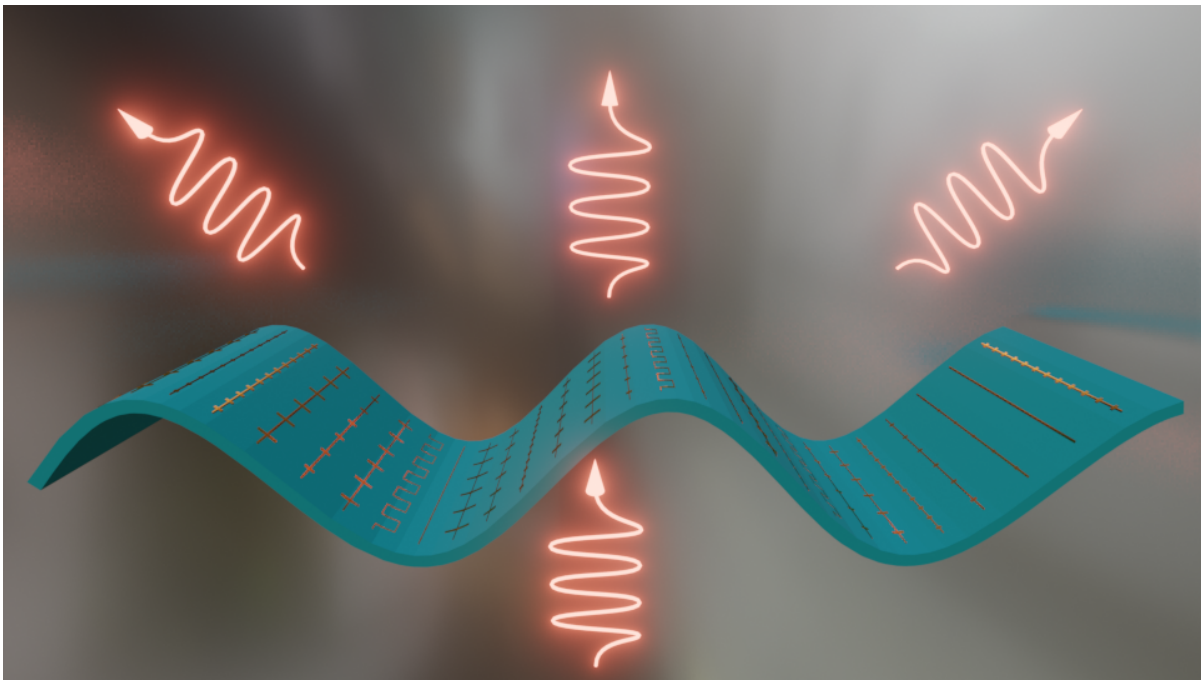

Figure 4.1: Illustration of an arbitrarily-shaped sparse metasurface transforming an arbitrary impinging wave into multiple beams.

established over the latter metasurface [100, 101, 102, 103, 104, 105, 106, 107]. A more rigorous analysis of conformal metasurfaces [109] utilizes generalized sheet transition conditions [108]. Unfortunately, this theoretical model deals with curvilinear coordinates and demands accurate analysis of the metasurface geometry, which makes the analysis exceptionally challenging. The design of conformal metasurface also involves analysis of the feeding source. In the reflectarray- and transmitarray-antenna configurations the simplest source is used: a horn antenna. It, however, makes the overall dimensions of an antenna system large. On the other hand, compact metasurface-based antennas were presented in Fabry-Perot cavity [98, 101, 172, 128, 173] and leaky-wave configurations [174, 175, 176, 113, 177, 130].

Although metagratings demonstrate an exceptional efficiency in controlling diffraction patterns, they are essentially periodic structures excited by a "periodic" illumination such as a plane wave. The periodicity makes the functionality of metagrating limited to control a discrete set of scattered plane waves. Furthermore, a plane-wave-like illumination assumes that in practice a feeding source is placed far from a metagrating that significantly reduces the feeding efficiency. In this Chapter, I elaborate on the analytical model of metagratings and show how numerical calculation of a Green's function can be employed to design conformal *sparse* metasurfaces capable of creating *arbitrary* radiation patterns for *arbitrary* external excitations. Conversely to metagratings, sparse metasurface are non-periodic structures. However, similarly

to metagratings, sparse metasurfaces have the inter-element distance of the order of the operating wavelength and can be described in terms of neither surface impedance nor local reflection and/or transmission coefficients being not subject to fundamental efficiency limitations as their "dense" counterparts [116, 118, 119, 126, 117]. At the same time, the sparseness allows to establish a *global* theoretical model and get a microscopic insight into the theoretical analysis of conformal metasurfaces. The proposed approach does not use any complex local coordinate system matched to a particular geometry such that *arbitrarily-shaped* metasurfaces can be considered without any accommodation. Finally, it is detailed how to realize these conformal sparse metasurfaces. To describe the design procedure, sparse metasurfaces of different geometries illuminated by an arbitrary complex wave configuration are demonstrated by means of 3D full-wave simulations and experimentally at microwave frequencies.

4.2. Theoretical concept

4.2.1 Inverse radiation problem

In order to introduce the concept, I consider the case of TE polarization and a 2D geometry. A translation symmetry is assumed along one of the three spatial dimensions. A sparse metasurface is composed of a *finite* set of N loaded wires distributed along the surface of an arbitrarily-shaped dielectric substrate, as illustrated in Fig. 4.1. The wires are oriented along the translation-invariant direction. Microscopically, a loaded wire represents itself as a chain of subwavelength meta-atoms. On the other hand, macroscopically, I model a loaded wire as uniform and having a deeply subwavelength effective radius r_0.

Electric field directed along x-axis of a background wave radiated by external sources excites polarization currents in the loaded wires. However, here I do not impose any condition on the external sources unlike plane wave excitation used for majority of metasurfaces presented in literature. The polarization currents I_q excited in the wires can shape the field radiated by a sparse metasurface in accordance with the following equation:

$$E_x(r,\varphi) = E_x^{(ext)}(r,\varphi) + \sum_{q=1}^{N} G_{xx}(r,\varphi;\mathbf{r}_q) I_q, \tag{4.1}$$

where r and φ are polar coordinates: radius and polar angle, respectively. The total field $E_x(r,\varphi)$ is represented by the superposition of the wave radiated by external sources $E_x^{(ext)}(r,\varphi)$

and waves $G(r, \varphi; \mathbf{r}_q)I_q$ scattered by the wires, with $G(r, \varphi; \mathbf{r}_q)$ being a Green's function corresponding to the q^{th} wire at $\mathbf{r}_q$. As the considered system does not have a translational symmetry in the 2D plane, a Green's function $G(r, \varphi; \mathbf{r}_q)$ is a function of the observation point $\mathbf{r}$ and the position of the wire $\mathbf{r}_q$ (not their difference). Importantly, $E_x^{(ext)}(\mathbf{r})$ and a Green's function should be calculated in the presence of the substrate and all other non-engineered elements of the sparse metasurface (such as for e.g., the substrate supporting external sources).

Sparse configuration of the metasurface allows one to accurately take into account the interactions between the wires via Ohm's law

$$Z_q I_q = E_x^{(ext)}(\mathbf{r}_q) - \sum_{p=1}^{N} Z_{qp}^{(m)} I_p. \tag{4.2}$$

A load-impedance density Z_q is a characteristic of a loaded wire and can be engineered for instance by tuning the geometrical parameters of meta-atoms constituting a wire. The right-hand side of Eq. (4.2) represents the total electric field at the position of the q^{th} wire, where

$$Z_{qp}^{(m)} = -G_{xx}(\mathbf{r}_q, \mathbf{r}_p) \tag{4.3}$$

is the mutual-impedance density (the electric field created by the p^{th} wire at the position of the q^{th} wire). The separation between two neighboring wires can be arbitrary as long as polarization currents in wires can be approximated by a 2D delta function. As it is demonstrated further, this simple model works surprisingly well even for complex designs. The self-action of the q^{th} wire and its interaction with a substrate and an environment is accounted via

$$Z_{qq}^{(m)} = -\frac{1}{2\pi r_0} \oint G_{xx}(\mathbf{r}; \mathbf{r}_q) \mathrm{d}\mathbf{r}, \tag{4.4}$$

where the integration is performed over the circumference of the wire of effective radius r_0. Although being very simple, Eq. (4.2) has an important practical implication: it allows one to know in advance the impact of one polarization current on another and to accordingly adjust the load-impedance densities. Conceptually, it means that the developed approach is *global*, being in strong contrast with theoretical models of phase gradient metasurfaces which are essentially local.

Meanwhile, by appropriately choosing Z_q and the number of wires N, one is able to construct desirable radiation patterns. Each term on the right-hand side of Eq. (4.1) at a given distance

r ($r \neq |\mathbf{r}_q|$ for all q) can be approximated by a partial Fourier sum over the polar angle φ:

$$E_x^{(ext)}(r,\varphi) = \sum_{n=-M}^{M} C_n^{(ext)} e^{in\varphi}, \quad G_{xx}(r,\varphi;\mathbf{r}_q) = \sum_{n=-M}^{M} C_n^{(q)} e^{in\varphi}. \tag{4.5}$$

M is the maximum Fourier harmonic defined as the minimum number M such that

$$|C_{\pm|M+r|}^{(ext,q)}|/\max|C_n^{(ext,q)}| \ll 1 \tag{4.6}$$

for all $r = 1, 2, \ldots$. The number M might affect many parameters (such as geometrical parameters and material properties of a sample, the distance r) but the most important one is the physical aperture $\max[|\mathbf{r}_q - \mathbf{r}_p|]$. The larger the aperture the greater is M. Evidently, the total electric field $E_x(r,\varphi)$ can also be represented by a partial Fourier sum $\sum_{n=-M}^{M} C_m e^{in\varphi}$ and the relation between the Fourier coefficients is as follows:

$$C_n = C_n^{(ext)} + \sum_{q=1}^{N} C_n^{(q)} I_q, \tag{4.7}$$

where $C_n^{(ext)}$ and $C_n^{(q)}$ are known. When a sparse metasurface is composed of at least $N = 2M+1$ loaded wires one can establish *arbitrary* azimuthal field distributions within the functional space of the $2M+1$ Fourier harmonics by adopting the Fourier coefficients C_n.

Corresponding load-impedance densities can be found from Eq. (4.2) after solving Eq. (4.7) with respect to I_q, which in this case has a single solution. Indeed, the matrix composed of coefficients $C_n^{(q)}$ is not degenerate since $G_{xx}(r,\varphi;\mathbf{r}_q)$ related to different points $\mathbf{r}_q$ are linearly independent. On the other hand, symmetries of the systems should be respected, e.g. a linear array of wires in vacuum radiates symmetrically and there is an additional constraint between the Fourier coefficients $C_n = C_{-n}$. As a matter of fact, there is no guarantee that analytically found Z_q would not require implementing active and/or lossy elements since $\Re[Z_q] \neq 0$ in a general case. In order to additionally deal with only reactive load-impedance densities $Z_q = i\Im[Z_q]$, one might need a number of wires $N \geq 2M+1$ for constructing *arbitrary* radiation patterns, as discussed in the Second Chapter. Essentially, the procedure described in this paragraph allows one to know in advance all possible configurations of the azimuthal field for a given geometry of metasurface and number of wires. It includes practical parameters such as beamwidth and side-lobes level.

To conclude this subsection, it should be noted that a crucial point of the above analysis is

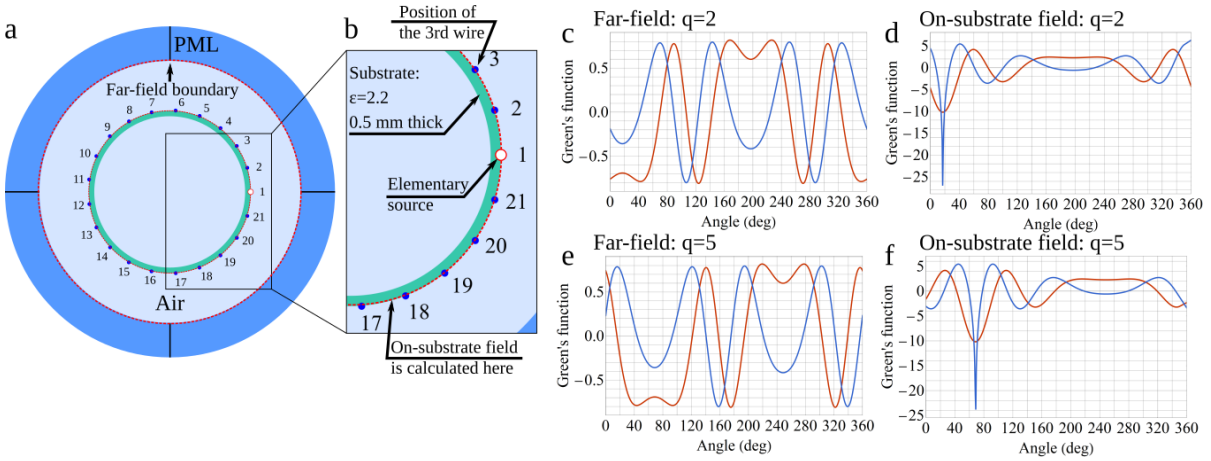

Figure 4.2: ***(a),(b)*** *Two-dimensional COMSOL simulation model: a cylindrical substrate of 50 mm radius is placed in the air region surrounded by a PML layer. The model is excited by an elementary source consequently placed at the positions of the wires. The elementary source is represented by a hollow disk of radius* $r_0 = 0.25/4$ *mm (its interior is excluded from the model) with applied at the red circe electric current density boundary condition* $1/(2\pi r_0)$ *A/m.* ***(c)–(f)*** *Green's function calculated in the far-field region* ***(c),(e)*** *and on the outer face of the substrate* ***(d),(f)*** *regions when the elementary source is at the position of the 2nd* ***(c),(d)*** *and the 5th* ***(e),(f)*** *wires.*

a Green's function which, being defined for an arbitrary finite-size system, does not have any applicable analytical form. Instead, I suggest to compute it numerically with the help of full-wave simulations. To that end, I built a 2D simulation model using the commercially available finite-element-method software COMSOL Multiphysics. Figures 4.2(a) and (b) demonstrate a schematics of the implemented simulation model used in the example shown in what follows. An elementary unit source is consequently placed at the different positions of loaded wires $\mathbf{r}_q$, $q = 1, 2, ..., N$. More precisely, this source is a *hollow* disk of radius r_0 with an electric surface current density used as a boundary condition and set equal to $1/(2\pi r_0)$ A/m. The electric field created by the source is recorded at each position along the substrate. There is no need to know a Green's function over the whole 2D plane but only at certain points. Namely, one extracts the electric field at the positions of the wires to construct the matrix of mutual-impedance densities $Z_{qp}^{(m)}$ and find input-impedance densities $Z_q^{(in)}$ and to control azimuthal wavefront at the distance r. In beam-forming applications, far-field calculations should be performed and the electric field in the far-field as a function of the azimuthal angle is recorded.

4.2.2 Numerical example via 2D simulation

Let me consider a simple example of a cylindrical sparse metasurface for far-field manipulation. The radius of the metasurface is fixed to $5\lambda_0/6$ (λ_0 is the vacuum operating wavelength) and it is excited by a point source placed in the center, creating a cylindrical background wave as

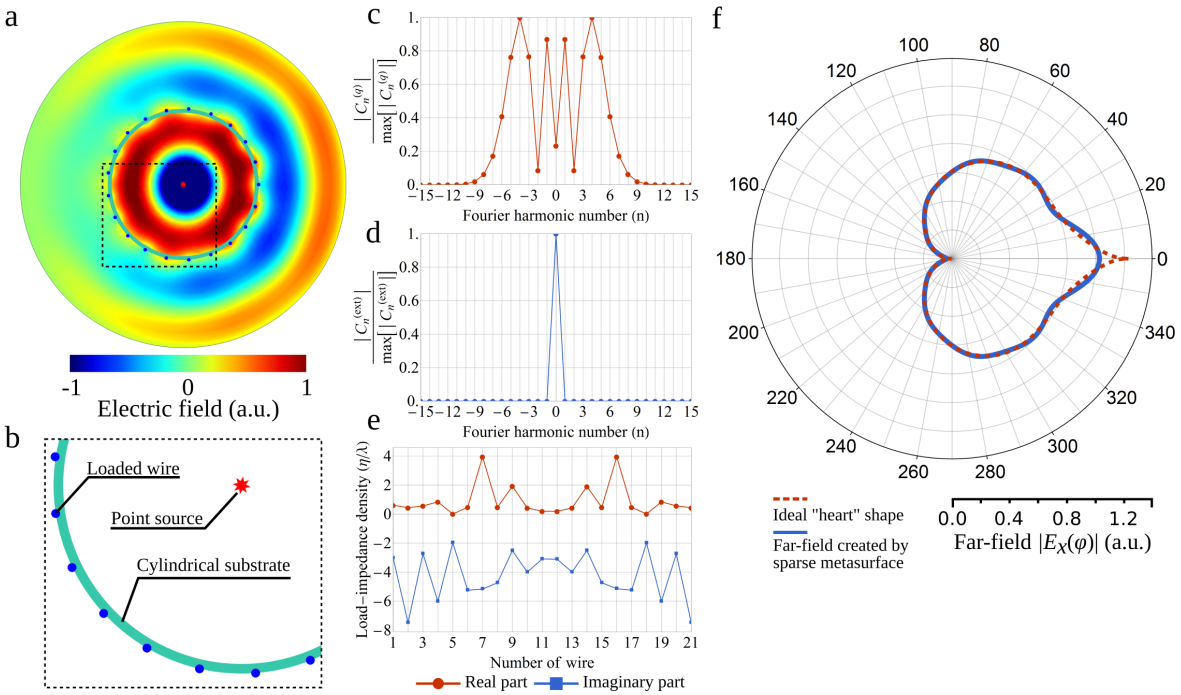

Figure 4.3: ***(a)*** *Profile of the electric field created by a cylindrical sparse metasurface. The metasurface is represented by* 21 *loaded wires uniformly distributed along a cylindrical substrate of thickness* $\lambda_0/120$ *and having the relative permittivity* 2.2*. The metasurface is excited by a point source placed in its center.* ***(b)*** *Zoom of a part of the sparse metasurface.* ***(c)*** $|C_n^{(q)}|/\max[|C_n^{(q)}|]$ ***(d)*** $|C_n^{(ext)}|/\max[|C_n^{(ext)}|]$ *vs. the number* n *of Fourier harmonic.* ***(e)*** *Load-impedance densities required to approximate the "heart" shaped far-field pattern.* ***(f)*** *Comparison of the far-field pattern created by the sparse metasurface (solid curve) and the ideal "heart" shape (dashed curve).*

illustrated in Figs. 4.3(a) and (b). Due to the symmetry, the Green's function $G_{xx}(r, \varphi; \mathbf{r}_q)$ corresponding to different positions of wires placed on the cylindrical substrate is simply shifted with respect to the angle φ. It means that in order to find the parameter M, one has to analyse the Fourier decomposition of the background wave and of the Green's function corresponding to a position of a single wire. Figures 4.2(a) and (b) demonstrate a schematics of the simulation model used to calculate the Green's function. The Green's function corresponding to the positions of the 2^{nd} and 5^{th} wires is shown in Figs. 4.2(c)-(f). Following the definition in Eq. (4.6), from Figs. 4.3(c) and (d), it can be seen that it is enough to have $N = 2 \times 10 + 1 = 21$ wires in order to be able to construct all possible far-field radiation patterns within the Fourier space of 21 harmonics $\exp[in\varphi]$. As an illustrative example, one can reconstruct in the far-field the shape of a "heart" after the required corresponding load-impedance densities are found from Eqs. (4.7) and (4.2). The desired far-field pattern is given by the following analytical function

$$E_{ff}(\varphi) = Ae^{j\theta}\left(\frac{\sin[\varphi]\sqrt{\cos[\varphi]}}{\sin[\varphi] + 7/5} - 2\sin[\varphi] + 2\right), \tag{4.8}$$

where A and θ were optimized to ensure $\mathrm{Re}[Z_q] \geq 0$ and equal 0.3 and 4.96 rad, respectively. The required load-impedance densities are plotted in Fig. 4.3(e) and correspond to passive elements ($\Re[Z_q] > 0$). The real part of Z_q can be engineered in a similar fashion as proposed in in Ref. [151]. Resulted far-field pattern is depicted in Fig. 4.3(f) and compared to the ideal shape of a "heart" defined by Eq. (4.8). Figure 4.3(a) shows the corresponding profile of the electric field in the proximity to the metasurface. In order to improve the accuracy of approximating some ideal curve, one needs to increase M which can be done by increasing the size of the metasurface (the radius in the considered case). Finally, it should be noted that, to best of my knowledge, there is no analytical formula for the Green's function of a system with a cylindrical substrate.

4.2.3 Optimization-aided design

After establishing the geometry of a sparse metasurface (flat, cylindrical, or any other shape), excitation type and positions of N wires, one calculates a Green's function $G_{xx}(r, \varphi; \mathbf{r}_q)$ and the background field $E_x^{(ext)}(r, \varphi)$ radiated by external sources. With Eqs. (4.1) and (4.2), a relation between the radiated field and load-impedance densities is established and the procedure related to Eq. (4.7) is used to find the number of wires and to determine possible functional characteristics of a sparse metasurface such as beamwidth and side-lobes level in beam-forming applications. It is important to note that the beam-forming represents only a subset of all possible far-field configurations when the power is maximized only in certain directions. Therefore, it might not be required to control all $2M+1$ of the Fourier harmonics and a lesser number of wires than $N = 2M + 1$ can be used for beam-forming. To solve the inverse scattering problem, the optimization procedure developed in Section 3.3 of the Third Chapter is used here with the only modification being the objective function. Indeed, Eqs. (4.1) and (4.2) represent substitutions of Eqs. (3.10) and (3.11). The discrete spectrum of propagating diffraction orders is substituted by the continuous function of the electric field which is discretized in the optimization procedure. The discretization is as fine as it is necessary to take into account all side lobes. The following objective function can be used to construct a single beam at the angle φ^* and minimize the level of side-lobes

$$f(G_q) = 20 \log_{10} \left[\frac{|E_{ff}(\varphi^*)|}{\max_\varphi |E_{ff}(\varphi)|} \right], \tag{4.9}$$

where $E_{ff}(\varphi)$ is the total electric field in the far-field region, the function max finds the maximum among discrete values of $E_{ff}(\varphi)$. The maximum of $|E_{ff}(\varphi)|^2$ is searched in all directions of a

discretized far-field pattern except from the range of angles corresponding to the desired beam. The optimization parameters are the geometrical parameters of meta-atoms composing the wires and the number of wires. Figure 3.3 shows a block diagram of the implemented particle swarm optimization.

4.3. Numerical examples via 3D simulations

In this section, I provide several examples of designs of conformal sparse metasurfaces operating in the microwave frequency range and demonstrating different beam-forming functionalities. The metasurfaces demonstrated in what follows represent a set of loaded wires uniformly distributed along the top face of a dielectric substrate (the bottom face is metal-free). Operating in the transmission mode, the metasurfaces transform an incident wavefront from one side into a desired wavefront on the other side. The designs are developed with the optimization-aided procedure and verified by means of 3D full-wave simulations. The impact of using different number of wires composing a sparse metasurface is analysed.

The design of loaded wires is performed within the local periodic approximation developed in the Third Chapter. The wires are built up from printed capacitors (left design of Fig. 4.4(a)) and inductors (right design of Fig. 4.4(a)), which provide a wide range of accessible load-impedance densities as shown in Figs. 4.4(b) and 4.5(a) for target 5 GHz and 10 GHz frequencies, respectively. A particular importance of the LPA should be emphasized: Sparse metasurfaces cannot be designed as their dense counterparts. In the design procedure it is important to retrieve the load-impedance density of a loaded wire which is its proper characteristic and depends on neither the substrate thickness nor the inter-wire distance, see Section 3.5. The developed local periodic approximation in this work allows one to do it.

It should be noted that the term corresponding to $Z_{qq}^{(m)}$ in Ohm's law (Eq. (4.2)) accounts for both the self-interaction and the interaction with a substrate and an environment, while in the LPA the mutual-impedance density subtracted on the right-hand side of Eq. (3.4) corresponds only to the interaction with a substrate and other wires in the uniform array. Therefore, Eq. (3.4) should be accordingly modified by subtracting from the right-hand side the self-interaction term which, luckily, can be accounted by a simple analytical expression $-k\eta H_0^{(2)}(kr_{eff})/4$. The final

expression of the equation allowing one to retrieve the *load*-impedance density is as follows

$$Z_q = \frac{E_0}{I} - \frac{k\eta}{4} H_0^{(2)}(kr_{eff}) - Z_m, \tag{4.10}$$

where Z_m is still given by Eq. (3.3). However, since transmitting metasurfaces are considered in this Chapter and, therefore, there is no a ground plane behind the dielectric substrate, one should modify as follows the expression for the Fresnel's reflection coefficient R_m^{TE} appearing in Eqs. (3.1), (3.3) and (3.4)

$$R_m^{\mathrm{TE}} = \frac{\frac{j}{2}\left(\frac{\beta_m}{\beta_m^s} - \frac{\beta_m^s}{\beta_m}\right)\tan(\beta_m^s h)}{1 + \frac{j}{2}\left(\frac{\beta_m}{\beta_m^s} + \frac{\beta_m^s}{\beta_m}\right)\tan(\beta_m^s h)}. \tag{4.11}$$

Here $\beta_m = \sqrt{k^2 - \xi_m^2}$ and $\beta_m^s = \sqrt{\varepsilon_s k^2 - \xi_m^2}$ are normal components of the wavevector of the m^{th} Floquet-Bloch mode outside and inside the substrate, respectively, $\xi_m = k\sin(\theta) + 2\pi m/d$ is the tangential component of the wavevector, d is the inter-wire distance and h is the thickness of the substrate.

4.3.1 Semi-cylindrical sparse metasurface

In the first example, I demonstrate a sparse metasurface operating at 5 GHz (vacuum wavelength $\lambda_0 \approx 60$ mm) and conformed to a semi-cylindrical shape of $1.67\lambda_0 = 100$ mm radius. $N = 29$ loaded wires are uniformly distributed along the top face of a $\lambda_0/120 = 0.5$ mm thick and $5.25\lambda_0 = 315$ mm long F4BM220 substrate and serve to control $2M + 1 = 29$ independent Fourier harmonics of the far-field as follows from Eqs. (4.6) and (4.7). The metasurface is illuminated by a point source put at $\lambda_0/4$ distance above a PEC wall joining the two ends of the semi-cylinder as shown in the inset of Fig. 4.4(c). In order to emulate the 2D configuration of the considered theoretical model, a narrow strip of the metasurface (of $\lambda_0/6$ width) is embedded in between two PEC plates which form a parallel-plate waveguide. The source is represented by a coaxial probe exciting the TEM waveguide mode. A schematics of the system is shown in Fig. 4.4(c).

Figures 4.4(d)–(f) demonstrate three different configurations of the far-field corresponding to three different designs of semi-cylindrical sparse metasurfaces. The directivity plotted in Figs. 4.4(d)–(f) is the two-dimensional directivity which is calculated as follows

$$D(\varphi) = 2\pi|E_{ff}(\varphi)|^2 \Big/ \int_0^{2\pi} |E_{ff}(\varphi)|^2 \mathrm{d}\varphi. \tag{4.12}$$

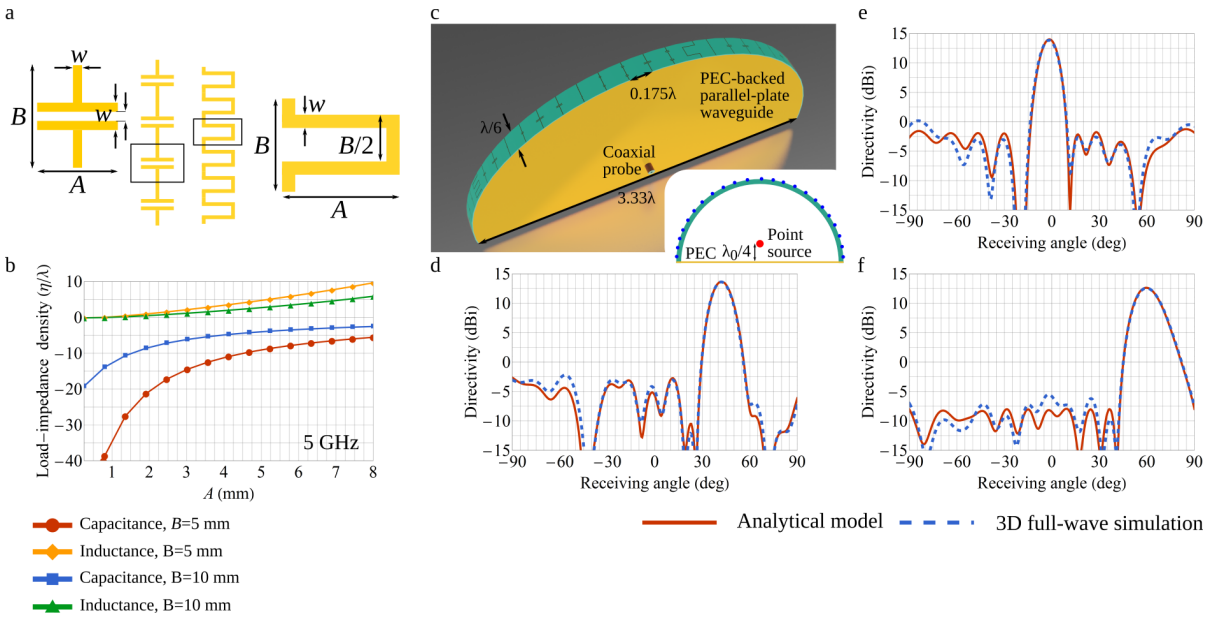

Figure 4.4: ***(a)*** *Schematics of a printed capacitance (left) and inductance (right), $w = 0.25$ mm ($r_0 = w/4$, see Ref. [149]).* ***(b)*** *Retrieved load-impedance densities (only imaginary parts are shown) of capacitively- and inductively-loaded wires at 5 GHz.* ***(c)*** *3D schematic of a semi-cylindrical sparse metasurfaces having 29 wires. The inset figure shows 2D schematic.* ***(d)–(f)*** *Two-dimensional directivity vs. angle of engineered radiation patterns. Predictions of the theoretical model (solid red curves) are compared to the results of 3D full-wave simulations of three different designs of sparse metasurfaces (dashed blue curves). The used substrate is F4BM220 of 0.5 mm thickness. Operating frequency is 5 GHz, $\lambda_0 \approx 60$ mm.*

The results of 3D simulations (dashed blue curves) are compared to the corresponding far-field patterns predicted by the analytical model in Eq. (4.1) (solid red curves). An almost perfect agreement is observed between the two. It proves a high accuracy of the established design procedure based on the LPA, even though a plane-wave excitation is used when retrieving the load-impedance density (Eq. (4.10)). Because of a very narrow, $\lambda_0/6$, aperture in the transverse direction, the radiation pattern presents a wide beam in the E-plane and therefore a 3D fan-shaped beam. However, if the distance between two PEC plates exceeds $\lambda_0/2$, higher order waveguide modes can be excited. It leads to a nonuniform field distribution along the x-direction which was assumed to be translation invariant. This problem can be overcome and a much narrower beam can be achieved in the E-plane by elaborating on the excitation source as discussed in the following Section.

4.3.2 Cavity-excited sparse metasurface

In the second example, I consider flat sparse metasurfaces placed on the top of an open rectangular PEC cavity excited by a coaxial probe. Results for two configurations with 10 and 20 wires are presented. For the given aperture size of $5\lambda_0$, the number $2M + 1$ of independent Fourier

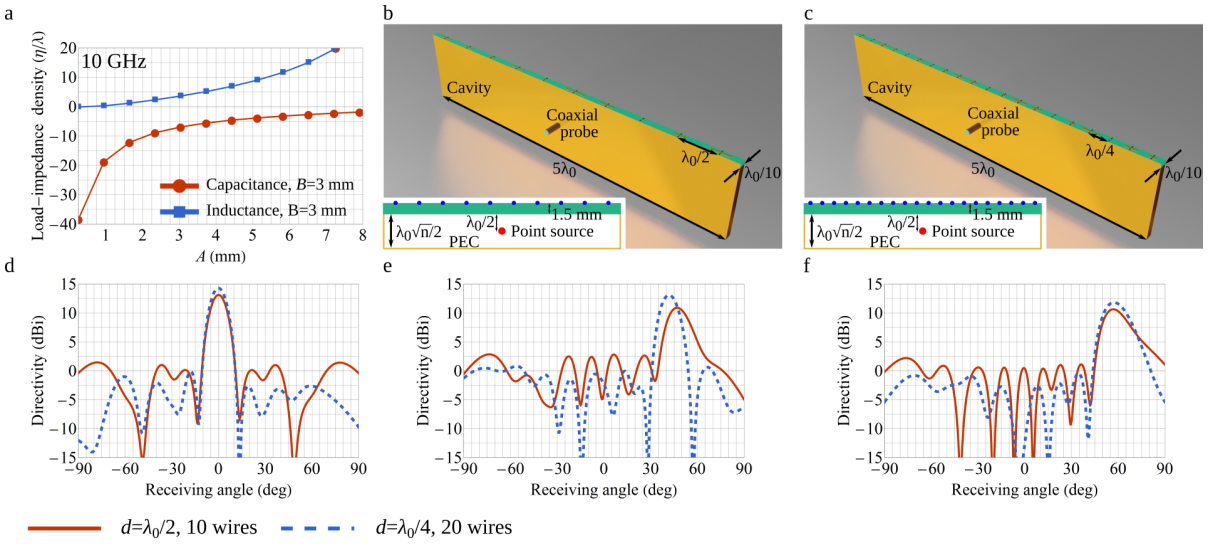

Figure 4.5: ***(a)*** *Retrieved load-impedance densities (only imaginary parts are shown) of capacitively- and inductively-loaded wires at 10 GHz, $w = 0.25$ mm. Schematics of the printed capacitor and inductor are shown in Fig. 4.4(a).* ***(b)***, ***(c)*** *3D schematics of cavity-excited flat sparse metasurfaces having* 10 ***(b)*** *and* 20 ***(c)*** *wires. The inset figures show 2D schematics of the corresponding configurations.* ***(d)***–***(f)*** *Two-dimensional directivity vs. angle of engineered radiation patterns corresponding to the results of 3D full-wave simulations of six different designs of sparse metasurfaces. Performances obtained with* 10 *wires and $\lambda_0/2$ inter-wire distance (solid red curves) are compared to the ones with* 20 *wires and $\lambda_0/4$ inter-wire distance (dashed blue curves). The used substrate is F4BM220 of* 1.5 *mm thickness, the cavity height is $\lambda_0\sqrt{n}/2 \approx 33.54$ mm, where n is the cavity length ($5\lambda_0$) divided over the wavelength λ_0. Operating frequency is* 10 *GHz, $\lambda_0 \approx 30$ mm.*

harmonics forming the far-field equals 42. While neither 10 nor 20 wires is enough to arbitrarily control 42 Fourier harmonics, it is possible to perform efficient beam-forming. Schematics of the configurations is shown in Figs. 4.5(b) and (c). Figures 4.5(d)–(f) demonstrate engineered radiation patterns obtained via 3D full-wave simulations and compare the performances of 10- and 20-element sparse metasurfaces. The comparison represents an important result: two times more wires lead to maximum of only 2 dBi improvement of the directivity. Therefore, one should carefully choose the number of wires as comparable performances can be achieved with a lesser effort what can be especially advantageous for reconfigurable designs. Fortunately, the presented analytical model allows one to optimize the number of elements by considering beforehand computed Green's function and without involving 3D full-wave simulations of real designs.

4.4. Experimental validation

For an experimental validation of the conformal antenna system, I designed three sparse metasurfaces using extremely thin ($\lambda_0/240 = 0.25$ mm) flexible substrates F4BM220, the pho-

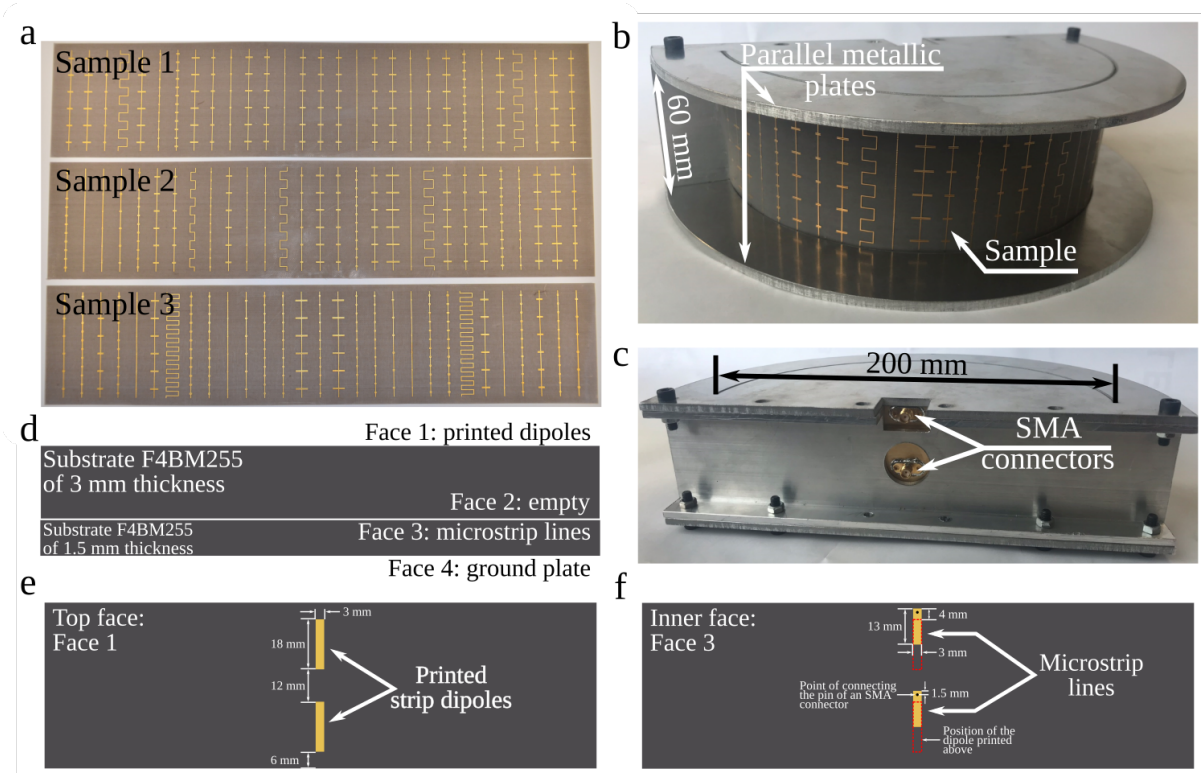

Figure 4.6: ***(a)*** *A photograph of fabricated sparse metasurfaces on a thin flexible substrate.* ***(b)***, ***(c)*** *Photographs of an assembled experimental prototype:* ***(b)*** *the front side and* ***(c)*** *the back side.* ***(d)*** *A schematic of the side view of a PCB of the excitation source.* ***(e)***, ***(f)*** *Schematics of the top face (e) and the inner face* ***(f)*** *of the PCB. The schematics contain all the information necessary to design the source used to excite the samples in the experiment. The design is performed following Ref. [178].*

tographs are shown in Fig. 4.6(a). The samples operating in the microwave frequency range with a central frequency fixed at 5 GHz were fabricated by means of conventional printed circuit board (PCB) technology. Each sample is composed of twenty nine wires equidistantly distributed along a $5.25\lambda_0 \approx 315$ mm long substrate, making the separation between two neighbouring wires approximately equal to $\lambda_0/5$. The ultra-thin samples are then conformed to create semi-cylindrical surfaces of 100 mm radius. A photograph of the assembled prototype is presented in Figs. 4.6(b) and (c). The external source exciting the samples is represented by two microstrip dipole antennas printed on a metal-backed substrate, whose design was performed following Ref. [178] and is detailed in Figs. 4.6(d)–(f). Each dipole is excited via an electromagnetically coupled microstrip line printed below it and fed by a coaxial probe.

The three samples are designed to show different beam-forming performances: a single broadside beam at 0°, a steered beam at 40° and a multibeam configuration with two beams at ±30° from broadside. The inverse scattering problem is solved by maximizing power in the desired direction and minimizing the side-lobes level (with respect to the geometrical parameters A and B of the loaded wires) radiated by the sparse metasurface in desired directions, and the maximiza-

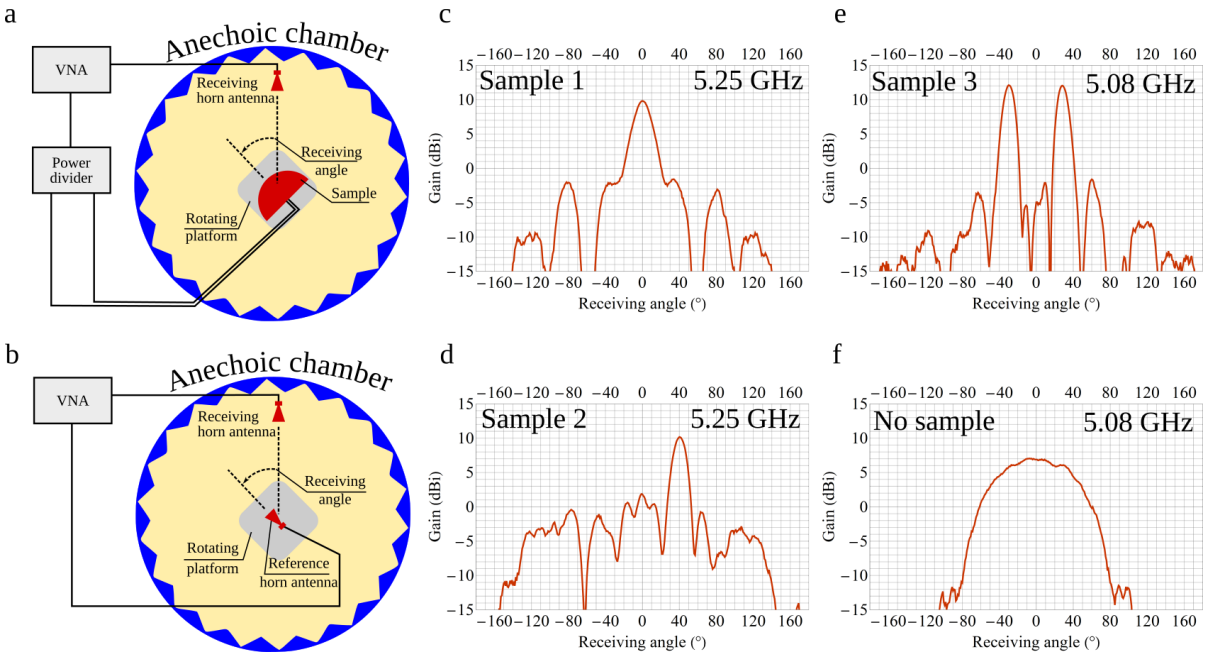

Figure 4.7: ***(a),(b)*** *Schematic illustration of the experimental setup used to measure the gain of the samples.* ***(c)–(f)*** *Measured gain of experimental samples:* ***(c)*** *Sample 1,* ***(d)*** *Sample 2,* ***(e)*** *Sample 3 and* ***(f)*** *the excitation source inside the parallel-plate waveguide when there is no any sample inserted.*

tion procedure is implemented as particle swarm optimization. The different configurations are experimentally validated by radiation patterns measurements performed in an anechoic chamber. A horn antenna used a receiver is kept fixed and the assembled prototype is mounted on a rotating platform as shown in Fig. 4.7(a). Figures 4.7(c)–(e) present experimentally measured gain for the three samples. The gain $G(\varphi)$ is found with the help of a reference horn antenna with known radiation characteristics by means of the following formula

$$G(\varphi) = G_{ref} + L_{PD} + P(\varphi) - \max_{\varphi}[P_{ref}(\varphi)], \tag{4.13}$$

where $G_{ref} = 11.8$ dBi is the gain of the reference horn antenna at 5 GHz provide by the manufacturer in the datasheet, $L_{PD} = 2$ dB is the measured insertion loss of the power divider, $P(\varphi)$ is the measured radiation pattern created by a sample and $P_{ref}(\varphi)$ is the measured radiation pattern of the reference horn antenna. Importantly, measured gain is 3D, in contrast to the 2D directivity calculated by means of Eq. (4.12) and plotted in Figs. 4.4 and 4.5. The level of spurious scattering (at operating frequencies) does not exceed -12 dB for the first sample, -9 dB for the second one and -13 dB for the third one. Figure 4.7(f) allows one to compare the radiations patterns created by the sparse metasurfaces to that of the excitation source alone.

Element number	Sample 1			Sample 2			Sample 3		
	Element type	B, mm	A, mm	Element type	B, mm	A, mm	Element type	B, mm	A, mm
1	capacitor	10	3,31	capacitor	10	2,58	capacitor	10	1,39
2	capacitor	10	4,78	capacitor	10	5,68	capacitor	5	1,04
3	capacitor	10	1,58	capacitor	10	4,46	capacitor	10	3,47
4	inductor	10	5,45	capacitor	5	1,06	capacitor	5	1,30
5	capacitor	10	4,81	capacitor	5	1,86	capacitor	10	0,53
6	capacitor	5	0,88	capacitor	10	4,46	capacitor	10	4,72
7	capacitor	5	1,99	capacitor	10	2,32	inductor	5	7,29
8	capacitor	10	4,73	capacitor	10	4,73	capacitor	5	1,53
9	capacitor	10	2,41	inductor	10	5,62	capacitor	5	1,18
10	capacitor	10	1,16	capacitor	5	0,45	capacitor	10	0,56
11	capacitor	10	4,31	capacitor	10	7,64	capacitor	10	1,33
12	capacitor	10	3,30	capacitor	10	3,85	capacitor	5	1,07
13	capacitor	10	0,60	capacitor	5	1,29	capacitor	5	1,04
14	capacitor	10	3,52	capacitor	10	2,78	capacitor	10	6,89
15	capacitor	10	3,42	capacitor	10	4,72	capacitor	5	0,97
16	capacitor	10	3,52	capacitor	10	1,64	capacitor	10	6,89
17	capacitor	10	0,60	inductor	10	4,20	capacitor	5	1,04
18	capacitor	10	3,30	capacitor	10	0,84	capacitor	5	1,07
19	capacitor	10	4,31	capacitor	10	0,74	capacitor	10	1,33
20	capacitor	10	1,16	capacitor	10	3,57	capacitor	10	0,56
21	capacitor	10	2,41	capacitor	5	0,82	capacitor	5	1,18
22	capacitor	10	4,73	inductor	10	3,00	capacitor	5	1,53
23	capacitor	5	1,99	capacitor	10	2,25	inductor	5	7,29
24	capacitor	5	0,88	capacitor	10	3,34	capacitor	10	4,72
25	capacitor	10	4,81	capacitor	5	1,29	capacitor	10	0,53
26	inductor	10	5,45	capacitor	10	1,41	capacitor	5	1,30
27	capacitor	10	1,58	capacitor	10	0,65	capacitor	10	3,47
28	capacitor	10	4,78	capacitor	10	0,35	capacitor	5	1,04
29	capacitor	10	3,31	capacitor	5	1,49	capacitor	10	1,39

Table 4.1: Geometrical parameters of the samples. Schematics of capacitor and inductor elements is illustrated in Fig. 4.4(a). The parameter w is the same for all elements and equals 0.25 *mm, the thickness of the copper cladding is* 35 μm.

4.5. Conclusion

In this Chapter, I have generalized the analytical model of metagratings to structures that I call sparse metasurfaces. The generalization is based on the knowledge of a Green's function of a considered metasurface configuration, i.e. its geometry and material parameters. Since the model suggests that arbitrary configurations can be considered, it has been proposed to calculate a Green's function for each particular configuration numerically with the help of full-wave simulations. On the basis of the analytical model in the form of Eqs. (4.1) and (4.2) and Fourier transformation (4.7), it has been demonstrated that arbitrary desired radiation patterns can be obtained with a sufficient number of wires found from Eq. (4.6). To validate this conclusion, 2D simulations have been performed to show that a cylindrical metasurface excited by a point source at its center can be used to create such an arbitrary radiation pattern as the shape of a "heart". Furthermore, a theoretical analysis of Eqs. (4.6) and (4.7) can be

used to approach problems of superdirectivity [179] and subdiffraction focusing [180]. It is important to note that the inverse radiation problem solved by means of Eq. (4.7) does not guarantee in a general case a solution in the form of reactive (or even passive) load-impedance densities of wires. To overcome this problem and to solve the inverse radiation problem for beam-forming applications, the analytical model of sparse metasurface has been accompanied by an optimization procedure, which represents a generalization of the one demonstrated in the Third Chapter. The design approach has been validated by 3D full-wave simulations and experimentally. Particularly, with the help of the optimization procedure, the impact of the number of wires on beam-steering efficiency has been studied. It has been demonstrated that when increasing the number of wires, the level of side lobes can be decreased. However, practical aspects (such as complexity, cost and etc.) of the final design of a sparse metasurface should be taken into account when selecting the number of wires. It can be particularly important for the design of a reconfigurable sparse metasurface. For the experimental validation three semi-cylindrical sparse metasurface have been designed to demonstrate different beam-forming functionalities: a single beam at the broadside, a single beam steered at 40° from the broadside and two beams at ±30° from the broadside. The experiments have been performed at microwave frequencies, but the theory is valid in any frequency range and may inspire research on novel applications of conformal metasurfaces at THz, optical and visible frequencies.

It is crucial to note that in the demonstrated simulation and experimental examples, the sparse metasurfaces are transmitting while possessing only electric response. On the other hand, conventional phase-gradient approach [1] to design transmitting metasurfaces demands implementing an *effective* magnetic response additionally to an electric one. An effective magnetic response can be conventionally engineered by considering multilayer design of metasurfaces [128, 117]. Both responses are necessary to achieve 2π-range phase response and be able to establish a required phase gradient along a metasurface [73]. A more rigorous approach is certainly based on engineering the electric and magnetic surface impedances [110, 116, 112, 109] and sometimes magneto-electric coupling [181, 117, 182], to manipulate wavefronts according to the electromagnetic equivalence principle [111, 110]. Following the theory presented in this study, realizing only electric response can be sufficient for an efficient control of wavefronts that might significantly simplify the design and fabrication of wavefront manipulation devices. Furthermore, one is able to overcome the fundamental efficiency constraint of conventional metasurfaces imposed by the conservation of normal power flow density [126, 143, 144].

To conclude, a method to consequently design conformal sparse metasurfaces without appealing to a complex theory has been demonstrated. The versatility of the approach allows one to consider different metasurface geometries and arbitrary excitation sources within the same framework. Interestingly, sparse metasurfaces implemented on flexible substrates can be also advantageous for realizing a reconfigurability mechanism based on mechanical deformations [104]. It can represent a fruitful approach to create an adaptive response without complicating a design with tunable elements (which also often bring additional ohmic losses) and bias networks.

Chapter 5

Strongly non-local reconfigurable sparse metasurfaces

Contents

5.1. Introduction

In the context of this PhD, I am interested in reconfigurable metasurface for radar applications. Following the review on state-of-the-art developments presented in the First Chapter, there are two major types of reconfigurable metasurfaces for wavefront manipulation: binary phase-state and continuous phase tuning metasurfaces. The operational principle of these metasurfaces is based on adjusting the local phase response of constituting meta-atoms in accordance with Eq. (1.1). Naturally, it is not an easy task to design a resonant meta-atom exhibiting 2π-phase response. Generally, single-layered transmissive configuration does not allow to achieve 2π phase shift and in most cases, several layers are used [73]. At microwave frequencies, PIN diodes and varactor diodes are usually implemented in meta-atoms for reconfigurability mechanism. While PIN diodes can offer only two different states (on and off), they have been widely used in digital meta-atoms to achieve binary phase states [35, 37, 39, 41, 42, 43, 44, 46, 48, 50, 52, 53, 54, 56]. Varactor diodes on their side provide a more flexible solution in achieving real-time reconfigurablity since the capacitance value can be modified continuously with a change in applied bias voltage. As such, dispersion compensation and dynamic functionality switching have been demonstrated in varactor-based metasurfaces [36, 45, 47, 49, 55, 122]. It should be noted that complicated designs of reconfigurable meta-atoms and ohmic losses inherent in electronic elements hold back the wide application of more advanced concepts of Huygens' [110, 116, 128] and bianisotropic metasurfaces [118, 117, 126] for reconfigurable metasurfaces. To the best of my knowledge, there are only a couple of studies that demonstrated experimentally reconfigurable Huygens' metasurfaces [36, 47].

While it can be advantageous to consider complex designs of reconfigurable meta-atoms, there are fundamental limitations on the performance of metasurfaces as a result of the local normal power flow conservation condition [116, 117, 118, 119]. Indeed, metasurfaces are theoretically considered as *continuous* surface impedances [108, 110, 112] and, being of deeply subwavelength thickness, they effectively realize an abrupt discontinuity of the electromagnetic field while forcing the equality between entering and leaving *local* power flows [116, 117]. In the case of an impenetrable (reflecting) metasurface, only the tangential component of power flow exists in its proximity [118]. A theoretical solution proposed to overcome this limitation suggests implementing a *strongly non-local* metasurface [126, 129, 144], which implies existence of a

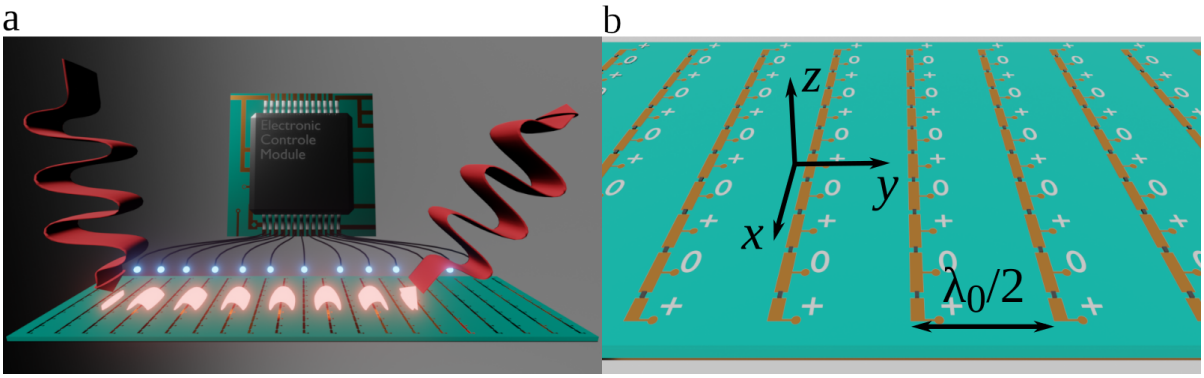

Figure 5.1: ***(a)*** *An illustration of a strongly non-local reconfigurable sparse metasurface converting a normally incident wave into an anomalously reflected wave via an excited surface wave. The surface wave propagates long the metasurface and manifests its strongly non-local response. The electronic control module represents a multichannel DC voltage source run by a Raspbery Pi nano-computer.* ***(b)*** *A close-up of a region of the sparse metasurface.*

substantial interaction between distant parts of the metasurface via surface waves propagating along it. So far, strong non-locality has never been implemented in conventional reconfigurable metasurfaces, making therefore their efficiency suffer from dissipation of energy in parasitic directions.

In this Chapter, I employ the analytical model of sparse metasurfaces presented in the Fourth Chapter to design a planar reconfigurable sparse metasurface operating in the reflectarray configuration and capable of controlling both far-field and near-field radiations. Theoretical efficiency of such a sparse metasurface in beam-steering application is compared to that of conventional gradient metasurfaces. After that, I design an electronically reconfigurable unit cell following the approach of the Third Chapter and experimentally characterize the fabricated sparse metasurface. Finally, I demonstrate experimentally the control of far-field radiation patterns and near-field focusing. The developed approach represents a radically new paradigm to dynamically manipulate electromagnetic wavefronts and allows me to experimentally demonstrate extreme examples of far-field and near-field functionalities such as beam-steering, multi-beam manipulation and subdiffraction focusing. The analysis of performances of the sample reveals indirect and direct evidences of its strongly non-local behavior.

5.2. Theoretical model

A sparse metasurface cannot be described in terms of local reflection and/or transmission coefficients and continuous surface impedances. Specifically, here we deal with a reflective sparse metasurface represented by a *finite* array of N loaded wires placed on top of a metal-backed

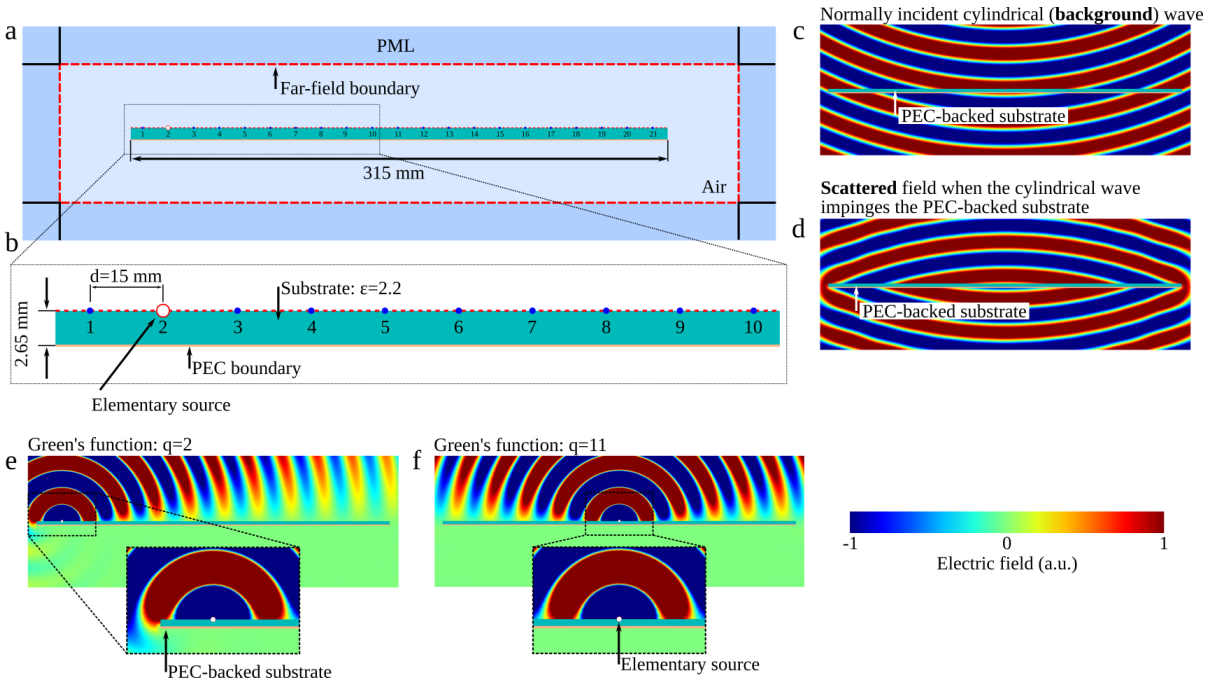

Figure 5.2: ***(a)***, ***(b)*** *Schematic of the simulation model (COMSOL Multiphysics) used to calculate Green's function. The model is represented by four principal parts: (i) PEC-backed dielectric substrate, (ii) an elementary source at the position of the* q^{th} *wire, (iii) the substrate is placed in an air region, (iv) PML layer of* λ_0*-thickness surrounds the air region. PEC and PML stand for perfect electric conductor and perfectly matched layer, respectively. The elementary source is represented by a hollow disk with surface current density* $1/(2\pi r_0)$ *A/m applied as a boundary condition (red circle),* r_0 *is the radius of the disc equal* 0.25/4 *mm in my simulations.* ***(c)***–***(f)*** *Simulated distributions of the electric field. The panel* ***(c)*** *shows the normally incident cylindrical (background) wave with the phase center* 35 *cm away from the substrate. The panel* ***(d)*** *shows the scattered wave when the cylindrical wave impinges the PEC-backed dielectric substrate. The panels* ***(e)*** *and* ***(f)*** *show the electric field created by the elementary source at the positions of the* 2^{nd} ***(e)*** *and* 11^{th} ***(f)*** *wires.*

dielectric substrate, as presented in Fig. 5.1(a). From the microscopic perspective, a loaded wire is built up of subwavelength meta-atoms arranged in a line, as schematically shown in Figure 5.1(b). Such system can be studied theoretically in accordance with the approach presented in the Fourth Chapter. Structured wires can be accurately approximated and modeled as uniform and having a deeply subwavelength effective radius r_0. The electric field of an incident wave polarized along the x-direction excites polarization currents in the loaded wires. The incident wave can be arbitrary and not only a plane wave. Each current I_q radiates the electric field $G_q(y,z)I_q$, with $G_q(y,z)$ being the Green's function corresponding to the q^{th} wire at y_q ($z_q = 0$). Then, the total scattered field $E_x(y,z)$ is a superposition (4.1) of waves re-radiated by the wires and the incident wave reflected in the specular manner from the substrate $E_x^{(r)}(y,z)$

$$E_x(y,z) = E_x^{(r)}(y,z) + \sum_{q=1}^{N} G_q(y,z)I_q. \tag{5.1}$$

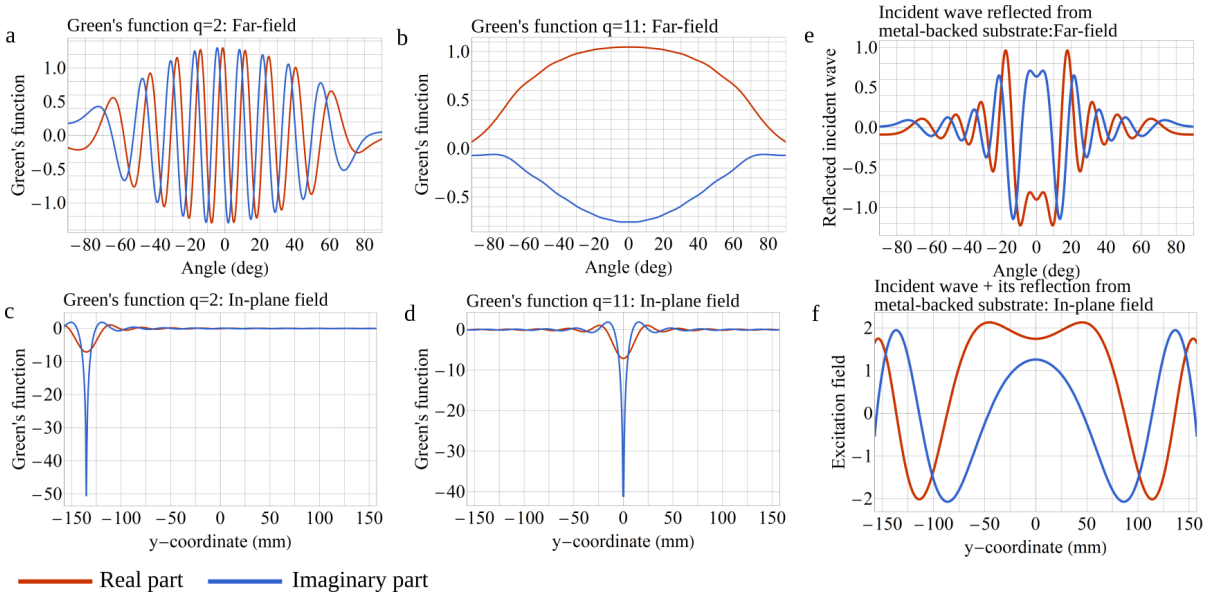

Figure 5.3: ***(a)–(d)*** *Examples of the Green's function calculated for the positions of 2nd and 11th wires in the far-field* ***(a)***, ***(b)*** *and in the plane of wires* ***(c)***, ***(d)***. ***(e)*** *The normally incident cylindrical wave reflected from the PEC-backed dielectric substrate in the far-field.* ***(f)*** *The excitation field (incident wave plus its reflection from the PEC-backed substrate) in the plane of wires.*

The scattering pattern is determined by values of the currents. Meanwhile, each current I_q is related via Ohm's law (4.2) to a load-impedance density Z_q of the corresponding wire and the total electric field induced at its position

$$Z_q I_q = E_x^{(exc)}(y_q, 0) - \sum_{p=1}^{N} Z_{qp}^{(m)} I_p, \tag{5.2}$$

with mutual-impedance densities being

$$Z_{qp}^{(m)} = -G_p(y_q, 0), \quad Z_{qq}^{(m)} = -\frac{1}{2\pi r_0} \oint G_q(y, z) \mathrm{d}l, \tag{5.3}$$

the integration is performed over the circumference of the q^{th} elementary source. Desirable scattering patterns can then be tailored by judiciously choosing Z_q and engineering the meta-atoms composing a wire. For instance, the inverse scattering problem can be solved by maximizing power scattered by the metasurface in desirable directions in the far-field or spots in the near-field focusing with respect to load-impedance densities. The maximization procedure is implemented as particle swarm optimization as detailed in the Third and Fourth Chapters.

Since this study deals with a complex *finite-size* system, there is not an applicable analytical formula for a Green's function. Following the results of the Fourth Chapter, I built a 2D simulation model using a commercially available FEM-based software, COMSOL Multiphysics,

to calculate Green's functions. The model is represented by a finite-size grounded dielectric substrate placed in free space. An elementary source is consequently placed at the positions of loaded wires, i.e. $y_q = qd$ ($q = 1, 2, ..., N$, $z_q = 0$). The schematic of the model is shown in Fig. 5.2, where a detailed description of the elementary source is also given in the caption. Since there is no need to know the Green's function over the whole 2D plane, we extract the electric field created by the source only at certain locations: (i) at the top of the dielectric substrate to construct the matrix of mutual-impedance densities $Z_{qp}^{(m)}$, (ii) in the far-field to show beam-forming performances, and (iii) in the desired focal plane to perform near-field focusing. Typical plots of the Green's function corresponding to different positions of wires are shown in Fig. 5.3. See also Fig. 5.2(e) and (f) for snapshots of the electric field created by the elementary source.

Additionally to the Green's function, one needs to know the incident wave reflected from the metal-backed dielectric substrate (in the absence of wires). The incident wave is created by an excitation source and is assumed to be given. In this work, the excitation source is a horn antenna with the phase center being 35 cm away from the sample. I approximate the incident wave by a cylindrical wave with its origin at the phase center of the horn antenna (Fig. 5.2(c)). Figure 5.3(e) shows the angular dependence of the incident wave reflected in the far-field (see also Fig. 5.2(d)). The incident wave plus its reflection from the metal-backed substrate constitute the excitation electric field, Fig. 5.3(f), which induces polarization currents in the wires.

5.3. Comparison to gradient metasurfaces

In order to estimate the efficiency of a sparse metasurface in comparison to a densely-packed traditional gradient metasurface based on the control of the local reflection coefficient, let me proceed by considering several examples of beam-steering at different angles. A sparse metasurface is represented by N reactively-loaded wires equidistantly distributed along the top surface of a PEC-backed dielectric substrate and the distance between two neighboring wires is d. Two cases are considered when $N = 21$, $d = \lambda_0/2$ and $N = 42$, $d = \lambda_0/4$. In these examples demonstrated by means of 2D full-wave simulations, the wires are modeled as hollow cylinders of radius r_0 with an electric surface current density boundary condition $E_x(y, z)/(2\pi r_0)/Z_q$, $\mathrm{Re}[Z_q] = 0$.

A gradient metasurface is represented by an electric sheet with the surface impedance $Z_{gr}(y)$ on top of a PEC-backed dielectric substrate and also modeled as an electric surface current

density boundary condition $E_x(y,z)/Z_{gr}(y)$. I consider two main types of gradient metasurfaces which implement control of only the phase or both the phase and the amplitude of the local reflection coefficient. In the first case, the surface impedance $Z_{gr}(y)$ is purely imaginary and calculated as follows [119] for the anomalous reflection at angle θ

$$Z_{gr}(y) = j\eta\left(\tan\left[\frac{\phi(y)}{2}\right] - \frac{\cot\left[\right]k_0\sqrt{\varepsilon_s}h]}{\sqrt{\varepsilon_s}}\right)^{-1}, \quad \phi(y) = k_0\left(\sqrt{D^2+y^2} - y\sin[\theta]\right). \tag{5.4}$$

In the second case, $\mathrm{Re}[Z_{gr}]$ can be greater than zero meaning that the local absorption can be adjusted in order to improve the scattering efficiency of a gradient metasurface. The surface impedance is found from the local reflection coefficient $R(y)$ as follows [119]

$$Z_{gr}(y) = \eta\left(\frac{1-R(y)}{1+R(y)} + j\frac{\cot\left(k_0\sqrt{\varepsilon_s}h\right)}{\sqrt{\varepsilon_s}}\right)^{-1}. \tag{5.5}$$

In its turn, the reflection coefficient is found from the ansatz of the incident (i) and the reflected (r) waves

$$R(y) = -1 + \frac{2\left(E_x^{(i)}(y,0) + E_x^{(r)}(y,0)\right)}{E_x^{(i)}(y,0) + E_x^{(r)}(y,0) + \eta\left(H_y^{(i)}(y,0) + H_y^{(r)}(y,0)\right)}. \tag{5.6}$$

The incident wave is a cylindrical wave with the center at $y=0, z=D$ and the reflected wave is a plane wave propagating at the angle θ from the broadside

$$\begin{aligned}
E_x^{(i)}(y,z) &= H_0^{(2)}[k_0\sqrt{y^2+(z-D)^2}],\\
H_y^{(i)}(y,z) &= \frac{j\,(z-D)}{\sqrt{y^2+(z-D)^2}}H_1^{(2)}[k_0\sqrt{y^2+(z-D)^2}],\\
E_x^{(r)}(y,z) &= Ae^{-jk_0(\sin[\theta]y+\cos[\theta]z)}, \quad H_y^{(r)}(y,z) = -\frac{A\cos[\theta]}{\eta}e^{-jk_0(\sin[\theta]y+\cos[\theta]z)}.
\end{aligned} \tag{5.7}$$

The amplitude of the plane wave A is chosen to ensure $|R(y)| \leq 1$ along the metasurface.

In simulations, the operating frequency is set to be 10 GHz ($\lambda_0 \approx 30$ mm). The excitation is set as a TE-polarized cylindrical wave incident at 0° (normal incidence) and having the phase center $D = 35$ cm away from the center of the metasurfaces. Figure 5.5 demonstrates results of beam-steering from 10° to 70° obtained with sparse and gradient metasurfaces. It is seen that a gradient metasurface controlling only the phase of the local reflection coefficient shows an increase in the level of side lobes when the steering angle increases. The −10 dB level of side lobes is achieved around 60° of the steering angle and quickly increases when going beyond this angle (compare blue dashed curves in Figs. 5.5(e) and (f)). When the amplitude of the local

reflection coefficient can be adjusted additionally to the phase, the level of side lobes remains low independently of the steering angle while the power in the main lobe constantly decreases because of the increasing absorption. Figures 5.5(c)–(f) demonstrate how the level of the main lobe lowers from -1 dB in the panel (c) to -4 dB in the panels (e) and (f). On the other hand, a sparse metasurface allows one to keep simultaneously low level of side lobes and high power in the main lobe independently on the steering angle. Furthermore, in strong contrast with a densely-packed gradient metasurface the inter-element distance in a sparse metasurface is as large as $\lambda_0/2$ and can be decreased to $\lambda_0/4$ when large steering angles are desired.

A key feature of a sparse metasurface, allowing one to outperform a gradient metasurface at large angles of anomalous reflection, is its strong non-locality. To better illustrate this mechanism, let me consider yet another example of extreme anomalous reflection at -65° when the cylindrical incident wave is at 45° as shown in the inset of Fig. 5.6(a). Such a configuration makes the separation between the specular reflection and the anomalously reflected wave equal to 110°. Figure 5.6(a) compares the radiation patterns created by a sparse metasurface with the $\lambda_0/2$ inter-wire distance (red solid curve) and gradient metasurfaces (blue dashed and green dot-dashed curves). The gradient metasurface implementing control of the phase of the local reflection coefficient (blue dashed curve) exhibits strong spurious scattering in the far-field which makes the power scattered in the desired direction twice less than in case of the sparse metasurface. On the other hand, introducing local absorption to reduce the level of side lobes (green dot-dashed curve) even further reduces the power in the main beam. To expose a strongly non-local response, I extract the scattered near-field at the distance $\lambda_0/10$ above the metasurfaces and perform discrete Fourier transform [183]. More precisely, the spectrum of the near-field is calculated as follows

$$e_m(z) = \frac{1}{P}\sum_{n=1}^{P} E_x^{(sct)}(y_n, z)\exp\left[j\frac{2\pi y_n m}{L}\right], \tag{5.8}$$

where $E_x^{(sct)}(y_n, z)$ is the complex amplitude of the scattered electric field recorded at the coordinate y_n and at the distance z from a metasurface, $e_m(z)$ is the m^{th} Fourier coefficient, P is the total number of measured points, $m = \frac{-P-1}{2}, \ldots, \frac{P+1}{2}$ and L is the length of the scanning area which coincides with the size of a metasurface. From Eq. (5.8), the tangential component of the wavevector can be defined as $k_y = 2\pi m/L$. Then, the normalized tangential wavevector is $k_y/k_0 = m\lambda_0/L$. The plot of the near-field spectrum demonstrated in the Fig. 5.6(e) shows the dependence of $\left|\frac{e_m(\lambda_0/10)}{\max[e_m(\lambda_0/10)]}\right|^2$ from the normalized tangential wavevector $m\lambda_0/L$. The vis-

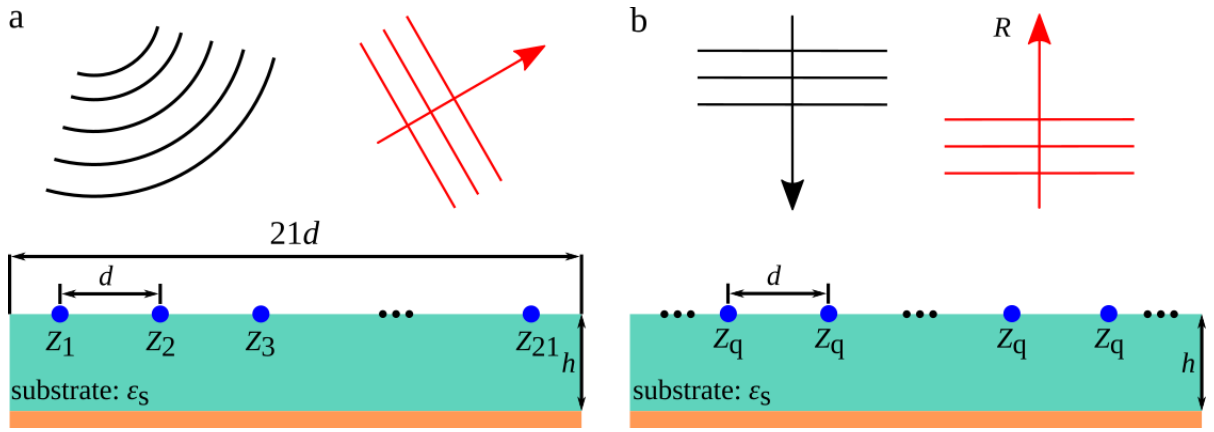

Figure 5.4: ***(a)*** *A sparse metasurface demonstrating an anomalous reflection when being illuminated by a cylindrical wave. The sparse metasurface is represented by a* ***finite*** *array of wires having different load-impedance densities Z_q.* ***(b)*** *A periodic array of wires having all the same load-impedance density Z_q. The array is illuminated by a normally incident plane wave and the reflection coefficient R is calculated by means of Eqs.* (3.1) *and* (3.4).

ible spectrum corresponds to the range of k_y/k_0 from -1 to 1. The waves outside the visible range correspond to evanescent surface waves decaying with distance from a metasurface. A strong peak manifesting a surface wave is present in the near-field spectrum corresponding to the sparse metasurface as highlighted by the red trace in Fig. 5.6(e). Although the interaction between elements of the sparse metasurface decreases with distance and well localized, as shown in Fig. 5.6(f), the surface wave propagates along the whole metasurface, representing a collective effect. Conversely, the spectra of the scattered near-field above the gradient metasurfaces (blue and green dots in Fig. 5.6(e)) do not exhibit any signature of surface waves.

The radiation patterns created by the gradient metasurfaces and shown in Fig. 5.6(a) correspond to the spatial profiles of the amplitude and the phase of the local reflection coefficient depicted in Figs. 5.6(b)–(d). In order to highlight the fact that one cannot apply the approach based on controlling the local reflection coefficient to design a sparse metasurface, in Figs. 5.6(b)–(d) there are also red points corresponding to the amplitude and the phase of the *fictitious* local reflection coefficient established along the sparse metasurface. While the meaning of the local reflection coefficient is clear in the case of a phase-gradient metasurface, it might not be that obvious for a sparse metasurface. Indeed, a sparse metasurface cannot be homogenized and, thus, it cannot be described in terms of a continuous local reflection coefficient. To demonstrate the example of Fig. 5.6(a), optimal load-impedance densities of wires constituting a sparse metasurface are found by assuming and following the procedure described in the previous section. After that, the reflection coefficient from a corresponding periodic array of loaded wires is calculated analytically by means of Eqs. (3.1) and (3.4) assuming that Z_q is known. Figure 5.4 outlines

this procedure.

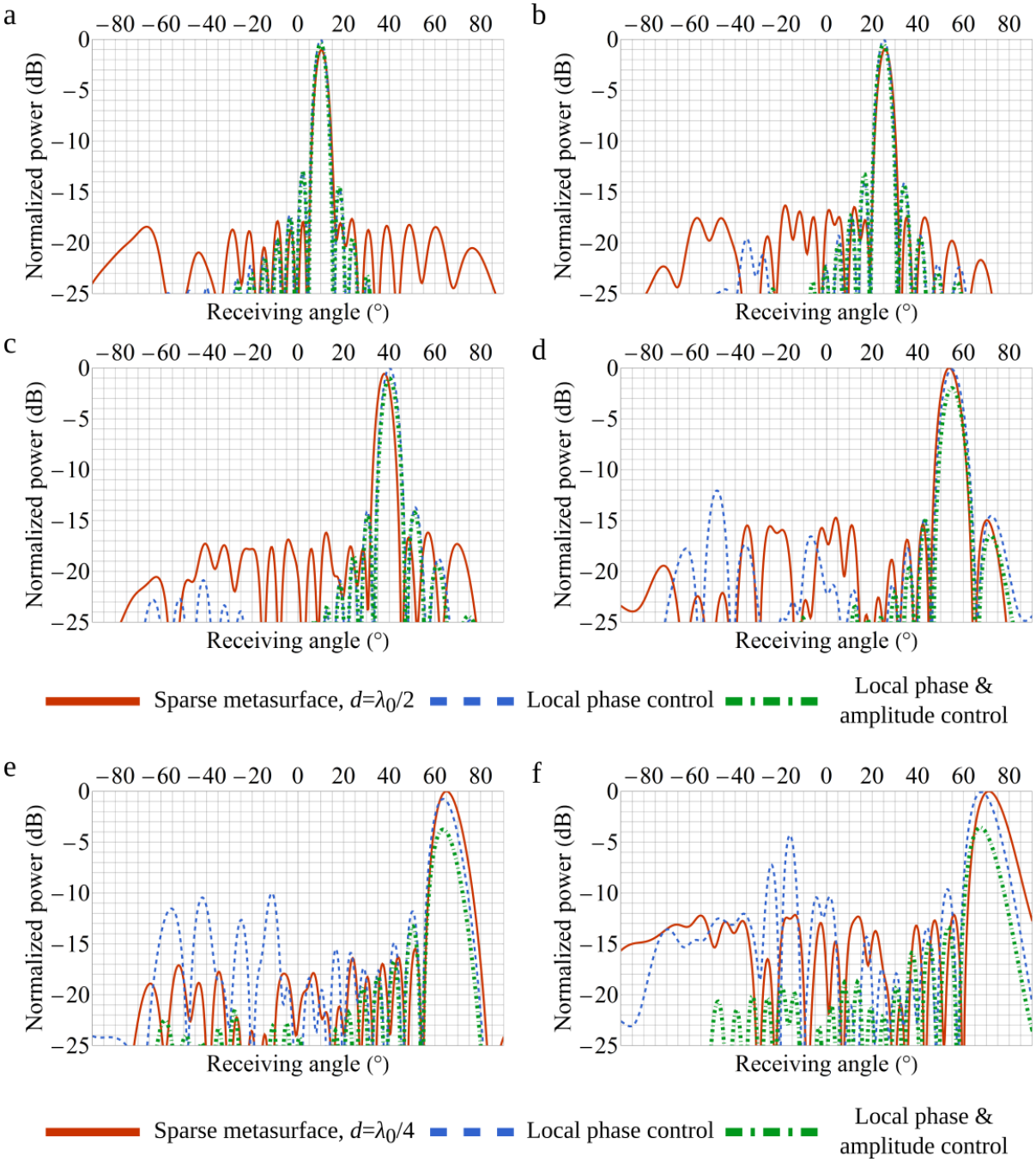

Figure 5.5: Simulation results of beam-steering at different angles performed by a sparse metasurface (solid red curves), a gradient metasurface implementing only local phase control (dashed blue curves) and a gradient metasurface implementing local phase and amplitude control (dot-dashed green curves). Normalized radiation patterns are plotted. In the panels ***(a)****–****(d)*** *the sparse metasurface is composed of* 21 *wires with the inter-wire distance of* $\lambda_0/2$*. In the panels* ***(e)****,****(f)*** *the number of wires in sparse metasurface is increased to* 42 *while the inter-wire distance is reduced to* $\lambda/4$ *to maintain the same aperture size of* 315 *mm. The gradient metasurfaces also have the aperture of* 315 *mm. The external excitation is a normally incident cylindrical wave having the center at* 35 *cm away from metasurfaces. The operating frequency set in the simulations is* 10 *GHz.*

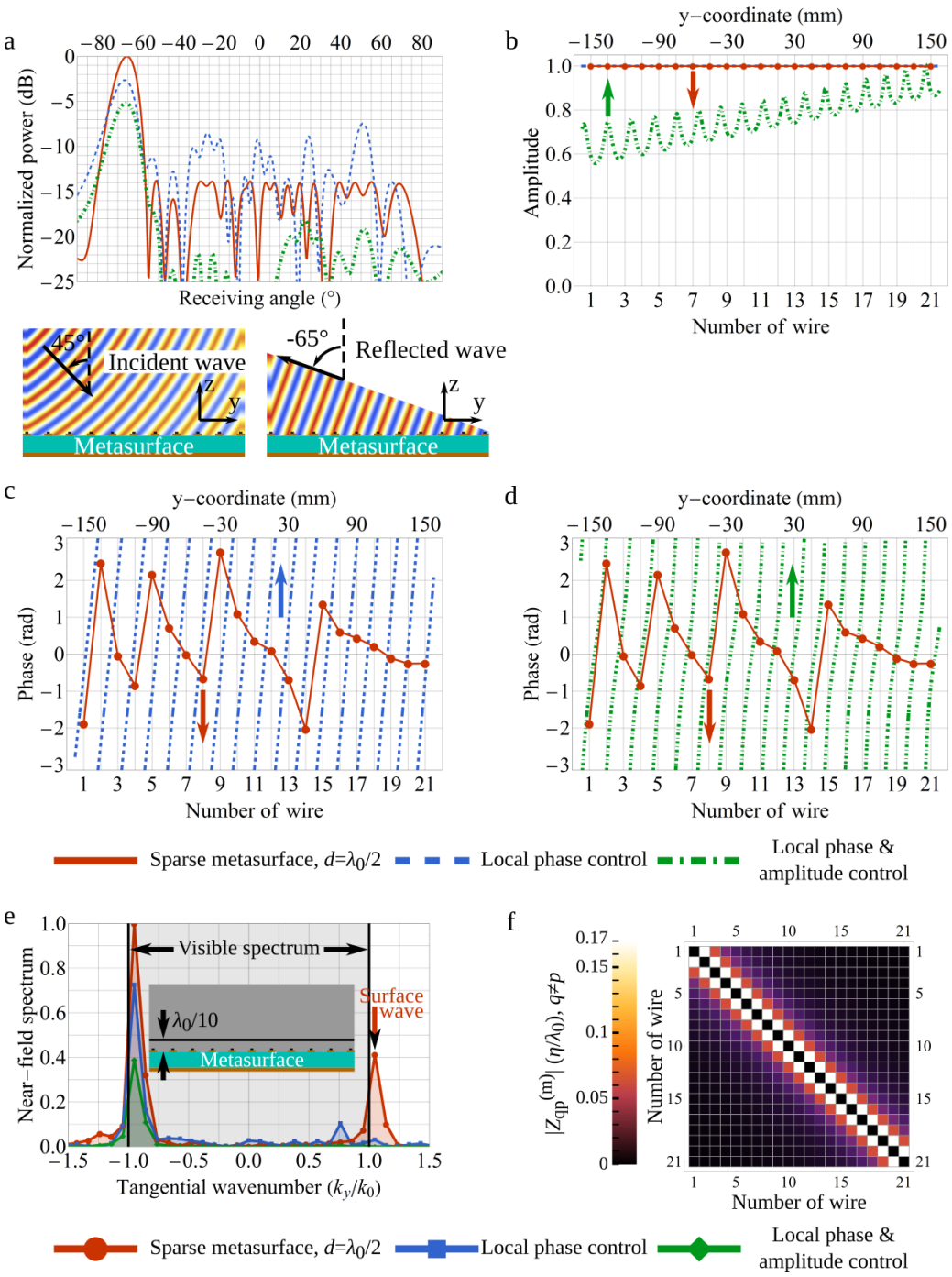

Figure 5.6: ***(a)*** *Simulation results of beam-steering at* $-65°$ *performed by a sparse metasurface (solid red curves), a gradient metasurface implementing only local phase control (dashed blue curves) and a gradient metasurface implementing local phase and amplitude control (dot-dashed green curves). Normalized radiation patterns are plotted. The inset figure illustrates the incident (left) and reflected (right) waves. The sparse metasurface is composed of* 21 *wires with the inter-wire distance of* $\lambda_0/2$*. The metasurfaces have the same aperture of* 315 *mm. The relative permittivity of substrates is* $\varepsilon_s = 2.2$ *and the thickness is* 2.65 *mm. The external excitation is a cylindrical wave incident at* 45° *and having the center at* 35 *cm away from the center of the metasurfaces. The operating frequency set in the simulations is* 10 *GHz.* ***(b)****–****(d)*** *Corresponding amplitude* ***(b)*** *and phase* ***(c)****,****(d)*** *of the local reflection coefficient along the metasurfaces. The local reflection coefficient corresponding to the sparse metasurface (red circles) is* ***fictitious*** *as explained in the main text.* ***(e)*** *Spectrum of the electric field above (at the distance* $\lambda_0/10$*) the metasurfaces.* ***(f)*** *Plot of the matrix of mutual-impedance densities of the sparse metasurface.*

5.4. Reconfigurable sparse metasurface

By gaining control over load-impedance densities Z_q of the wires, one is able to adjust the currents I_q and manipulate the scattered field dynamically. In order to realize real-time control over load-impedance densities at microwave frequencies, I use a radio-frequency varactor diode where the capacitance can be tuned by an applied bias voltage. Two different designs of reconfigurable meta-atoms were developed and tested in the course of the work. The schematic layouts are shown in Figs. 5.7(a) and (b). The design procedure is based on the local periodic approximation established in the Third Chapter; the conventional design methods of dense metasurfaces being not applicable for sparse metasurfaces (see for e.g. Ref. [112]). The design of the second reconfigurable meta-atom, presented in Fig. 5.7(b), evolves from the first one and better accounts for Ohmic losses of the chosen varactor diode. Three principal parts of the elementary cell can be distinguished in both designs: a varactor loaded microstrip line (top), a microstrip line (middle), and a bias line (alongside). The microstrip lines together with the varactor diode form an equivalent parallel RLC circuit. The middle microstrip line plays the role of an inductance that allows one to effectively decrease the minimal capacitance of the varactor diode and expand the dynamic range of accessible load-impedance densities Z_q without increasing the density of meta-atoms. The latter is extremely important when one tends to decrease the Ohmic losses of varactor diodes. The bias voltage is applied to the varactor diode through the metallized via connecting the top and bottom layers.

On the basis of the developed designs, two experimental samples were fabricated using printed circuit board (PCB) technique and surface-mount component soldering. Similar to the numerical examples considered above, both samples are composed of 21 loaded wires, each represented by a chain of the designed meta-atoms. Close-up photographs of the fabricated samples are shown in Figs. 5.7(c) and (d). The samples represent six-layer PCBs with the bottom layer reserved for the bias network of the varactor diodes. Three woven-glass dielectric substrates F4BM220 (relative permittivity is 2.2, loss tangent is 0.001) were used: the two top substrates correspond to the specifications given in Figs. 5.7(a) and (b), the thickness of the bottom substrate not shown in Fig. 5.7 is 0.5 mm. Thickness of the copper cladding is 35 μm. Selected varactor diode (MAVR-011020-1411) has capacitance varying in the range from 0.045 pF to 0.25 pF as specified by the manufacturer in the datasheet [184]. Metallic vias of 0.25 mm radius are used

to apply bias voltage to varactors. In the datasheet, the characterization of the varactor diode is presented at 1 MHz for the capacitance range and at 50 MHz for the quality factor. Therefore, a more accurate characterization of the varactor diode in the target frequency range (around 10 GHz) is required.

Individual control of each wire in the metasurface is implemented by a bias network appearing behind the metal-backed substrate and powered by an electronic control module. The module was developed upstream and consists of a Raspberry Pi 3 B+, an ARM processor single board nano-computer, and a stack of two electronic cards integrating 16 independent DC voltage outputs each. A photograph of the electronic control module is shown in Fig. 5.7(e). The nano-computer is used as an operating unit for the two electronic cards and allows one to control the DC voltage of each of the 32 outputs from 0 to 30 V. To facilitate the control, a human-machine interface in Python was developed. On the electronic side, each card is supplied with a fixed voltage of 30 V and operational amplifiers are used in a comparator assembly to control the voltage of each output. Each output is therefore controlled via the nano-computer using the SPI communication protocol.

Once a reconfigurable metasurface is fabricated, it should be characterized. The aim of the experimental characterization of a sample is to establish the dependence between the applied biasing voltage V and the load-impedance density of the loaded wires comprising a sparse metasurface. Photographs and schematics of experimental setups are shown in Fig 5.8. The setup in Figs. 5.8(a) and (b) is used for sample 1 and the incidence angle is set to 5° to avoid the appearance of grating lobes at frequencies above 10 GHz. The measurements are performed up to 16 GHz. For sample 2, the setup shown in Figs. 5.8(c) and (d) is used, the incidence angle is 45° and the highest frequency is 11.5 GHz. The frequency dependence of the complex amplitude of the specularly reflected wave from the sample as a function of the applied bias voltage is measured. The same bias voltage is applied to all varactor diodes. The complex amplitude is normalized to the one measured from a metallic plate of the same size and thickness as the sample. The absolute value of the reflection coefficient is plotted in Figs. 5.9(a) and (e) for sample 1 and sample 2, respectively. Then, the experimental frequency dependencies are correlated with the ones obtained via 3D full-wave numerical simulations of the unit cells shown in Figs. 5.7(a) and (b) with applied periodic boundary conditions (see Figs. 5.9 (b) and (f)). In the simulations, the varactor diode is modeled as a lumped RC-circuit with the impedance $Z_v = R_v - j/(\omega C_v)$, where R_v is the series resistance and C_v is the capacitance. It is assumed

that R_v and C_v depend on neither the frequency nor the bias voltage. The parameter R_v was used to match the depth and the width of the resonances obtained in simulations to the ones observed experimentally. Eventually, R_v was estimated to be 8.5 Ω to allow one to accurately predict in simulations the parameters of the experimental resonances at lower frequencies (up to approximately 10.5 GHz) within the approximation that R_v and C_v are frequency independent. By comparing the positions of the experimental and theoretical resonances (Figs. 5.9(c) and (g)), I obtain the relation between the bias voltage and the varactor's capacitance presented in Figs. 5.9(d) and (h). The small difference between the extracted dependencies $C_v(v)$ for sample 1 and 2, Figs. 5.9(d) and (h), may stem from inaccuracies of the model of the varactor diode and/or the characterization procedure itself. In any case, as experimental results presented in what follows suggest, these inaccuracies do not affect the performance significantly. Eventually, with $C_v = C_v(V)$ known, one is able to find $Z_q = Z_q(V)$.

Figure 5.10 demonstrates the retrieved dependencies of the load-impedance density on the bias voltage for both samples at different frequencies and allows one to compare the two designs. The target central frequency was chosen to be 10 GHz. At this frequency, sample 1 exhibits a strongly resonant response where the dynamic range of the reactance corresponds to a narrow range of bias voltages. This and the enhanced resistance due to the resonance resulted in a very poor performance of sample 1 at this frequency as followed from to the adopted theoretical model in Section 5.2. However, as it is demonstrated by Figs. 5.10(b)–(d), when increasing the frequency the resonance widens and shifts to higher bias voltages. It actually suggests that by reducing the density of unit cells in the x-direction (increasing the length of the segments constituting a wire) the desired reconfigurable response can be obtained at the target frequency. Furthermore, when reducing the density, the number of lossy varactor diodes decreases also and one can expect that the overall absorption will be lower. Based on these conclusions, the design of sample 2 was developed. Figures 5.10(e)–(h) show the retrieved load-impedance density in the frequency range from 8.5 GHz to 10 GHz. At 10 GHz frequency, sample 2 demonstrates a wide capacitive response within a broad range of bias voltages that allows convenient experimental reconfigurability. In what follows, only the experimental results obtained with sample 2 are demonstrated.

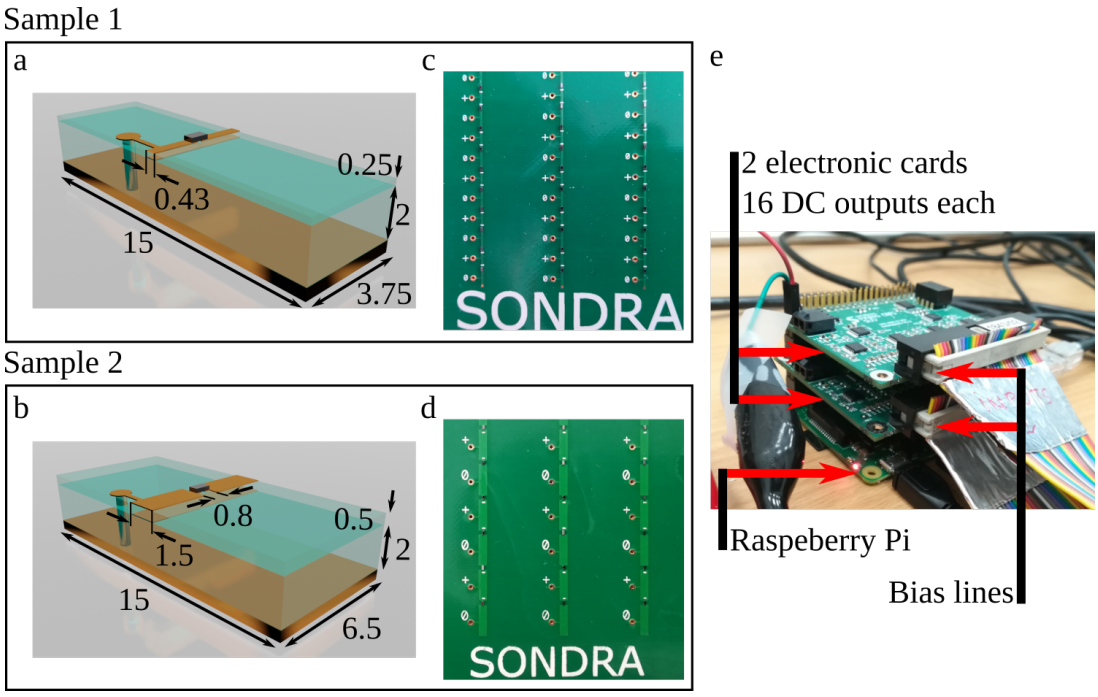

Figure 5.7: ***(a)***, ***(b)*** *Schematics of an elementary varactor-loaded meta-atoms composing experimental samples 1* ***(a)*** *and 2* ***(b)****. All the dimensions are given in millimeters.* ***(c)***, ***(d)*** *Photographs of the fabricated experimental samples 1* ***(c)*** *and 2* ***(d)****, approximately equal areas of the samples are shown.* ***(e)*** *A photograph of the electronic control module.*

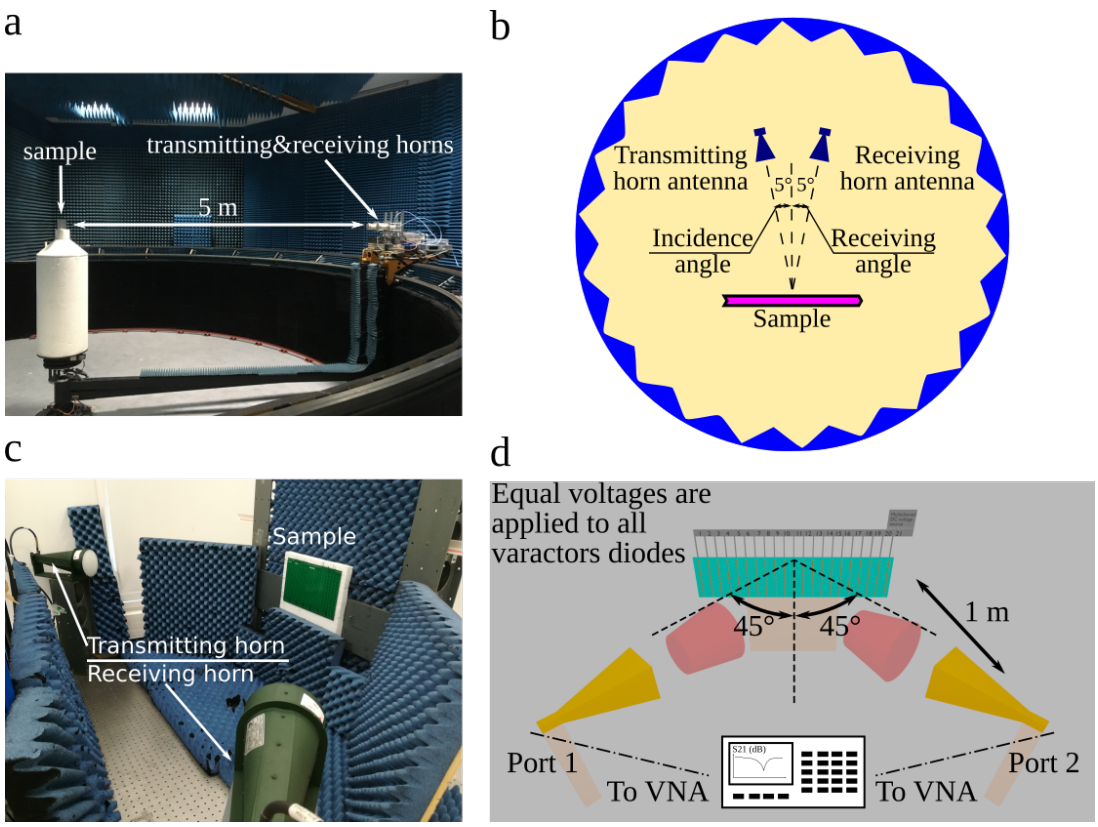

Figure 5.8: Photographs ***(a)***,***(c)*** *and schematics* ***(b)***,***(d)*** *of the experimental setups used to characterize sample 1* ***(a)***,***(b)*** *and sample 2* ***(c)***,***(d)****.*

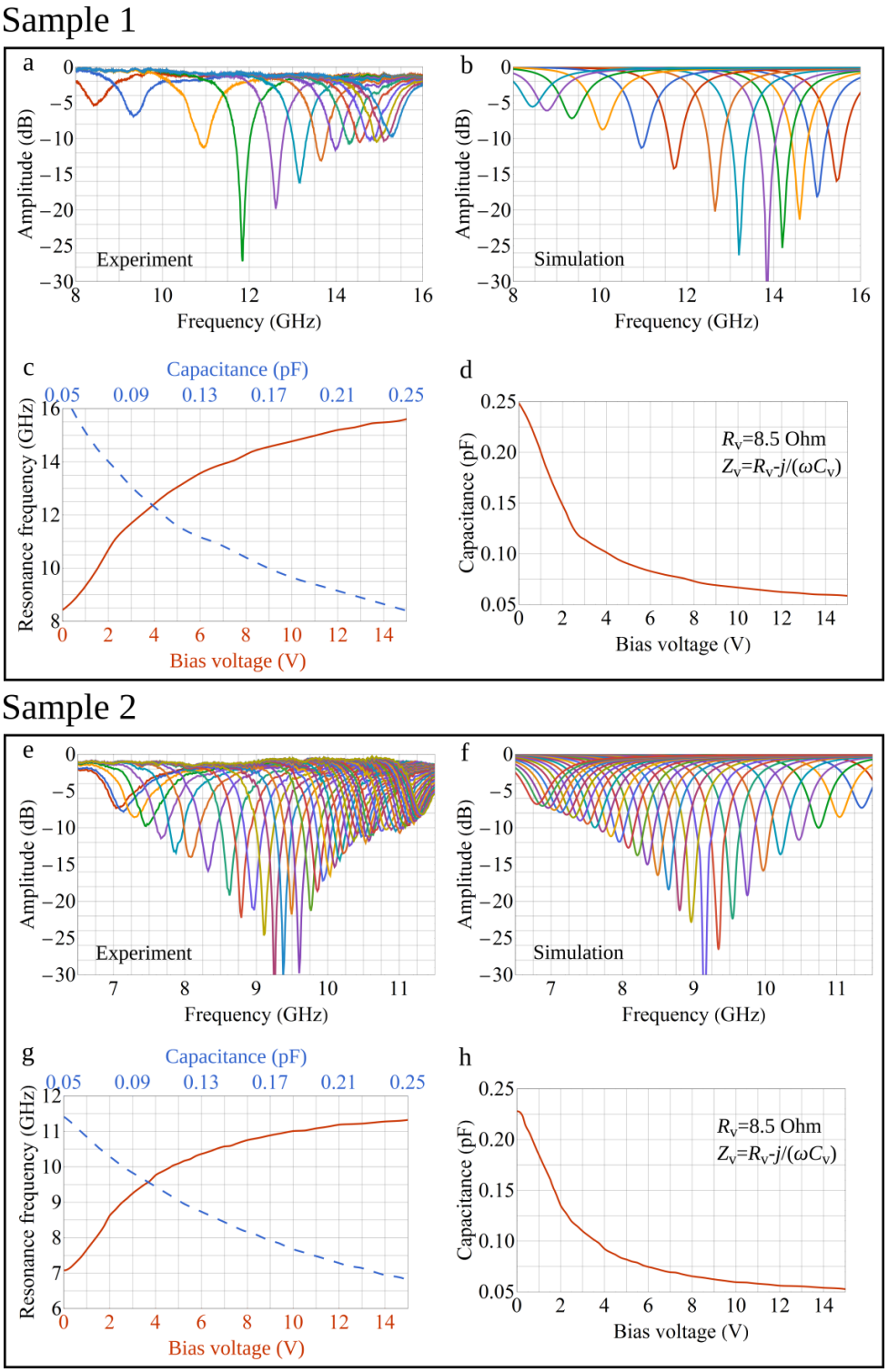

Figure 5.9: Experimentally measured ***(a)***, ***(e)*** *and simulated* ***(b)***, ***(f)*** *amplitudes of the specularly reflected wave vs. the frequency). In the experiment, the bias voltage was changed in the range from 0 to 15 V. In the simulation, a parametric sweep with respect to the capacitance of the modeled varactor diode was performed in the range from* 0.05 *to* 0.25 *pF according to the datasheet [184].* ***(c)***, ***(g)*** *The dependence of the resonance frequency on the bias voltage (red solid curve, measured experimentally) and on the capacitance (blue dashed curve, simulated).* ***(d)***, ***(h)*** *The dependence of the capacitance on the bias voltage retrieved from the panels* ***(c)*** *and* ***(g)****, respectively. The panels* ***(a)****–****(d)*** *and* ***(e)****–****(h)*** *correspond to the sample 1, Fig. 5.7(c), and the sample 2, Fig. 5.7(d), respectively.*

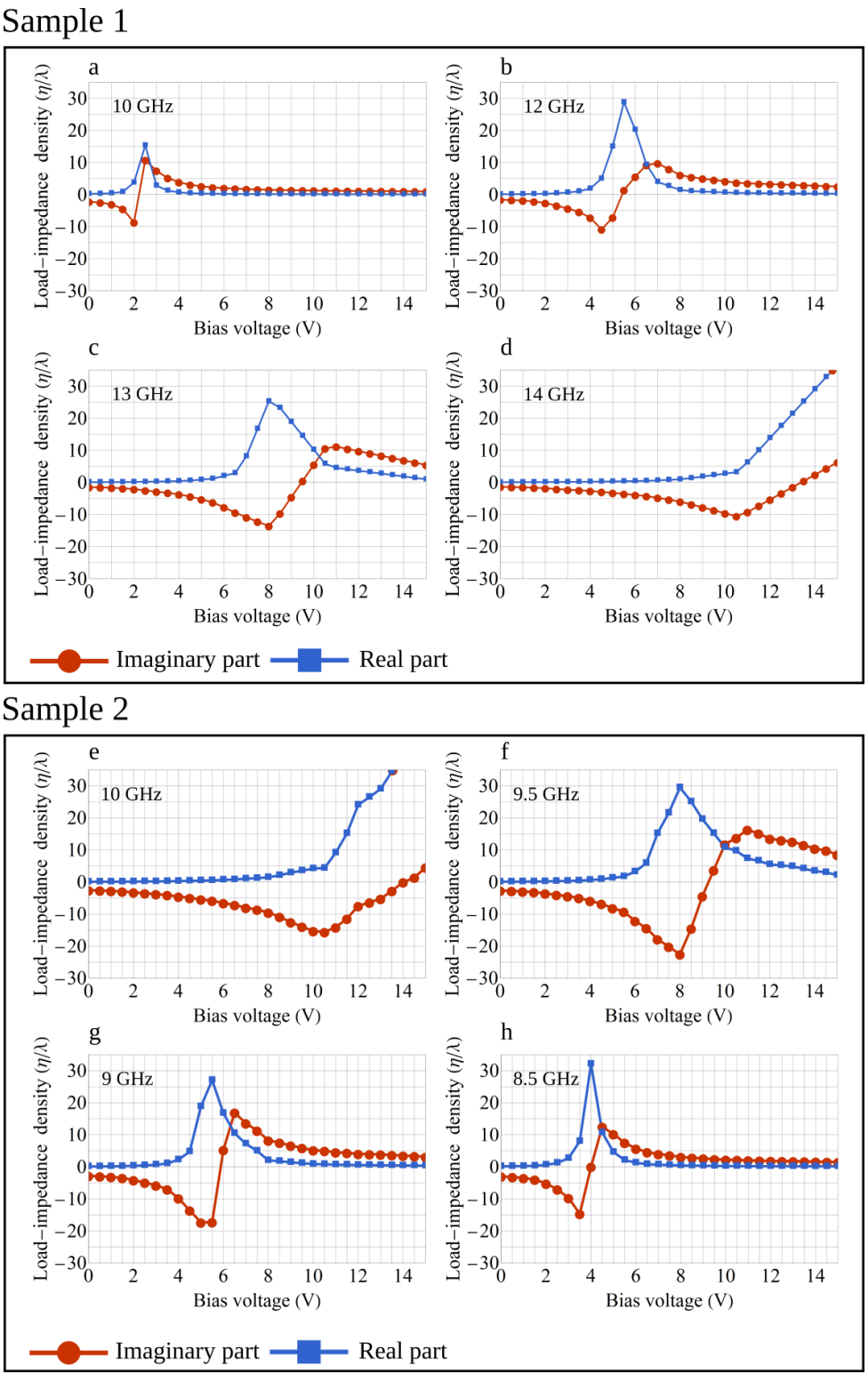

Figure 5.10: Retrieved load-impedance density of the varactor-loaded wire constituting the sparse metasurface vs. the bias voltage. The panels show examples at different frequencies indicated in top right corner. It is seen how the position of the resonance shifts when the frequency is changed. The panels ***(a)****–****(d)*** *and* ***(e)****–****(h)*** *correspond to the sample 1, Fig. 5.7(c), and the sample 2, Fig. 5.7(d), respectively.*

5.5. Experimental results: beam-forming

The experimental setup used to demonstrate the dynamic far-field manipulation capabilities of the proposed metasurface is schematically illustrated in Fig. 5.11(a), and photographs of the setup are shown in Figs. 5.11(b) and (c). The sample and a feeding horn antenna are both placed on a rotating platform to be used as a transmitter and the radiation pattern is measured by a receiving horn antenna. The feeding horn is placed approximately 35 cm away from the sample, which makes it a compact radiation system. However, other sources (like a patch antenna) can also be used in order to excite the sample and further reduce the size of the system.

In the first set of measurements, the incidence angle is set to 0° in concordance with the numerical example above, and the operating frequency is fixed to 10 GHz. Figures 5.12(a)–(c) demonstrate dynamic beam steering from 10° up to 65° at three different frequencies: 9 GHz, 9.5 GHz and 10 GHz. The spurious scattering in the far-field region remains low being in good agreement with the numerical results of Fig. 5.5. Even though a *sparse* metasurface is considered, the employed design approach does not impose any restriction on the achievable beam-steering angle, which is in strong contrast with periodic metasurfaces. More complex examples of beam-forming are illustrated in Fig. 5.13(a), which demonstrates the ability to dynamically control the number of radiated beams. When applying successive sequence of pre-registered bias voltage profiles plotted in Fig. 5.13(b), one beam is firstly radiated at 60°, then two symmetrical beams at −30° and 30°, and three beams centered around 0°. The number of beams is only limited by the beamwidth and, thus, the physical aperture of the metasurface. Figure 5.13(c) shows simultaneous excitation of six beams at desired angles. As in the case of a single beam, dynamic steering beam-steering of multiple beams can be performed as demonstrated in Figs. 5.13(d)–(f) on the example of two beams at 9.5 GHz. It should be noted that the level of side lobes does not increase when changing the number of beams. Moreover, in all examples shown in Fig. 5.13 the level of side lobes does not exceed −10 dB. The high scattering efficiency of the sample is due to the rigorous theoretical model behind. It accounts for the mutual interactions between the elements, considers real-type excitation (non-planar incident wavefront in our specific case) and precisely solves the inverse scattering problem. The instantaneous operating bandwidth of the sample also depends on the configuration and is estimated to be 5%. On the other hand, the reconfigurability mechanism allows the sample

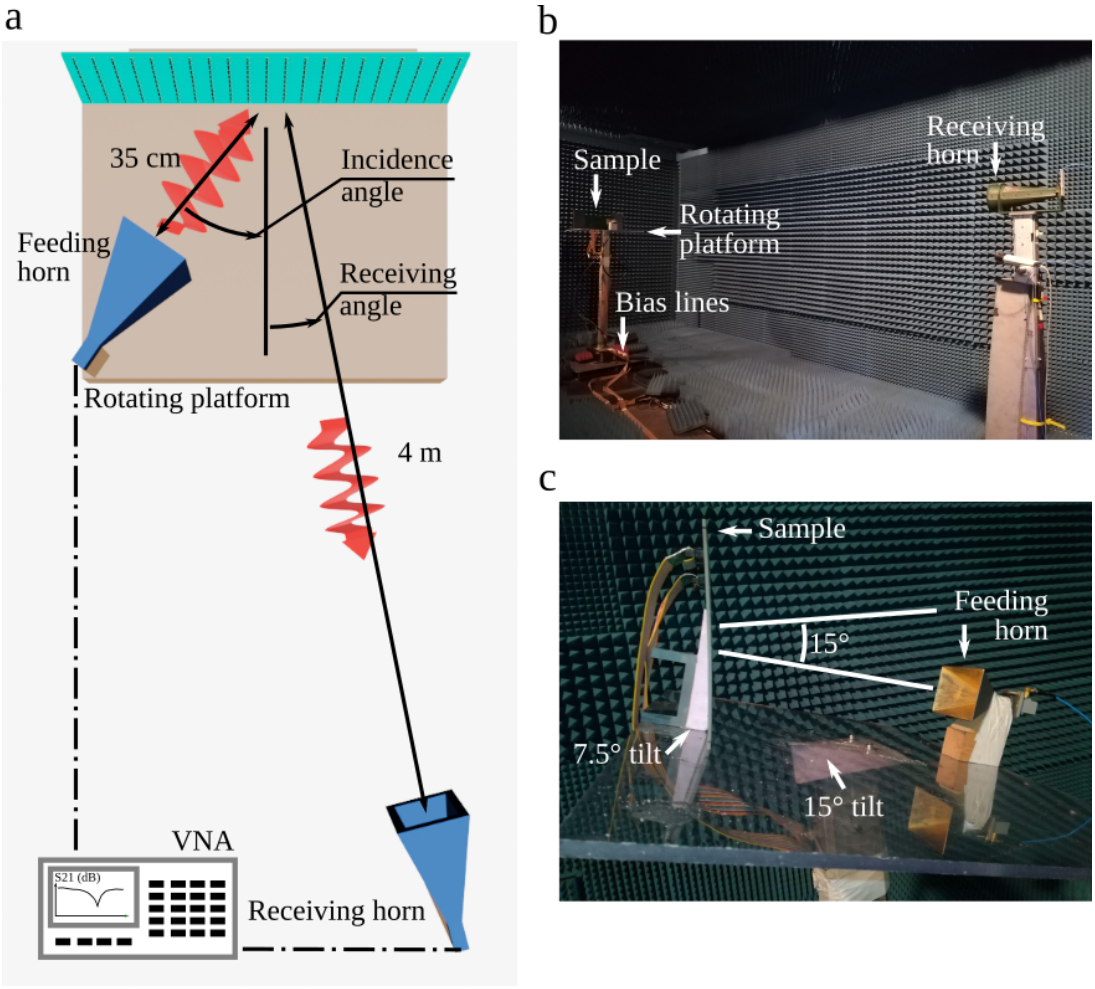

Figure 5.11: A schematic illustration ***(a)*** *and photographs* ***(b)***, ***(c)*** *of the experimental setup to measure far-field radiation patterns.*

to demonstrate frequency agility over a broad frequency range around centre frequency of 9.25 GHz (16%). Section 5.6 provides additional details on the performances of the sample for beam-steering applications demonstrated in Figs. 5.12(a)–(c).

5.5.1 Indirect evidence of strongly non-local response

To conform the conditions of the numerical example shown in Fig. 5.6 and also highlight the sample's agility with respect to the excitation, the incidence angle is changed to 45°. The operating frequency is fixed to 10 GHz. Figure 5.12(d) demonstrates dynamic beam steering from 20° up to −70°, and the side-lobes level, being well beyond the limits of gradient metasurfaces for large steering angles as discussed in details in Section 5.3. As follows from the conclusions derived when analyzing Figs. 5.6(a) and (e), the efficient large-angle anomalous reflection serves as an indirect manifestation of a strong non-locality by the fabricated reconfigurable sparse metasurface.

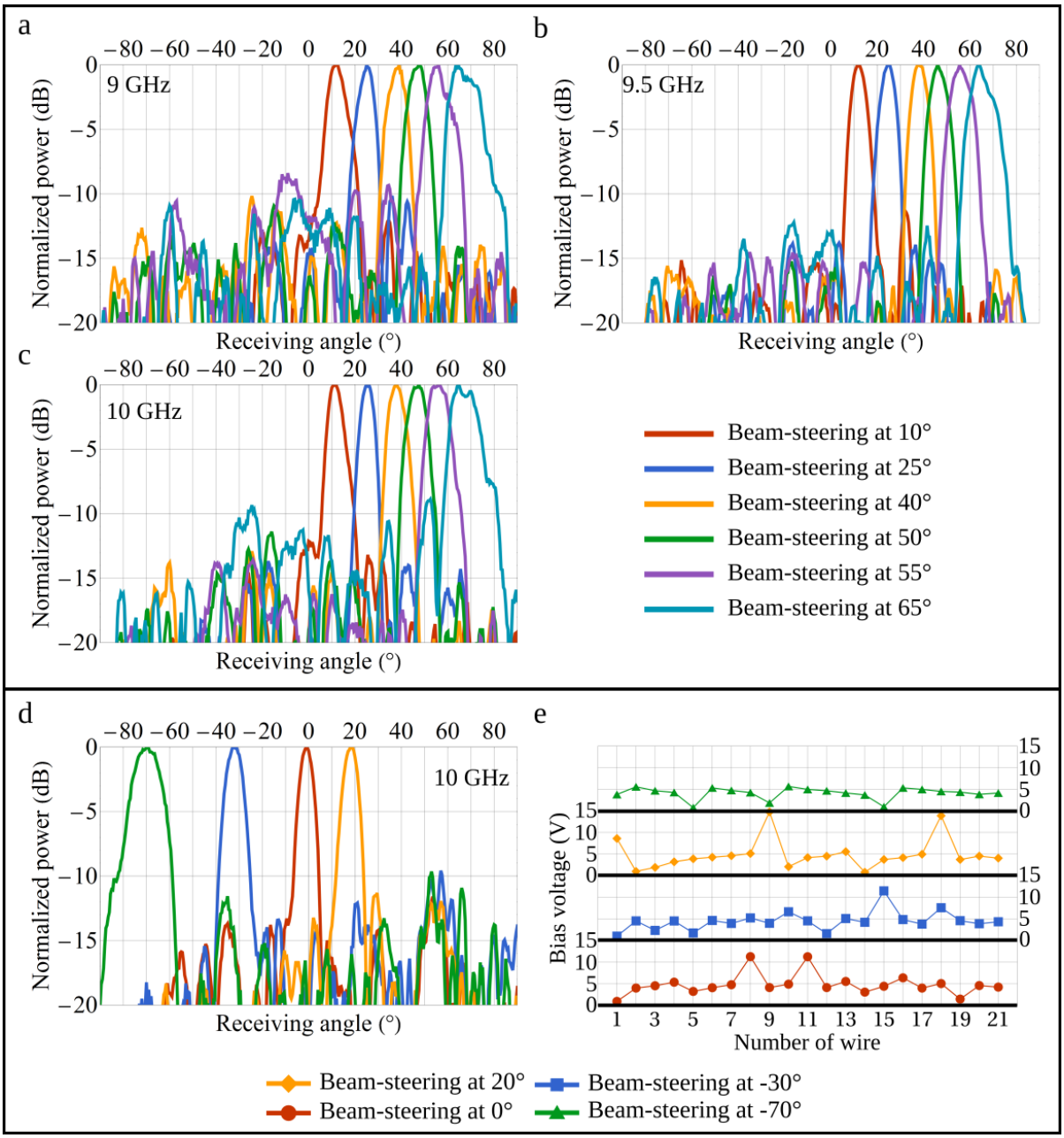

Figure 5.12: Experimental examples of beam-steering capabilities of the sample. The panels ***(a)****–****(c)*** *demonstrate beam-steering at three different frequencies when the feeding horn antenna is at normal incidence: 9 GHz* ***(a)****, 9.5 GHz* ***(b)*** *and 10 GHz* ***(c)****. The panel* ***(d)*** *demonstrates beam-steering at 10 GHz when the feeding horn antenna is at 45° incidence. The panel* ***(e)*** *shows applied bias voltages corresponding to the examples of the panel* ***(d)****.*

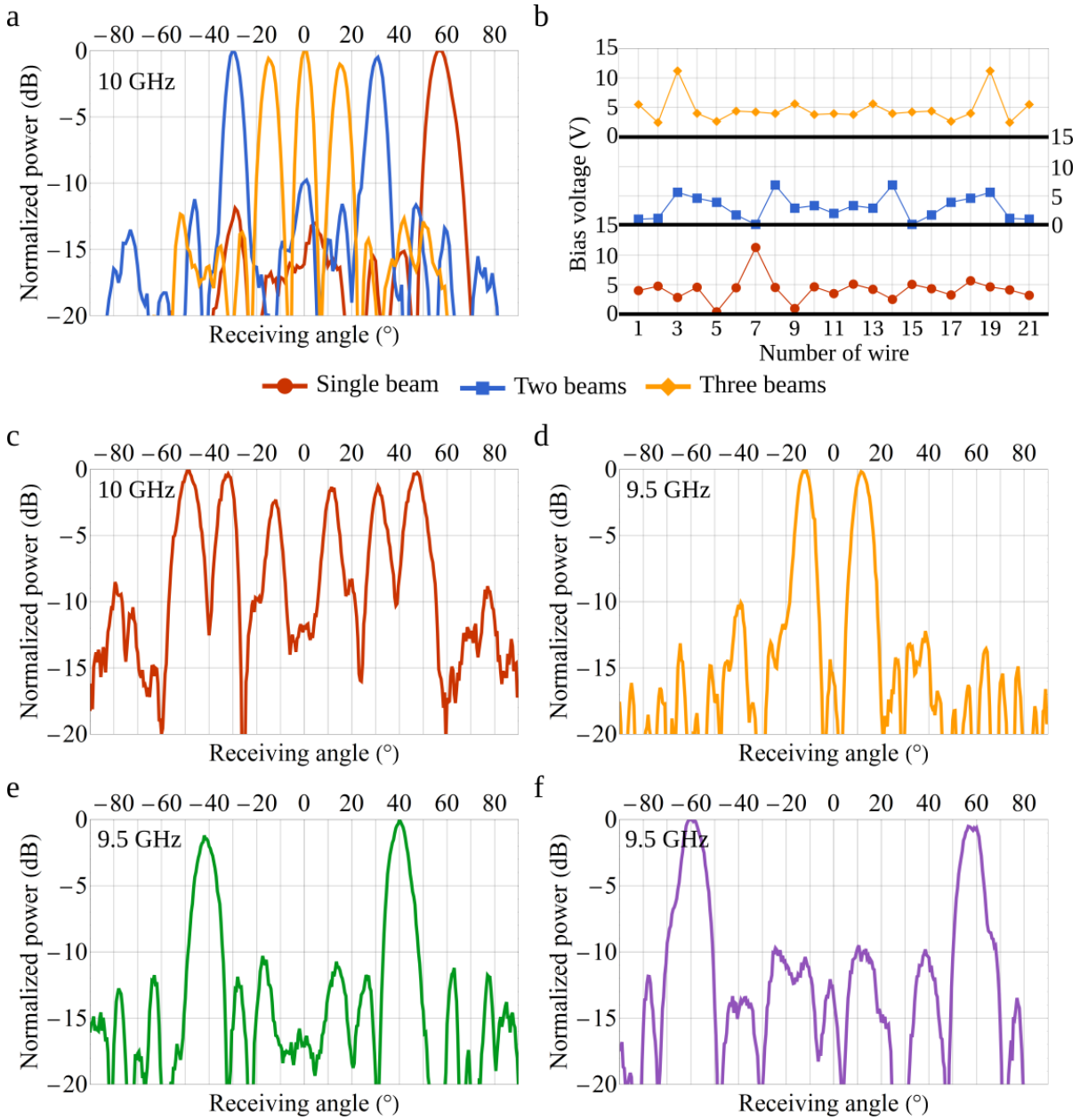

Figure 5.13: Experimental examples of exciting and manipulating multiple beams with the sample. The panel ***(a)*** *demonstrates dynamic control of the number of beams at* 10 *GHz. The panel* ***(b)*** *shows corresponding bias voltages applied to the wires in the examples of the panel* ***(a)****. The panel* ***(c)*** *demonstrates the excitation of six beams at* 10 *GHz. The panels* ***(d)****–****(f)*** *demonstrate symmetric steering of two beams at* 9.5 *GHz. The sample is illuminated by a single horn antenna at normal incidence, the distance between the horn and the sample is* 35 *cm.*

5.6. Analysis of beam-steering efficiency

The total efficiency of the sample can be computed by means of the following formula

$$\epsilon_{tot} = (1 - A)\epsilon_{sct}, \tag{5.9}$$

where A is the absorption (the portion of the incident power absorbed by the sample) and ϵ_{sct} is the portion of the reflected power scattered in desired directions (lobes). The absorption can be calculated as follows

$$A = 1 - \int_{-90^\circ}^{90^\circ} P_S(\varphi)\mathrm{d}\varphi \Big/ \int_{-90^\circ}^{90^\circ} P_{MP}(\varphi)\mathrm{d}\varphi, \tag{5.10}$$

where $P_S(\varphi)$ and $P_{MP}(\varphi)$ are, respectively, the measured power scattered from the sample (in different configurations) and the metallic plate of the same size (see Fig. 5.11). The incidence angle and the distance to the illuminating horn antenna are kept the same for the sample and the metallic plate. The scattering efficiency can be estimated by integrating the power in the desired lobe over the total reflected power

$$\epsilon_{sct} = \int_{\text{lobe}} P_S(\varphi)\mathrm{d}\varphi \Big/ \int_{-90^\circ}^{90^\circ} P_S(\varphi)\mathrm{d}\varphi. \tag{5.11}$$

As it can be seen from Fig. 5.14, the absorption and the scattering efficiency depend on the configuration of the sample. It should be noted that while we consider the scattering efficiency with respect to the *total* reflected power, in many studies the efficiency is estimated with respect to the discrete number of diffraction orders. The level of absorption can be further reduced at lower frequencies. At the target frequency range of 10 GHz, varactor diodes are relatively lossy and the retrieved resistance of used varactor diodes is 8.5 Ω.

It can be also useful to compare the directivity of the radiation pattern produced by the sample with the one created by a uniform aperture. The directivity of the uniform aperture is considered to be the practical maximum of an antenna's directivity. Therefore, one can make conclusions about the scattering efficiency of the sample. The 2D radiation pattern produced

by a uniform aperture is given by [125]

$$P_{UA}(\varphi) = \left(\cos[\varphi] \frac{\sin\left[\frac{ka}{2}(\sin[\varphi] - \sin[\varphi_{max}])\right]}{\frac{ka}{2}(\sin[\varphi] - \sin[\varphi_{max}])} \right)^2, \tag{5.12}$$

where k is the wavenumber in free space, $a = Nd = 315$ mm is the aperture size and φ_{max} is the direction of the maximum power. The 2D directivity D is the power radiated in a given direction over the averaged total power

$$D = 360^\circ P(\varphi) \Big/ \int_{-90^\circ}^{90^\circ} P(\varphi) \mathrm{d}\varphi. \tag{5.13}$$

The angle φ_{max} in Eq. (5.12) is the steering angle corresponding to the one in a considered configuration of the sample. Figure 5.15 allows one to compare the 2D directivity of the sample in the configurations of Fig. 5.12 and the uniform aperture.

To summarize, the estimated level of absorption lies in the range from 0.5 to 0.7 and depends on the particular configuration. Generally, the highest scattering efficiency corresponds to smaller steering angles, but even for 55° and 65° it reaches 90% and 85%, respectively. Calculated 2D directivity of the sample confirms high scattering efficiency when being compared to the 2D directivity of the uniform aperture. Indeed, for small steering angles the directivity of the sample is approximately 2 dBi less than of the uniform aperture. The difference is less than 1 dBi for large angles.

I do not consider here the efficiency in the configurations of the sample corresponding to excitation of multiple beams as each beam changes differently with respect to the frequency and it is not trivial to define the scattering efficiency in these cases.

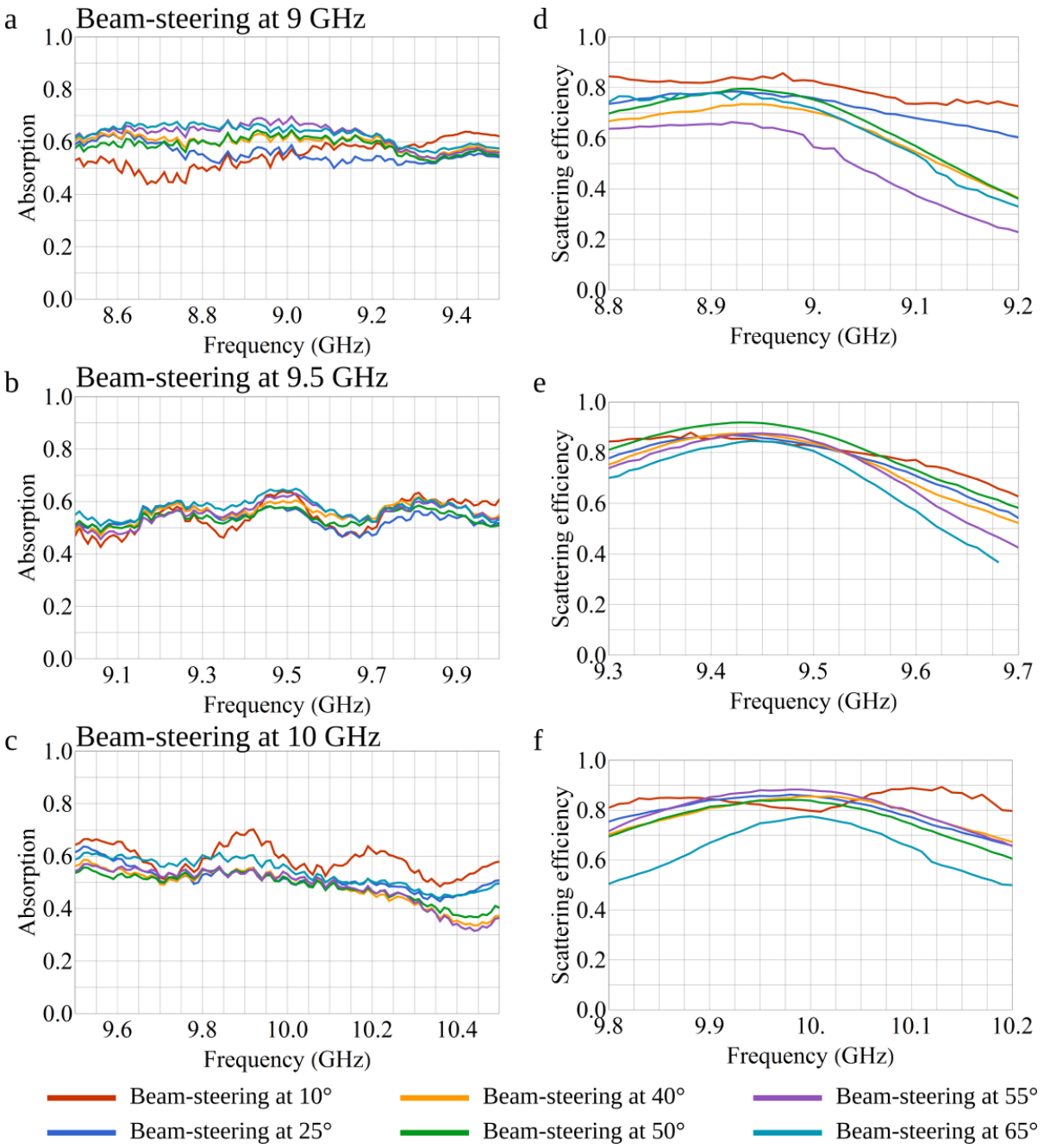

Figure 5.14: Calculated absorption ***(a)****–****(c)*** *and scattering efficiency* ***(d)****–****(f)*** *of the experimental sample in different configurations. These data are related to the radiation patterns shown in Fig. 5.12. The panels* ***(a)*** *and* ***(d)*** *correspond to the panel (a) of Fig. 5.12, the panels* ***(b)*** *and* ***(d)*** *correspond to the panel (b) of Fig. 5.12 and the panels* ***(c)*** *and* ***(d)*** *correspond to the panel (c) of Fig. 5.12. The color code corresponds to the one of Figs. 5.12(a)–(c).*

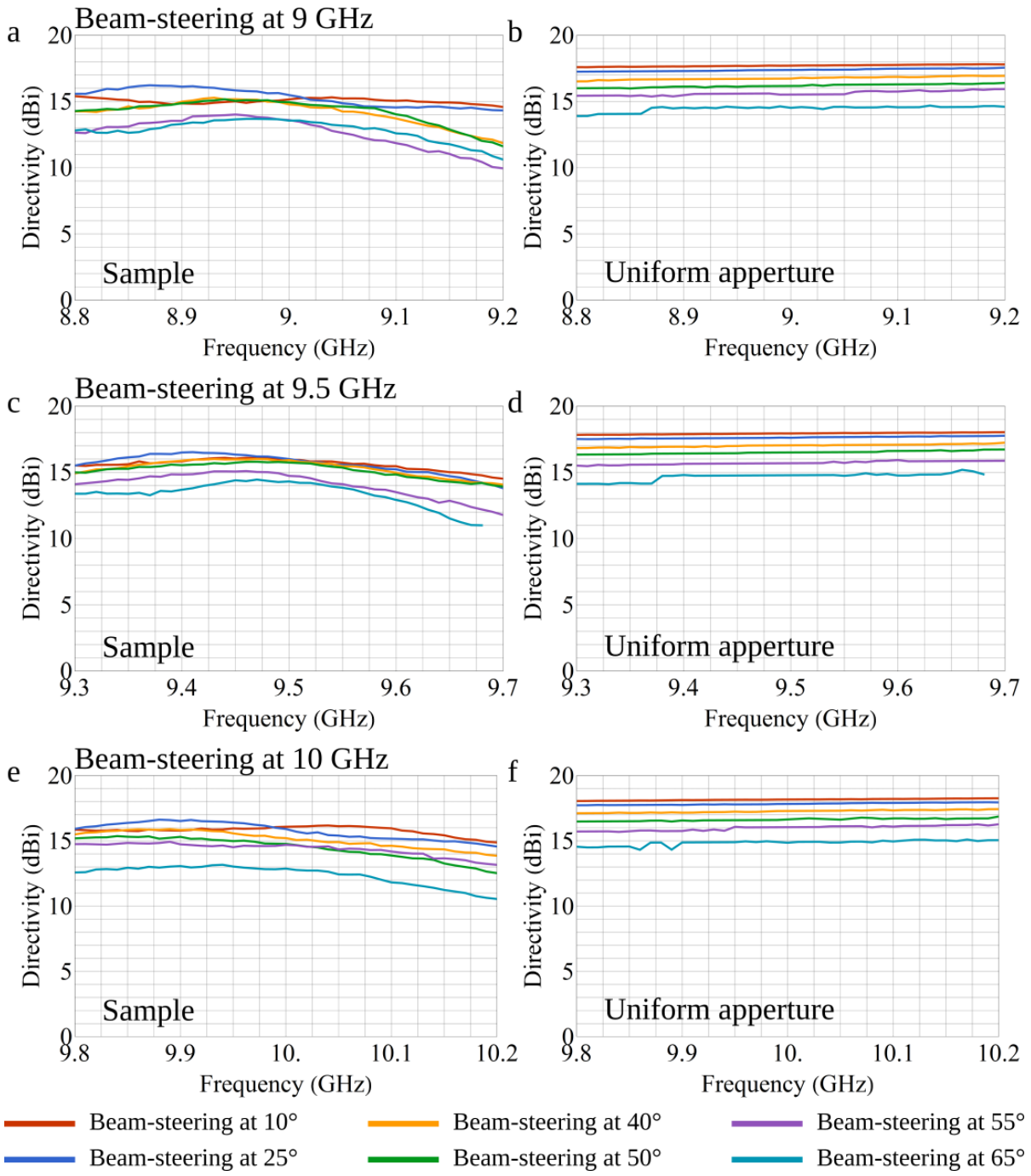

Figure 5.15: Calculated 2D directivity of the radiation patterns created by the sample in different configurations compared to the corresponding directivity of a uniform aperture. The panels ***(a)***,***(c)***,***(e)*** *correspond to the sample and the panels* ***(b)***,***(d)***,***(f)*** *correspond to the uniform aperture. The panels* ***(a)*** *and* ***(b)*** *correspond to the panel (a) of Fig. 5.12, the panels* ***(c)*** *and* ***(d)*** *correspond to the panel (b) of Fig. 5.12 and the panels* ***(e)*** *and* ***(f)*** *correspond to the panel (c) of Fig. 5.12. The color code corresponds to the one of Figs. 5.12(a)–(c).*

5.7. Experimental results: Near-field focusing

To further demonstrate the vast capabilities of the approach in manipulating fields, I have studied the flexibility and efficiency of the proposed reconfigurable metasurface for dynamic shaping of the near-field. To that end, the following objective function was selected

$$f(V_q) = t^t \left(\prod_{n\in\mathbb{D}} |E_{nf}(y_n, z_f)|^2 \right) \Big/ \left(\int_{y_{min}}^{y_{max}} |E_{nf}(y, z_f)|^2 \mathrm{d}y \right)^t,$$
$$E_{nf}(y, z_f) = E_x^{(r)}(y, z_f) + \sum_{q=1}^{N} G_q(y, z_f) I_q. \tag{5.14}$$

It maximizes the field intensity at desired focal points (y_n, z_f) defined by the index n and minimizes the level of secondary lobes in the given focal plane, $\mathbb{D}$ represents a discrete set of desired points and t is the size of this set. The coordinates y_{min} and y_{max} in the integral correspond to the lateral boundaries of the scanned region infront of the sample. Currents I_q are related to load-impedance densities Z_q via Eq. (5.2). In its turn, the load-impedance density is related to the bias voltage V_q via the characterization procedure and Figs. 5.10(e)–(h).

Another experimental setup was mounted to measure the distribution of the electric field (both the phase and the amplitude) in front of the sample with a moving dielectric probe as shown in Fig. 5.16. The sample, in this case, is illuminated at normal incidence by a cylindrical wave radiated by a horn antenna, as illustrated by the corresponding measured electric field profile in Fig. 5.17(a). In the first sequence of voltage settings, the sample acts as a high numerical aperture (NA) diffractive lens and focuses the incident wave at the distance λ as shown in Fig. 5.17(b). With the physical aperture of the sample being $21\lambda_0/2 = 315$ mm and the focal length of $\lambda \approx 31.6$ mm, the NA is approximately 0.98. The experimentally measured spot size being 0.47λ, which is smaller (for the given NA) than the size of Airy spot $0.61\lambda/\mathrm{NA}$ establishing the diffraction limit [185, 186], demonstrates subdiffraction focusing. Meanwhile, the minimum spot size of a subdiffraction focal point is found to be $0.38\lambda/\mathrm{NA}$ [180]. The depth of focus (DOF), characterized as full width of the focal spot in the longitudinal direction at half maximum, is experimentally measured to be 1.3λ, which agrees very well with the theoretical estimation $\mathrm{DOF} = \lambda/(1 - \sqrt{1 - \mathrm{NA}^2}) \approx 1.25\lambda$ [180]. The imaging efficiency and the level of secondary lobes are 68% and −8.5 dB in this configuration, respectively. The imaging efficiency ϵ_{img} is calculated as the reflected power in the focal spot divided over the total reflected power

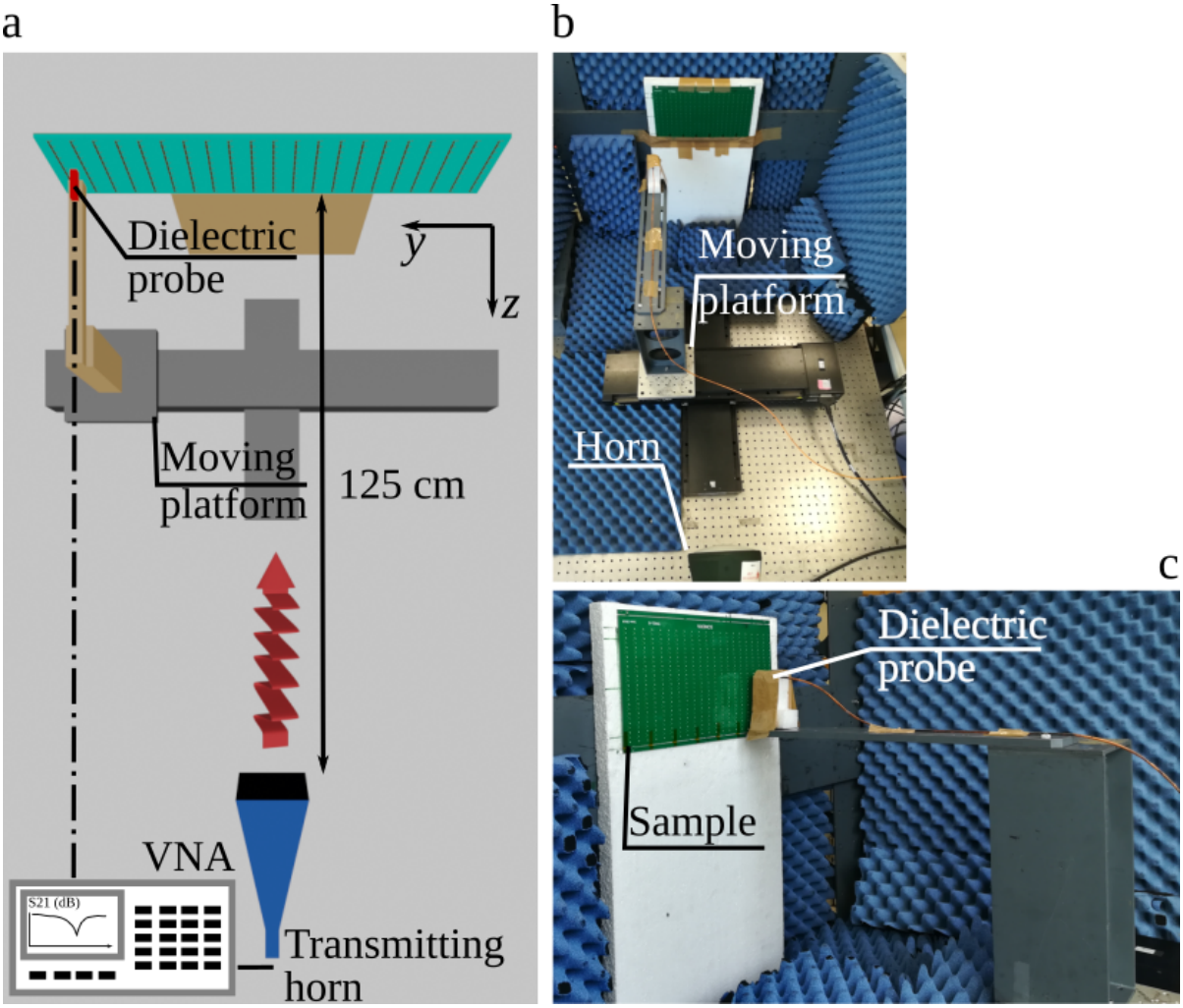

Figure 5.16: A schematic illustration ***(a)*** *and photographs* ***(b),(c)*** *of the experimental setup to measure distribution of the electric field.*

in the focal plane

$$\epsilon_{img} = \left(\int_{y_1}^{y_2} |E_x(y, z_f) - E_x^{(inc)}(y, z_f)|^2 \mathrm{d}y\right) \Big/ \left(\int_{y_{min}}^{y_{max}} |E_x(y, z_f) - E_x^{(inc)}(y, z_f)|^2 \mathrm{d}y\right), \quad (5.15)$$

where the coordinates y_1 and y_2 refer to the lateral limits of the focal spot.

By changing the applied voltage sequence and thus the load-impedance densities, one can move the focal spot further away from the sample and change the NA of the lens, from 0.98 in Fig. 5.17(b) to 0.83 in Fig. 5.17(d). The spot size of 0.67λ is still smaller than the size 0.74λ of the corresponding Airy spot. Multiple subdiffraction focal spots can also be created and independently controlled (Fig. 5.17(e) and Figs. 5.18 and 5.19), demonstrating the high efficiency and manipulation flexibility of the real-time reconfigurable metasurface. In Figs. 5.17(d) and (e), the measured DOF and its corresponding theoretical estimation is, respectively, 2.4λ and 2.26λ. The imaging efficiency and the level of secondary lobes are measured to be 78% and -12

dB for the λ distance single focal point configuration and 88% and -10.9 dB in the case of the 3λ distance double focal points.

5.7.1 Direct evidence of strongly non-local response

Extracting the amplitude and phase of the electric field in the proximity of the sample allows one to *directly* observe surface waves manifesting strong non-locality. Performing discrete Fourier transform (Eq. (5.8)) on the measured electric field at the distance $\lambda/10$ from the metasurface reveals two strong peaks outside the visible range ($k_y/k_0 > 1$), as shown in Figure 5.17(c). The peaks correspond to two surface waves propagating along the sample in opposite directions. Although the surface waves contribute to the aperture field creating the subdiffraction focal spot, being evanescent they are not responsible for breaking the diffraction limit for focal length of λ. Indeed, the spectrum of the field in the focal plane consists in only propagating waves as shown in Fig. 5.20. On the other hand, if one moves the focal point closer to the metasurface, surface waves can be used to perform super-focusing and achieve the spot size much less than that of the subdiffraction limit (0.38λ, NA ≈ 1). To that end a denser, but still sparse, metasurface is required. In Fig. 5.21, an example of a sparse metasurface with the inter-wire distance of $\lambda_0/4$ demonstrates focusing of the incident wave at $\lambda/10$ focal length to the spot size of 0.15λ. In strong contrast to the phenomenon of super-oscillations [180], which also allows to overcome the subdiffraction limit, the level of side lobes remains very low due to the surface waves contributing significantly to the formation of the focal spot as revealed. The results are also compared to the case of $\lambda_0/2$ inter-wire distance and 21-wire metasurface, it is seen that the level of secondary lobes is much lower with the 41-wire metasurface and $\lambda_0/4$ inter-wire distance.

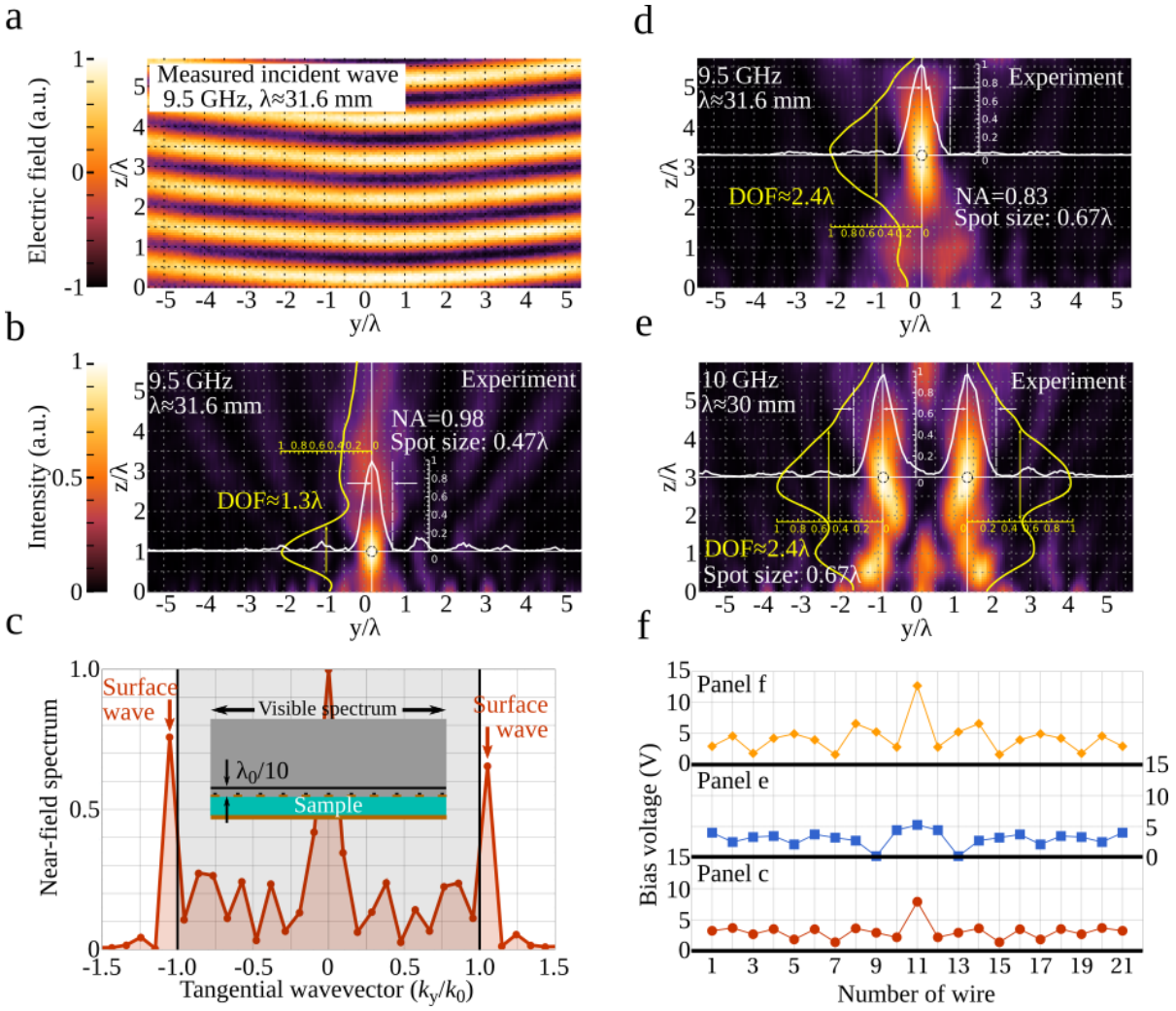

Figure 5.17: ***(a)*** *The measured electric field of the incident wave radiated by the transmitting horn antenna.* ***(b)***, ***(d)***, ***(e)*** *The measured normalized intensity of the scattered wave* $|E_x(y,z) - E_x^{(inc)}(y,z)|^2$ *for three different configurations of the reconfigurable sparse metasurface: single focal point at the distance* λ ***(b)*** *and* 3λ ***(d)***, *when frequency is* 9.5 *GHz,* ***(e)*** *two focal points at the distance* 3λ, *when frequency is* 10 *GHz.* ***(c)*** *Spectrum of the electric field along the sample measured at the distance* $\lambda/10$ *from the sample in the configuration presented in the panel* ***(b)***, *showing surface waves propagating in opposite directions along the metasurface.* ***(f)*** *Bias voltages applied to each wire in the different configurations shown in the panels* ***(b)***,***(d)***,***(e)***.

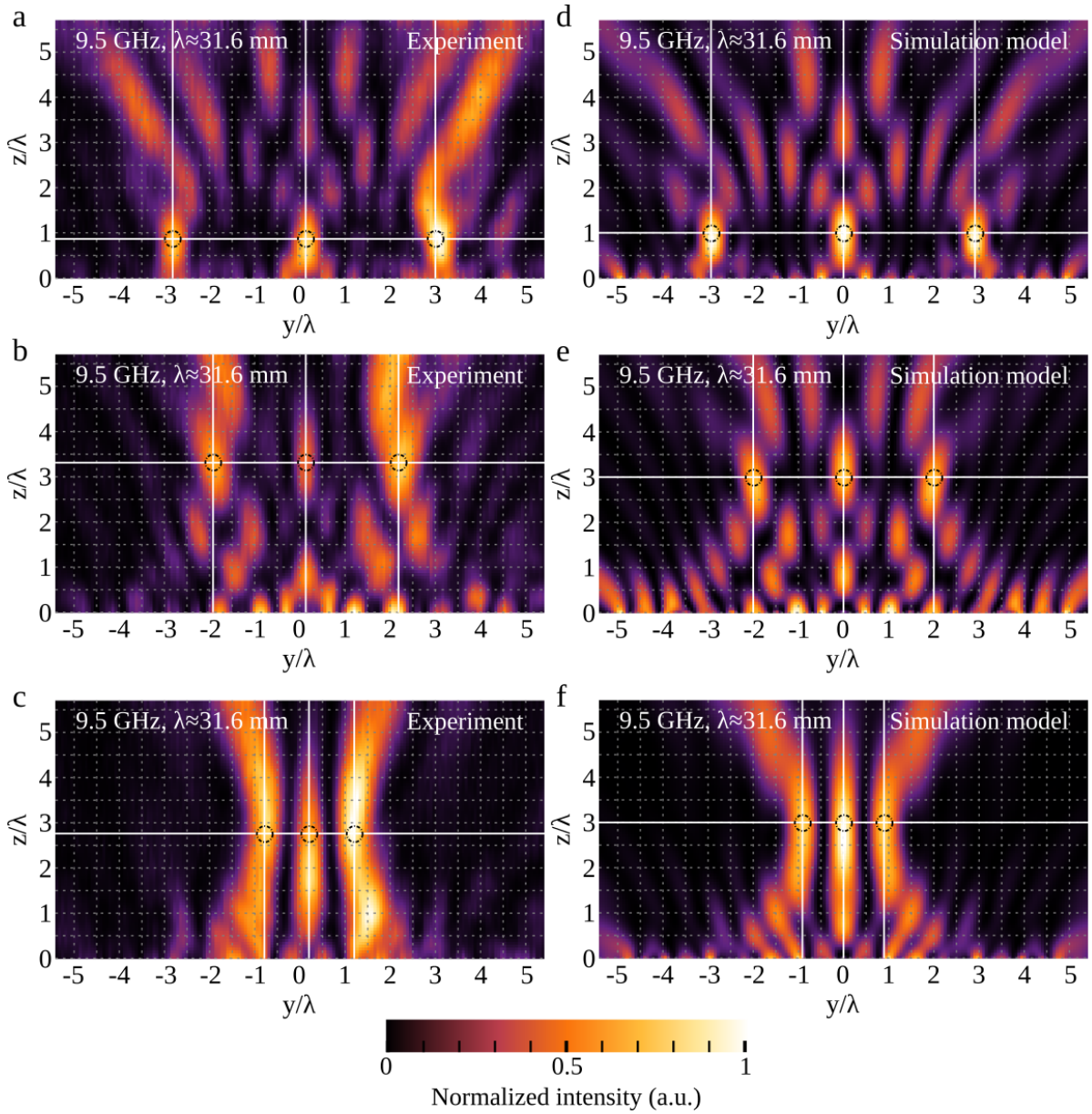

Figure 5.18: Different examples of creating three focal spots at 9.5 GHz. The panels ***(a)–(c)*** *and* ***(d)–(f)*** *show experimental and corresponding simulation results, respectively.*

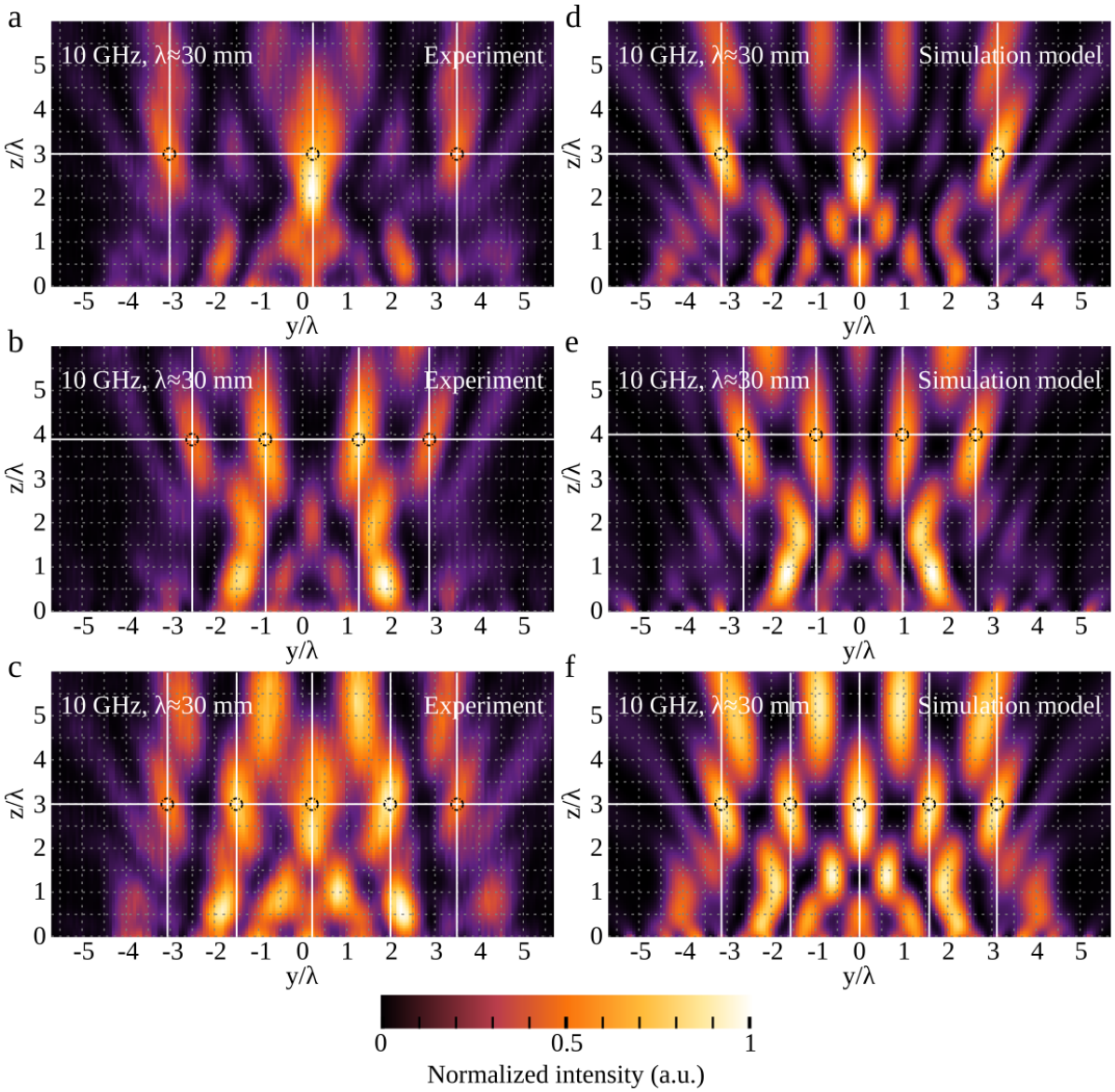

Figure 5.19: Different examples of creating three ***(a)****, four* ***(b)*** *and five* ***(c)*** *focal spots at 10 GHz. The panels* ***(a)****–****(c)*** *and* ***(d)****–****(e)*** *show experimental and corresponding simulation results, respectively.*

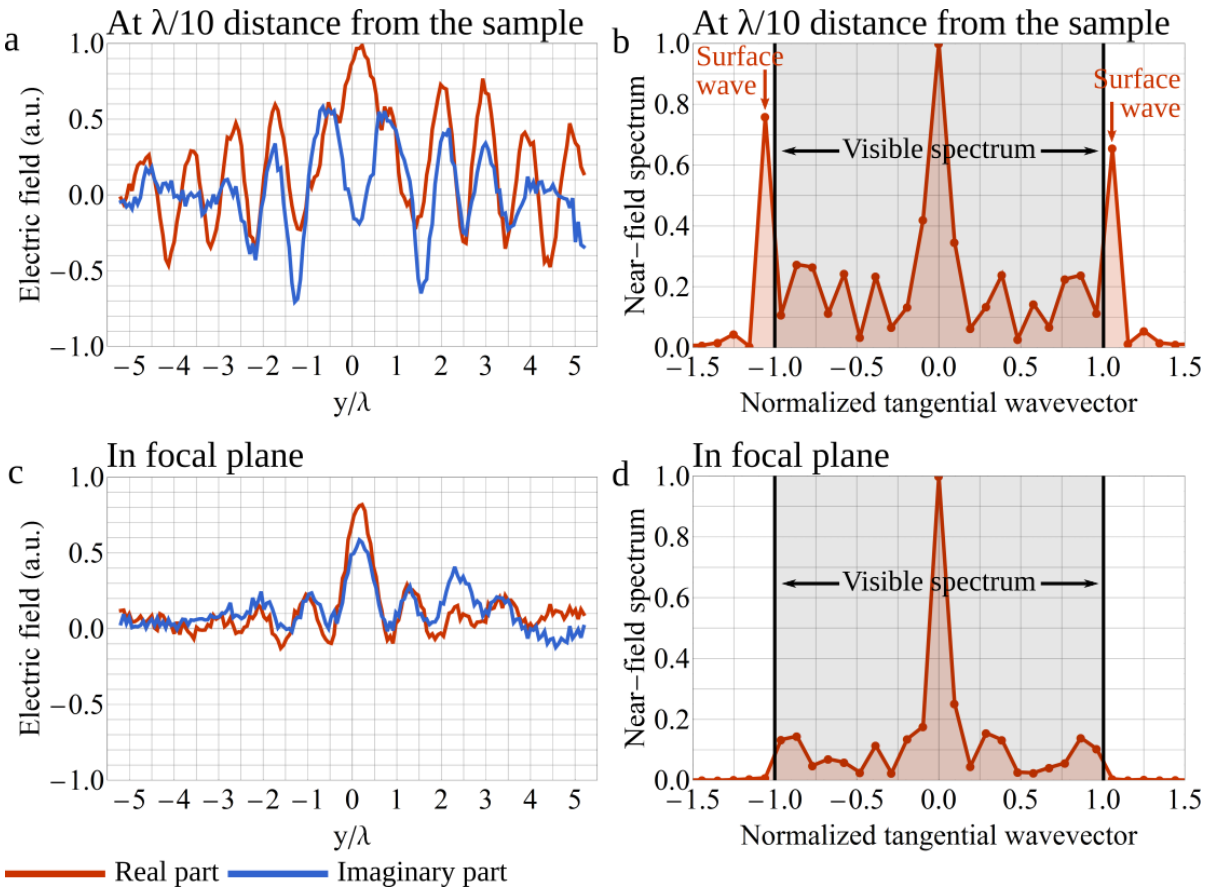

Figure 5.20: Experimental data when the sample performs a single spot on-axis focusing at λ distance. The panels ***(a)*** *and* ***(c)*** *show 1D spatial profiles of the scattered electric field measured* ***(a)*** *in the proximity to the sample (at λ/10 distance) and* ***(c)*** *in the focal plane (at λ distance). The corresponding 2D spatial distribution of the normalized intensity is shown in Fig. 5.17(b). The panels* ***(b)*** *and* ***(c)*** *show normalized spectrum of the scattered electric field* ***(b)*** *at λ/10 distance and* ***(d)*** *in the focal plane (λ distance).*

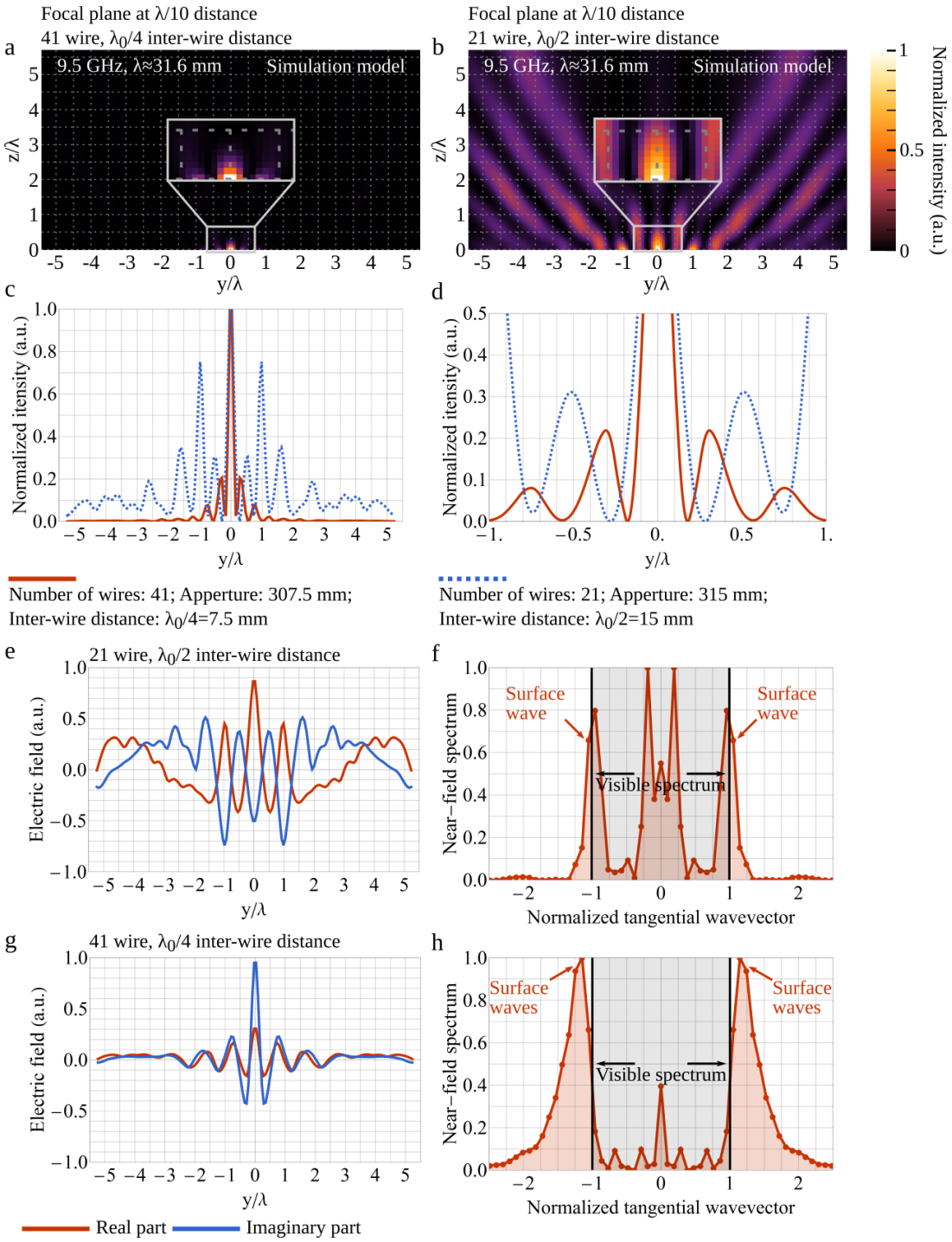

Figure 5.21: The panels ***(a)*** *and* ***(b)*** *show 2D spatial distributions of the normalized intensity obtained from the simulation model of focusing at* $\lambda/10$ *by sparse metasurfaces composed of 41* ***(a)*** *and 21* ***(b)*** *reactively-loaded wires. The inset figures in the panels* ***(a)*** *and* ***(b)*** *are close-ups of the corresponding regions. The inter-wire distances are 7.5 mm for the 41-wire metasurface and 15 mm for the 21-wire metasurface. The dielectric substrate is the same in both cases, the relative permittivity is* 2.2 *and the thickness is* 2.65 *mm, respectively. The panel* ***(c)*** *shows 1D spatial profiles of the normalized intensities in the focal planes. The panels* ***(d)*** *is the close-up of the corresponding regions in the panel* ***(c)****. The panels* ***(e)*** *and* ***(g)*** *show 1D spatial profiles of the scattered electric field recorded in the proximity to the sparse metasurface (at* $\lambda/10$ *distance). The panels* ***(f)*** *and* ***(h)*** *show normalized near-field spectrum corresponding to the panels* ***(e)*** *and* ***(g)****, respectively.*

5.8. Conclusion

In this Chapter, I have demonstrated the application of the analytical model developed for sparse metasurfaces presented in the Fourth Chapter for the design and analysis of reconfigurable sparse metasurfaces. The main practical consequence of this work is that I have demonstrated a little bit counter-intuitive result: by reducing the density of meta-atoms and, thus, complexity of the sparse metasurface design and its fabrication, one is actually able to outperform conventional metasurfaces which often requires a more sophisticated design. It can be especially useful for implementation of reconfigurable metasurfaces at optical and visible frequencies where they suffer a lot from efficiency problems. The design procedure is no longer based on a simple adjustment of the phase response of a meta-atom according to Eq. (1.1), but on calculating a Green's function, accurately modelling the excitation source and solving the inverse scattering problem. As a direct endorsement of the proposed approach, a reconfigurable sparse metasurface loaded with controllable varactor diodes has been proposed to efficiently and dynamically manipulate fields in both near-field and far-field regions with an arbitrary incident wave illumination. The analytical model has thus demonstrated its robustness with respect to inaccuracies of the simple characterization procedure of the sample and varactor diodes, inaccuracies of the positioning the feeding horn with respect to the sample and its idealistic modeling as a point source. Fundamentally, I have experimentally demonstrated direct and indirect evidences of surface waves propagating along the reconfigurable sparse metasurface manifesting its strongly non-local response and allowing to perform subdiffraction focusing and anomalous reflection at extreme angles beyond limits of conventional metasurface designs. Furthermore, excitation and dynamic control of multiple beams (up to six) in the far-field and multiple focal spots in the near-field have been demonstrated. The ability of the proposed sparse metasurface to dynamically manipulate near- and far-fields in real-time should pave the way to applications in reconfigurable devices such as lenses, antennas and imaging systems with superior performances.

General Conclusions and Outlooks

In the course of this PhD, I have studied conventional concepts and tools to describe and design reconfigurable metasurfaces, determined their limitations and the source of these limitations. In literature, metasurfaces are generally described by means of local reflection and transmission coefficients or electric and magnetic surface impedances which, being effective-medium models, substantially rub out microscopic features of a metasurface design and fundamentally limit its efficiency. I have also studied principal configurations of metasurface-based reconfigurable antennas and tunable elements used to implement a reconfigurability mechanism at microwave frequencies. The main results of this part of the research work have been summarized in the First Chapter. In the rest four chapters of the manuscript, I have developed and presented microscopic analytical models and design approaches of one-dimensional arrays of structured wires for manipulation of electromagnetic waves.

In the Second Chapter, a theoretical model for periodic arrays of scatterers, which I refer to as metagratings, has been presented. The question of the number of degrees of freedom necessary for the manipulation of propagating diffraction orders at will has been studied. Thus, it has been shown that the power of an incident wave can be arbitrarily redistributed between M propagating diffraction orders by means of $N = M$ loaded wires per period. Since it generally requires engineering active and lossy loads, I have also demonstrated that accurate adjustment of the near-field is possible by introducing additional wires in a supercell and facilitates the power balancing with purely reactive metagratings. A semi-analytical design procedure of microwave metagratings and an experimental validation of the developed concept has been presented. Even though the fabricated metagratings remind a lot of conventional dense metasurfaces, an attempt to describe them in terms of surface impedances would lead to a contradictory conclusion: resulted surface impedances would have non-trivial real parts (positive or negative), when in

fact the structures are purely reactive. It highlights yet another time the importance of adopted theoretical models which may lead to opposite conclusions, even when applied to describe the same physical structures.

In the Third Chapter, an analytical retrieval approach has been developed, which, when accompanied by full-wave simulations, has allowed to consider arbitrarily complex geometries of meta-atoms for metagratings and sparse metasurfaces operating from microwave to optical domains. In bright contrast to the local periodic approximation used for designing conventional metasurfaces, the simple and accurate analytical formulas have been proposed in the manuscript to subtract the field induced on the central wire by the metal-backed dielectric substrate and the neighboring wires. It makes the developed design approach not only fast but also a rigorous one to design metagratings and conformal sparse metasurfaces represented by nonuniform and non-planar arrays of wires. The approach has been validated by means of numerous 3D full-wave simulations and experimental tests of periodic metagratings, semi-cylindrical sparse metasurfaces and reconfigurable planar sparse metasurfaces, which shows its wide generality.

In the Fourth Chapter, the analytical model of metagratings has been generalized from planar to *arbitrarily-shaped* distributions of engineered wires by means of numerical calculation of a Green's function. The concept of conformal sparse metasurfaces has been introduced and represents a radically new approach to design metasurfaces of desired geometries within the same framework and without any adaptation. In strong contrast to metagratings, sparse metasurfaces are considered as non-periodic structures that can be excited by *arbitrary external sources* and are not functionally confined to manipulating diffraction orders. To solve the inverse scattering problem and find an optimal number of wires for constructing conformal sparse metasurfaces in each particular configuration, an optimization procedure has been developed on the basis of particle swarm optimization algorithm. The high accuracy of the developed analytical model and the design procedure of conformal sparse metasurfaces have been demonstrated through examples of semi-cylindrical and cavity-excited sparse metasurfaces. Designs of several semi-cylindrical sparse metasurfaces with different functionalities have been validated experimentally at microwave frequencies, where beam-steering and excitation of multiple beams are demonstrated. In all examples, excitation fields are complex and if conventional design approaches were used, it would deteriorate the efficiency of metasurfaces as discussed in the First Chapter. On the other hand, the developed analytical model allows one to include in the analysis all features of the excitation field and significantly improve the efficiency of metasurfaces in

comparison to conventional approaches. It is also crucial to note that in the demonstrated simulation and experimental examples, the sparse metasurfaces are transmitting while possessing only electric response and being represented by single-layer designs. Meanwhile, conventional approaches to design transmitting metasurfaces demand implementing an effective magnetic response additionally to an electric one or using multilayer designs.

Finally, in the Fifth Chapter, the analytical model of sparse metasurfaces has been applied to design a reconfigurable planar sparse metasurface incorporating varactor diodes as tunable elements. A fabricated sample has experimentally demonstrated dynamic far-field and near-field control. Namely, beam-steering beyond 60°, excitation and dynamic control of multiple beams (up to six) in the far-field and multiple focal spots in the near-field have been shown. Manipulation of multiple beams and focal spots has been demonstrated under the illumination of single horn antenna and, thus, does not require multiple feeding sources. Extreme examples of an anomalous reflection at $-70°$ under the illumination of a wave incident at 45° and high numerical aperture subdiffraction focusing have fundamentally revealed indirect and direct evidences of surface waves propagating along the reconfigurable sparse metasurface manifesting its strongly non-local response. In the results of the work, the analytical model has proved its robustness with respect to inaccuracies of the characterization procedure of the sample, inaccuracies of the experimental setup in positioning the feeding horn with respect to the sample and idealistic modeling of the horn as a point source.

To conclude, I believe that future works in the following directions can be particularly fruitful:

- **Reconfigurable conformal sparse metasurface** can be developed by merging the results of the Fourth and Fifth Chapters. However, a particular focus should be made on characterization of a fabricated conformal metasurface. The procedure used for planar reconfigurable metasurface may not be directly applicable in case of conformal designs. Particularly, the characterization of a unit cell in a waveguide or a cavity can prove useful when corresponding analytical formulas are developed to retrieve the impedance of a reconfigurable element and not of a whole unit cell.

- **Two-dimensional sparse metasurfaces** composed of 2D arrays of electric dipoles will allow one to perform 2D beam-steering and simultaneously deal with both polarizations without involving magnetic meta-atoms. The models of arrays of wires developed in the manuscript can be quite easily generalized to two-dimensional distributions of point dipoles. However, the model of a point dipole may not be accurate for scatterers of a finite size and particular care should be taken to develop a more precise approximation.

- **Independent beam-forming at different frequencies** will allow sparse metasurfaces to further approach the functionality of active electrically scanned antenna arrays. A possible way to approach this problem is to implement an optimization procedure that would take into account frequency dispersion of meta-atoms. However, before that, a theoretical

study should be performed on the possibility and limitations of such a functionality with passive structures.

- **Optical metagratings and sparse metasurfaces**: Although the proof-of-concept demonstrations have been done at microwave frequencies, the main theoretical results are independent of the frequency. Compared to dense metasurfaces widely studied by the optical community [1, 187, 188], significantly decreasing the number of unit cells per wavelength can greatly relax the fabrication constraints and makes it easier to develop metagratings and sparse metasurfaces operating in the optical domain and capable of manipulating wavefronts.

- **Acoustical metagratings and sparse metasurfaces**: Recent advances in the area of manipulating acoustic wavefronts [154, 155, 156, 157] suggest that the developed theory can be also generalized for the needs of the acoustics community. The possibility to develop metagratings for other domains of physics opens an avenue for a plethora of applications.

- **Reconfigurable conformal metasurfaces based on mechanical deformations**: Sparse metasurfaces implemented on flexible substrates can be also advantageous to realize a reconfigurability mechanism based on mechanical deformations [104]. It can represent a fruitful approach to create an adaptive response without complicating a design with tunable elements (which also often bring additional ohmic losses) and bias networks.

Bibliography

[1] N. Yu, P. Genevet, M. A. Kats, F. Aieta, J.-P. Tetienne, F. Capasso, and Z. Gaburro. Light propagation with phase discontinuities: generalized laws of reflection and refraction. *Science*, 334(6054):333–337, 2011.

[2] X. Ni, N. K. Emani, A. V. Kildishev, A. Boltasseva, and V. M. Shalaev. Broadband light bending with plasmonic nanoantennas. *Science*, 335(6067):427–427, 2012.

[3] F. Aieta, P. Genevet, N. Yu, M. A. Kats, Z. Gaburro, and F. Capasso. Out-of-plane reflection and refraction of light by anisotropic optical antenna metasurfaces with phase discontinuities. *Nano Letters*, 12(3):1702–1706, 2012.

[4] S. Sun, K-Y. Yang, C-M. Wang, T-K. Juan, W. T. Chen, C. Y. Liao, Q. He, S. Xiao, W-T. Kung, G-Y. Guo, L. Zhou, and D. P. Tsai. High-efficiency broadband anomalous reflection by gradient meta-surfaces. *Nano Letters*, 12(12):6223–6229, 2012.

[5] A. Díaz-Rubio, V. S. Asadchy, A. Elsakka, and S. A. Tretyakov. From the generalized reflection law to the realization of perfect anomalous reflectors. *Science Advances*, 3(8), 2017.

[6] V. S. Asadchy, A. Díaz-Rubio, S. N. Tcvetkova, D.-H. Kwon, A. Elsakka, M. Albooyeh, and S. A. Tretyakov. Flat engineered multichannel reflectors. *Phys. Rev. X*, 7:031046, Sep 2017.

[7] C. Pfeiffer and A. Grbic. Metamaterial huygens' surfaces: Tailoring wave fronts with reflectionless sheets. *Phys. Rev. Lett.*, 110:197401, May 2013.

[8] Francesco Monticone, Nasim Mohammadi Estakhri, and Andrea Alù. Full control of nanoscale optical transmission with a composite metascreen. *Phys. Rev. Lett.*, 110:203903, May 2013.

[9] M. Kim, A. M. H. Wong, and G. V. Eleftheriades. Optical huygens' metasurfaces with independent control of the magnitude and phase of the local reflection coefficients. *Phys. Rev. X*, 4:041042, Dec 2014.

[10] Y. Yuan, K. Zhang, X. Ding, B. Ratni, S. N. Burokur, and Q. Wu. Complementary transmissive ultra-thin meta-deflectors for broadband polarization-independent refractions in the microwave region. *Photon. Res.*, 7(1):80–88, Jan 2019.

[11] H-X. Xu, L. Han, Y. Li, Y. Sun, J. Zhao, S. Zhang, and C-W. Qiu. Completely spin-decoupled dual-phase hybrid metasurfaces for arbitrary wavefront control. *ACS Photonics*, 6(1):211–220, 2018.

[12] X. Chen, L. Huang, H. Mühlenbernd, G. Li, B. Bai, Q. Tan, G. Jin, C-W. Qiu, S. Zhang, and T. Zentgraf. Dual-polarity plasmonic metalens for visible light. *Nature communications*, 3:1198, 2012.

[13] F. Aieta, P. Genevet, M. A. Kats, N. Yu, R. Blanchard, Z. Gaburro, and F. Capasso. Aberration-free ultrathin flat lenses and axicons at telecom wavelengths based on plasmonic metasurfaces. *Nano Letters*, 12(9):4932–4936, 2012.

[14] X. Ni, S. Ishii, A. V. Kildishev, and V. M. Shalaev. Ultra-thin, planar, babinet-inverted

plasmonic metalenses. *Light: Science & Applications*, 2(4):e72, 2013.

[15] X. Ding, F. Monticone, K. Zhang, L. Zhang, D. Gao, S. N. Burokur, A. de Lustrac, Q. Wu, C-W. Qiu, and A. Alù. Ultrathin pancharatnam–berry metasurface with maximal cross-polarization efficiency. *Advanced Materials*, 27(7):1195–1200, 2015.

[16] A. Alù and N. Engheta. Achieving transparency with plasmonic and metamaterial coatings. *Phys. Rev. E*, 72:016623, Jul 2005.

[17] P-Y. Chen, C. Argyropoulos, and A. Alù. Broadening the cloaking bandwidth with non-foster metasurfaces. *Phys. Rev. Lett.*, 111:233001, Dec 2013.

[18] T. V. Teperik, S. N. Burokur, A. de Lustrac, G. Sabanowski, and G-P. Piau. Experimental validation of an ultra-thin metasurface cloak for hiding a metallic obstacle from an antenna radiation at low frequencies. *Applied Physics Letters*, 111(5):054105, 2017.

[19] S. Sun, Q. He, S. Xiao, Q. Xu, X. Li, and L. Zhou. Gradient-index meta-surfaces as a bridge linking propagating waves and surface waves. *Nature materials*, 11(5):426, 2012.

[20] S. N. Tcvetkova, D.-H. Kwon, A. Díaz-Rubio, and S. A. Tretyakov. Near-perfect conversion of a propagating plane wave into a surface wave using metasurfaces. *Phys. Rev. B*, 97:115447, Mar 2018.

[21] V. Popov, A. Díaz-Rubio, V. Asadchy, S. Tcvetkova, F. Boust, S. Tretyakov, and S. N. Burokur. Omega-bianisotropic metasurface for converting a propagating wave into a surface wave. *Phys. Rev. B*, 100:125103, Sep 2019.

[22] L Huang, X. Chen, H. Mühlenbernd, G. Li, B. Bai, Q. Tan, G. Jin, T. Zentgraf, and S. Zhang. Dispersionless phase discontinuities for controlling light propagation. *Nano Letters*, 12(11):5750–5755, 2012.

[23] M. Q. Mehmood, S. Mei, S. Hussain, K. Huang, S. Y. Siew, L. Zhang, T. Zhang, X. Ling, H. Liu, J. Teng, A. Danner, S. Zhang, and C-W. Qiu. Visible-frequency metasurface for structuring and spatially multiplexing optical vortices. *Advanced Materials*, 28(13):2533–2539, 2016.

[24] G. Li, L. Wu, K. F. Li, S. Chen, C. Schlickriede, Z. Xu, S. Huang, W. Li, Y. Liu, E. Y. B. Pun, T. Zentgraf, K. W. Cheah, Y. Luo, and S. Zhang. Nonlinear metasurface for simultaneous control of spin and orbital angular momentum in second harmonic generation. *Nano Letters*, 17(12):7974–7979, 2017.

[25] K. Zhang, Y. Yuan, D. Zhang, X. Ding, B. Ratni, S. N. Burokur, M. Lu, K. Tang, and Q. Wu. Phase-engineered metalenses to generate converging and non-diffractive vortex beam carrying orbital angular momentum in microwave region. *Opt. Express*, 26(2):1351–1360, Jan 2018.

[26] H-X. Xu, G. Hu, Y. Li, L. Han, J. Zhao, Y. Sun, F. Yuan, G-M. Wang, Z. H. Jiang, X. Ling, T. J. Cui, and C-W. Qiu. Interference-assisted kaleidoscopic meta-plexer for arbitrary spin-wavefront manipulation. *Light: Science & Applications*, 8(1):3, 2019.

[27] K. Zhang, Y. Yuan, X. Ding, B. Ratni, S. N. Burokur, and Q. Wu. High-efficiency metalenses with switchable functionalities in microwave region. *ACS Applied Materials & Interfaces*, 11(31):28423–28430, 2019.

[28] Y. Yifat, M. Eitan, Z. Iluz, Y. Hanein, A. Boag, and J. Scheuer. Highly efficient and broadband wide-angle holography using patch-dipole nanoantenna reflectarrays. *Nano Letters*, 14(5):2485–2490, 2014.

[29] D. Wen, F. Yue, G. Li, G. Zheng, K. Chan, S. Chen, M. Chen, K. F. Li, P. W. H. Wong, K. W. Cheah, E. Y. B. Pun, S. Zhang, and X. Chen. Helicity multiplexed broadband metasurface holograms. *Nature communications*, 6:8241, 2015.

[30] X. Li, L. Chen, Y. Li, X. Zhang, M. Pu, Z. Zhao, X. Ma, Y. Wang, M. Hong, and X. Luo. Multicolor 3d meta-holography by broadband plasmonic modulation. *Science Advances*, 2(11), 2016.

[31] X. Ni, A. V. Kildishev, and V. M. Shalaev. Metasurface holograms for visible light. *Nature*

communications, 4:2807, 2013.

[32] W. Wan, J. Gao, and X. Yang. Metasurface holograms for holographic imaging. *Advanced Optical Materials*, 5(21):1700541, 2017.

[33] Z. Wang, X. Ding, K. Zhang, B. Ratni, S. N. Burokur, X. Gu, and Q. Wu. Huygens metasurface holograms with the modulation of focal energy distribution. *Advanced Optical Materials*, 6(12):1800121, 2018.

[34] J. Y. Lau and S. V. Hum. Reconfigurable transmitarray design approaches for beamforming applications. *IEEE Transactions on Antennas and Propagation*, 60(12):5679–5689, Dec 2012.

[35] A. Clemente, L. Dussopt, R. Sauleau, P. Potier, and P. Pouliguen. Wideband 400-element electronically reconfigurable transmitarray in x band. *IEEE Transactions on Antennas and Propagation*, 61(10):5017–5027, Oct 2013.

[36] B. O. Zhu, K. Chen, N. Jia, L. Sun, J. Zhao, T. Jiang, and Y. Feng. Dynamic control of electromagnetic wave propagation with the equivalent principle inspired tunable metasurface. *Scientific reports*, 4(1):1–7, 2014.

[37] Tie Jun Cui, Mei Qing Qi, Xiang Wan, Jie Zhao, and Qiang Cheng. Coding metamaterials, digital metamaterials and programmable metamaterials. *Light: Science & Applications*, 3(10):e218, 2014.

[38] C. Della Giovampaola and N. Engheta. Digital metamaterials. *Nature materials*, 13(12):1115, 2014.

[39] N. Kaina, M. Dupré, G. Lerosey, and M. Fink. Shaping complex microwave fields in reverberating media with binary tunable metasurfaces. *Scientific reports*, 4(1):1–8, 2014.

[40] W. Zhu, Q. Song, L. Yan, W. Zhang, P-C. Wu, L. K. Chin, H. Cai, D. P. Tsai, Z. X. Shen, T. W. Deng, S. K. Ting, Y. Gu, G. Q. Lo, D. L. Kwong, Z. C. Yang, R. Huang, A-Q. Liu, and N. Zheludev. A flat lens with tunable phase gradient by using random access reconfigurable metamaterial. *Advanced Materials*, 27(32):4739–4743, 2015.

[41] M. Dupré, P. del Hougne, M. Fink, F. Lemoult, and G. Lerosey. Wave-field shaping in cavities: Waves trapped in a box with controllable boundaries. *Phys. Rev. Lett.*, 115:017701, Jul 2015.

[42] H.-X. Xu, S. Sun, S. Tang, S. Ma, Q. He, G.-M. Wang, T. Cai, H.-P. Li, and L. Zhou. Dynamical control on helicity of electromagnetic waves by tunable metasurfaces. *Scientific reports*, 6(1):1–10, 2016.

[43] H. Yang, X. Cao, F. Yang, J. Gao, S. Xu, M. Li, X. Chen, Y. Zhao, Y. Zheng, and S. Li. A programmable metasurface with dynamic polarization, scattering and focusing control. *Scientific reports*, 6:35692, 2016.

[44] Y. B. Li, L. L. Li, B. B. Xu, W. Wu, R. Y. Wu, X. Wan, Q. Cheng, and T. J. Cui. Transmission-type 2-bit programmable metasurface for single-sensor and single-frequency microwave imaging. *Scientific reports*, 6:23731, 2016.

[45] H.-X. Xu, S. Tang, S. Ma, W. Luo, T. Cai, S. Sun, Q. He, and L. Zhou. Tunable microwave metasurfaces for high-performance operations: dispersion compensation and dynamical switch. *Scientific reports*, 6:38255, 2016.

[46] P. del Hougne, F. Lemoult, M. Fink, and G. Lerosey. Spatiotemporal wave front shaping in a microwave cavity. *Phys. Rev. Lett.*, 117:134302, Sep 2016.

[47] K. Chen, Y. Feng, F. Monticone, J. Zhao, B. Zhu, T. Jiang, L. Zhang, Y. Kim, X. Ding, S. Zhang, A. Alù, and C.-W. Qiu. A reconfigurable active huygens' metalens. *Advanced Materials*, 29(17):1606422, 2017.

[48] L. Li, T. J. Cui, W. Ji, S. Liu, J. Ding, X. Wan, Y. B. Li, M. Jiang, C.-W. Qiu, and S. Zhang. Electromagnetic reprogrammable coding-metasurface holograms. *Nature communications*, 8(1):1–7, 2017.

[49] B. Ratni, A. de Lustrac, G.-P. Piau, and S. N. Burokur. Reconfigurable meta-mirror for

wavefronts control: applications to microwave antennas. *Opt. Express*, 26(3):2613–2624, Feb 2018.

[50] P. del Hougne, M. F Imani, T. Sleasman, J. N. Gollub, M. Fink, G. Lerosey, and D. R. Smith. Dynamic metasurface aperture as smart around-the-corner motion detector. *Scientific reports*, 8(1):1–10, 2018.

[51] A. Komar, R. Paniagua-Dominguez, A. Miroshnichenko, Y. F. Yu, Y. S. Kivshar, A. I. Kuznetsov, and D. Neshev. Dynamic beam switching by liquid crystal tunable dielectric metasurfaces. *ACS Photonics*, 5(5):1742–1748, 2018.

[52] P. del Hougne and G. Lerosey. Leveraging chaos for wave-based analog computation: Demonstration with indoor wireless communication signals. *Phys. Rev. X*, 8:041037, Nov 2018.

[53] L. Li, Y. Shuang, Q. Ma, H. Li, H. Zhao, M. Wei, C. Liu, C. Hao, C.-W. Qiu, and T. J. Cui. Intelligent metasurface imager and recognizer. *Light: Science & Applications*, 8(1):1–9, 2019.

[54] Q. Ma, G. D. Bai, H. B. Jing, C. Yang, L. Li, and T. J. Cui. Smart metasurface with self-adaptively reprogrammable functions. *Light: Science & Applications*, 8(1):1–12, 2019.

[55] F. Liu, O. Tsilipakos, A. Pitilakis, A. C. Tasolamprou, M. S. Mirmoosa, N. V. Kantartzis, D-H. Kwon, J. Georgiou, K. Kossifos, M. A. Antoniades, M. Kafesaki, C. M. Soukoulis, and S. A. Tretyakov. Intelligent metasurfaces with continuously tunable local surface impedance for multiple reconfigurable functions. *Phys. Rev. Applied*, 11:044024, Apr 2019.

[56] P. del Hougne, M. Fink, and G. Lerosey. Optimally diverse communication channels in disordered environments with tuned randomness. *Nature Electronics*, 2(1):36–41, 2019.

[57] A. Leitis, A. Heßler, S. Wahl, M. Wuttig, T. Taubner, A. Tittl, and H. Altug. All-dielectric programmable huygens' metasurfaces. *Advanced Functional Materials*, page 1910259, 2020.

[58] Y. Hadad, D. L. Sounas, and A. Alù. Space-time gradient metasurfaces. *Phys. Rev. B*, 92:100304, Sep 2015.

[59] J. Zhao, X. Yang, J. Y. Dai, Q. Cheng, X. Li, N. H. Qi, J. C. Ke, G. D. Bai, S. Liu, S. Jin, A. Alù, and T. J. Cui. Programmable time-domain digital-coding metasurface for non-linear harmonic manipulation and new wireless communication systems. *National Science Review*, 6(2):231–238, 11 2018.

[60] L. Zhang, X. Q. Chen, S. Liu, Q. Zhang, J. Zhao, J. Y. Dai, G. D. Bai, X. Wan, Q. Cheng, G. Castaldi, V. Galdi, and T. J. Cui. Space-time-coding digital metasurfaces. *Nature communications*, 9(1):1–11, 2018.

[61] M. Liu, D. A. Powell, Y. Zarate, and I. V. Shadrivov. Huygens' metadevices for parametric waves. *Phys. Rev. X*, 8:031077, Sep 2018.

[62] M. M. Salary, S. Jafar-Zanjani, and H. Mosallaei. Electrically tunable harmonics in time-modulated metasurfaces for wavefront engineering. *New Journal of Physics*, 20(12):123023, dec 2018.

[63] C. Caloz, A. Alù, S. Tretyakov, D. Sounas, K. Achouri, and Z.-L. Deck-Léger. Electromagnetic nonreciprocity. *Phys. Rev. Applied*, 10:047001, Oct 2018.

[64] J.W. Zang, D. Correas-Serrano, J.T.S. Do, X. Liu, A. Alvarez-Melcon, and J.S. Gomez-Diaz. Nonreciprocal wavefront engineering with time-modulated gradient metasurfaces. *Phys. Rev. Applied*, 11:054054, May 2019.

[65] J.W. Zang, A. Alvarez-Melcon, and J.S. Gomez-Diaz. Nonreciprocal phased-array antennas. *Phys. Rev. Applied*, 12:054008, Nov 2019.

[66] M.S. Mirmoosa, G.A. Ptitcyn, V.S. Asadchy, and S.A. Tretyakov. Time-varying reactive elements for extreme accumulation of electromagnetic energy. *Phys. Rev. Applied*, 11:014024, Jan 2019.

[67] G. Ptitcyn, M. S. Mirmoosa, and S. A. Tretyakov. Time-modulated meta-atoms. *Phys. Rev. Research*, 1:023014, Sep 2019.

[68] S. Ebadi, R. V. Gatti, and R. Sorrentino. Linear reflectarray antenna design using 1-bit digital phase shifters. In *2009 3rd European Conference on Antennas and Propagation*, pages 3729–3732, 2009.

[69] S. Montori, F. Cacciamani, R. V. Gatti, E. Carrasco, M. Barba, J. Encinar, and R. Sorrentino. Wideband dual-polarization reconfigurable elementary cell for electronic steerable reflectarray at ku-band. In *Proceedings of the Fourth European Conference on Antennas and Propagation*, pages 1–5, 2010.

[70] J. Perruisseau-Carrier, F. Bongard, R. Golubovic-Niciforovic, R. Torres-Sánchez, and J. R. Mosig. Contributions to the modeling and design of reconfigurable reflecting cells embedding discrete control elements. *IEEE Transactions on Microwave Theory and Techniques*, 58(6):1621–1628, 2010.

[71] A. Clemente, L. Dussopt, R. Sauleau, P. Potier, and P. Pouliguen. 1-bit reconfigurable unit cell based on pin diodes for transmit-array applications in x -band. *IEEE Transactions on Antennas and Propagation*, 60(5):2260–2269, 2012.

[72] S. V. Hum and J. Perruisseau-Carrier. Reconfigurable reflectarrays and array lenses for dynamic antenna beam control: A review. *IEEE Transactions on Antennas and Propagation*, 62(1):183–198, Jan 2014.

[73] S. B. Glybovski, S. A. Tretyakov, P. A. Belov, Y. S. Kivshar, and C. R. Simovski. Metasurfaces: From microwaves to visible. *Physics Reports*, 634:1 – 72, 2016. Metasurfaces: From microwaves to visible.

[74] R. J. Mailloux. *Phased Array Antenna Handbook, Third Edition*. Artech House, Norwood, 2017.

[75] D. M. Pozar, S. D. Targonski, and H. D. Syrigos. Design of millimeter wave microstrip reflectarrays. *IEEE Transactions on Antennas and Propagation*, 45(2):287–296, Feb 1997.

[76] X. Wan, M. Q. Qi, T. Y. Chen, and T. J. Cui. Field-programmable beam reconfiguring based on digitally-controlled coding metasurface. *Scientific reports*, 6:20663, 2016.

[77] Q. He, S. Sun, and L. Zhou. Tunable/reconfigurable metasurfaces: Physics and applications. *Research*, 2019:1849272, 2019.

[78] T. Cui, B. Bai, and H.-B. Sun. Tunable metasurfaces based on active materials. *Advanced Functional Materials*, 29(10):1806692, 2019.

[79] H. Yang, F. Yang, X. Cao, S. Xu, J. Gao, X. Chen, M. Li, and T. Li. A 1600-element dual-frequency electronically reconfigurable reflectarray at x/ku-band. *IEEE Transactions on Antennas and Propagation*, 65(6):3024–3032, 2017.

[80] P. Nayeri, F. Yang, and A. Z. Elsherbeni. Design and experiment of a single-feed quad-beam reflectarray antenna. *IEEE Transactions on Antennas and Propagation*, 60(2):1166–1171, 2012.

[81] P. Nayeri, F. Yang, and A. Z. Elsherbeni. Design of single-feed reflectarray antennas with asymmetric multiple beams using the particle swarm optimization method. *IEEE Transactions on Antennas and Propagation*, 61(9):4598–4605, 2013.

[82] R. Mittra, editor. *Developments in Antenna Analysis and Design: Volume 2*. Electromagnetic Waves. Institution of Engineering and Technology, 2018.

[83] S. Liu, T. J. Cui, L. Zhang, Q. Xu, Q. Wang, X. Wan, J. Q. Gu, W. X. Tang, M. Qing Qi, J. G. Han, W. L. Zhang, X. Y. Zhou, and Q. Cheng. Convolution operations on coding metasurface to reach flexible and continuous controls of terahertz beams. *Advanced Science*, 3(10):1600156, 2016.

[84] C. Zhang, J. Yang, L. X. Yang, J. C. Ke, M. Z. Chen, W. K. Cao, M. Chen, Z. H. Wu, J. F. Chen, Q. Cheng, and T. J. Cui. Convolution operations on time-domain digital coding metasurface for beam manipulations of harmonics. *Nanophotonics*, (0):20190538, 2020.

[85] X. G. Zhang, Q. Yu, W. X. Jiang, Y. L. Sun, L. Bai, Q. Wang, C.-W. Qiu, and T. J. Cui. Polarization-controlled dual-programmable metasurfaces. *Advanced Science*, page

1903382, 2020.

[86] W. W. Lam, C. F. Jou, H. Z. Chen, K. S. Stolt, N. C. Luhmann, and D. B. Rutledge. Millimeter-wave diode-grid phase shifters. *IEEE Transactions on Microwave Theory and Techniques*, 36(5):902–907, 1988.

[87] R. B. Waterhouse and N. V. Shuley. Scan performance of infinite arrays of microstrip patch elements loaded with varactor diodes. *IEEE Transactions on Antennas and Propagation*, 41(9):1273–1280, 1993.

[88] L. B. Sjogren, Hong-Xia Liu, Xiaohui Qin, C. W. Domier, and N. C. Luhmann. Phased array operation of a diode grid impedance surface. *IEEE Transactions on Microwave Theory and Techniques*, 42(4):565–572, 1994.

[89] D. F. Sievenpiper, J. H. Schaffner, H. J. Song, R. Y. Loo, and G. Tangonan. Two-dimensional beam steering using an electrically tunable impedance surface. *IEEE Transactions on Antennas and Propagation*, 51(10):2713–2722, 2003.

[90] S. V. Hum and M. Okoniewski. An electronically tunable reflectarray using varactor diode-tuned elements. In *IEEE Antennas and Propagation Society Symposium, 2004.*, volume 2, pages 1827–1830 Vol.2, 2004.

[91] S. V. Hum, M. Okoniewski, and R. J. Davies. Realizing an electronically tunable reflectarray using varactor diode-tuned elements. *IEEE Microwave and Wireless Components Letters*, 15(6):422–424, June 2005.

[92] G. Perez-Palomino, M. Barba, J. A. Encinar, R. Cahill, R. Dickie, P. Baine, and M. Bain. Design and demonstration of an electronically scanned reflectarray antenna at 100 ghz using multiresonant cells based on liquid crystals. *IEEE Transactions on Antennas and Propagation*, 63(8):3722–3727, 2015.

[93] Electronically reconfigurable reflectarrays with nematic liquid crystals. *Electronics Letters*, 42:899–900(1), August 2006.

[94] R. Marin, A. Moessinger, F. Goelden, S. Mueller, and R. Jakoby. 77 ghz reconfigurable reflectarray with nematic liquid crystal. *IET Conference Proceedings*, pages 9–9(1), January 2007.

[95] W. Hu, R. Cahill, J. A. Encinar, R. Dickie, H. Gamble, V. Fusco, and N. Grant. Design and measurement of reconfigurable millimeter wave reflectarray cells with nematic liquid crystal. *IEEE Transactions on Antennas and Propagation*, 56(10):3112–3117, 2008.

[96] A Gaebler, A Moessinger, F Goelden, A Manabe, M Goebel, R Follmann, D Koether, C Modes, A Kipka, M Deckelmann, et al. Liquid crystal-reconfigurable antenna concepts for space applications at microwave and millimeter waves. *International Journal of Antennas and Propagation*, 2009, 2009.

[97] G. Perez-Palomino, R. Florencio, J. A. Encinar, M. Barba, R. Dickie, R. Cahill, P. Baine, M. Bain, and R. R. Boix. Accurate and efficient modeling to calculate the voltage dependence of liquid crystal-based reflectarray cells. *IEEE Transactions on Antennas and Propagation*, 62(5):2659–2668, 2014.

[98] S. N. Burokur, J.-P. Daniel, P. Ratajczak, and A. de Lustrac. Tunable bilayered metasurface for frequency reconfigurable directive emissions. *Applied Physics Letters*, 97(6):064101, 2010.

[99] R. Guzmán-Quirós, A. R. Weily, J. L. Gómez-Tornero, and Y. J. Guo. A Fabry-Pérot antenna with two-dimensional electronic beam scanning. *IEEE Transactions on Antennas and Propagation*, 64(4):1536–1541, 2016.

[100] H. Li, C. Ma, F. Shen, K. Xu, D. Ye, J. Huangfu, C. Li, L. Ran, and T. A. Denidni. Wide-angle beam steering based on an active conformal metasurface lens. *IEEE Access*, 7:185264–185272, 2019.

[101] D. Germain, D. Seetharamdoo, S. N. Burokur, and A. de Lustrac. Phase-compensated metasurface for a conformal microwave antenna. *Applied Physics Letters*, 103(12):124102,

2013.

[102] D. J. Gregoire. 3-D conformal metasurfaces. *IEEE Antennas and Wireless Propagation Letters*, 12:233–236, 2013.

[103] L. Liang, M. Qi, J. Yang, X. Shen, J. Zhai, W. Xu, B. Jin, W. Liu, Y. Feng, C. Zhang, H. Lu, H-T. Chen, L. Kang, W. Xu, J. Chen, T. J. Cui, P. Wu, and S. Liu. Anomalous terahertz reflection and scattering by flexible and conformal coding metamaterials. *Advanced Optical Materials*, 3(10):1374–1380, 2015.

[104] S. Walia, C. M. Shah, P. Gutruf, H. Nili, D. R. Chowdhury, W. Withayachumnankul, M. Bhaskaran, and S. Sriram. Flexible metasurfaces and metamaterials: A review of materials and fabrication processes at micro- and nano-scales. *Applied Physics Reviews*, 2(1):011303, 2015.

[105] Jierong Cheng, Samad Jafar-Zanjani, and Hossein Mosallaei. All-dielectric ultrathin conformal metasurfaces: lensing and cloaking applications at 532 nm wavelength. *Scientific reports*, 6:38440, 2016.

[106] S. M. Kamali, A. Arbabi, E. Arbabi, Y. Horie, and A. Faraon. Decoupling optical function and geometrical form using conformal flexible dielectric metasurfaces. *Nature communications*, 7:11618, 2016.

[107] H-X. Xu, S. Tang, C. Sun, L. Li, H. Liu, X. Yang, F. Yuan, and Y. Sun. High-efficiency broadband polarization-independent superscatterer using conformal metasurfaces. *Photon. Res.*, 6(8):782–788, Aug 2018.

[108] E. F. Kuester, M. A. Mohamed, M. Piket-May, and C. L. Holloway. Averaged transition conditions for electromagnetic fields at a metafilm. *IEEE Transactions on Antennas and Propagation*, 51(10):2641–2651, Oct 2003.

[109] K. Wu, P. Coquet, Q. J. Wang, and P. Genevet. Modelling of free-form conformal metasurfaces. *Nature communications*, 9(1):3494, 2018.

[110] C. Pfeiffer and A. Grbic. Metamaterial Huygens' surfaces: Tailoring wave fronts with reflectionless sheets. *Physical Review Letters*, 110(19):1–5, 2013.

[111] S. A. Schelkunoff. Some equivalence theorems of electromagnetics and their application to radiation problems. *The Bell System Technical Journal*, 15(1):92–112, Jan 1936.

[112] A. Epstein and G. V. Eleftheriades. Huygens' metasurfaces via the equivalence principle: design and applications. *J. Opt. Soc. Am. B*, 33(2):A31–A50, Feb 2016.

[113] C. Pfeiffer and A. Grbic. Controlling vector bessel beams with metasurfaces. *Phys. Rev. Applied*, 2:044012, Oct 2014.

[114] Z. Lin, X. Li, R. Zhao, X. Song, Y. Wang, and L. Huang. High-efficiency bessel beam array generation by huygens metasurfaces. *Nanophotonics*, 8(6):1079–1085, 2019.

[115] W. Hao, M. Deng, S. Chen, and L. Chen. High-efficiency generation of airy beams with huygens' metasurface. *Phys. Rev. Applied*, 11:054012, May 2019.

[116] Ariel Epstein and George V. Eleftheriades. Passive lossless huygens' metasurfaces for conversion of arbitrary source field to directive radiation. *IEEE Transactions on Antennas and Propagation*, 62(11):5680–5695, 2014.

[117] A. Epstein and G. V. Eleftheriades. Arbitrary power-conserving field transformations with passive lossless omega-type bianisotropic metasurfaces. *IEEE Transactions on Antennas and Propagation*, 64(9):3880–3895, Sept 2016.

[118] V. S. Asadchy, M. Albooyeh, S. N. Tcvetkova, A. Díaz-Rubio, Y. Ra'di, and S. A. Tretyakov. Perfect control of reflection and refraction using spatially dispersive metasurfaces. *Phys. Rev. B*, 94:075142, Aug 2016.

[119] N. Mohammadi Estakhri and A. Alù. Wave-front transformation with gradient metasurfaces. *Phys. Rev. X*, 6:041008, Oct 2016.

[120] Q. Wang, E. T.F. Rogers, B. Gholipour, C-M. Wang, G. Yuan, J. Teng, and N. I. Zhe-

ludev. Optically reconfigurable metasurfaces and photonic devices based on phase change materials. *Nature Photonics*, 10(1):60, 2016.

[121] Y.-W. Huang, H. W. H. Lee, R. Sokhoyan, R. A. Pala, K. Thyagarajan, S. Han, D. P. Tsai, and H. A. Atwater. Gate-tunable conducting oxide metasurfaces. *Nano letters*, 16(9):5319–5325, 2016.

[122] B. Ratni, Z. Wang, K. Zhang, X. Ding, A. de Lustrac, G.-P. Piau, and S. N. Burokur. Dynamically controlling spatial energy distribution with a holographic metamirror for adaptive focusing. *Phys. Rev. Applied*, 13:034006, Mar 2020.

[123] M.-.A Milon, D. Cadoret, R. Gillard, and H. Legay. 'surrounded-element' approach for the simulation of reflectarray radiating cells. *IET Microwaves, Antennas Propagation*, 1(2):289–293, 2007.

[124] C. Yann, R. Loison, R. Gillard, M. Labeyrie, and J. Martinaud. A new approach combining surrounded-element and compression methods for analyzing reconfigurable reflectarray antennas. *IEEE Transactions on Antennas and Propagation*, 60(7):3215–3221, 2012.

[125] Constantine A Balanis. *Antenna theory: analysis and design*. John Wiley & Sons, 2016.

[126] A. Epstein and G. V. Eleftheriades. Synthesis of passive lossless metasurfaces using auxiliary fields for reflectionless beam splitting and perfect reflection. *Phys. Rev. Lett.*, 117:256103, Dec 2016.

[127] A. Epstein, J. P. S. Wong, and G. V. Eleftheriades. Low-profile antennas with 100% aperture efficiency based on cavity-excited omega-type biansiotropic metasurfaces. *2016 10th European Conference on Antennas and Propagation, EuCAP 2016*, pages 17–20, 2016.

[128] A. Epstein, J. P. S. Wong, and G. V. Eleftheriades. Cavity-excited huygens' metasurface antennas for near-unity aperture illumination efficiency from arbitrarily large apertures. *Nature communications*, 7:10360, 2016.

[129] D.-H. Kwon and S. A. Tretyakov. Perfect reflection control for impenetrable surfaces using surface waves of orthogonal polarization. *Phys. Rev. B*, 96:085438, Aug 2017.

[130] E. Abdo-Sánchez, M. Chen, A. Epstein, and G. V. Eleftheriades. A leaky-wave antenna with controlled radiation using a bianisotropic huygens' metasurface. *IEEE Transactions on Antennas and Propagation*, 67(1):108–120, 2019.

[131] M. Chen, A. Epstein, and G. V. Eleftheriades. Design and experimental verification of a passive huygens' metasurface lens for gain enhancement of frequency-scanning slotted-waveguide antennas. *IEEE Transactions on Antennas and Propagation*, 67(7):4678–4692, 2019.

[132] M. Born, E. Wolf, A. B. Bhatia, P. C. Clemmow, D. Gabor, A. R. Stokes, A. M. Taylor, P. A. Wayman, and W. L. Wilcock. *Principles of Optics: Electromagnetic Theory of Propagation, Interference and Diffraction of Light*, chapter Elements of the theory of diffraction, pages 412 — 516. Cambridge University Press, 7 edition, 1999.

[133] R.W. Wood. The echelette grating for the infra-red. *The London, Edinburgh, and Dublin Philosophical Magazine and Journal of Science*, 20(118):770–778, 1910.

[134] Henry A. Rowland. Gratings in theory and practice. *The London, Edinburgh, and Dublin Philosophical Magazine and Journal of Science*, 35(216):397–419, 1893.

[135] R. F. Stamm and J. J. Whalen. Energy distribution of diffraction gratings as a function of groove form (calculations by an equation of henry a. rowland). *JOSA*, 36(1):2–12, 1946.

[136] M. Breidne, S. Johansson, L-E. Nilsson, and H. Åhlèn. Blazed holographic gratings. *Optica Acta: International Journal of Optics*, 26(11):1427–1441, 1979.

[137] A. Hessel, J. Schmoys, and D. Y. Tseng. Bragg-angle blazing of diffraction gratings. *J. Opt. Soc. Am.*, 65(4):380–384, Apr 1975.

[138] M. Breidne and D. Maystre. Perfect blaze in non-littrow mountings. *Optica Acta: International Journal of Optics*, 28(10):1321–1327, 1981.

[139] T. Itoh and R. Mittra. An analytical study of the echelette grating with application to open resonators. *IEEE Transactions on Microwave Theory and Techniques*, 17(6):319–327, June 1969.

[140] N. Yu and F. Capasso. Flat optics with designer metasurfaces. *Nature materials*, 13(2):139–150, 2014.

[141] M. Chen, E. Abdo-Sánchez, A. Epstein, and G. V. Eleftheriades. Theory, design, and experimental verification of a reflectionless bianisotropic huygens' metasurface for wide-angle refraction. *Phys. Rev. B*, 97:125433, Mar 2018.

[142] G. Lavigne, K. Achouri, V. S. Asadchy, S. A. Tretyakov, and C. Caloz. Susceptibility derivation and experimental demonstration of refracting metasurfaces without spurious diffraction. *IEEE Transactions on Antennas and Propagation*, 66(3):1321–1330, March 2018.

[143] A. Díaz-Rubio, V. S. Asadchy, A. Elsakka, and S. A. Tretyakov. From the generalized reflection law to the realization of perfect anomalous reflectors. *Science Advances*, 3(8), 2017.

[144] D. Kwon. Lossless scalar metasurfaces for anomalous reflection based on efficient surface field optimization. *IEEE Antennas and Wireless Propagation Letters*, 17(7):1149–1152, July 2018.

[145] Y. Ra'di, D. L. Sounas, and A. Alù. Metagratings: Beyond the limits of graded metasurfaces for wave front control. *Phys. Rev. Lett.*, 119:067404, Aug 2017.

[146] A. Epstein and O. Rabinovich. Unveiling the properties of metagratings via a detailed analytical model for synthesis and analysis. *Phys. Rev. Applied*, 8:054037, Nov 2017.

[147] L. B. Felsen and N. Marcuvitz. *Radiation and scattering of waves*, volume 31. John Wiley & Sons, 1994.

[148] O. Rabinovich and A. Epstein. Analytical design of printed circuit board (pcb) metagratings for perfect anomalous reflection. *IEEE Transactions on Antennas and Propagation*, 66(8):4086–4095, Aug 2018.

[149] S. Tretyakov. *Analytical modeling in applied electromagnetics*. Artech House, 2003.

[150] O. Luukkonen, C. Simovski, G. Granet, G. Goussetis, D. Lioubtchenko, A. V. Raisanen, and S. A. Tretyakov. Simple and accurate analytical model of planar grids and high-impedance surfaces comprising metal strips or patches. *IEEE Transactions on Antennas and Propagation*, 56(6):1624–1632, June 2008.

[151] X. C. Wang, A. Díaz-Rubio, A. Sneck, A. Alastalo, T. Mäkelä, J. Ala-Laurinaho, J. F. Zheng, A. V. Räisänen, and S. A. Tretyakov. Systematic design of printable metasurfaces: Validation through reverse-offset printed millimeter-wave absorbers. *IEEE Transactions on Antennas and Propagation*, 66(3):1340–1351, March 2018.

[152] J. A. Stratton and L. J. Chu. Diffraction theory of electromagnetic waves. *Phys. Rev.*, 56:99–107, Jul 1939.

[153] J. A. Stratton. *Electromagnetic theory*. John Wiley & Sons, Hoboken, New Jersey, 2007.

[154] Y. Li, X. Jiang, R. Li, B. Liang, X. Zou, L. Yin, and J. Cheng. Experimental realization of full control of reflected waves with subwavelength acoustic metasurfaces. *Phys. Rev. Applied*, 2:064002, Dec 2014.

[155] J. Li, C. Shen, A. Díaz-Rubio, S. A. Tretyakov, and S. A. Cummer. Systematic design and experimental demonstration of bianisotropic metasurfaces for scattering-free manipulation of acoustic wavefronts. *Nature communications*, 9(1):1342, 2018.

[156] D. Torrent. Acoustic anomalous reflectors based on diffraction grating engineering. *Phys. Rev. B*, 98:060101, Aug 2018.

[157] P. Packo, A. N. Norris, and D. Torrent. Inverse grating problem: Efficient design of anomalous flexural wave reflectors and refractors. *Phys. Rev. Applied*, 11:014023, Jan 2019.

[158] H. Chalabi, Y. Ra'di, D. L. Sounas, and A. Alù. Efficient anomalous reflection through near-field interactions in metasurfaces. *Phys. Rev. B*, 96:075432, Aug 2017.

[159] V. Popov, F. Boust, and S. N. Burokur. Constructing the near field and far field with reactive metagratings: Study on the degrees of freedom. *Phys. Rev. Applied*, 11:024074, Feb 2019.

[160] R. Marqués, F. Medina, and R. Rafii-El-Idrissi. Role of bianisotropy in negative permeability and left-handed metamaterials. *Phys. Rev. B*, 65:144440, Apr 2002.

[161] B. Sauviac, C. R. Simovski, and S. A. Tretyakov. Double split-ring resonators: Analytical modeling and numerical simulations. *Electromagnetics*, 24(5):317–338, 2004.

[162] S. Babar and J. H. Weaver. Optical constants of Cu, Ag, and Au revisited. *Appl. Opt.*, 54(3):477–481, Jan 2015.

[163] J. Kischkat, S. Peters, B. Gruska, M. Semtsiv, M. Chashnikova, M. Klinkmüller, O. Fedosenko, S. Machulik, A. Aleksandrova, G. Monastyrskyi, Y. Flores, and W. T. Masselink. Mid-infrared optical properties of thin films of aluminum oxide, titanium dioxide, silicon dioxide, aluminum nitride, and silicon nitride. *Appl. Opt.*, 51(28):6789–6798, Oct 2012.

[164] R. C. Compton, L. B. Whitbourn, and R. C. McPhedran. Strip gratings at a dielectric interface and application of babinet's principle. *Appl. Opt.*, 23(18):3236–3242, Sep 1984.

[165] Ieee standard for definitions of terms for antennas. *IEEE Std 145-2013 (Revision of IEEE Std 145-1993)*, pages 1–50, 2014.

[166] L. Josefsson and P. Persson. *Introduction*, pages 1–13. 2006.

[167] P. Nayeri, F. Yang, and A. Elsherbeni. *Reflectarray Antennas: Theory, Designs and Applications*. Wiley Online Library, 2018.

[168] H. Chireix. Antennes à rayonnement zénithal réduit. *L'Onde Electrique*, 15:440–456, 1936.

[169] H. L. Knudsen. The field radiated by a ring quasi-array of an infinite number of tangential or radial dipoles. *Proceedings of the IRE*, 41(6):781–789, 1953.

[170] J Dorey and G Garnier. Rias, synthetic impulse and antenna radar. *ONDE ELECTRIQUE*, 69(6):36–44, 1989.

[171] J.-M. Colin. Phased array radars in france: present and future. In *Proceedings of International Symposium on Phased Array Systems and Technology*, pages 458–462, 1996.

[172] B. Ratni, W. A. Merzouk, A. de Lustrac, S. Villers, G. Piau, and S. N. Burokur. Design of phase-modulated metasurfaces for beam steering in fabry–perot cavity antennas. *IEEE Antennas and Wireless Propagation Letters*, 16:1401–1404, 2017.

[173] H. Li, Y. B. Li, J. L. Shen, and T. J. Cui. Low-profile electromagnetic holography by using coding fabry–perot type metasurface with in-plane feeding. *Advanced Optical Materials*, n/a(n/a):1902057.

[174] S. Maci, G. Minatti, M. Casaletti, and M. Bosiljevac. Metasurfing: Addressing waves on impenetrable metasurfaces. *IEEE Antennas and Wireless Propagation Letters*, 10:1499–1502, 2011.

[175] M. Ettorre, S. M. Rudolph, and A. Grbic. Generation of propagating bessel beams using leaky-wave modes: Experimental validation. *IEEE Transactions on Antennas and Propagation*, 60(6):2645–2653, 2012.

[176] M. Ettorre and A. Grbic. Generation of propagating bessel beams using leaky-wave modes. *IEEE Transactions on Antennas and Propagation*, 60(8):3605–3613, 2012.

[177] G. Minatti, M. Faenzi, E. Martini, F. Caminita, P. De Vita, D. González-Ovejero, M. Sabbadini, and S. Maci. Modulated metasurface antennas for space: Synthesis, analysis and realizations. *IEEE Transactions on Antennas and Propagation*, 63(4):1288–1300, 2015.

[178] P. Katehi and N. Alexopoulos. On the modeling of electromagnetically coupled microstrip antennas–the printed strip dipole. *IEEE Transactions on Antennas and Propagation*, 32(11):1179–1186, November 1984.

[179] S. A. Schelkunoff. A mathematical theory of linear arrays. *The Bell System Technical Journal*, 22(1):80–107, Jan 1943.

[180] K. Huang, F. Qin, H. Liu, H. Ye, C-W. Qiu, M. Hong, B. Luk'yanchuk, and J. Teng. Planar diffractive lenses: Fundamentals, functionalities, and applications. *Advanced Materials*, 30(26):1704556, 2018.

[181] V. S. Asadchy, Y. Ra'di, J. Vehmas, and S. A. Tretyakov. Functional metamirrors using bianisotropic elements. *Phys. Rev. Lett.*, 114:095503, Mar 2015.

[182] V. S. Asadchy, A. Díaz-Rubio, and S. A. Tretyakov. Bianisotropic metasurfaces: physics and applications. *Nanophotonics*, 7(6):1069–1094, 2018.

[183] A. V. Oppenheim and R. W. Schafer. *Discrete-time Signal Processing*. Prentice-Hall, Inc., Upper Saddle River, NJ, USA, 1989.

[184] Mavr-011020-1411, www.macom.com/products/product-detail/mavr-011020-1411.

[185] E. Abbe. Beiträge zur theorie des mikroskops und der mikroskopischen wahrnehmung. *Archiv für mikroskopische Anatomie*, 9(1):413–418, 1873.

[186] L. Novotny and B. Hecht. *Principles of nano-optics*. Cambridge university press, 2012.

[187] C. Pfeiffer, N. K. Emani, A. M. Shaltout, A. Boltasseva, V. M. Shalaev, and A. Grbic. Efficient light bending with isotropic metamaterial huygens' surfaces. *Nano letters*, 14(5):2491–2497, 2014.

[188] N. Yu, P. Genevet, F. Aieta, M. A. Kats, R. Blanchard, G. Aoust, J. Tetienne, Z. Gaburro, and F. Capasso. Flat optics: Controlling wavefronts with optical antenna metasurfaces. *IEEE Journal of Selected Topics in Quantum Electronics*, 19(3):4700423–4700423, 2013.

List of publications

Publication in scientific journals
in the framework of the PhD work

1. **V. Popov**, F. Boust, and S. N. Burokur. Controlling diffraction patterns with metagratings. Phys. Rev. Applied, 10:011002, Jul 2018.

2. **V. Popov**, F. Boust, and S. N. Burokur. Constructing the near field and far field with reactive metagratings: Study on the degrees of freedom. Phys. Rev. Applied, 11:024074, Feb 2019.

3. **V. Popov**, M. Yakovleva, F. Boust, J-L. Pelouard, F. Pardo, and S. N. Burokur. Designing metagratings via local periodic approximation: From microwaves to infrared. Phys. Rev. Applied, 11:044054, Apr 2019.

4. **V. Popov**, A. Díaz-Rubio, V. Asadchy, S. Tcvetkova, F. Boust, S. Tretyakov, and S. N. Burokur. Omega-bianisotropic metasurface for converting a propagating wave into a surface wave. Phys. Rev. B, 100:125103, Sep 2019.

5. **V. Popov**, F. Boust, and S. N. Burokur. Beamforming with metagratings at microwave frequencies: Design procedure and experimental demonstration. IEEE Transactions on Antennas and Propagation, 68(3): 1533–1541, March 2020.

6. **V. Popov**, S. N. Burokur, and F. Boust. Conformal sparse metasurfaces for wavefront manipulation, 2020, Under review at *Physical Review Applied*.

7. **V. Popov**, B. Ratni, S. N. Burokur, and F. Boust. Strongly non-local reconfigurable sparse metasurface, 2020, Under review at *Nature Communications*.

Publication in scientific journals
outside the framework of the PhD work

1. **V. Popov**, A. V. Lavrinenko, and A. Novitsky. Operator approach to effective medium theory to overcome a breakdown of maxwell garnett approximation. Phys. Rev. B, 94:085428, Aug 2016.

2. **V. Popov**, A. V. Lavrinenko, and A. Novitsky. Surface waves on multilayer hyperbolic metamaterials: Operator approach to effective medium approximation. Phys. Rev. B, 97:125428, Mar 2018.

3. **V. Popov**, S. Tretyakov, and A. Novitsky. Brewster effect when approaching exceptional points of degeneracy: Epsilon-near-zero behavior. Phys. Rev. B, 99:045146, Jan 2019.

International conferences
in the framework of the PhD work

1. **V. Popov**, F. Boust, S. N. Burokur. Conversion of TE propagating waves into TE surface waves with non-constant gradient metasurfaces. Third International Workshop on Metamaterials-by-Design, Madrid, Spain, Dec 14-15, 2017.

2. **V. Popov**, F. Boust, S. N. Burokur. Highly efficient multichannel reflection with metagratings. Metamaterials2018, Espoo, Finland, Aug 27 - Sep 1, 2018.

3. **V. Popov**, F. Boust, S. N. Burokur. Metagratings for efficient control of diffraction patterns. Workshop GRADIENT, Lille, France, Oct 18-19, 2018.

4. **V. Popov**, F. Boust, S. N. Burokur. Designing metagratings via local periodic approximation. International Symposium on Electromagnetic Theory (EMTS), San Diego, CA USA, May 27-31, 2019.

5. **(Invited) V. Popov**, F. Boust, S. N. Burokur. Constructing scattering patterns with metagratings: From theory to design. IV International Conference on Metamaterials and Nanophotonics, St. Petersburg, Russia, Jul 15-19, 2019.

6. **V. Popov**, F. Boust, S. N. Burokur. Beamforming with reconfigurable metagrating: Design and experimental demonstration. Asia-Pacific Microwave Conference (APMC 2019), Singapore, Dec 10-13, 2019.

7. **V. Popov**, B. Ratni, F. Boust, S. N. Burokur. Reconfigurable sparse metasurface: Beamforming beyond phase gradient heuristics. EuCAP 2020, Copenhagen, Denmark, Mar 15-20, 2020.

French conferences & Scientific days

1. **(Invited) V. Popov**, F. Boust, S. N. Burokur. Engineering multichannel reflections from metagratings. Journée "Matériaux fonctionnalisés pour le rayonnement d'antennes". GDR Ondes/CCT CNES, Paris, Oct 18, 2018.

2. **V. Popov**, F. Boust, S. N. Burokur. Généralisation des réseaux d'antennes passifs. Conférence plénière GDR Ondes, Gif-sur-Yvette, Oct 28-29, 2019.

3. **V. Popov**, F. Boust, B. Ratni, S. N. Burokur. Métasurfaces à faible densité d'éléments: Application aux antennes. Journées scientifiques du CNFRS "Réseaux du futur: 5G et au-delà", Palaiseau, Mar 11-13, 2020.

International conferences
outside the framework of the PhD work

1. **V.V. Popov**, A.V. Novitsky. Generalized hyperbolic metamaterials. 58th Scientific Conference for Young Students of Physics and Natural Sciences Open Readings 2015, Vilnius, Lithuania, Mar, 2015.

2. **V. Popov**. Asymmetric hyperbolic metamaterials. Days on diffraction 2015, Saint-Petersburg, Russia, May 25-29 , 2015.

3. **V. Popov**, A. Novitsky. Elliptic-hyperbolic metamaterials on the base of uniaxial crystals. V Congress of Belarusian Physicists, Minsk, Belarus, Oct 27-30, 2015.

4. **V. Popov**, A. Novitsky. Propagation of adjoined Bloch waves in stratified periodic structures with isotropic layers. Saint-Petersburg OPEN 2016, Saint-Petersburg, Russia, Mar 28–30, 2016.

5. (**3rd prize in Student Paper Competition**) **V. Popov**, A. Novitsky. Advanced effective medium approximation for subwavelength multilayers to overcome Maxwell-Garnet approach breakdown. Metamaterials2016, Crete, Greece, Sep 17-22, 2016.

6. **V. Popov**, A. Novitsky. Spatially-dispersive surface modes on interfaces of layered hyperbolic metamaterials. METANANO 2017, Russia, Vladivostok, Sep 18-22, 2017.

7. **(Invited) V. Popov**, S. Tretyakov, A. Novitsky. Epsilon-Near-Zero Properties of Periodic Multilayers Operating in Photonic Crystal Regime. International Symposium on Electromagnetic Theory (EMTS), San Diego, CA USA, May 27-31, 2019.

université PARIS-SACLAY

ÉCOLE DOCTORALE
Physique et ingénierie : Electrons, Photons, Sciences du vivant (EOBE)

Titre: Métasurfaces éparses conformes et reconfigurables: modèles analytiques avancés et applications antennaires

Mots clés: Métaréseau, Fonction de Green, Métasurface Conforme, Métasurface Reconfigurable, Dépointage de Faisceau, Focalisation

Résumé: Cette thèse de doctorat traite des métasurfaces constituées de diffuseurs sub-longueur d'onde conçus pour contrôler les fronts d'ondes électromagnétiques. Elle introduit des modèles analytiques et numériques inédits qui résolvent le problème de diffusion inverse en tenant compte des interactions entre éléments de la métasurface. Le manuscrit se concentre plus particulièrement sur des réseaux, périodiques ou non, de fils structurés, permettant la réalisation d'antennes reconfigurables électroniquement. Le manuscrit est divisé en deux grandes parties, l'une sur des arrangements périodiques de fils appelés métaréseaux et l'autre sur des métasurfaces éparses sans caractère périodique. Dans les deux cas, des réalisations expérimentales dans le domaine microondes viennent appuyer les développements théoriques. Dans la première partie, les conditions théoriques conduisant à un contrôle total des ordres de diffraction rayonnés par des métaréseaux, dont la période est composée de plusieurs fils structurés individuellement, sont établies et l'importance du contrôle du champ proche est alors soulignée. Par ailleurs, une expression analytique des paramètres effectifs des fils, s'appuyant sur une simulation numérique, a également été établie. Il devient ainsi possible d'exploiter des géométries quelconques pour des métaréseaux fonctionnant dans les domaines allant des microondes à l'optique. Dans la deuxième partie de la thèse, le modèle analytique des métaréseaux, réservé aux distributions périodiques planes, est généralisé aux distributions non périodiques de fils disposés sur des surfaces quelconques en s'appuyant sur le calcul de la fonction de Green. Ce concept est appliqué à des métasurfaces éparses intervenant dans une cavité Fabry-Perot ou dans une antenne semi-cylindrique. Enfin, la démarche est utilisée pour concevoir une métasurface éparse plane reconfigurable. Un prototype a été réalisé et utilisé pour démontrer expérimentalement le contrôle dynamique de l'onde, en champ lointain et en champ proche, via des applications telles que le dépointage de faisceau, la création de faisceaux multiples ou encore la focalisation au-delà de la limite de diffraction.

Title: Conformal and reconfigurable sparse metasurfaces: advanced analytical models and antenna applications

Keywords: Metagrating, Green's function, Conformal Metasurface, Reconfigurable Metasurface, Beam-steering, Focusing

Abstract: This PhD thesis deals with electromagnetic metasurfaces for wavefront manipulation represented by arrays of scatterers engineered at sub-wavelength scale. The manuscript develops novel analytical and numerical models that allow one to solve the inverse scattering problem by taking into account all interactions between elements of a metasurface. Specifically, the manuscript focuses on sparse arrays, periodic or not, of structured wires for the application to electronically reconfigurable antennas. The manuscript is divided into two main parts, one on periodic arrangements of wires called metagratings and one on sparse metasurfaces when there is no periodicity imposed. Each part is endorsed by experiments performed at microwave frequencies. In the first part, theoretical conditions for arbitrary control of the diffraction patterns with metagratings, whose period is composed of multiple individually-engineered wires, are established and importance of the near-field regulation is highlighted. Moreover, an analytical retrieval technique is developed and allows one to consider, with the help of full-wave simulations, arbitrarily structured wires for metagratings operating from microwave to optical domains. In the second part of the thesis, the analytical model of metagratings is generalized, from planar periodic, to arbitrarily-shaped non-periodic distributions of wires by means of numerical calculation of a Green's function. The concept is applied to design sparse metasurfaces in Fabry-Perot cavity and semi-cylindrical antenna configurations. Finally, the approach is applied to design a reconfigurable planar sparse metasurface. A fabricated sample is exploited to experimentally demonstrate dynamic control of the far-field radiation pattern and the near-field intensity distribution. As such beam-steering, multi-beam manipulation and subdiffraction focusing are shown.

Université Paris-Saclay
Espace Technologique / Immeuble Discovery
Route de l'Orme aux Merisiers RD 128 / 91190 Saint-Aubin, France